Inaugural-Dissertation

zur
Erlangung der Doktorwürde
der
Naturwissenschaftlich-Mathematischen Gesamtfakultät
der
Ruprecht-Karls-Universität
Heidelberg

vorgelegt von
Thomas Wick, M. Sc.
aus Siegen-Weidenau

Tag der mündlichen Prüfung: _____

Adaptive Finite Element Simulation of Fluid-Structure Interaction with Application to Heart-Valve Dynamics

4. November 2011

Gutachter: Prof. Dr. Dr. h. c. Rolf Rannacher

Gutachter: _____

Abstract

The goal of this work is the development of concepts for the efficient numerical solution of fluid-structure interaction (FSI) problems with applications to heart-valve dynamics. The main motivation for further development in this field is an increasing demand from the medical community for scientifically rigorous investigations of cardiovascular diseases, which are responsible for the major fraction of mortalities in industrialized countries.

In this work, the ALE (arbitrary Lagrangian Eulerian) description of fluid equations is utilized for the numerical modeling and simulation of fluid-structure interactions. Using this approach, the fluid equations can easily be coupled with structural deformations. The focal goal is the modeling, numerical analysis, and simulation of prototypical heart-valve dynamics, which requires the investigation of the following issues: the analysis of various fluid-mesh motion techniques, a comparison of different second-order time-stepping schemes, and the prescription of specific boundary conditions on the artificial outflow boundary. To control computational costs, we apply a simplified version of an a posteriori error estimation using the dual weighted residual (DWR) method. This method is used for mesh adaption during the computation. The last, novel aspect comprises a discussion of optimal control problems for wall stress minimization, in which the state is determined by a fluid-structure interaction system.

The concepts developed in this work are demonstrated with several numerical tests in two and three dimensions. The programming code is validated by computing several FSI benchmark tests. The focal computation is related to a prototypical two-dimensional aortic heart-valve simulation. The concepts illustrated by this example were developed in cooperation with a cardiologist.

Zusammenfassung

Das Ziel dieser Arbeit ist die Entwicklung effizienter numerischer Konzepte zum Lösen von Fluid-Struktur Interaktionen (FSI) mit Anwendung auf Herzklappensimulationen. Die Hauptmotivation zu einem weiteren Beitrag in diesem Forschungsgebiet ist durch eine steigende Nachfrage der Medizingemeinschaft, an wissenschaftlich rigorosen Untersuchungen von Krankheiten des Herz-Kreislaufsystems, begründet. Diese Krankheiten sind die häufigste Todesursache in der westlichen industrialisierten Welt.

Bei der hier behandelten FSI-Problematik wird das Fluidproblem mittels einer ALE ('arbitrary Lagrangian Eulerian') Transformation auf eine feste Referenzkonfiguration abgebildet. Durch diesen Ansatz kann vergleichsweise einfach das Fluid mit den Strukturgleichungen gekoppelt werden. Das Hauptziel, Modellierung, numerische Analyse und Simulation von prototypischen Herzklappendynamiken erfordern die nachfolgend erklärten Vorarbeiten. Speziell werden verschiedene Gleichungen zur Definition der ALE-Abbildung untersucht, eine vergleichende Studie verschiedener Zeitschrittverfahren zweiter Ordnung durchgeführt sowie spezielle Randbedingungen am künstlichen Ausflussrand studiert. Zur Kontrolle des Rechenaufwands leiten wir eine vereinfachte Form der a posteriori Fehlerabschätzung mit dual gewichteten Residuen (DWR) her. Diese Methodik wird zur Gitteradaption verwendet. Darüber hinaus werden prototypische Optimalsteuerungsprobleme zur Wandspannungsminimierung besprochen, bei denen der Zustand durch ein FSI-System gegeben ist.

Die entwickelten Konzepte werden mittels verschiedener numerischer Tests in 2D und 3D gefestigt. Insbesondere wird der Programmcode durch den Abgleich mit FSI Benchmark Resultaten validiert. Den Schwerpunkt bilden prototypische Tests zu 2D-Herzklappensimulationen. Die Konzeption dieser Tests ist in Zusammenarbeit mit einem Kardiologen entstanden.

Contents

1 Introduction

In this work, we design efficient numerical algorithms for fluid-structure interactions (FSI), focusing on the main component of the human circulatory system: the heart. More specifically, we are interested in the modeling and simulation of the dynamics of the aortic heart-valve, which ejects oxygenated blood from the left ventricle into the aorta. This process implies the interaction of blood (the fluid) with both the heart walls (modeled as a structure) and the blood vessel walls (again modeled as a structure). The development of numerical algorithms for this application was inspired by a collaboration with a cardiologist [103].

The majority of mortalities in industrialized countries are due to cardiovascular diseases. For this reason, there is an increasing demand from the medical community for rigorous and quantitative investigations of the human cardiovascular system, with the goal of detecting and predicting diseases, such as atherosclerosis, aneurysms, and aortic dissections (e.g., [80, 81, 103, 110], and the many references cited therein).

However, the mathematical modeling and numerical simulations of processes of the human circulatory system remain challenging. For instance, it remains to find appropriate structural boundary conditions on the outflow section in a compliant blood vessel with elastic walls. Additionally, numerical simulations have a high computational cost for three-dimensional simulations of the whole cardiovascular system. Consequently, such simulations are still prohibitive; despite further development of hardware-oriented code and parallel programming in the last years. Thus, the final goals to deliver patient specific information and to compare simulations with clinical data remains a tough task. Third, it remains to develop methods for steering physical processes in the cardiovascular system. For example, a medical doctor recognized a certain deficiency; namely, too high wall stress due to hypertension: what can be done to minimize the wall stress. This situation can be modeled as an optimal control problem in which the wall stress is minimized.

In this study, we aim to give further input to resolve the difficulties that are raised in the previous paragraph, but more from the prototypical point of view. A key aspect is a focus on structural boundary conditions on the outflow section. This subject should not be neglected because the radius of the aorta may vary by up to ten per cent between diastole and systole (the two phases in the cardiac cycle) [56]. This is a large displacement of the blood vessel wall, which affects both the flow field and the blood vessel dynamics. A deeper investigation of such dynamics in valve-blood-wall interactions is a novel contribution. For standard blood vessel computations, a first investigation for coupling fluid and structural boundary conditions on the outflow is made in a prior work [55].

Second, we investigate efficient methods to reduce the computational cost for finite element simulations, without the necessity to develop a fully parallelized programming code. Our solution approach is based on the development of efficient strategies for adaptive mesh refinement that is applied to heart-valve related dynamics. Finally, an optimal control approach is utilized to minimize too high stresses in the arterial wall. The mathematical formulation in terms of unconstrained optimization subject to fluid-structure interaction is novel.

In summary, with the development of the previous explained methods, we provide fundamental concepts for the efficient numerical solution of fluid-structure interaction with application to heart-valve dynamics. In fact, each of these mentioned directions can be further developed beyond the presented content. We shall give some hints in the conclusions.

In the following paragraphs, we describe in more detail our solution approach. As already mentioned previously, the mathematical method of choice for the construction of appropriate models for heart-valve settings is based on monolithically coupled fluid-structure interactions. More specifically, the *monolithic* framework, where the coupled equations are solved simultaneously in a fully coupled fashion, belongs to the class of *strongly coupled* approaches. In this framework, the interface conditions, the continuity of the velocities and the normal stresses across the interface are satisfied after temporal discretization. The use of a monolithic formulation plays a key role in our investigations, and it is motivated by three considerations:

- The so-called added-mass effect (where the densities of the fluid and the structure are of the same order).
- Goal-oriented error estimation with the dual weighted residual (DWR) method.
- The solution of optimal control problems with the Euler-Lagrange method.

A monolithic framework of the coupled problem provides good stability properties for the solution algorithm (which is related to the first item). It is an absolute necessity to address the other two issues.

Several solution algorithms for treating heart-valve dynamics have already been proposed [90, 109, 120, 128, 140]. Presently, the predominant means of treating (realistic) heart-valve simulations in the biomedical context uses fictitious domain methods (see, e.g., [4]). Because we are interested in a fully coupled monolithic formulation that can easily be utilized for goal-oriented error estimation and gradient-based optimization, in the current study, we employ the well-known *arbitrary Lagrangian Eulerian (ALE) method*. In this method, the fluid is reformulated on an arbitrary moving mesh that matches the structural coordinates so as to compensate for the discrepancy between Eulerian coordinates (used for fluids) and the Lagrangian framework (used for structures) [40, 60, 76, 85, 108]. The advantages of the ALE method are the use of a common mesh for the coupled problem, the exact representation of the fluid-structure interface (interface-tracking), and the consequently clearly defined quadrature rules in each mesh cell. To track the interface has the advantage to control the mesh resolution near the interface (i.e., to refine the mesh geometrically).

The fluid mesh motion is driven by the motion of the interface. However, the major disadvantage of the ALE method is the limitation of arbitrarily designed meshes due to a degeneration of fluid mesh cells when dealing with large structural deflections. For instance, this drawback can be resolved using sophisticated mesh motion models (as addressed below and studied in [70, 126, 149]) or with the construction of a new reference configuration for the ALE fluid formulation, which is known as the remeshing technique. Finally, we mention that the ALE approach is not capable of modeling topological changes such as those occurring when two valves come into contact. However, this last point is of reduced importance in our studies.

To achieve the goal of prototypical heart-valve simulations, we perform the steps listed below. Their outcomes are the novel topics raised in this thesis. Specifically, we study the following:

- A comparison of different fluid mesh motion models for fluid-structure interactions.
- Modeling blood vessel walls with hyperbolic structure equations, which leads to significant reflections of structure waves at the outflow boundary in the presence of standard Dirichlet or Neumann conditions. In this mode, the question is how to prevent the backflow of structural waves induced by the hyperbolic nature of the structure equations. This problem is resolved by prescribing a damped hyperbolic wave equation in an artificial layer that is attached to the physical domain of interest. This investigation implies new aspects for both the theory and the numerical simulation; both are examined here. However, this prescription is questionable from the physical point of view because it remains an open question as to which boundary conditions most accurately reproduce physical behavior [59, 138].
- A priori stability estimates of the coupled problem with incorporation of the damped hyperbolic structure equations. These results are derived for the continuous level and the time-discretized level (for second-order time-stepping schemes).
- The coupling of boundary conditions for the fluid and pressure (absorbing conditions) with the aforementioned structural conditions. This coupling is used to study the interaction between the different boundary conditions and their influence on the dynamics of the coupled problem. For computations in a straight channel, this coupling should be able to reduce the propagation of pressure and structural waves.
- The coupling of multiple structures with varying coefficients and different constitutive tensors (that reflect the different physical behavior of the heart and the aorta) is examined in a monolithic fashion for which we state the corresponding structural interface conditions. Finally, these findings are used to model prototypical heart-valve dynamics with two layers of arterial tissue and various structural models.
- Application of the DWR method to fluid-structure interaction with application to heart-valve settings.
- Optimal control problems where the state is given in terms of fluid-structure interactions. In this approach, we aim to minimize the wall stresses along the interface between the blood and the arterial section.

Outline of this thesis

Chapter 2: Notations, Spaces, and Equations

First, we introduce the basic notation used throughout this thesis. A brief introduction to the usual Lebesgue and Sobolev spaces is given. Next, we introduce the basics of kinematics and we derive the equations fluids and structures in their natural frameworks. We close this chapter by introducing the hyperbolic structure equations with linear weak and linear strong damping.

Chapter 3: Fluid-Structure Interaction in ALE Coordinates

In Chapter 3, we derive a monolithic setting for the coupled problem by transforming the fluid equations via the arbitrary Lagrangian-Eulerian (ALE) approach. Moreover, we explain different ways of constructing the fluid mesh motion, i.e., the concrete definition of the ALE transformation. We state the coupled problem (including the damped wave equation) in two different fashions. First, we work with the fluid equations in moving domains, which is convenient for proving a priori stability estimates. Second, we state the practicable problems, with all equations being described in a fixed domain. In Section 3.5, we couple the damped wave equation with absorbing fluid/pressure conditions. The latter conditions account for pressure waves that are caused by the compliance of blood vessels and pulsatile fluid flows.

Chapter 4: Optimal Control for Steady-State FSI in ALE Coordinates

Chapter 4 addresses the numerical solution of constrained optimization problems in which the constraint is given by means of a fluid-structure interaction system. We adopt the minimization of wall stresses measured on the interface between the blood and the arterial wall as a cost functional. The control acts either as an nonhomogeneous Neumann condition on an additional boundary (see, e.g., an additional inflow through a bypass) or, in a second setting, we control the stiffness of the valves via the Lamé parameter (e.g., development of artificial heart valves). The numerical solution of similar problems (such as parabolic equations and steady-state Navier-Stokes equations) has been extensively investigated over the last several years. We apply these well-developed algorithms to our framework using well-tested optimization algorithms [16] and various choices for finite elements [8]. The outcome is a new software library package [58].

Chapter 5: Discretization

This chapter is devoted to the discretization of the continuous problems introduced in the previous chapters. We address aspects of the implementation of a temporal discretization, that is based on finite differences. Specifically, we present One-Step-θ schemes (e.g., in[133]) and the Fractional-Step-θ scheme [62] in a practicable ALE fashion for the monolithic problem. We proceed with the stability analysis of a variant of the second-order Crank-Nicolson scheme on moving meshes. This analysis is first elaborated for pure fluid problems and subsequently extended to a fully coupled fluid-structure interaction problem. We close by suggesting a way to achieve stable long-term computations for fluid-structure interaction problems. This result is substantiated with numerical tests.

The spatial discretization is performed using a standard Galerkin finite element approach. The solution of the nonlinear discretized system can be achieved with a Newton method, which is attractive because it provides robust and rapid convergence. The Jacobian matrix is derived by exact linearization. To solve the linear equation systems, we use a direct solver (UMFPACK [37]). This choice is reasonable because we are mainly interested in long-term computations with a low number of spatial unknowns. The development of iterative linear solvers is difficult for fully coupled problems; however, suggestions have been made [5, 68, 69, 116]. We use one of these ideas (following [68]) to develop such a solver.

Chapter 6: Adaptive Mesh Refinement

In Chapter 6, we provide an introduction to automatic mesh adaptation techniques. We restrict our considerations to spatial refinement and we neglect temporal adaptation. We consider refinement techniques based on heuristic arguments, such as geometry-based indicators and smoothness-based indicators derived from the computed discrete solution. We also introduce the *dual weighted residual* (DWR) method, which can be used to estimate the error of a given goal functional. This method is used to extract mesh refinement indicators to drive an automatic mesh adaption procedure.

Chapter 7: Numerical Results for Stationary Problems

To derive the goal of a prototypical heart-valve simulation, we perform several numerical tests that serve to evaluate the specific difficulties that must be overcome to reach our final goal, beginning with numerical tests in steady-state regimes.

We perform a test case from computational structure mechanics (CSM) that is used to compare three different mesh motion models. We continue with a test in which different local mesh refinement techniques are studied. Next, we analyze an optimal control problem with wall stress minimization, where the state is given by a fluid-structure interaction system. We close this chapter with a study of a three-dimensional test case. In this example, our three-dimensional programming code for nonstationary problems is validated for two different mesh motion models by computing a quasi-stationary example.

Chapter 8: Numerical Results for Nonstationary Problems

In Chapter 8, we consider numerical tests for solving nonstationary fluid-structure interaction problems. We start with a study of three different mesh motion models and a comparison of different structure models. Second, we consider the fluid-structure interaction benchmark test FSI 2 [30, 84], which is used to compare the different mesh models for fully dynamic processes. In the third test case, we analyze the consequences of weak and strong damping, and we couple absorbing fluid/pressure conditions with our proposed damped structure equations in a compliant channel. Finally, we present the *core* simulation of this thesis, in this case, we verify our theoretical considerations of the damped structure equations and their energy absorbing properties. Work forming a part of this section received the *Jan Szmelter Award* of the Polish Association for Computational Mechanics in May, 2011. We close this section with a numerical example of a coupled fluid-multiple-structure interaction problem. This verification has important consequences

for possible future applications of arterial tissue modeling with prestressed material models [56, 78, 79]. All computations were performed with the software packages deal.II and DOpE [8, 58]. Specifically, we developed a tutorial-like program in which we explain how to solve monolithically coupled fluid-structure interactions in deal.II [150]. The Visit [142] visualization toolkit is used to visualize the numerical solutions.

Chapter 9: Conclusions and Outlook

We close the thesis by a recapitulation of the presented focal results and we give ideas for future work.

References

Several results of the thesis at hand have been published previously in peer-reviewed journals, conference proceedings, or recently submitted: [89, 118, 146–150]. Our programming code for solving nonstationary fluid-structure interactions was first validated with the help of the FSI-benchmark tests (see [30] and later in this thesis). Our contributed results are summarized in [135], p. 419, 422, and 423 (Method 2b).

Outlook to the next chapter

With the outline and goals of this thesis in mind, we begin in the next chapter with the presentation of the basic relations and equations, which are required to formulate fluid-structure interaction problems.

2 Notation, Spaces, and Equations

In this chapter, we introduce the notation that is used throughout this thesis. Moreover, we present the equations for the fluid and the structure in their natural frameworks. Specifically, fluid flows are normally described in an Eulerian framework, whereas structural deformations are modeled in Lagrangian coordinates. Furthermore, we introduce the arbitrary Lagrangian Eulerian (ALE) framework. We close this chapter by introducing the second-order (in time) hyperbolic equation. This equation is supplemented with linear weak and linear strong damping terms.

2.1 Basic notation

Throughout this thesis, we use standard function spaces. Let $\Omega \subseteq \mathbb{R}^d, d \in \{2,3\}$ be a bounded domain with boundary $\partial\Omega$. We generally assume the boundary to be Lipschitzian. A precise definition is given in [1, 66]. The outer unit normal vector to $\partial\Omega$ is denoted by n.

We denote by $\Omega := \Omega(t) \subset \mathbb{R}^d$, $d = 2, 3$, the domain of the fluid-structure interaction problem. This domain consists of two time-dependent subdomains $\Omega_f(t)$ and $\Omega_s(t)$. The interface between both domain is denoted by $\Gamma_i(t) = \partial\Omega_f(t) \cap \partial\Omega_s(t)$. The initial (or later reference) domains are denoted by $\widehat{\Omega}_f$ and $\widehat{\Omega}_s$, respectively, with the interface $\widehat{\Gamma}_i = \partial\widehat{\Omega}_f \cap \partial\widehat{\Omega}_s$. Furthermore, we denote the outer boundary by $\partial\widehat{\Omega} = \widehat{\Gamma} = \widehat{\Gamma}_D \cup \widehat{\Gamma}_N$ where $\widehat{\Gamma}_D$ and $\widehat{\Gamma}_N$ denote Dirichlet and Neumann boundaries, respectively. For the convenience of the reader and when we expect no confusion, we omit the explicit time-dependence and we use $\Omega := \Omega(t)$ to indicate time-dependent domains. Throughout this thesis, we indicate with 'f' and 's' suffixes, fluid and structure related terms, respectively.

Function spaces on fixed domains

We adopt standard notation for the usual Lebesgue and Sobolev spaces [1, 152]. Let $X \subset \mathbb{R}^d, d = 2, 3$ be a time-independent domain. For instance, we later use $X := \widehat{\Omega}_f$ or $X := \widehat{\Omega}_s$. We indicate by $L^p(X), 1 \leq p \leq \infty$ the standard Lebesgue space that consists of measurable functions u, which are Lebesgue-integrable to the p-th power. The set $L^p(X)$ forms a Banach space with the norm $\|u\|_{L^p(X)}$. The Sobolev space $W^{m,p}(X), m \in \mathbb{N}, 1 \leq p \leq \infty$ is the space of functions in $L^p(X)$ that have distributional derivatives of order up to m, which belong to $L^p(X)$. For $p = 2, H^m(X) := W^{m,2}(X)$ is a Hilbert space equipped with the norm $||\cdot||_{H^m(X)}$ [152]. Finally, we indicate the subspace $W^{m,p}(X)$ of functions with zero trace

on ∂X by $W_0^{m,p}(X)$. Specifically, we define $H_0^1(X) = \{u \in H^1(X) : u = 0 \text{ on } \Gamma_D \subset \partial X\}$. We use frequently the short notation

$$\hat{V}_X := H^1(X), \quad \hat{V}_X^0 := H_0^1(X),$$

and

$$\hat{L}_X := L^2(X), \quad \hat{L}_X^0 := L^2(X)/\mathbb{R}.$$

Specifically, we introduce the trial and the test space of the velocity variables in the fluid domain,

$$\hat{V}_{f,\hat{v}}^0 := \{\hat{v}_f \in H_0^1(\widehat{\Omega}_f) : \hat{v}_f = \hat{v}_s \text{ on } \widehat{\Gamma}_i\}.$$

Moreover, we introduce the trial and the test spaces for the artificial displacement (for the mesh moving) in the fluid domain,

$$\hat{V}_{f,\hat{u}}^0 := \{\hat{u}_f \in H_0^1(\widehat{\Omega}_f) : \hat{u}_f = \hat{u}_s \text{ on } \widehat{\Gamma}_i\},$$
$$\hat{V}_{f,\hat{u},\widehat{\Gamma}_i}^0 := \{\hat{\psi}_f \in H_0^1(\widehat{\Omega}_f) : \hat{\psi}_f = \hat{\psi}_s \text{ on } \widehat{\Gamma}_i \subset \partial X\}.$$

The dual space of $H_0^m(X)$ is denoted by $H^{-m}(X)$. We indicate the duality pairing between $H^{-m}(X)$ and $H_0^m(X)$ by

$$\langle f, u\rangle, \quad f \in H^{-m}(X), \quad u \in H_0^m(X).$$

The dual space is a Banach space with the norm

$$\|f\|_{H^{-m}(X)} := \sup_{\varphi \in H_0^m(X)} \frac{\langle f, \varphi\rangle}{|\varphi|_{H^m(X)}}.$$

Let γ be an open regular, i.e., Lipschitz continuous, and measurable subset of ∂X. We denote with $H^{1/2}(\gamma)$ the space of functions defined on γ that are traces of functions in $H^1(X)$ [61]. Furthermore, we recall the Poincaré inequality [61]

$$\|u\|_{L^2(X)}^2 \leq C_P(X)\|\nabla u\|_{L^2(X)}^2 \quad \forall u \in H_0^1(X)^d,$$

with a positive constant $C_P(X)$ depending on the domain X. We also remind the trace inequality [152]

$$\|u\|_{L^2(\partial X)} \leq C_T(X)\|u\|_{H^1(X)} \quad \forall u \in H^1(X)^d,$$

with a positive constant $C_T(X)$ depending on the domain X. For Korn's inequality [26, 33], let $\hat{u}_s \in H^1(\widehat{\Omega}_s)$ and $\hat{\epsilon} = \frac{1}{2}(\widehat{\nabla}\hat{u}_s + \widehat{\nabla}\hat{u}_s^T) \in L^2(\widehat{\Omega}_s)$. Then,

$$\|\hat{u}_s\|_{H^1(\widehat{\Omega}_s)} \leq C_K\Big(|\hat{u}_s|_{L^2(\widehat{\Omega}_s)}^2 + |\hat{\epsilon}|_{L^2(\widehat{\Omega}_s)}^2\Big)^{1/2} \quad \forall \hat{u}_s \in H^1(\widehat{\Omega}_s),$$

and some constant C_K.

Function spaces on moving domains

For the stability analysis of our equations, it is convenient to work in time-dependent domains. Thus, we introduce (on a moving domain Ω):

$$V := \{v : \Omega \times I \to \mathbb{R}^d : v \circ \hat{\mathcal{A}} = \hat{v},\, \hat{v} \in [H^1(\widehat{\Omega})]^d\},$$
$$L := \{p : \Omega \times I \to \mathbb{R} : p \circ \hat{\mathcal{A}} = \hat{p},\, \hat{p} \in [L^2(\widehat{\Omega})]\},$$

where $\hat{\mathcal{A}} : \widehat{\Omega} \to \Omega$ denotes the ALE transformation that is explained below. The admissibility of the spaces is given by the relations

$$V \subseteq [H^1(\Omega)]^d, \quad \text{and} \quad L \subseteq [L^2(\Omega)].$$

This relation was proven by Formaggia and Nobile [51] and is recalled in Section 3.3.1. A deeper discussion of fluid-structure interaction in moving domains can be found in Formaggia et al. [53] (chapter 3) and the many references cited therein.

Convention for vector-valued functions

For the corresponding spaces of the d-dimensional vector-valued functions, we bear the notation $L^p(X)^d$, $H^1(X)^d$, etc. in mind, equipped with the usual product norm. The scalar products and corresponding norms are defined in an analogous way as those for scalar functions. We expect that the reader is familiar with the Navier-Stokes equations and structural mechanics in d-dimensions. Consequently, we do not differentiate between one-dimensional and d-dimensional spaces and the corresponding solution variables.

Notational conventions

For the reader's convenience, we often use

$$(\cdot,\cdot)_X := (\cdot,\cdot)_{L^2(X)} \quad \text{and} \quad ||\cdot||_X := ||\cdot||_{L^2(X)},$$

where $X = \Omega_f, \Omega_s$ or the corresponding spaces in the fixed reference domains $\widehat{X} = \widehat{\Omega}_f, \widehat{\Omega}_s$. Furthermore, in time-dependent spaces in which we need explicitly the dependence on time, we use

$$(\cdot,\cdot)_{X^n} := (\cdot,\cdot)_{L^2(X^n)} \quad \text{and} \quad ||\cdot||_{X^n} := ||\cdot||_{L^2(X^n)}.$$

In other cases, we denote explicitly the used scalar product and the induced norm, for instance,

$$(\cdot,\cdot)_{H^1(X^n)} \quad \text{and} \quad ||\cdot||_{H^1(X^n)}.$$

2.2 Continuum mechanics

In this section, we briefly introduce the basics of continuum mechanics that are used to derive the equations for fluids and structures. They are both based on the assumption of the conservation of such properties as mass, momentum, and energy. In continuum mechanics, we assume that the quantities of interest (e.g., stresses) can be described by (at least piecewise) continuous functions. They exist at each point of a locally homogenized body. The presentation in this section mainly follows the standard literature [53, 78, 86], but we also refer to [114].

Kinematics

Kinematics comprises the study of motion and deformation. A deformation of $\widehat{\Omega}$ is a smooth one-to-one mapping

$$\widehat{T} : \widehat{\Omega} \to \Omega \quad \text{with } \hat{x} \mapsto x = \widehat{T}(\hat{x}).$$

This mapping associates each point $\hat{x} \in \widehat{\Omega}$ (of a reference domain) to a new position $x \in \Omega$ (of the physical domain). The displacement of a material point $\hat{x}$ is defined by

$$\hat{u}(\hat{x}) = \widehat{T}(\hat{x}) - \hat{x}. \tag{2.1}$$

We utilize quite frequently the deformation gradient $\widehat{F} : \widehat{\Omega} \to \mathbb{R}^{d\times d}$ and its determinant $\hat{J}$. They are defined as

$$\widehat{F} := \widehat{F}(\hat{u}) := \widehat{\nabla}\widehat{T} = \hat{I} + \widehat{\nabla}\hat{u}, \qquad \hat{J} := \det \widehat{F}, \tag{2.2}$$

where $\hat{I}$ denotes the identity tensor in $\mathbb{R}^{d\times d}$. Moreover, let $\hat{f} : \widehat{\Omega} \to \mathbb{R}^d$ be a vector-valued function and $f : \Omega \to \mathbb{R}^d$ is defined as $f(x) = \hat{f}(\widehat{T}^{-1}(x))$. Then, we have

$$\widehat{\nabla}\hat{f} = \nabla f \widehat{F}. \tag{2.3}$$

All physical quantities can either be defined in the Lagrangian sense or in the Eulerian framework, or later in an ALE formulation. We extend the concept of the deformation to the time-dependent case such that $\widehat{T}(\hat{x}, t) : \widehat{\Omega} \times I \to \Omega(t)$ for a fixed time $t \in I = [0, T]$ with the end time T. For instance, we have (thanks to the invertibility of $\widehat{T}$):

$$\hat{f}(\hat{x}, t) = f(x, t), \quad x = \widehat{T}(\hat{x}, t), \quad \hat{x} \in \widehat{\Omega},\, t \in I.$$

With the help of this relation, we define quantities for the deformation, velocity, etc.

To compute fluid-structure interaction problems using the ALE framework, we neither can use Eulerian coordinates nor the Lagrangian framework. The Eulerian framework causes problems because the fluid domain must follow the displacement of the fluid-structure interface. The Lagrangian framework is also not the appropriate framework because we are not interested to track the evolution of single fluid particles. Therefore, we introduce an intermediate reference framework: the ALE reference configuration, which permits us to rewrite the fluid equations in artificial coordinates. For simplicity's sake, we denote this

(fixed) reference configuration as $\widehat{\Omega}$ because it has a close relationship with the reference configuration introduced above. From the evolution of the interface $\Gamma_i(t)$, we define

$$\hat{\mathcal{A}} : \widehat{\Omega} \times I \to \Omega, \quad (\hat{x}, t) \mapsto x = \hat{\mathcal{A}}(\hat{x}, t).$$

We assume that $\hat{\mathcal{A}}$ to be an homeomorphism and we assume further that

$$t \to x = x(\hat{x}, t), \quad \hat{x} \in \widehat{\Omega},$$

is differentiable almost everywhere in the time interval I. Using the ALE formulation, we must deal with two different motions. First, the standard motion of the media (the fluid and the structure). Second, we must consider the additional motion of the computational domain. In a similar way as before, we carry over the definition of the quantities in both domains:

$$\hat{f}(\hat{x}, t) = f(x, t), \quad x = \hat{\mathcal{A}}(\hat{x}, t), \quad \hat{x} \in \widehat{\Omega},\, t \in I.$$

With help of the ALE transformation, we define the *domain velocity* as

$$\hat{w}(\hat{x}, t) = \partial_t \hat{\mathcal{A}}(\hat{x}, t), \quad \forall \hat{x} \in \widehat{\Omega},$$

with $w(\cdot, t) = \hat{w}(\cdot, t) \circ \hat{\mathcal{A}}^{-1}$. We emphasize that the two velocities $\hat{v}$ (that denotes later the fluid velocity) and $\hat{w}$ do not coincide in general.

2.3 Lagrangian, Eulerian, and ALE time-derivatives

We briefly explain the relations between different time derivatives for different frameworks (such as the Lagrangian, the Eulerian, and the ALE frameworks). In a Lagrangian setting, the total and the partial derivatives coincide:

$$d_t \hat{f}(\hat{x}, t) = \partial_t \hat{f}(\hat{x}, t).$$

In an Eulerian framework, we find the following standard relation between the *material time-derivative* (the total time derivative) $d_t f$ and the partial time derivative $\partial_t f$:

$$d_t f(x, t) = v \cdot \nabla f + \partial_t f(x, t),$$

where the additional term $v \cdot \nabla f$ is referred to as a transport term. In an analogous fashion, we extend this concept to define the *ALE time-derivative*

$$\hat{\partial}_t f(x, t) := \partial_t|_{\hat{\mathcal{A}}} f(x, t) = w \cdot \nabla f + \partial_t f(x, t), \tag{2.4}$$

where the transport term appears due to the motion of the computational domain. In a Lagrangian description, we have $w = 0$. In contrast, it holds $w = v$ in an Eulerian framework. The ALE time-derivative has important ramifications for the numerical discretization of ALE equations; for a deeper discussion, we refer to [53], p. 88.

Remark 2.1. The description of the equations at the continuous level leads to an equivalent representation of the ALE formulation of the fluid and of its Eulerian description. In this situation, the Eulerian time-derivative is well-defined. Therefore, it is sufficient to use the ALE framework only for descriptions at the discrete level [53].

2.4 The equations for fluids and structures

The conservation principles are used in this section, to model the equations for fluids and structures. From these principles, and using the Reynolds transport formula (see, e.g., [53, 114]), we derive the standard equation for the conservation of momentum:

$$\rho\partial_t v + \rho(v \cdot \nabla)v - \mathrm{div}\sigma = \rho f \quad \text{in } \Omega,\, t \in I. \tag{2.5}$$

The Cauchy stress tensor is not yet specified in Equation (2.5). At this point, the concepts for fluid equations and structure equations diverge. The relation between kinematics and the Cauchy stress tensor is called the *constitutive law* that characterizes the specific material, i.e., the fluid or the structure.

2.4.1 The Navier-Stokes equations in the Eulerian framework

In a Newtonian incompressible fluid, the Cauchy stress tensor is linked to the strain rate $D(v_f) := \frac{1}{2}(\nabla v_f + \nabla v_f^T)$ and it holds:

$$\sigma_f := \sigma_f(v_f, p_f) = -p_f I + 2\rho_f \nu_f D(v_f), \tag{2.6}$$

with the velocity v_f, the pressure p_f, the identity matrix I, the density ρ_f, and the (kinematic) viscosity ν_f.

Using the equations for momentum and continuity together with the Cauchy stress tensor, we get the Navier-Stokes Equations:

$$\begin{aligned} \rho_f\partial_t v_f + \rho_f(v_f \cdot \nabla)v_f - 2\mathrm{div}(\rho_f\nu_f D(v_f)) + \nabla p_f = \rho_f f, \quad &\text{in } \Omega_f,\, t \in I, \\ \mathrm{div}\, v_f = 0, \quad &\text{in } \Omega_f,\, t \in I. \end{aligned} \tag{2.7}$$

These equations are supplemented by appropriate boundary conditions. The first type are Dirichlet conditions (a prescribed velocity):

$$v_f = g \quad \text{on } \Gamma_{f,D} \subset \partial\Omega_f,$$

with a given function $g : \Gamma_{f,D} \times I \to \mathbb{R}^d$. Such a Dirichlet condition is seen in the velocity domain on the interface Γ_i in the case of a fluid-structure interaction setting, i.e.,

$$v_f = v_s \quad \text{on } \Gamma_i.$$

The second natural type are Neumann boundary conditions (applied stresses):

$$\sigma_f n_f = \left[-p_f I + 2\rho_f \nu_f D(v_f)\right] n_f = h \quad \text{on } \Gamma_{f,N} \subset \partial\Omega_f,$$

with a given vector-valued function $h = h(x,t)$. This condition is mostly used for the outflow boundary (*do-nothing condition* [72]). However, the do-nothing condition implies a constant pressure on this boundary that is not physiological in bio-medical applications [54, 110].

2.4.2 The equations for structures in Lagrangian coordinates

The equation for the conservation of momentum (2.5) is formulated in a Lagrangian framework (with the help of the of the Piola transform) and it is well-known as the equation of *elastodynamics*:

$$\hat{\rho}_s \partial_t^2 \hat{u}_s - \widehat{\mathrm{div}}(\widehat{\Pi}) = \hat{\rho}_s \hat{f}, \quad \text{in } \widehat{\Omega}_s,\ t \in I,$$

where the tensor $\widehat{\Pi} = \hat{J}\hat{\sigma}_s \widehat{F}^{-T}$ is referred to as the *first Piola-Kirchhoff stress tensor*. This constitutive tensor is unsymmetric and it is often rewritten in terms of the *second Piola-Kirchhoff* stress tensor $\widehat{\Sigma}$:

$$\widehat{\Sigma} = \widehat{F}^{-1}\widehat{\Pi} = \hat{J}\widehat{F}^{-1}\hat{\sigma}_s \widehat{F}^{-T} \quad \Leftrightarrow \quad \widehat{F}\widehat{\Sigma} = \widehat{\Pi} = \hat{J}\hat{\sigma}_s \widehat{F}^{-T}. \tag{2.8}$$

Then, we arrive at

$$\hat{\rho}_s \partial_t^2 \hat{u}_s - \widehat{\mathrm{div}}(\widehat{F}\widehat{\Sigma}) = \hat{\rho}_s \hat{f}, \quad \text{in } \widehat{\Omega}_s,\ t \in I. \tag{2.9}$$

This second-order (in time) equation is supplemented by appropriate initial conditions and boundary conditions. As for the fluid equations, we prescribe Dirichlet boundary conditions (fixing the displacements):

$$\hat{u}_s = \hat{g} \quad \text{on } \widehat{\Gamma}_{s,D} \subset \partial\widehat{\Omega}_s,$$

where $\hat{g}$ is a given function. We can also employ Neumann boundary condition (surface stresses):

$$\widehat{F}\widehat{\Sigma}\hat{n}_s = \hat{J}\hat{\sigma}_s \widehat{F}^{-T}\hat{n}_s = \hat{h} \quad \text{on } \widehat{\Gamma}_{s,N} \subset \partial\widehat{\Omega}_s,$$

in which $\hat{h}$ is a given vector-valued function. Such a condition is seen from the structure side on the interface in case of a fluid-structure interaction problem, i.e.,

$$\widehat{F}\widehat{\Sigma}\hat{n}_s = -\hat{J}\hat{\sigma}_f \widehat{F}^{-T}\hat{n}_f \quad \text{on } \widehat{\Gamma}_i.$$

Often, constitutive laws are written by means of the *Green-Lagrange* strain tensor that is defined as

$$\widehat{E} = \frac{1}{2}(\widehat{F}^T\widehat{F} - \hat{I}). \tag{2.10}$$

To describe the physics of structures, we follow [78] and introduce the concept of constitutive equations for *hyperelastic materials*. This formulation provides for the description of a wide range of materials and permits a compact notation for later purposes. In these equations, the *strain-energy function* $W : \mathbb{R}^{d\times d} \to \mathbb{R}^+$ is used to characterize different materials, from which the Cauchy stress tensor $\widehat{\sigma}_s$ for a specific structure can be derived. Throughout this work, we consider only homogeneous, isotropic materials. First, we derive equations for two incompressible materials, such as the *neo-Hookean* (INH) model and the *Mooney-Rivlin* (IMR) model for rubber-like materials. The latter material can withstand large deformations and large strains. The INH model is the simplest model for studying nonlinear deformations, having one parameter that characterizes the mechanical properties of the structures. In contrast, the IMR model contains two parameters for the description of the material under consideration and is often used in computations [56, 78].

For incompressible materials it holds that $\hat{J} = 1$ (conservation of volume), and we start with the general form of the strain-energy function

$$W := W(\widehat{F}) - \hat{p}_s(\hat{J} - 1),$$

where the scalar pressure $\hat{p}_s$ can be regarded as a Lagrange multiplier. From the strain-energy function, we derive a general formulation of the Cauchy stress tensor. The formulation of the Cauchy stress tensor for incompressible isotropic hyperelastic materials reads [78]:

$$\widehat{\sigma}_s = -\hat{p}_s\hat{I} + 2\frac{\partial W}{\partial I_1}\widehat{F}\widehat{F}^T - 2\frac{\partial W}{\partial I_2}\widehat{F}^{-T}\widehat{F}^{-1}, \tag{2.11}$$

where I_1 and I_2 denote the strain invariants and are defined as

$$I_1 := I_1(A) = \mathrm{tr}A, \quad I_2 := I_2(A) = \frac{1}{2}[(\mathrm{tr}A)^2 - \mathrm{tr}A^2]$$

for a symmetric tensor A [78, 114].

The strain-energy functions of the previously introduced two materials are given by

$$\begin{aligned} W &= \frac{\mu_1}{2}(I_1 - 3) && \text{(INH)},\\ W &= \frac{\mu_1}{2}(I_1 - 3) - \frac{\mu_2}{2}(I_2 - 3) && \text{(IMR)}. \end{aligned}$$

Differentiation of (2.11) with respect to the principal invariants I_1 and I_2 leads to:

$$\begin{aligned} \widehat{\sigma}_s &= -\hat{p}_s\hat{I} + \mu_1\widehat{F}\widehat{F}^T && \text{(INH)},\\ \widehat{\sigma}_s &= -\hat{p}_s\hat{I} + \mu_1\widehat{F}\widehat{F}^T + \mu_2\widehat{F}^{-T}\widehat{F}^{-1} && \text{(IMR)}. \end{aligned} \tag{2.12}$$

The strain-energy function of the so-called *Saint-Venant Kirchhoff* (STVK) material reads

$$W := W(\widehat{E}) = \frac{\lambda_s}{2}(\mathrm{tr}\widehat{E})^2 + \mu_s\widehat{E}^2,$$

where the material is characterized by the Lamé coefficients λ_s and μ_s. The nonlinear, compressible STVK model is often employed for metals. It is suitable to model large displacements with moderate strains.

To derive a representation in terms of the second Piola-Kirchhoff stress tensor, we use the following link between the strain-energy function and the stress tensor (see, e.g., [78]):

$$\widehat{\Sigma} = \frac{\partial W}{\partial E}. \tag{2.13}$$

Then, with the help of (2.8):

$$\widehat{F}\widehat{\Sigma} = \widehat{F}(\lambda_s(\mathrm{tr}\widehat{E})\hat{I} + 2\mu_s\widehat{E}).$$

Often, the elasticity of structures is characterized by the Poisson ratio ν_s ($\nu_s < \frac{1}{2}$ for compressible materials) and the Young modulus E_Y. The relationship to the Lamé coefficients μ_s and λ_s is given by:

$$\begin{aligned} \nu_s &= \frac{\lambda_s}{2(\lambda_s+\mu_s)}, \qquad & E_Y &= \frac{\mu_s(\lambda_s+2\mu_s)}{(\lambda_s+\mu_s)}, \\ \mu_s &= \frac{E_Y}{2(1+\nu_s)}, \qquad & \lambda_s &= \frac{\nu_s E_Y}{(1+\nu_s)(1-2\nu_s)}. \end{aligned} \tag{2.14}$$

More realistic constitutive equations for tissue modeling and myocardium

For the accurate modeling of living tissues, it is recommended to use more sophisticated constitutive equations than the previously introduced models, with the main reason being that the three introduced models do not differentiate between the *zero load* and *zero stress* configurations [78, 81, 86, 103]. A well-known strain-energy function is recommended by Fung (see [56], p. 58):

$$\hat{\rho}_s W = \frac{c}{2}(\exp(Q) - Q - 1) + \frac{q}{2},$$

where c is some constant, and q and Q are quadratic forms of the Green-Lagrange tensor. For c equals zero, we deduce

$$\hat{\rho}_s W = \frac{q}{2},$$

in which q (for example) is determined by

$$q := \mu_1(I_1 - 3) - \mu_2(I_2 - 3),$$

such that the IMR strain-energy is obtained. Today, the Fung model has been further modified by Holzapfel and coworkers. For instance, living tissues must be modeled as composite reinforced fibers, and with an accounting for prestressed configurations [81]. However, in summary, the simple models, introduced previously, are useful to begin the development of a fluid-structure solver that provides information for studying basic responses and numerical effects in simulations of blood vessels walls or valves. By this reason, we restrict us to the use of INH, IMR, and STVK materials.

2.5 The hyperbolic equation with damping terms

Due to flow disturbances and the pulsatile character of blood flow, pressure and velocity waves propagates in the aorta and the large arteries. These waves propagates with a certain (finite) speed throughout the arterial tree. However, the computational cost of such simulations makes it necessary to truncate the physical domain instead to perform a simulation of the whole cardiovascular system. This truncation results in (at least) two artificial boundary sections, where pressure waves are reflected. To account for these reflections, much effort has been focused on the accurate modeling of specific boundary conditions [38, 49, 50, 53, 87, 110, 141], and we also refer to Section 3.5. However, the consideration of appropriate structure conditions becomes important when dealing with large deflections of the blood vessel walls. Specifically, we are interested in their capability to absorb outgoing waves (and their energy) to prevent the backflow of waves when using Dirichlet or Neumann conditions. However, the complete prevention of backward-traveling waves is not the best condition for cardiovascular applications because wave reflections naturally arise, for instance, from bifurcations and variations in wall properties.

Originally, the need for numerical schemes for wave problems occurred in acoustics, electromagnetics, and elastodynamics [7, 44, 112]. Various approximate boundary conditions have been considered to absorb outgoing waves. For complex situations they have some major disadvantages; for instance, accumulation of error contributions over the whole time interval. To avoid these problems, higher order derivatives of the problem at hand can be used, which makes the implementation difficult. Another approach to eliminate reflections was suggested by appending an artificial layer to the computational domain. This layer is supposed to absorb the waves. Specifically, one can use a perfectly matched layer (PML) [19]. This approach has been extended and analyzed for various problems and many applications; see [20] and the many references cited therein. In this thesis, we employ the PML approach to our coupled setting by extending the computational domain that is intended to absorb the energy of outgoing waves. A comparison of absorbing conditions with the PML approach and application to biomedical problems was made by Rabinovich et al. [111].

In biomedical applications it remains an open problem and it is not clear from physical point of view, which boundary conditions must be prescribed for the structure on the outflow section [54, 55, 59, 104, 110, 138]. Therefore, we must address the challenge that the radius of the computational domain changes significantly in prototypical heart-valve simulations (see Figure 8.17). Thus, we utilize the PML approach to extend the computational domain with an artificial layer $\widehat{\Omega}_s^{\text{ext}}$ (see Figure 2.1) and we prescribe the structure with *damping terms* instead of using the *normal* structure equations . The intention of this artificial configuration is to absorb the energy of the physical configuration.

In the following, we introduce linear damping terms for the hyperbolic structure equations. For *strong* damping, we use the linearized Green-Lagrange strain tensor

$$\widehat{E}(\hat{u}_s) \approx \hat{\epsilon}(\hat{u}_s) = \frac{1}{2}(\widehat{\nabla}\hat{u}_s + \widehat{\nabla}\hat{u}_s^T).$$

Furthermore, we assume that the elasticity tensor, that is linked with $\widehat{F}\widehat{\Sigma} := \widehat{F}\widehat{\Sigma}(\hat{u}_s)$, is symmetric and positive definite, which is taken as an assumption for the most standard configurations. A deeper discussion can be found in Rannacher [114], p. 61-63.

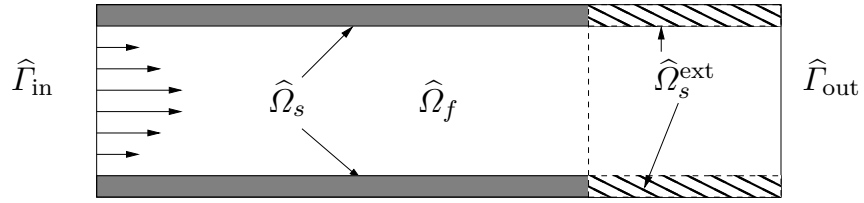

Figure 2.1. A prototypical configuration how to employ the artificial layer $\widehat{\Omega}_s^{\text{ext}}$.

The modified structure problem in the extended domain is defined as:

$$\hat{\rho}_s \partial_t^2 \hat{u}_s - \widehat{\text{div}}(\widehat{F}\widehat{\Sigma}(\hat{u}_s)) + \gamma_w \partial_t \hat{u}_s - \gamma_s \partial_t \widehat{\text{div}}(\hat{\epsilon}(\hat{u}_s)) = \hat{\rho}_s \hat{f}_s \quad \text{in } \widehat{\Omega}_s^{\text{ext}},\ t \in I, \tag{2.15}$$

with $\gamma_s, \gamma_w \geq 0$. The first damping term is referred to as *weak damping* whereas the second damping term is called *strong damping*. Using strong damping, the full operator is used for damping, leading to an additional condition on the interface that has to be considered for the coupling with fluids. Assuming that temporal and spatial differentiation can be changed, we obtain for strong damping:

$$-\gamma_s \partial_t \widehat{\text{div}}(\hat{\epsilon}(\hat{u}_s)) = -\gamma_s \widehat{\text{div}}(\hat{\epsilon}(\partial_t \hat{u}_s)) = -\gamma_s \widehat{\text{div}}(\hat{\epsilon}(\hat{v}_s)), \quad \text{with } \hat{v}_s = \partial_t \hat{u}_s.$$

The change of temporal and spatial differentiation is invalid for nonlinear strong damping, where we could have been used the full nonlinear operator, i.e.,

$$-\gamma_s \partial_t \widehat{\text{div}}(\widehat{F}\widehat{\Sigma}(\hat{u}_s)) \not\approx -\gamma_s \widehat{\text{div}}(\widehat{F}\widehat{\Sigma}(\hat{v}_s)). \tag{2.16}$$

Next, we pose a standard mixed formulation of the structure equations,

$$\begin{aligned} \hat{\rho}_s \partial_t \hat{v}_s - \widehat{\text{div}}(\widehat{F}\widehat{\Sigma}(\hat{u}_s)) + \gamma_w \hat{v}_s - \gamma_s \widehat{\text{div}}(\hat{\epsilon}(\hat{v}_s)) &= \hat{\rho}_s \hat{f}_s \quad \text{in } \widehat{\Omega}_s^{\text{ext}},\ t \in I, \\ \hat{\rho}_s(\partial_t \hat{u}_s - \hat{v}_s) &= 0 \quad \text{in } \widehat{\Omega}_s^{\text{ext}},\ t \in I, \end{aligned} \tag{2.17}$$

where $\hat{\epsilon}(\hat{v}_s)$ is defined by

$$\hat{\epsilon}(\hat{v}_s) = \frac{1}{2}(\widehat{\nabla}\hat{v}_s + \widehat{\nabla}\hat{v}_s^T).$$

The modified structure problem (2.17) reduces to the original problem (2.9) when the damping parameters are set to $\gamma_w = \gamma_s = 0$.

Remark 2.2 (Possible clinical relevance of structural damping using $\widehat{\Omega}_s^{ext}$). The introduced approach is not as arbitrary as it seems. By the careful determination of both damping parameters, it is possible to determine suitable values for these parameters to account for reflections in the remaining system. From this perspective, this idea could also be used in a

clinical context for medical engineering. For example, a higher damping parameter would represent a stiffer material and therefore greater reflections at this boundary section. In contrast, the choice of a low damping parameter allows the structural waves to propagate throughout the whole structure. However, in this case the unreflected wave is reflected by the homogenous Dirichlet boundary conditions at the end of the artificial layer (see Figure 8.17).

Remark 2.3. The consequences of different kinds of damping on the existence and boundedness of solutions, extensions to global solutions, and energy blow-up in finite time have been analyzed to date by others ([57], and the many references cited in their introduction). To the best of our knowledge, the equations have been analyzed for linear and nonlinear weak damping, and linear strong damping. The extension to nonlinear strong damping has not been analyzed so far. Indeed, we observed non-convergence of the nonlinear solution algorithm (the Newton method) when we used nonlinear damping as proposed in Equation (2.16).

Remark 2.4. The incorporation of damping terms into the hyperbolic structure equations leads to a higher regularity in the structural solutions. In this case, it is possible to couple the fluid with the structure on the interface. This fact was used in [36] to demonstrate well-posedness and existence for nonstationary fluid-structure interaction dynamics. We refer the reader to a discussion of this topic in Section 3.6.

Outlook to the next chapter

In this chapter, we introduced the descriptions of fluids and structures in their natural coordinates. In the next chapter, we discuss an appropriate coupling strategy of these equations and their definition in a monolithic framework.

3 Fluid-Structure Interaction in ALE Coordinates

In the present chapter, we discuss fluid-structure interaction problems in ALE coordinates. The ALE mapping is defined by solving an additional partial differential equation, for which we present three possibilities. With the help of this mapping, we realize the fluid mesh motion. Next, the coupled framework is described in a fully coupled fashion, leading to a monolithic representation of the fluid-structure interaction. Our terminology to describe the *practicable* monolithic setting is based on [41–43, 82, 83, 118]. Furthermore, we present the a priori stability of the monolithically coupled problem on the continuous level. Moreover, in Section 3.5, we introduce absorbing fluid conditions (that account for the propagation of pressure waves in a compliant channel).

In the final Section 3.6, we briefly recall results of the analysis of fluid-structure interaction problems regarding the regularity of solutions found in the literature. Specifically, there is a lack of regularity that prohibits (from the theoretical point of view) the coupling of fluid equations with structural deformations along the interface. However, supplementing the structural equations with damping terms yields a solution of higher regularity such that coupling is allowed. Finally, we provide an overview of other solution algorithms used for solving fluid-structure interactions.

3.1 The Navier-Stokes equations in the ALE framework

The Navier-Stokes equations (2.7) in combination with (2.4) in a moving domain Ω_f read:

$$\begin{aligned} \rho_f \hat{\partial}_t v_f + \rho_f (v_f - w) \cdot \nabla v_f - 2\rho_f \nu_f \mathrm{div}\Big(D(v_f)\Big) + \nabla p_f = \rho_f f \quad &\text{in } \Omega_f,\, t \in I, \\ \mathrm{div}\, v_f = 0 \qquad &\text{in } \Omega_f,\, t \in I, \end{aligned} \tag{3.1}$$

where the additional convection term $(w \cdot \nabla) v_f$ accounts for the movement of the fluid domain. To derive a weak formulation to this problem, we multiply first with some test function and we take then the integrals. Let v_f^D a suitable extension of Dirichlet inflow data, then:

Problem 3.1 (ALE fluid problem in a moving domain). *Find* $\{v_f, p_f\} \in \{v_f^D + V_f^0\} \times L_f^0$ *such that the initial data satisfy* $v_f(0) = v_f^0$*, and for almost all time steps* $t \in I$ *holds:*

$$\begin{aligned} \rho_f(\hat{\partial}_t v_f, \psi^v)_{\Omega_f} + \rho_f\Big((v_f - w)\cdot\nabla v_f, \psi^v\Big)_{\Omega_f} \\ +(\sigma_f, \nabla\psi^v)_{\Omega_f} - \langle \sigma_f n_f, \nabla\psi^v\rangle_{\Gamma_{f,N}\cup\Gamma_i} + \rho_f(f,\psi^v)_{\Omega_f} = 0 \quad \forall \psi^v \in V_f^0, \\ (div\, v_f, \psi^p)_{\Omega_f} = 0 \quad \forall \psi^p \in L_f^0, \end{aligned} \tag{3.2}$$

with the Cauchy stress tensor

$$\sigma_f = -p_f I + 2\rho_f\nu_f D(v_f) = -p_f I + \rho_f\nu_f(\nabla v_f + \nabla v_f^T),$$

and a correction term on the outflow boundary ([72]):

$$g := -\rho_f\nu_f \nabla v_f^T \quad \text{on } \Gamma_{f,N} = \Gamma_{out}.$$

Using the fundamental theorem of calculus [95] in higher dimensions, we obtain the Navier-Stokes equations on a fixed domain. This formulation introduces additional geometric nonlinearities and they are formulated in terms of the deformation tensor $\widehat{F}$ and its determinant $\hat{J}$. In this application, we are concerned with two different representations of fluid equations, but both representations have advantages that are employed in the following. The previous formulation hides the transformation $\widehat{F}$ and $\hat{J}$ and is more convenient for stability and error estimates. The following formulation in a fixed domain $\widehat{\Omega}$ gives a practicable version of the fluid equations, such that they can directly implemented in a software package.

The boundary of $\widehat{\Omega}_f$ is divided into three non-overlapping parts $\partial\widehat{\Omega}_f = \widehat{\Gamma}_{f,D} \cup \widehat{\Gamma}_{f,N} \cup \widehat{\Gamma}_i$, where $\widehat{\Gamma}_i$ denotes later the interface and it coincides with $\widehat{\Gamma}_{f,N}$ in the case of pure fluid problems. We prescribe

$$\begin{aligned} \hat{u} = \hat{u}_D, \quad \text{and} \quad \hat{v} = \hat{v}_D \quad \text{on } \widehat{\Gamma}_{f,D}, \\ \hat{J}\hat{\sigma}_f\widehat{F}^{-T}\hat{n}_f = \hat{g} \quad \text{on } \widehat{\Gamma}_{f,N}. \end{aligned}$$

Let $\hat{v}_f^D$ a suitable extension of Dirichlet inflow data. Then, the variational form in $\widehat{\Omega}_f$ reads:

Problem 3.2 (Practicable ALE fluid problem in a fixed domain). *Find* $\{\hat{v}_f, \hat{p}_f\} \in \{\hat{v}_f^D + \hat{V}_f^0\} \times \hat{L}_f^0$ *such that the initial data* $\hat{v}_f(0) = \hat{v}_f^0$ *are satisfied, and for almost all time steps* $t \in I$ *holds:*

$$\begin{aligned} \hat{\rho}_f(\hat{J}\partial_t\hat{v}_f, \hat{\psi}^v)_{\widehat{\Omega}_f} + \hat{\rho}_f(\hat{J}\widehat{F}^{-1}(\hat{v}_f - \hat{w})\cdot\widehat{\nabla}\hat{v}_f, \hat{\psi}^v)_{\widehat{\Omega}_f} + (\hat{J}\hat{\sigma}_f\widehat{F}^{-T}, \widehat{\nabla}\hat{\psi}^v)_{\widehat{\Omega}_f} \\ = \langle \hat{J}\hat{g}_f\widehat{F}^{-T}\hat{n}_f, \hat{\psi}^v\rangle_{\widehat{\Gamma}_{f,N}} + \langle \hat{J}\hat{\sigma}_f\widehat{F}^{-T}\hat{n}_f, \hat{\psi}^v\rangle_{\widehat{\Gamma}_i} + \hat{\rho}_f(\hat{J}\hat{f}_f, \hat{\psi}^v)_{\widehat{\Omega}_f}, \\ (\widehat{div}(\hat{J}\widehat{F}^{-1}\hat{v}_f, \hat{\psi}^p)_{\widehat{\Omega}_f} = 0, \end{aligned}$$

for all $\hat{\psi}^v \in \hat{V}_f^0$ *and* $\hat{\psi}^p \in \hat{L}_f^0$*, and with the transformed Cauchy stress tensor*

$$\widehat{\sigma}_f = -\hat{p}_f \hat{I} + 2\hat{\rho}_f \nu_f \widehat{D}(\hat{v}_f) = -\hat{p}_f \hat{I} + 2\hat{\rho}_f \nu_f (\widehat{\nabla} \hat{v}_f \widehat{F}^{-1} + \widehat{F}^{-T} \widehat{\nabla} \hat{v}_f^T), \tag{3.3}$$

which can be derived with help of relation (2.3)*.*

As before, $\hat{g}_f$ accounts for (possible) Neumann data, for instance, a correction term for the do-nothing outflow condition:

$$\hat{g}_f = -\hat{\rho}_f \nu_f \widehat{F}^{-T} \widehat{\nabla} \hat{v}_f^T \quad \text{on } \widehat{\Gamma}_{f,N} = \widehat{\Gamma}_{\text{out}}. \tag{3.4}$$

Remark 3.1. Coupling fluid flows with structural deformations along an interface $\widehat{\Gamma}_i$ requires the fulfillment of two coupling conditions. Fluid flows require a Dirichlet condition on $\widehat{\Gamma}_i$, i.e., the continuity of the velocities is strongly enforced in the corresponding Sobolev spaces. The structural problem is driven by the normal stresses that act on $\widehat{\Gamma}_i$ caused by the fluid. These normal stresses are achieved with the boundary term:

$$\langle \hat{J} \widehat{\sigma}_f \widehat{F}^{-T} \hat{n}_f, \hat{\psi}^v \rangle_{\widehat{\Gamma}_i} \quad \text{on } \widehat{\Gamma}_i.$$

Remark 3.2. Finally, we note that the do-nothing conditions implicitly normalizes the pressure by

$$\int_{\widehat{\Gamma}_{\text{out}}} \hat{p} \, \mathrm{d}\hat{s} = 0.$$

In such a case, it is sufficient to work with the space $\hat{L}_f$ instead of $\hat{L}_f^0$.

3.2 The structure equations in the ALE framework

The equations for structures are already defined in a Lagrangian sense, therefore, in a fixed domain $\widehat{\Omega}_s$. Consequently, there is no additional effort to define them in the ALE framework. The boundary of $\widehat{\Omega}_s$ is again split into the three types of boundaries as already discussed before.

The sought physical unknowns are the vector-valued displacement $\hat{u}_s$, the vector-valued velocity $\hat{v}_s$, and a scalar pressure $\hat{p}_s$. The latter variable is only required when we deal with incompressible materials, i.e., INH or IMR. In these cases, the pressure is incorporated as Lagrange multiplier.

As for fluid flows, let $\hat{v}_s^D$ and $\hat{u}_s^D$ be suitable extensions of Dirichlet inflow data. We use the mixed formulation (2.17), to obtain the variational formulation of the structure equations:

Problem 3.3 (Incompressible structure problems). *Find* $\{\hat{v}_s, \hat{u}_s, \hat{p}_s\} \in \hat{L}_s \times \{\hat{u}_s^D + \hat{V}_s^0\} \times \hat{L}_s^0$, *such that* $\hat{v}_s(0) = \hat{v}_s^0$ *and* $\hat{u}_s(0) = \hat{u}_s^0$ *are satisfied, and for almost all time steps* $t \in I$ *holds:*

$$\begin{aligned}(\hat{\rho}_s \partial_t \hat{v}_s, \hat{\psi}^v)_{\widehat{\Omega}_s} + (\widehat{F}\widehat{\Sigma}, \widehat{\nabla}\hat{\psi}^v)_{\widehat{\Omega}_s} - \langle \widehat{F}\widehat{\Sigma}\hat{n}_s, \hat{\psi}^v \rangle_{\widehat{\Gamma}_i \cup \widehat{\Gamma}_N} \\ + \gamma_w(\hat{v}_s, \hat{\psi}^v)_{\widehat{\Omega}_s} + \gamma_s(\hat{\epsilon}(\hat{v}_s), \widehat{\nabla}\hat{\psi}^v)_{\widehat{\Omega}_s} \\ - \gamma_s \langle \hat{\epsilon}(\hat{v}_s)\hat{n}_s, \hat{\psi}^v \rangle_{\widehat{\Gamma}_i \cup \widehat{\Gamma}_N} - (\hat{\rho}_s \hat{f}_s, \hat{\psi}^v)_{\widehat{\Omega}_s} = 0 \quad \forall \hat{\psi}^v \in \hat{V}_s^0, \\ \hat{\rho}_s(\partial_t \hat{u}_s - \hat{v}_s, \hat{\psi}^u)_{\widehat{\Omega}_s} = 0 \quad \forall \hat{\psi}^u \in \hat{L}_s, \\ (\hat{J} - 1, \hat{\psi}^p)_{\widehat{\Omega}_s} = 0 \quad \forall \hat{\psi}^p \in \hat{L}_s^0,\end{aligned}$$

where $\hat{\rho}_s$ *denotes the structure density,* $\hat{n}_s$ *the outer normal vector on* $\widehat{\Gamma}_i$ *and* $\widehat{\Gamma}_N$, *respectively. The Cauchy stress tensors for the material models are given by*

$$\begin{aligned}\widehat{\sigma}_s &:= -\hat{p}_s \hat{I} + \mu_s \hat{F}\hat{F}^{-T}, \\ \widehat{\sigma}_s &:= -\hat{p}_s \hat{I} + \mu_s \hat{F}\hat{F}^{-T} + \mu_2 \hat{F}^{-T}\hat{F}^{-1},\end{aligned} \tag{3.5}$$

with the coefficients μ_s *and* μ_2 *. They can be transformed via relation* (2.8) *into the second Piola-Kirchhoff stress tensor. External volume forces are described by the term* $\hat{f}_s$.

For compressible structures (such as the STVK) material, we obtain the following problem:

Problem 3.4 (Compressible structure problems). *Find* $\{\hat{v}_s, \hat{u}_s\} \in \hat{L}_s \times \{\hat{u}_s^D + \hat{V}_s^0\}$, *such that* $\hat{v}_s(0) = \hat{v}_s^0$ *and* $\hat{u}_s(0) = \hat{u}_s^0$ *are satisfied, and for almost all time steps* $t \in I$ *holds:*

$$\begin{aligned}(\hat{\rho}_s \partial_t \hat{v}_s, \hat{\psi}^v)_{\widehat{\Omega}_s} + (\widehat{F}\widehat{\Sigma}, \widehat{\nabla}\hat{\psi}^v)_{\widehat{\Omega}_s} - \langle \widehat{F}\widehat{\Sigma}\hat{n}_s, \hat{\psi}^v \rangle_{\widehat{\Gamma}_i \cup \widehat{\Gamma}_N} \\ + \gamma_w(\hat{v}_s, \hat{\psi}^v)_{\widehat{\Omega}_s} + \gamma_s(\hat{\epsilon}(\hat{v}_s), \widehat{\nabla}\hat{\psi}^v)_{\widehat{\Omega}_s} \\ - \gamma_s \langle \hat{\epsilon}(\hat{v}_s)\hat{n}_s, \hat{\psi}^v \rangle_{\widehat{\Gamma}_i \cup \widehat{\Gamma}_N} - (\hat{\rho}_s \hat{f}_s, \hat{\psi}^v)_{\widehat{\Omega}_s} = 0 \quad \forall \hat{\psi}^v \in \hat{V}_s^0, \\ \hat{\rho}_s(\partial_t \hat{u}_s - \hat{v}_s, \hat{\psi}^u)_{\widehat{\Omega}_s} = 0 \quad \forall \hat{\psi}^u \in \hat{L}_s,\end{aligned}$$

with all quantities as defined before. In this problem, the stress tensor is given by:

$$\widehat{F}\widehat{\Sigma} := \hat{F}(\lambda_s(tr\hat{E})\hat{I} + 2\mu_s \hat{E}), \tag{3.6}$$

with the Lamé coefficients λ_s *and* μ_s. *For the STVK material, the compressibility is related to the Poisson ratio* ν_s *(*$\nu_s < \frac{1}{2}$*).*

In this thesis, we do not only couple a fluid with a structure, but we also couple two or more structures. Hence, we state the coupling conditions for two structures:

$$\begin{aligned}\hat{u}_{s,1} &= \hat{u}_{s,2} \quad \text{on } \widehat{\Gamma}_i, \\ \widehat{F}\widehat{\Sigma}_{s,1} &= \widehat{F}\widehat{\Sigma}_{s,2} \quad \text{on } \widehat{\Gamma}_i.\end{aligned} \tag{3.7}$$

Moreover, using the strong damping term, i.e., $\gamma_s > 0$, the second coupling condition must be supplemented by an additional term on the interface such that

$$\widehat{F}\widehat{\Sigma}_{s,1}\hat{n}_{s,1} + \gamma_s\hat{\epsilon}_{s,1}(\hat{v}_s)\hat{n}_{s,1} = \widehat{F}\widehat{\Sigma}_{s,2}\hat{n}_{s,2} + \gamma_s\hat{\epsilon}_{s,2}(\hat{v}_s)\hat{n}_{s,2} \quad \text{on } \widehat{\Gamma}_i.$$

The reasoning for this modification can be verified by using integration by parts for the strong damping operator.

The multi-structure model becomes important when we consider prototypical heart-valve simulations. The different parts of the structure (i.e., the sections of the heart, the valves, and the aorta) are described by the same material model but with varying coefficients. Consequently, the constitutive tensors are unsteady on the interface where the different structures meet. We do not expect difficulties in using different constitutive models for the different structure parts; however it is important to verify this assumption because the medical community is interested in modeling blood vessels with more sophisticated material models [78, 80, 81, 94]. In contrast to the coupling of fluids and structures (where the Cauchy stress tensor changes entirely) the type of structural coupling is of a lower level because the stress tensors have similar meaning and should not cause any difficulties. We address this subject in a numerical example below, where our expectations could be established in the numerical Examples 8.4.4 and 8.4.5.

3.3 The coupled fluid-structure problem in the ALE framework

Because we work with both moving spaces and fixed spaces for fluid flows, we recall the findings of [107], which provide the regularity conditions of the ALE mapping. Next, we introduce three partial differential equations that are used to realize the fluid mesh motion.

3.3.1 Conditions for the regularity of the ALE mapping

Problem 3.5. *The ALE mapping $\hat{\mathcal{A}}$ has to be defined such that $\hat{v} \in H^1(\widehat{\Omega})$ if and only if $v = \hat{v} \circ \hat{\mathcal{A}}^{-1} \in H^1(\Omega)$.*

Using classical function spaces, a sufficient condition is that $\hat{\mathcal{A}}$ is a C^1-diffeomorphism:

$$\hat{\mathcal{A}} \in C^1(\overline{\widehat{\Omega}}), \quad \hat{\mathcal{A}}^{-1} \in C^1(\overline{\Omega})$$

and

$$\widehat{F} \in L^\infty(\widehat{\Omega}), \quad F \in L^\infty(\Omega)$$

This requirement must be weakened because classical function spaces are inappropriate when approximate solutions with help of a Galerkin finite element scheme are computed.

Lemma 3.1. *Let $\widehat{\Omega}$ be a bounded domain with $C^{1,1}$-boundary (see, e.g., [152]). Let $\hat{\mathcal{A}}$ be invertible in the closure of $\widehat{\Omega}$ and there holds for each $t \in I$ the two conditions*

- *$\Omega = \hat{\mathcal{A}}(\widehat{\Omega})$ is bounded and $\partial\Omega$ is Lipschitz-continuous.*
- *Let $\hat{\mathcal{A}} \in W^{1,\infty}(\widehat{\Omega})$ and $\hat{\mathcal{A}}^{-1} \in W^{1,\infty}(\Omega)$.*

Then, $v \in H^1(\Omega)$ if and only if $\hat{v} = v \circ \hat{\mathcal{A}} \in H^1(\widehat{\Omega})$. Moreover, the corresponding norms are equivalent.

For a proof of this Lemma, we refer to [107].

Lemma 3.2. *Let us assume that $x(\hat{x}, t) \in H^1(I, W^{1,\infty}(\widehat{\Omega}))$ holds. If $\hat{v} \in H^1(I, H^1(\widehat{\Omega}))$, then $v \in \hat{v} \circ \hat{\mathcal{A}}^{-1} \in H^1(I, H^1(\Omega))$ and we obtain the following regularity result for the ALE time-derivative*

$$\hat{\partial}_t v \in L^2(I, H^1(\Omega)).$$

For a proof of this Lemma, we refer to [107].

3.3.2 Interface coupling conditions and mesh motion models

In this section, we state the interface coupling conditions for the fluid-structure interaction. The coupling of the fluid with the structure equations must satisfy three conditions: continuity of velocities, continuity of normal stresses, and geometrical coupling. In the main part of this section, we focus our attention on formulations for defining the ALE mapping $\hat{\mathcal{A}}$.

Continuity of velocity and stress

The velocity field must be continuous on the interface (which is a Dirichlet-like condition seen from the fluid side). Sufficient regularity for the structure velocity is taken as assumption, such that this velocity can be given to the fluid problem. In detail, we have

$$v_f = w = v_s \quad \text{on } \Gamma_i. \tag{3.8}$$

To complete the structure problem, we must enforce the balance of the normal stresses on the interface:

$$\hat{J}\hat{\sigma}_f \widehat{F}^{-T} \hat{n}_f + \widehat{F}\widehat{\Sigma}\hat{n}_s + \gamma_s \hat{\epsilon}(\hat{v}_s)\hat{n}_s = 0 \quad \text{on } \widehat{\Gamma}_i. \tag{3.9}$$

This condition corresponds to a Neumann-like boundary condition for the structure subsystem.

Geometric coupling

Before we study three types of fluid mesh motion models, we recall the basic findings from the literature. For fluid-structure interaction based on the 'arbitrary Lagrangian-Eulerian' framework (ALE), the choice of appropriate fluid mesh movement is important. In general, an additional elasticity equation is solved [30, 42, 126, 130]. For moderate

deformations, one can pose an auxiliary Laplace problem that is known as harmonic mesh motion. More advanced equations from linear elasticity are also available [119, 130]. The pseudo-material parameters in both approaches were used to control the mesh deformation. If the parameters do not depend on the mesh position and geometric information, both approaches can only deal with moderate fluid mesh deformations. This problem is resolved by using mesh-position dependent material parameters that are used to increase the stiffness of cells near the interface [130]. There are several techniques for choosing these parameters to retain an optimal mesh, such as a Jacobian-based stiffening power that is eventually governed by appropriate remeshing techniques. We use an ad-hoc approach for these parameters, measuring the distance to the elastic structure and adapting the parameters to prevent mesh cell distortion as long as possible.

In this thesis, we also use (for mesh moving) the biharmonic equation that others have studied for fluid flows in ALE coordinates [70]. It was also shown there, that using the biharmonic model provides greater freedom in the choice of boundary and interface conditions. In general, the biharmonic mesh motion model leads to a smoother mesh (and larger deformations of the structure) compared to the mesh motion models based on second order partial differential equations [149]. As a third approach, we use the biharmonic operator for deforming the mesh with two types of boundary conditions. Although, the mesh behavior of the harmonic and the biharmonic mesh motion models were analyzed in [70] for different applications, we upgrade these concepts to fluid-structure interaction problems. Moreover, we provide quantitative comparisons of the three mesh motion models (we refer the reader to the Examples 7.1, 8.1, and 8.2).

In the discrete setting of the coupled problem, the moving fluid domain follows the motion of the interface (it is therefore a geometrical coupling):

$$\hat{u}_f = \hat{u}_s \quad \text{on } \widehat{\Gamma}_i, \tag{3.10}$$

from which we obtain immediately $\hat{w} = \hat{v}_s$ with temporal differentiation.

We define the ALE mapping in terms of the displacement variable, such that we obtain from Equation (2.1)

$$\hat{u}(\hat{x}) = \hat{\mathcal{A}}(\hat{x}) - \hat{x}.$$

Inside the fluid domain $\widehat{\Omega}_f$ this operation is arbitrary and it is described by means of a partial differential equation, such that we produce a smooth evolution of the fluid mesh. In the following, we discuss the three possible partial differential equations in detail, which can be used for fluid mesh moving. In two dimensional configurations, the mesh moves in x- and y-direction, which allows us to find a vector-valued artificial displacement variable

$$\hat{u}_f := (\hat{u}_f^{(1)}, \hat{u}_f^{(2)}) := (\hat{u}_f^{(x)}, \hat{u}_f^{(y)}).$$

We need the single components of $\hat{u}_f$ below to apply different types of boundary conditions to the biharmonic mesh motion model. In the following, the formal description of the first two mesh motion models coincides and only differ in the definition of the stress tensors $\widehat{\sigma}_{\text{mesh}}$.

Mesh motion with a harmonic model

The simplest model is based on the harmonic equation, which reads in strong formulation:

$$-\widehat{\mathrm{div}}(\hat{\sigma}_{\mathrm{mesh}}) = 0, \quad \hat{u}_f = \hat{u}_s \text{ on } \widehat{\Gamma}_i, \quad \hat{u}_f = 0 \text{ on } \partial\widehat{\Omega}_f \setminus \widehat{\Gamma}_i, \tag{3.11}$$

with

$$\widehat{\sigma}_{\mathrm{mesh}} = \alpha_u \widehat{\nabla} \hat{u}_f.$$

The diffusion parameter $\alpha_u := \alpha_u(\hat{x})$ is chosen such that a good fluid mesh quality is guaranteed. For instance, we can choose

$$\alpha_u(\hat{x}) = a + b\exp(-c\hat{d}), \tag{3.12}$$

with certain constants $a, b, c > 0$. The Euclidian distance of a point $\hat{x}$ to the interface $\widehat{\Gamma}_i$ is denoted by $\hat{d} = |\hat{x} - \widehat{\Gamma}_i|$. Another, even simpler, strategy was proposed by Tezduyar et al. [130], which was further developed by Stein et al. [126]. They propose to choose

$$\alpha_u(\hat{x}) = \hat{J}^{-1}. \tag{3.13}$$

This choice works fine because mesh cell distortion appears in the vicinity of $\widehat{\Gamma}_i$. That means $\hat{J} \searrow 0$ near $\widehat{\Gamma}_i$, and consequently $\alpha_u(\hat{x}) \gg 0$ near $\widehat{\Gamma}_i$. By reason that high diffusion causes low mesh movement, the quality of the fluid mesh is maintained. For a comparison of different choices of $\alpha_u := \alpha_u(\hat{x})$, we refer to [149].

Mesh motion with a linear elastic model

The equation of linear elasticity is formally based on the well-known momentum equations from structural mechanics as introduced previously. In a steady-state regime, we obtain the following equation defining a static equilibrium:

$$-\widehat{\mathrm{div}}(\widehat{\sigma}_{\mathrm{mesh}}) = 0, \quad \hat{u}_f = \hat{u}_s \text{ on } \widehat{\Gamma}_i, \quad \hat{u}_f = 0 \text{ on } \partial\widehat{\Omega}_f \setminus \widehat{\Gamma}_i,$$

where $\widehat{\sigma}_{\mathrm{mesh}}$ is formally equivalent to the STVK constitutive tensor in Equation (3.6). It is given by

$$\widehat{\sigma}_{\mathrm{mesh}} := \alpha_\lambda(\mathrm{tr}\,\hat{\epsilon})\hat{I} + 2\alpha_\mu\hat{\epsilon}, \tag{3.14}$$

where $\hat{\epsilon} = \frac{1}{2}(\widehat{\nabla}\hat{u}_f + \widehat{\nabla}\hat{u}_f^T)$ denotes the linearized version of the strain tensor $\widehat{E}$. The mesh parameters $\alpha_\lambda := \alpha_\lambda(\hat{x})$ and $\alpha_\mu := \alpha_\mu(\hat{x})$ are chosen in a way, such that a good fluid mesh quality is guaranteed. By virtue of (2.14), we compute α_λ and α_μ from the Young modulus E_Y and the Poisson ration ν_s. Therefore, we choose E_Y according to (3.12) or (3.13). Further, we choose a negative Poisson ratio (recall that $\nu_s \in (-1, 0.5]$). Materials with negative Poisson ratio belongs to auxetic materials and they become thinner in the perpendicular direction, when they are compressed. This is a useful property for the evolution of the fluid mesh. We refer the reader again to [126] (and references cited therein) for other choices of α_λ and α_μ.

Mesh motion with a biharmonic model

Using the biharmonic mesh model provides much more freedom in choosing boundary conditions [34, 70]. In this thesis, solving the biharmonic equation is introduced as a third possible fluid mesh deformation. This model is considered in a mixed formulation in the sense of Ciarlet [34]. As before, an artificial material parameter is used to control the mesh motion. Then, we deduce

$$\hat{\eta}_f = -\alpha_u \hat{\Delta} \hat{u}_f \quad \text{and} \quad -\alpha_u \hat{\Delta} \hat{\eta}_f = 0. \tag{3.15}$$

It is more convenient to consider the single component functions $\hat{u}_f^{(1)}$ and $\hat{u}_f^{(2)}$,

$$\begin{aligned} \hat{\eta}_f^{(1)} &= -\alpha_u \hat{\Delta} \hat{u}_f^{(1)} \quad \text{and} \quad -\alpha_u \hat{\Delta} \hat{\eta}_f^{(1)} = 0, \\ \hat{\eta}_f^{(2)} &= -\alpha_u \hat{\Delta} \hat{u}_f^{(2)} \quad \text{and} \quad -\alpha_u \hat{\Delta} \hat{\eta}_f^{(2)} = 0. \end{aligned}$$

We utilize two types of boundary conditions. First, we pose the *first type of boundary conditions* (that corresponds to conditions of a clamped plate)

$$\hat{u}_f^{(k)} = \partial_n \hat{u}_f^{(k)} = 0 \quad \text{on } \partial\widehat{\Omega}_f \setminus \widehat{\Gamma}_i, \quad \text{for } k = 1, 2.$$

Second, we are concerned with a mixture of boundary conditions (see Figure 7.1)

$$\begin{aligned} \hat{u}_f^{(1)} = \partial_n \hat{u}_f^{(1)} = 0 \quad \text{and} \quad \hat{\eta}_f^{(1)} = \partial_n \hat{\eta}_f^{(1)} = 0 \quad \text{on } \widehat{\Gamma}_{\text{in}} \cup \widehat{\Gamma}_{\text{out}}, \\ \hat{u}_f^{(2)} = \partial_n \hat{u}_f^{(2)} = 0 \quad \text{and} \quad \hat{\eta}_f^{(2)} = \partial_n \hat{\eta}_f^{(2)} = 0 \quad \text{on } \widehat{\Gamma}_{\text{wall}}, \end{aligned} \tag{3.16}$$

which we call *second type of boundary conditions*. In particular, the conditions

$$\hat{\eta}_f^{(k)} = \partial_n \hat{\eta}_f^{(k)} = 0 \quad \text{on } \widehat{\Gamma}_{\text{in}} \cup \widehat{\Gamma}_{\text{out}}, \quad \text{for } k = 1, 2,$$

mean, that a plate is left free along this boundary part. Using biharmonic mesh motion, we also must enforce two conditions on the interface:

$$\hat{u}_f = \hat{u}_s \quad \text{and} \quad \partial_n \hat{u}_f = \partial_n \hat{u}_s \quad \text{on } \widehat{\Gamma}_i.$$

We emphasize that the biharmonic model does not require a careful choice of a mesh-dependent parameter. Using this model, we simply choose a small number $\alpha_u > 0$ as parameter.

Remark 3.3. Using the second type of boundary conditions in a rectangular domain where the coordinate axes match the Cartesian coordinate system, as shown in Figure 7.1, leads to mesh movement only in the tangential direction. This effect reduces mesh cell distortion because only the perpendicular directions of $\hat{u}_f$ and $\hat{\eta}_f$ are constrained to zero at the different parts of $\partial\widehat{\Omega}$. These boundary conditions are examined in two numerical examples in Section 7.1.

3.3.3 The practicable FSI problem in the reference domain

With the previous preparations at hand, in this section, we define the *practicable* monolithically coupled fluid-structure interaction problems. Thus, we define the setting in a fixed domain and formulate the equations in a fashion that can be used in a straightforward way for the implementation. The coupled strong problem (with the fluid equations defined in a moving domain Ω) can be formulated as illustrated previously, see [53], p. 120-121, and [12]. The corresponding weak formulations have also been derived elsewhere [12, 104].

The definitions of the fully coupled problems include three types of nonlinearities that are divided into two groups. The physical nonlinearities includes the convection term for the fluid and the nonlinear structure model, whereas the additional nonlinearity induced by the ALE transformation is a so-called geometric nonlinearity.

Then, the weak form reads:

Problem 3.6 (FSI with harmonic and linear-elastic mesh motion). *Find* $\{\hat{v}_f, \hat{v}_s, \hat{u}_f, \hat{u}_s, \hat{p}_f, \hat{p}_s\} \in \{\hat{v}_f^D + \hat{V}_{f,\hat{v}}^0\} \times \hat{L}_s \times \{\hat{u}_f^D + \hat{V}_{f,\hat{u}}^0\} \times \{\hat{u}_s^D + \hat{V}_s^0\} \times \hat{L}_f^0 \times \hat{L}_s^0$, *such that* $\hat{v}_f(0) = \hat{v}_f^0$, $\hat{v}_s(0) = \hat{v}_s^0$, $\hat{u}_f(0) = \hat{u}_f^0$, *and* $\hat{u}_s(0) = \hat{u}_s^0$ *are satisfied, and for almost all time steps* $t \in \hat{I}$ *holds:*

$$
\begin{aligned}
(\hat{J}\hat{\rho}_f \partial_t \hat{v}_f, \hat{\psi}^v)_{\widehat{\Omega}_f} + (\hat{\rho}_f \hat{J}(\widehat{F}^{-1}(\hat{v}_f - \hat{w}) \cdot \widehat{\nabla})\hat{v}_f), \hat{\psi}^v)_{\widehat{\Omega}_f} & \\
+(\hat{J}\widehat{\sigma}_f \widehat{F}^{-T}, \widehat{\nabla}\hat{\psi}^v)_{\widehat{\Omega}_f} - \langle \hat{g}_f, \hat{\psi}^v \rangle_{\widehat{\Gamma}_N} - (\hat{\rho}_f \hat{J} \hat{f}_f, \hat{\psi}^v)_{\widehat{\Omega}_f} = 0 \quad & \forall \hat{\psi}^v \in \hat{V}_{f,\widehat{\Gamma}_i}^0, \\
(\hat{\rho}_s \partial_t \hat{v}_s, \hat{\psi}^v)_{\widehat{\Omega}_s} + (\widehat{F}\widehat{\Sigma}, \widehat{\nabla}\hat{\psi}^v)_{\widehat{\Omega}_s} & \\
+\gamma_w(\hat{v}_s, \hat{\psi}^v)_{\widehat{\Omega}_s} + \gamma_s(\hat{\epsilon}(\hat{v}_s), \widehat{\nabla}\hat{\psi}^v)_{\widehat{\Omega}_s} - (\hat{\rho}_s \hat{f}_s, \hat{\psi}^v)_{\widehat{\Omega}_s} = 0 \quad & \forall \hat{\psi}^v \in \hat{V}_s^0, \\
(\widehat{\sigma}_{mesh}, \widehat{\nabla}\hat{\psi}^u)_{\widehat{\Omega}_f} = 0 \quad & \forall \hat{\psi}^u \in \hat{V}_{f,\hat{u},\widehat{\Gamma}_i}^0, \\
\hat{\rho}_s(\partial_t \hat{u}_s - \hat{v}_s, \hat{\psi}^u)_{\widehat{\Omega}_s} = 0 \quad & \forall \hat{\psi}^u \in \hat{L}_s, \\
(\widehat{div}(\hat{J}\widehat{F}^{-1}\hat{v}_f), \hat{\psi}^p)_{\widehat{\Omega}_f} = 0 \quad & \forall \hat{\psi}^p \in \hat{L}_f^0, \\
(\hat{P}_s, \hat{\psi}^p)_{\widehat{\Omega}_s} = 0 \quad & \forall \hat{\psi}^p \in \hat{L}_s^0,
\end{aligned}
$$

with $\hat{\rho}_f$, $\hat{\rho}_s$, ν_f, μ_s, λ_s, $\widehat{F}$, *and* $\hat{J}$ *as defined before. The stress tensors* $\widehat{\sigma}_f$, $\widehat{\Sigma}$, *and* $\widehat{\sigma}_{mesh}$ *are defined in the Equations* (3.3), (3.5), (3.6), *and in* (3.11) *and* (3.14), *respectively. The pressure-related quantity in the last equation is determined by* $\hat{P}_s = \hat{J} - 1$ *(volume conserving), using incompressible materials, such as the INH or the IMR material. In the case of the STVK material, we define an artificial pressure such that* $\hat{P}_s = \hat{p}_s$.

Next, we state the monolithic setting for fluid-structure interaction with a biharmonic mesh motion model utilizing the first type of boundary conditions:

Problem 3.7 (FSI with biharmonic mesh motion). *Find* $\{\hat{v}_f, \hat{v}_s, \hat{u}_f, \hat{u}_s, \hat{\eta}_f, \hat{\eta}_s, \hat{p}_f, \hat{p}_s\} \in \{\hat{v}_f^D + \hat{V}_{f,\hat{v}}^0\} \times \hat{L}_s \times \{\hat{u}_f^D + \hat{V}_{f,\hat{u}}^0\} \times \{\hat{u}_s^D + \hat{V}_s^0\} \times \hat{V}_f \times \hat{V}_s \times \hat{L}_f^0 \times \hat{L}_s^0$, *such that* $\hat{v}_f(0) = \hat{v}_f^0$, $\hat{v}_s(0) = \hat{v}_s^0$, $\hat{u}_f(0) = \hat{u}_f^0$, $\hat{u}_s(0) = \hat{u}_s^0$ *are satisfied, for almost all time steps* $t \in I$, *and*

$$
\begin{aligned}
(\hat{J}\hat{\rho}_f \partial_t \hat{v}_f, \hat{\psi}^v)_{\widehat{\Omega}_f} + (\hat{\rho}_f \hat{J}(\widehat{F}^{-1}(\hat{v}_f - \hat{w}) \cdot \widehat{\nabla})\hat{v}_f), \hat{\psi}^v)_{\widehat{\Omega}_f} \\
+(\hat{J}\hat{\sigma}_f \widehat{F}^{-T}, \widehat{\nabla}\hat{\psi}^v)_{\widehat{\Omega}_f} - \langle \hat{g}_f, \hat{\psi}^v \rangle_{\widehat{\Gamma}_N} - (\hat{\rho}_f \hat{J}\hat{f}_f, \hat{\psi}^v)_{\widehat{\Omega}_f} = 0 \quad \forall \hat{\psi}^v \in \hat{V}_{f,\widehat{\Gamma}_i}^0, \\
(\hat{\rho}_s \partial_t \hat{v}_f, \hat{\psi}^v)_{\widehat{\Omega}_s} + (\widehat{F}\widehat{\Sigma}, \widehat{\nabla}\hat{\psi}^v)_{\widehat{\Omega}_s} \\
+\gamma_w(\hat{v}_s, \hat{\psi}^v)_{\widehat{\Omega}_s} + \gamma_s(\hat{\epsilon}(\hat{v}_s), \widehat{\nabla}\hat{\psi}^v)_{\widehat{\Omega}_s} - (\hat{\rho}_s \hat{f}_s, \hat{\psi}^v)_{\widehat{\Omega}_s} = 0 \quad \forall \hat{\psi}^v \in \hat{V}_s^0, \\
(\alpha_u \hat{\eta}_f, \hat{\psi}^\eta)_{\widehat{\Omega}_f} - (\alpha_u \widehat{\nabla}\hat{u}_f, \widehat{\nabla}\hat{\psi}^\eta)_{\widehat{\Omega}_f} = 0 \quad \forall \hat{\psi}^\eta \in \hat{V}_f, \\
(\alpha_u \hat{\eta}_s, \hat{\psi}^\eta)_{\widehat{\Omega}_s} - (\alpha_u \widehat{\nabla}\hat{u}_s, \widehat{\nabla}\hat{\psi}^\eta)_{\widehat{\Omega}_s} = 0 \quad \forall \hat{\psi}^\eta \in \hat{V}_s, \\
(\alpha_u \widehat{\nabla}\hat{\eta}_f, \widehat{\nabla}\hat{\psi}^u)_{\widehat{\Omega}_f} = 0 \quad \forall \hat{\psi}^u \in \hat{V}_{f,\hat{u},\widehat{\Gamma}_i}^0, \\
\hat{\rho}_s(\partial_t \hat{u}_s - \hat{v}_s, \hat{\psi}^u)_{\widehat{\Omega}_s} = 0 \quad \forall \hat{\psi}^u \in \hat{L}_s, \\
(\widehat{div}(\hat{J}\widehat{F}^{-1}\hat{v}_f), \hat{\psi}^p)_{\widehat{\Omega}_f} = 0 \quad \forall \hat{\psi}^p \in \hat{L}_f^0, \\
(\hat{P}_s, \hat{\psi}^p)_{\widehat{\Omega}_s} = 0 \quad \forall \hat{\psi}^p \in \hat{L}_s^0,
\end{aligned}
$$

with all quantities as defined in Problem 3.6 and some diffusion parameter α_u *defined in* (3.15).

Remark 3.4. The monolithic variational formulation for the second type of boundary conditions is formally equivalent as demonstrated in Problem 3.7. Only the definition of the function spaces for trial and test functions of the displacement variables $\hat{u}$ and $\hat{\eta}$ changes.

For later purposes, we also state a stationary version of the coupled equations:

Problem 3.8 (Stationary FSI with harmonic and linear-elastic mesh motion). *Find* $\{\hat{v}_f, \hat{u}_f, \hat{u}_s, \hat{p}_f, \hat{p}_s\} \in \{\hat{v}_f^D + \hat{V}_{f,\hat{v}}^0\} \times \{\hat{u}_f^D + \hat{V}_{f,\hat{u}}^0\} \times \{\hat{u}_s^D + \hat{V}_s^0\} \times \hat{L}_f^0 \times \hat{L}_s^0$, *such that*

$$
\begin{aligned}
(\hat{\rho}_f \hat{J}(\widehat{F}^{-1}\hat{v}_f \cdot \widehat{\nabla})\hat{v}_f), \hat{\psi}^v)_{\widehat{\Omega}_f} \\
+(\hat{J}\hat{\sigma}_f \widehat{F}^{-T}, \widehat{\nabla}\hat{\psi}^v)_{\widehat{\Omega}_f} - \langle \hat{g}_f, \hat{\psi}^v \rangle_{\widehat{\Gamma}_N} - (\hat{\rho}_f \hat{J}\hat{f}_f, \hat{\psi}^v)_{\widehat{\Omega}_f} = 0 \quad \forall \hat{\psi}^v \in \hat{V}_{f,\hat{v}}^0, \\
(\widehat{F}\widehat{\Sigma}, \widehat{\nabla}\hat{\psi}^v)_{\widehat{\Omega}_s} - (\hat{\rho}_s \hat{f}_s, \hat{\psi}^v)_{\widehat{\Omega}_s} = 0 \quad \forall \hat{\psi}^v \in \hat{V}_s^0, \\
(\widehat{\sigma}_{mesh}, \widehat{\nabla}\hat{\psi}^u)_{\widehat{\Omega}_f} = 0 \quad \forall \hat{\psi}^u \in \hat{V}_{f,\hat{u},\widehat{\Gamma}_i}^0, \\
(\widehat{div}(\hat{J}\widehat{F}^{-1}\hat{v}_f), \hat{\psi}^p)_{\widehat{\Omega}_f} = 0 \quad \forall \hat{\psi}^p \in \hat{L}_f^0, \\
(\hat{P}_s, \hat{\psi}^p)_{\widehat{\Omega}_s} = 0 \quad \forall \hat{\psi}^p \in \hat{L}_s^0,
\end{aligned}
$$

with all quantities as defined in Problem 3.6.

The Problem 3.8 offers further insight of key differences between stationary and nonstationary fluid-structure interactions. We do not search any longer for a velocity solution $\hat{v}_s$ in the structure because it is zero in a stationary setting. Consequently, the damping terms vanish because they are defined by means of $\hat{v}_s$. Likewise, the fluid domain velocity $\hat{w}$ vanishes too.

In all three previously defined problems, using the STVK material model, because the last term is redundant, i.e.,

$$(\hat{P}_s, \hat{\psi}^p)_{\widehat{\Omega}_s} = 0 \quad \forall \hat{\psi}^p \in \hat{L}^0_s,$$

because there is no physical pressure $\hat{p}_s$ in compressible structures.

The weak continuity of the normal stresses of Equation (3.9) that is required on $\widehat{\Gamma}_i$ becomes an implicit condition computing nonstationary fluid-structure interactions:

$$(\hat{J}\hat{\sigma}_f\hat{F}^{-T}\hat{n}_f, \hat{\psi}^v)_{\widehat{\Omega}_f} + (\hat{F}\hat{\Sigma}\hat{n}_s, \hat{\psi}^v)_{\widehat{\Omega}_s} + \gamma_s(\hat{\epsilon}(\hat{v}_s)\hat{n}_s, \hat{\psi}^v)_{\widehat{\Omega}_s} = 0 \quad \forall \hat{\psi}^v \in \hat{V}^0.$$

In stationary settings, we deal with

$$(\hat{J}\hat{\sigma}_f\hat{F}^{-T}\hat{n}_f, \hat{\psi}^v)_{\widehat{\Omega}_f} + (\hat{F}\hat{\Sigma}\hat{n}_s, \hat{\psi}^v)_{\widehat{\Omega}_s} = 0 \quad \forall \hat{\psi}^v \in \hat{V}^0.$$

Extension to multiple-structure problems

The frameworks introduced in the Problems 3.6 and 3.7 also serve for the coupling of multiple structures with fluid flows. In such cases, the second coupling condition in Equation (3.7) becomes an implicit condition. The Dirichlet-like condition of Equation (3.7) is strongly imposed in the corresponding Sobolev space.

In the previously stated problems, the structure stress tensors are combined in one single tensor:

$$\widehat{\Sigma} := \sum_i^n \hat{\chi}_i \widehat{\Sigma}_i, \quad n \in \mathbb{N},$$

where $\hat{\chi}_i(\hat{x}) := 1$ for $\hat{x} \in \widehat{\Omega}_i$ and $\hat{\chi}_i(\hat{x}) := 0$ for $\hat{x} \in \widehat{\Omega}_k$ for $k \neq i$.

Example 3.1 (Multiple structures for heart-valve dynamics). *Let $\widehat{\Omega}_s = \widehat{\Omega}_s^{heart} \cup \widehat{\Omega}_s^{valve} \cup \widehat{\Omega}_s^{aorta} \cup \widehat{\Omega}_s^{ext}$. Let the following constitutive tensors be given:*

$$\begin{aligned} &\widehat{\Sigma}^{heart}_{INH,1} \quad in\ \widehat{\Omega}_s^{heart}, \quad \widehat{\Sigma}^{valve}_{INH,2} \quad in\ \widehat{\Omega}_s^{valve}, \quad \mu_{INH,1} \neq \mu_{INH,2}, \\ &\widehat{\Sigma}^{aorta}_{STVK,1} \quad in\ \widehat{\Omega}_s^{aorta}, \quad \widehat{\Sigma}^{ext}_{STVK,2} \quad in\ \widehat{\Omega}_s^{ext}, \quad \mu_{STVK,1} \neq \mu_{STVK,2}. \end{aligned}$$

On each interface between two structures, we consider the coupling conditions (3.7)*. Then, the combined structure tensor can be written as*

$$\widehat{\Sigma} = \hat{\chi}_s^{heart}\widehat{\Sigma}^{heart}_{INH,1} + \hat{\chi}_s^{valve}\widehat{\Sigma}^{valve}_{INH,2} + \hat{\chi}_s^{aorta}\widehat{\Sigma}^{aorta}_{STVK,1} + \hat{\chi}_s^{ext}\widehat{\Sigma}^{ext}_{STVK,2}.$$

3.4 A priori energy balance for the FSI problem

One of the key advantages of monolithic solution approaches is their robustness with respect to numerical stability. In this section, we show that our coupled problem is indeed stable in the energy norm. The proof follows the philosophy of Fernández and Gerbeau [48]; their statement was derived for a coupling between one single structure model and the fluid equations. We extend their result to the case of a coupling with damped structure equations and multiple structure models. However, the latter issue causes no difficulties because the material can be written in terms of the strain-energy function, which implicitly comprises the different structure models. This finding was illustrated previously in terms of the constitutive tensors. In contrast to the practicable version of the previous section, we use time-dependent domains to set up the fluid problem. These equations were introduced in Problem 3.1.

The energy loss of the systems originates from the viscosity of the fluid and the damping terms that have been added to the structure. The energy exchanged over the interface is exactly balanced, due to the coupling conditions for the velocity and the stresses (see the Relations (3.8) and (3.9)). Specifically, the coupling conditions of the different structure models are fulfilled (see Equation (3.7)).

We prove the following theorem with light conditions regarding the interface conditions (3.8). Moreover, we neglect the do-nothing outflow condition and the right-hand-side forces, and we assume that the system is isolated, i.e., $v_f = \hat{u}_s = 0$ on all outer boundaries.

For the first result, we employ the damped structure equations in the whole subdomain $\widehat{\Omega}_s$. The total energy of the coupled system at time step t is denoted by $E(t)$ with

$$E(t) := \frac{\rho_f}{2}||v_f||^2_{\Omega_f} + \frac{\hat{\rho}_s}{2}||\hat{v}_s||^2_{\widehat{\Omega}_s} + \int\limits_{\widehat{\Omega}_s} W(\hat{E})\, d\hat{x}.$$

For (linear) strong damping with the help of $\hat{\epsilon}(\hat{v}_s)$, the scalar product induces the energy norm

$$||\hat{\epsilon}(\cdot)||^2_E := (\hat{\epsilon}(\cdot), \widehat{\nabla}\cdot)_{\widehat{\Omega}_s}. \tag{3.17}$$

The right term is positive thanks to the Korn inequality.

Theorem 3.3. *Let the coupled fluid-structure problem be isolated, i.e., $v_f = 0$ on $\partial\Omega_f \setminus \Gamma_i$ and a stress-free state $\widehat{F}\widehat{\Sigma}\hat{n}_s = 0$ on $\partial\widehat{\Omega}_s \setminus \widehat{\Gamma}_i$ and (if $\gamma_s > 0$) $\hat{\epsilon}(\hat{v}_s)\hat{n}_s = 0$ on $\partial\widehat{\Omega}_s \setminus \widehat{\Gamma}_i$. Then, the following a priori energy estimate holds true:*

$$\begin{aligned}
&\frac{d}{dt}\left[\frac{\rho_f}{2}\|v_f\|^2_{\Omega_f} + \frac{\hat{\rho}_s}{2}\|\hat{v}_s\|^2_{\widehat{\Omega}_s} + \int\limits_{\widehat{\Omega}_s} W(\widehat{E})\ \mathrm{d}\hat{x}\right] \\
&+ 2\rho_f\nu_f\|D(v_f)\|^2_{\Omega_f} + \gamma_w\|\hat{v}_s\|^2_{\widehat{\Omega}_s} + \gamma_s||\hat{\epsilon}(\hat{v}_s)||^2_E \\
&= 0.
\end{aligned}$$

That implies the following energy decay property:

$$E(t) = E(0) - \int_0^t \Big[\gamma_w ||\hat{v}_s(\tau)||^2_{\widehat{\Omega}_s} + \gamma_s ||\hat{\epsilon}(\hat{v}_s)(\tau)||^2_E + 2\rho_f \nu_f ||D(v_f)(\tau)||^2_{\Omega_f}\Big]\, d\tau.$$

Proof. We proof the argument with a standard energy technique. The outline is analogous to [48]. The equations are multiplied through by v_f and $\hat{v}_s$, respectively. We start with the fluid equations, defined in the weak formulation in Problem 3.1. We use $\psi^v = v_f$ and $\psi^p = p_f$, and obtain for the first term:

$$\begin{aligned}
\rho_f(\hat{\partial}_t v_f, v_f)_{\Omega_f} &= \rho_f(\hat{J}\partial_t \hat{v}_f, \hat{v}_f)_{\widehat{\Omega}_f} \\
&= \frac{\rho_f}{2}\int_{\widehat{\Omega}_f} \partial_t[\hat{J}\,|\hat{v}_f|^2]\,\mathrm{d}\hat{x} - \frac{\rho_f}{2}\int_{\widehat{\Omega}_f} \hat{J}\,\widehat{\mathrm{div}}\,\hat{w}\,|\hat{v}_f|^2\,\mathrm{d}\hat{x} \\
&= d_t\frac{\rho_f}{2}||v_f||^2_{\Omega_f} - \frac{\rho_f}{2}\int_{\Omega_f} \mathrm{div}\, w\,|v_f|^2\,\mathrm{d}x. \qquad (3.18)
\end{aligned}$$

The second term (the ALE convection term) is treated as follows (using integration by parts):

$$\begin{aligned}
\rho_f\Big((v_f - w)\cdot\nabla v_f, v_f\Big)_{\Omega_f} &= \frac{\rho_f}{2}\int_{\Omega_f}(v_f - w)\cdot\nabla\,|v_f|^2\,\mathrm{d}x \\
&= \frac{\rho_f}{2}\int_{\Gamma_{f,N}}(v_f - w)\,n_f\,|v_f|^2\,\mathrm{d}s - \frac{\rho_f}{2}\int_{\Omega_f}\nabla\cdot(v_f - w)\,|v_f|^2\,\mathrm{d}x.
\end{aligned}$$

Now, we use $v_f = w$ on Γ_i and $v_f = 0$ on $\partial\Omega_f\backslash\Gamma_i$. Furthermore, we use the incompressibility of the fluid, i.e., $\nabla\cdot v_f = 0$ on the continuous level. This implies

$$\rho_f\Big((v_f - w)\cdot\nabla\, v_f, v_f\Big)_{\Omega_f} = \frac{\rho_f}{2}\int_{\Omega_f}\nabla\cdot w\,|v_f|^2\,\mathrm{d}x. \qquad (3.19)$$

This term cancels with the last term of the first relation (3.18). Next, we treat the term including the Cauchy stress tensor (using again the incompressibility of the fluid) and the symmetry of $D(v_f)$:

$$\begin{aligned}
-(\nabla\cdot\sigma_f, v_f)_{\Omega_f} &= -\langle\sigma_f n_f, v_f\rangle_{\Gamma_{f,N}\cup\Gamma_i} + (\sigma_f, \nabla v_f)_{\Omega_f} \\
&= -\langle\sigma_f n_f, v_f\rangle_{\Gamma_{f,N}\cup\Gamma_i} + (-p_f, \nabla\cdot v_f)_{\Omega_f} + 2\rho_f\nu_f\Big(D(v_f), \nabla v_f\Big)_{\Omega_f} \\
&= -\langle\sigma_f n_f, v_f\rangle_{\Gamma_{f,N}\cup\Gamma_i} + 2\rho_f\nu_f\Big(D(v_f), D(v_f)\Big)_{\Omega_f}. \qquad (3.20)
\end{aligned}$$

Summarizing (3.18), (3.19), and (3.20), gives us:

$$d_t\frac{\rho_f}{2}||v_f||^2_{\Omega_f} + 2\rho_f\nu_f||D(v_f)||^2_{\Omega_f} - \langle\sigma_f n_f, v_f\rangle_{\Gamma_{f,N}\cup\Gamma_i}. \qquad (3.21)$$

In a fully isolated system, i.e. , $\Gamma_{f,N} = \emptyset$, the following boundary term in Equation (3.21) remains on the interface Γ_i:

$$-\langle \sigma_f n_f, v_f \rangle_{\Gamma_{f,N} \cup \Gamma_i} = -\langle \sigma_f n_f, v_f \rangle_{\Gamma_i}.$$

We continue with the mass term of the structure. We multiply in Equation (2.15) through by $\hat{v}_s = \partial_t \hat{u}_s$ and integrate over $\widehat{\Omega}_s$. Then, we deduce

$$\hat{\rho}_s (\partial_t^2 \hat{u}_s, \partial_t \hat{u}_s)_{\widehat{\Omega}_s} = d_t \frac{\hat{\rho}_s}{2} ||\hat{v}_s||^2_{\widehat{\Omega}_s}. \tag{3.22}$$

The second term is treated as follows (using partial integration):

$$\begin{aligned} -(\widehat{\nabla} \cdot (\widehat{F}\widehat{\Sigma}), \hat{v}_s)_{\widehat{\Omega}_s} &= (\widehat{F}\widehat{\Sigma}, \widehat{\nabla}\hat{v}_s)_{\widehat{\Omega}_s} - \int\limits_{\widehat{\Gamma}_{s,N} \cup \widehat{\Gamma}_i} \widehat{F}\widehat{\Sigma}\hat{n}_s \cdot \hat{v}_s \, \mathrm{d}s \\ &= (\widehat{F}\widehat{\Sigma}, \widehat{\nabla}\hat{v}_s)_{\widehat{\Omega}_s} - \int\limits_{\widehat{\Gamma}_i} \widehat{F}\widehat{\Sigma}\hat{n}_s \cdot \hat{v}_s \, \mathrm{d}s. \end{aligned} \tag{3.23}$$

In the last term of Equation (3.23), we use the boundary condition $\widehat{F}\widehat{\Sigma}\hat{n}_s = 0$ on $\partial\widehat{\Omega}_s \setminus \widehat{\Gamma}_i$ that was part of our assumptions. We rearrange the first term as follows with the help of the component-wise multiplication operator (for second order tensors A and B holds $A : B = \sum_{ij} A_{ij} B_{ij}$):

$$\begin{aligned} \widehat{F}\widehat{\Sigma} : \widehat{\nabla}\hat{v}_s &= \widehat{F}\widehat{\Sigma} : \widehat{\nabla}\partial_t \hat{u}_s = \widehat{F}\widehat{\Sigma} : \partial_t \widehat{\nabla}\hat{u}_s \\ &= \widehat{F}\widehat{\Sigma} : \partial_t [\widehat{\nabla}\hat{u}_s + \hat{I}] = \widehat{F}\widehat{\Sigma} : \partial_t \widehat{F} \\ &= \widehat{\Sigma} : \partial_t \widehat{F}\widehat{F} = \widehat{\Sigma} : \partial_t \widehat{E}, \quad \text{with } \widehat{E} = \frac{1}{2}(\widehat{F}^T\widehat{F} - \hat{I}) \\ &= \partial_E W : \partial_t \widehat{E}, \quad \text{with } \widehat{\Sigma} = \partial_E W \\ &= \partial_t W(\widehat{E}), \end{aligned}$$

where we use the Green-Lagrange tensor and the definition of hyperelasticity (see Equation (2.13)) of the material model. The definitions of the time derivative of material tensors can be found in Holzapfel [78]. We plug the previous relation into (3.23):

$$\begin{aligned} (\widehat{F}\widehat{\Sigma}, \widehat{\nabla}\hat{v}_s)_{\widehat{\Omega}_s} - \int\limits_{\widehat{\Gamma}_i} \widehat{F}\widehat{\Sigma}\hat{n}_s \cdot \hat{v}_s \, \mathrm{d}\hat{s} &= \int\limits_{\widehat{\Omega}_s} \partial_t W(E) \, \mathrm{d}\hat{x} - \int\limits_{\widehat{\Gamma}_i} \widehat{F}\widehat{\Sigma}\hat{n}_s \cdot \hat{v}_s \, \mathrm{d}\hat{s} \\ &= d_t \int\limits_{\widehat{\Omega}_s} W(E) \, \mathrm{d}\hat{x} - \int\limits_{\widehat{\Gamma}_i} \widehat{F}\widehat{\Sigma}\hat{n}_s \cdot \hat{v}_s \, \mathrm{d}\hat{s}. \end{aligned} \tag{3.24}$$

Summarizing (3.22) and (3.24), we finally get:

$$d_t \frac{\hat{\rho}_s}{2} ||\hat{v}_s||^2_{\widehat{\Omega}_s} + d_t \int\limits_{\widehat{\Omega}_s} W(\widehat{E}) \, \mathrm{d}\hat{x} - \int\limits_{\widehat{\Gamma}_i} \widehat{F}\widehat{\Sigma}\hat{n}_s \cdot \hat{v}_s \, \mathrm{d}\hat{s}.$$

Combining this result with the fluid equations, we obtain

$$d_t\Big[\frac{\rho_f}{2}||v_f||^2_{\Omega_f} + \frac{\hat{\rho}_s}{2}||\hat{v}_s||^2_{\widehat{\Omega}_s} + \int\limits_{\widehat{\Omega}_s} W(\widehat{E})\,\mathrm{d}\hat{x}\Big]$$
$$+ 2\rho_f\nu_f||D(v_f)||^2_{\Omega_f} - \langle\sigma_f n_f, v_f\rangle_{\Gamma_i} - \langle\widehat{F}\widehat{\Sigma}\hat{n}_s, \hat{v}_s\rangle_{\widehat{\Gamma}_i}.$$

The both interface terms cancel, thanks to the coupling conditions, such that

$$\langle\sigma_f n_f, v_f\rangle_{\Gamma_i} + \langle\widehat{F}\widehat{\Sigma}\hat{n}_s, \hat{v}_s\rangle_{\widehat{\Gamma}_i} = \langle\hat{J}\hat{\sigma}_f\widehat{F}^{-T}\hat{n}_f, \hat{v}_f\rangle_{\widehat{\Gamma}_i} + \langle\widehat{F}\widehat{\Sigma}\hat{n}_s, \hat{v}_s\rangle_{\widehat{\Gamma}_i} = 0.$$

It remains to consider the damping terms of the structure Equation (2.15). We multiply again by $\partial_t\hat{u}_s = \hat{v}_s$. Using integration by parts for strong damping, we obtain

$$\gamma_w(\partial_t\hat{u}_s, \partial_t\hat{u}_s)_{\widehat{\Omega}_s} - \gamma_s(\nabla\cdot\hat{\epsilon}(\partial_t\hat{u}_s), \partial_t\hat{u}_s)_{\widehat{\Omega}_s}$$
$$= \gamma_w||\hat{v}_s||^2_{\widehat{\Omega}_s} + \gamma_s(\hat{\epsilon}(\hat{v}_s), \widehat{\nabla}\hat{v}_s)_{\widehat{\Omega}_s} - \gamma_s\langle\hat{\epsilon}(\hat{v}_s)\hat{n}_s, \hat{v}_s\rangle_{\widehat{\Gamma}_i}.$$

The middle term is positive thanks to the Korn inequality. Thus, the scalar product induces the norm (an energy norm)

$$(\hat{\epsilon}(\hat{v}_s), \widehat{\nabla}\hat{v}_s)_{\widehat{\Omega}_s} =: ||\hat{\epsilon}(\hat{v}_s)||^2_E.$$

Moreover, the incorporation the strong damping induces an additional term on the interface. That means, for $\gamma_s > 0$, we get a modification of the coupling conditions on the interface. It holds:

$$(\hat{J}\hat{\sigma}_f\widehat{F}^{-T}\hat{n}_f, \hat{v}_f)_{\widehat{\Gamma}_i} + (\widehat{F}\widehat{\Sigma}\hat{n}_s, \hat{v}_s)_{\widehat{\Gamma}_i} + \gamma_s(\hat{\epsilon}(\hat{v}_s)\hat{n}_s, \hat{v}_s)_{\widehat{\Gamma}_i} = 0 \quad \text{on } \widehat{\Gamma}_i,$$

which corresponding strong form is stated in Equation (3.9). This concludes the proof of the first assertion. The energy decay (the second argument) can be proven by integration over the time interval, which immediately shows the assertion. □

For later purposes, we are interested in using different structure equations in $\widehat{\Omega}_s = \widehat{\Omega}_s^{\text{phys}} \cup \widehat{\Omega}_s^{\text{ext}}$. Specifically, we apply the standard (undamped) structure equations in $\widehat{\Omega}_s^{\text{phys}}$ and the supplementation of damping is only used in $\widehat{\Omega}_s^{\text{ext}}$. Thus, on the interface $\widehat{\Gamma}_i^{\text{in}} = \widehat{\Omega}_s^{\text{phys}} \cap \widehat{\Omega}_s^{\text{ext}}$, we deal with the following coupling condition for the continuity of the normal stresses:

$$\widehat{F}\widehat{\Sigma}_s\hat{n}_s = \widehat{F}\widehat{\Sigma}_s^{\text{ext}}\hat{n}_s^{\text{ext}} + \gamma_s\hat{\epsilon}_s(\hat{v}_s)\hat{n}_s^{\text{ext}} \quad \text{on } \widehat{\Gamma}_i^{\text{in}}. \tag{3.25}$$

The total energy of the coupled system at time step t is denoted by $E(t)$, which is defined as

$$E(t) := \frac{\rho_f}{2}||v_f||^2_{\Omega_f} + \frac{\hat{\rho}_s}{2}||\hat{v}_s||^2_{\widehat{\Omega}_s\cup\widehat{\Omega}_s^{\text{ext}}} + \int\limits_{\widehat{\Omega}\cup\widehat{\Omega}_s^{\text{ext}}} W(\hat{E})\,d\hat{x}.$$

Then, we obtain

Corollary 3.4. *Let the assumptions hold of Theorem 3.3. In addition, we divide the structure subdomain into a physical domain and an artificial domain:* $\widehat{\Omega}_s = \widehat{\Omega}_s^{phys} \cup \widehat{\Omega}_s^{ext}$. *The structural damping terms are only added in* $\widehat{\Omega}_s^{ext}$. *If* (3.25) *holds true, then*

$$\frac{d}{dt}\left[\frac{\rho_f}{2}\|v_f\|^2_{\Omega_f} + \frac{\hat{\rho}_s}{2}\|\hat{v}_s\|^2_{\widehat{\Omega}_s} + \int\limits_{\widehat{\Omega}_s} W(\widehat{E})\ \mathrm{d}\hat{x}\right] + 2\rho_f\nu_f\|D(v_f)\|^2_{\Omega_f}$$
$$+ \frac{d}{dt}\left[\frac{\hat{\rho}_s}{2}\|\hat{v}_s\|^2_{\widehat{\Omega}_s^{ext}} + \int\limits_{\widehat{\Omega}_s^{ext}} W(\widehat{E})\ \mathrm{d}\hat{x}\right] + \gamma_w\|\hat{v}_s\|^2_{\widehat{\Omega}_s^{ext}} + \gamma_s||\hat{\epsilon}(\hat{v}_s)||^2_E.$$

Thus, the energy decay property reads

$$E(t) = E(0) - \int\limits_0^t \left[\gamma_w||\hat{v}_s(\tau)||^2_{\widehat{\Omega}_s^{ext}} + \gamma_s||\hat{\epsilon}(\hat{v}_s)(\tau)||^2_E + 2\rho_f\nu_f||D(v_f)(\tau)||^2_{\Omega_f}\right] d\tau. \qquad (3.26)$$

Proof. The proof is straightforward shown with the help of the proof of Theorem 3.3. We derive the result in $\widehat{\Omega}_s^{\mathrm{phys}}$ by setting $\gamma_w = \gamma_s = 0$. Then, we work with $\gamma_w > 0$ and $\gamma_s > 0$ in the artificial domain $\widehat{\Omega}_s^{\mathrm{ext}}$. Finally, we note that not only the structure domain is extended by an artificial layer but also the fluid domain. Because we use the same fluid equations in Ω_f and Ω_f^{ext}, we omit their differentiation. Consequently, we obtain the assertion. □

Using Corollary 3.4, the desired energy dissipation in $\widehat{\Omega}_s^{\mathrm{ext}}$ is achieved with a careful choice of the (artificial) damping parameters γ_w and γ_s.

Indeed, it can be inferred from the energy decay property (3.26) that:

- For $\gamma_w, \gamma_s \to 0$ the artificial energy dissipation gets lost.
- For $\gamma_w, \gamma_s \to \infty$ the structure system tends to freeze in $\widehat{\Omega}_s^{\mathrm{ext}}$.

In fact, for $\gamma_w, \gamma_s \to 0$ it only remains a natural energy dissipation that comes through the Cauchy stress term in the fluid domain. In our computations in the Sections 8.4 and 8.3, we made the experience that the *best* dissipation rates were obtained for $\gamma_w \approx 10^4$ and $\gamma_s \approx 10^3$. A deeper analysis for the (qualitatively) *best* damping of a super-linear hyperbolic equation was made by Gazzola and Squassina [57] (see Theorem 3.8).

3.5 Coupling with absorbing fluid conditions

In the present section, we consider one particular aspect for fluid-wall interactions in hemodynamic applications. Because the outer walls are modeled as an elastic material that is not fixed by Dirichlet boundary conditions, pulse pressure waves propagate with time. In fact, flow simulations in a channel with rigid walls do not induce such behavior. As explained previously, the pressure waves have physical meaning; however, they are reflected at the artificial boundaries ($\widehat{\Gamma}_{\mathrm{in}}$ and $\widehat{\Gamma}_{\mathrm{out}}$) of the computational domain using standard boundary conditions. These reflections comprise no physics. Specifically, a larger

artery leads to greater pressure wave propagation, and larger reflections at the artificial boundaries. From mathematical and physical point of view, it is a rather complex task to determine the proper boundary conditions and this subject has been investigated for several years.

The *geometrical multiscale approach* (introduced by Formaggia et al. [49]), is often used to account for this deficiency. With this method, higher-dimensional models (in 3D or 2D) are coupled with lower-dimensional models (in 0D or 1D). The reason to introduce such a coupling originates from the fact that modeling and simulation are too difficult to perform for the whole human cardiovascular system. However, because the local flow dynamics in a specific region inside a blood vessel are strictly related to the global flow dynamics ([54, 103, 110], and the many references cited therein), their influence must not be neglected. Otherwise, only partial information can be extracted from the simulation and be used for further analysis and clinical applications. The need for the development of such models is motivated by the fact that specific data are not available (or are too difficult to measure), otherwise, the appropriate boundary conditions could be constructed from known data [54, 59, 103].

The goal of our considerations in this thesis is to investigate the interchange of the proposed boundary conditions for the structure outflow in the artificial layer with a simple choice of outflow conditions for the fluid and pressure. This coupling is novel and it is studied for a prototypical situation. Specifically, we are interested in blood vessel movement due to wave backflow of the structure and pulse pressure.

First, we start to recall possible boundary conditions for the Navier-Stokes equations for the artificial boundaries. The classical conditions are either Dirichlet or Neumann conditions

$$\hat{v}_f = \hat{g} \quad \text{on } \widehat{\Gamma}_D, \quad \widehat{\sigma}_f \cdot \hat{n} = \hat{h} \quad \text{on } \widehat{\Gamma}_N.$$

In the following, we introduce the concept of *defective* boundary conditions that are well-known in the blood flow community [53, 110]. Using defective boundary conditions, we deal with averaged data (i.e., the mean velocity and the mean pressure instead of vector-like conditions as mentioned above). The mean pressure on each free artificial section can be computed with help of

$$\frac{1}{|\Gamma_{\text{in,out}}|} \int\limits_{\Gamma_{\text{in,out}}} p \, \mathrm{d}s = P_{\Gamma_{\text{in,out}}}(t).$$

The net flux condition reads:

$$\int\limits_{\Gamma_{\text{in,out}}} v_f \cdot n_f \, \mathrm{d}s = Q(t).$$

The difficulty in those cases is to guarantee the well-posedness of the resulting system. It is done for a special configuration in Heywood et al. [72]. The outcome of their analysis is the do-nothing condition, that is here stated for an unsymmetric stress tensor:

$$(p - \rho_f \nu_f \partial_n v_n)|_{\Gamma_k} = P_{\Gamma_{\text{in,out}}}(t) \quad \text{and} \quad \partial_n v_t|_{\Gamma_{\text{in,out}}} = 0.$$

Specifically, the pressure is implicitly normalized to zero over the outflow section. The extension to symmetric stress tensors $D(v_f)$ is discussed in [72].

The geometrical multiscale approach was simplified by Moura et al. [87, 104] to a specific pressure condition on the outflow boundary, i.e., by adding a constant mean pressure value at each time step to the zero mean pressure from the do-nothing condition. This pressure correction is a so-called *absorbing condition* for the fluid problem, that is applied on the artificial outflow boundary Γ_{out} of the domain of interest.

The absorbing condition can be derived from a 1D reduced model (see [87]) for the flow field and it is computed in the reference configuration for each time step $n = 0, 1, 2, \ldots$ by

$$\bar{p}^{n+1} \approx \hat{R}\hat{Q}^n \quad \text{on } \widehat{\Gamma}_{\text{out}},$$

where $\bar{p}$ is a mean value for the pressure, $\hat{R}$ (the resistance) is some constant with information on the geometry, structural properties, and fluid properties:

$$\hat{R} = \frac{\sqrt{\hat{\rho}_f \beta}}{\sqrt{2}\hat{D}^{5/4}}, \quad \text{and } \hat{\beta} = \frac{\sqrt{\pi}\,\hat{h}E_Y}{1-\nu_s}, \tag{3.27}$$

where $\hat{D}$ denotes the diameter of the blood vessel and $\hat{\rho}_f$ the density of the fluid. Furthermore, $\hat{h}$ denotes the height of the structure domain (the thickness of the blood vessel wall) in the reference configuration, E_Y the Young modulus of the structure, and ν_s the Poisson ratio.

The flux value $\hat{Q}^n$ of the velocity is measured on $\widehat{\Gamma}_{\text{out}}$ by:

$$\hat{Q}^n = \int_{\widehat{\Gamma}_{\text{out}}} \hat{v}_f^n \cdot \hat{n}_f \, \mathrm{d}s, \quad n = 0, 1, 2, \ldots.$$

This condition accounts for global flow dynamics in the remaining parts of the cardiovascular system. However, a complete absorption of pressure waves is not necessarily physiological because backflow of waves can be induced by bifurcations, for instance see [54, 104]. The constant $\hat{R}$ in Equation (3.27) of the above model was derived for a three dimensional blood vessel. However, we use this condition as approximation for two-dimensional problems.

The novel aspect in this work is the coupling of absorbing fluid conditions and the damped wave equation [105]. Although the physics of this coupling needs further investigations, it is the first time to make such a coupling (beside a prior study in another context in [55]). In fact, in most cases of hemodynamic simulations, the movement of the vessel walls was assumed small (see, e.g., [104]). This assumption is invalid for our heart-valve simulations.

We also refer to Fung [56], where the author studies the relations between velocity waves, pressure waves, and structure waves. The author starts with some simplifications and he supplements more and more ingredients to make the system more complex. This investigation helps a lot for a better understanding of *wave propagation* in tubes with elastic walls.

3.6 Theoretical results: review of literature

We close Chapter 3 with a brief account on the theory for fluid-structure interaction problems. Finally, a review of other solution approaches for solving fluid-structure interaction problems is provided. For instance, an active research field over the last five years has been the investigation of semi-implicit solution approaches.

3.6.1 Results on existence, regularity, and convergence analysis

We give a short account what has been done so far for theoretical investigations of fluid-structure interaction. Specifically, using standard fluid and structure equations, the structure velocity does not provide enough regularity on the interface to be coupled with the fluid equations:

$$v_f \neq v_s \quad \text{on } \Gamma_i.$$

Thus, we always assume a priori enough regularity. But since we introduced some additional terms for the structure equations (apart from being physically artificial), we discuss in this section the impact of linear strong damping on the structure velocity regularity.

Existence of stationary FSI

In the case of stationary fluid-structure problems, we refer to the results obtained by Grandmont [63]. In this study, the author works with the ALE-transformed fluid equations and the standard elasticity equations. The existence of the problem is derived via the Schauder-Tychonov fixed-point theorem. The uniqueness of the solution cannot be assured with this argument. However, for sufficiently small data (for instance, data of the right-hand-side and the boundary), uniqueness can be obtained. It is important to note that both equations (i.e., those for the fluid and the structure) in steady-state configurations are governed by elliptic operators. Beyond this pioneering work, there exist various articles proofing existence (and uniqueness) for special configurations. Recently, an existence result for a specific configuration of the interaction of the Navier-Stokes equations with an elastic plate was proven by Grandmont [64].

Existence of nonstationary FSI

The previous arguments demonstrating the existence of fluid-structure interactions fail for nonstationary settings. In these cases the fluid equations have parabolic character, whereas the structure equations are governed by hyperbolic partial differential equations (as discussed in the previous chapters). The different behavior of these equations leads to a lack of regularity at the interface between the fluid and the structure. To illustrate this phenomenon, we provide a brief account of the regularity results. For nonstationary fluid-structure interaction, the proofs of well-posedness and existence (and uniqueness) were derived by Coutand and Shkoller [35, 36]. The authors also provide a literature review what has been done before to prove existence.

In the following, we formulate time-dependent functions in the Bochner spaces [152].

Regularity of the standard fluid equations in a fixed domain

Problem 3.9 ([129], p. 190). *Let $\hat{f}_f$ and $\hat{v}_f^0$ be given by*

$$\hat{f}_f \in L^2(I; H^{-1}(\widehat{\Omega}_f)), \quad v_f^0 \in \hat{L}(\widehat{\Omega}_f).$$

Find: $\hat{v}_f \in L^2(I; H^1(\widehat{\Omega}_f))$ such that the standard Navier-Stokes equations (as defined, e.g., by Temam [129]) are solved with the initial data $\hat{v}_f(0) = \hat{v}_f^0$.

Theorem 3.1 in [129] tells us that at least one solution to the previous defined problem exists, i.e., it holds

$$\hat{v}_f \in L^2(I, H^1(\widehat{\Omega}_f)).$$

The main consequence for fluid-structure interaction is that $\hat{v}_f \in H^{1/2}(\widehat{\Gamma}_i)$.

Regularity of the structure equations

Problem 3.10 ([67], p. 351). *Let $\hat{f}_s \in L^2(I, L^2(\widehat{\Omega}_s)$. Find*

$$\hat{u}_s \in L^2(I, H_0^1(\widehat{\Omega}_s)) \quad \textit{and} \quad \hat{v}_s = d_t \hat{u}_s \in L^2(I, L^2(\widehat{\Omega}_s)),$$

such that the hyperbolic structure equations

$$\begin{aligned} d_t^2 \hat{u}_s - \Delta \hat{u}_s &= \hat{f}_s \quad \textit{in } I \times \widehat{\Omega}_s, \\ \hat{u}_s &= 0 \quad \textit{on } I \times \partial\widehat{\Omega}_s, \end{aligned}$$

are solved with the initial data $\hat{u}_s(0) = \hat{u}_s^0$ and $\hat{v}_s(0) = \hat{v}_s^0$.

In Grossmann and Roos [67], Theorem 5.6 tells us that this problem has a unique solution. The regularity of that solution is given by

$$\hat{u}_s \in L^2(I, H_0^1(\widehat{\Omega}_s)) \quad \text{and} \quad \hat{v}_s = d_t \hat{u}_s \in L^2(I, L^2(\widehat{\Omega}_s)).$$

Consequently, we cannot expect $\hat{v}_s \in H^{1/2}(\widehat{\Omega}_s)$. Thus, condition (3.8) is only formally valid. For this reason, we assumed a priori enough regularity of the hyperbolic structure equations. This was also observed (and resolved) in two theoretically-oriented articles with focus on proofs of existence of fluid-structure interaction problems [35, 36]. However, this lack of regularity can be resolved by adding some diffusion terms (that act on the velocity variables) to the structure equations. This coincides with the terms introduced in Equation (2.15).

To analyze the regularity of structural deformations in more detail, we consider the following hyperbolic equation with weak and linear strong damping.

Problem 3.11 ([57]). *Let $\hat{f}_s$ be sufficient regular. Let $\gamma_s \geq 0$ and $\gamma_w > -\gamma_s \lambda_1$, where λ_1 is the first eigenvalue of the $-\Delta$ operator under homogeneous Dirichlet boundary conditions. Find*

$$\hat{u}_s \in L^2(I, H_0^1(\widehat{\Omega}_s)) \quad \text{and} \quad \hat{v}_s = d_t \hat{u}_s \in L^2(I, L^2(\widehat{\Omega}_s)),$$

such that the hyperbolic structure equations with weak and strong damping

$$\begin{aligned} d_t^2 \hat{u}_s - \Delta \hat{u}_s + \gamma_w d_t \hat{u}_s - \gamma_s d_t \Delta \hat{u}_s &= \hat{f}_s \quad \text{in } I \times \widehat{\Omega}_s, \\ \hat{u}_s &= 0 \quad \text{on } I \times \partial\widehat{\Omega}_s, \end{aligned}$$

are solved with the initial data $\hat{u}_s(0) = \hat{u}_s^0$ and $\hat{v}_s(0) = \hat{v}_s^0$.

For example, in the work from Gazzola and Squassina [57], the first statement on p. 189 tells us that this problem has a unique solution. In particular, the regularity of $\hat{v}_s$ is given by

$$\hat{v}_s = d_t \hat{u}_s \in L^2(I, H_0^1(\widehat{\Omega}_s)),$$

for arbitrary $\gamma_s > 0$; hence, $\hat{v}_s \in H^{1/2}(\widehat{\Gamma}_i)$. Thus, linear strong damping provides more regularity of the solution, specifically for $\hat{v}_s$, such that the coupling condition (3.8) holds true. We finally notice that we only consider regularity properties of linear structure equations. Thus, typical nonlinearities of the structural operators are neglected.

Convergence Analysis for FSI

For a linearized implicitly-coupled fluid-structure interaction problem, optimal convergence rates using the Crank-Nicolson scheme and the backward Euler scheme were proven by Tallec and Mani in a pioneering work [127]. The main assumption was made by using a fixed configuration. Indeed, the ALE convection term vanishes in nonmoving domains. However, this term causes the main problems for deriving stability analysis of fluid-structure interaction.

Presently, the development of semi-implicit coupling schemes is subject of active research. These algorithms are a compromise between monolithic algorithms and explicit schemes because they are cheaper to solve than monolithic schemes but they are more stable than explicit schemes. Recently, for a semi-implicit coupling of fluid-structure interaction (see, e.g., [2]) the time convergence was analyzed for a linear fluid-structure interaction problem [3]. As shown in [127], a fixed configuration is used for the analysis. Despite these simplifications, the previously cited articles provide a good insight how to perform convergence analysis for fluid-structure interaction.

3.6.2 Other solution algorithms for fluid-structure interaction

The most common solution approaches for the treatment of fluid-structure interaction problems are the *partitioned* and the *monolithic* frameworks (see [12, 29, 30] and the many references cited therein). The partitioned approach can be further classified into loosely and strongly coupled algorithms. The main difference between the two frameworks are the treatment of the interface conditions: the continuity of the velocities and the normal stresses. Satisfying these conditions after time discretization leads to a *strongly coupled* approach, which always holds true for monolithically coupled problems. In this framework, the two subproblems are combined into one problem over the whole domain using the same discretization techniques for spatial and temporal discretization [12, 83].

In the partitioned approach, each problem is solved separately and the information for the other problem is given explicitly via the interface conditions to the other problem. Well-tested solvers for each of the problems can be used, which makes this approach interesting. However, the accuracy of the force balance at the interface cannot be taken for granted. Several iterations are required to obtain the desired accuracy, which implies no (or minor) difficulties in aero-elasticity in cases where the densities of the fluid and the structure differs significantly. In contrast, in biomedical applications, the densities are of the same order, leading to many subiterations (a *strongly* coupled approach). These subiterations are caused by stability problems due to the similar order of the densities; this phenomenon is the aforementioned *added-mass effect* [32, 143].

Presently, a third strategy, the so-called *semi-implicit* coupling, has become increasingly important. This scheme overcomes the stability problems of the explicit schemes, but it is computationally less costly to solve than the monolithic coupling scheme. Thus, this strategy is a compromise between the other two schemes. The main idea is to perform an explicit-implicit splitting that is based on a projection scheme (for more details we refer the reader to [2]).

In all the three solution methods, we must overcome the discrepancy caused by mismatch in the coordinate systems for the fluid and the structure. The natural coordinates for fluid flows are Eulerian coordinates, whereas structures are formulated in Lagrangian coordinates. Apart from the ALE approach (used in this thesis), there exist fixed mesh approaches. Various methodologies have been introduced in the literature to embody the concept of a fixed mesh. In this approach, the interface of the coupled problem can either be treated explicitly with interface markers or by treating the structure with Lagrangian coordinates [29], p. 328. Alternatively, the interface is given implicitly using level-set functions [92, 93].

Other possible concepts of fixed-mesh methods include the immersed boundary method [109] and Lattice Boltzmann methods [96, 97]. The immersed boundary method includes both Eulerian and Lagrangian variables that are linked on the discrete level by a smoothed Dirac delta function. This scheme is closely related to the Lattice Boltzmann methods. Furthermore, the immersed boundary method can be coupled with a Lattice Boltzmann method to solve fluid-particle interaction problems [46]. Another approach for computing

fluid-structure interaction problems with the Lattice Boltzmann method is discussed in [125]. The third method in this class is the eXtended finite element (XFEM) method, which is currently subject of active research; see Wall et al. [144], and the references cited therein.

The third strategy is a relatively new approach: a fully Eulerian framework in which the structure equations are rewritten in the Eulerian sense [41–43, 118]. Specifically, the structure is transformed such that the structure coordinates match those of the fixed fluid mesh. In this sense, the fully Eulerian framework can be seen as a natural counterpart of the ALE approach. A similar approach was employed to model the transport of viscoelastic bodies in a fluid [100]. The major difficulty of the fully Eulerian framework is the treatment of the interface and development of quadrature rules for cells that are truncated by the interface. In contrast to the ALE approach, where the interface can always be identified at the edges of two cells, this assumption is no longer valid in the fully Eulerian approach. In this framework, the interface is allowed to intersect a cell such that two different constitutive equations must be computed in each cell [42].

Outlook to the next chapters

In this chapter, we derived the coupled problems that are based on a monolithic coupling scheme. As already emphasized in the introduction of this thesis, the monolithic coupling leads to common setting of the equations that permits us to formulate gradient-based optimization methods as discussed in Chapter 4. In addition, we are able to formulate a common discretization of the problem (Chapter 5). Finally, a closed monolithic setting is an indispensable tool to formulate a reliable a posteriori error estimator with the help of the DWR method (Chapter 6).

4 Optimal Control for Steady-State FSI in ALE Coordinates

In this chapter, we consider optimal control problems in which the state is given in terms of a monolithically coupled fluid-structure interaction system. The solution approach is based on derivative-based optimization algorithms. The derivatives are obtained with help of the Lagrange formalism, leading to the so-called optimality system. To date, the optimality conditions are formally derived such that they are suitable for the given implementation. Although the approach described above for solving such optimization problems has been utilized previously in various works [14, 73, 75, 102, 139], the extension to the consideration of fluid-structure interaction problems is novel. The implementation was designed in a new software package [58] that employs algorithmic information from RoDoBo [16] and makes use of various types of finite elements from deal.II [8].

Because the control variable is already finite-dimensional in our configurations, we only need to discretize the state equation. To solve the nonlinear problem, we employ Newton's method, and we concentrate on the exact computation of the derivatives. This approach is particularly important for the convergence of optimization algorithms [15]. The discretization with a Galerkin scheme provides a native way of expressing the discrete adjoint equations because the Galerkin approach allows us to switch between discretization and optimization, meaning that the *discretize-then-optimize* approach is equivalent to the *optimize-then-discretize* approach.

We consider cost functionals for minimizing the wall stresses along the interface between the fluid and the structure. In the first setting, the control acts as an nonhomogeneous Neumann boundary condition on holes of the channel walls. Such a configuration was used by Becker [14] to compute optimal control problems for fluid flows and it was extended for fluid-structure interaction problems [121, 134]. However, the authors of [121, 134] circumvented the use of the optimality system (and thus the computation of derivatives), and they used a simplex algorithm to compute the optimal control. In a second setting, the material parameter of the structure is used as a control.

The chapter is organized as follows. First, we formulate the setting, and then we formulate the optimal control problem as an unconstrained optimization problem. Next, we (formally) derive the Lagrangian and the optimality system. After this, we explain the solution approach and derive analytically computed derivatives for the solution process. We close this chapter with a brief discussion of the discretization and algorithmic aspects of optimization problems.

4.1 Formulation of the setting

Let $\widehat{\Omega} = \widehat{\Omega}_f \cup \widehat{\Omega}_s$ be a two-dimensional domain. The outer boundary $\partial\widehat{\Omega}$ is split into the parts $\partial\widehat{\Omega} = \widehat{\Gamma}_{\text{bypass}} \cup \widehat{\Gamma}_{\text{wall}} \cup \widehat{\Gamma}_{\text{in}} \cup \widehat{\Gamma}_{\text{out}}$. A prototypical configuration is sketched in Figure 7.10. Later, we use $\widehat{\Gamma}_Q = \widehat{\Gamma}_{\text{bypass}}$ to indicate the control boundary.

In the more general case, the control acts as an piecewise-constant Neumann boundary condition:

$$\varepsilon\partial_n\hat{v} = \beta\hat{q}_i \quad \text{on } \widehat{\Gamma}_{Q_i}, \quad i = 1, 2, \ldots, N,$$

where $\varepsilon, \beta > 0$. This condition describes the local change of fluid flow at each of the holes $\widehat{\Gamma}_{Q_i}$, which can be regarded as a prescription of a mean pressure at each of the holes. With that, we limit our considerations to the case of a finite dimensional control space. Specifically, we are interested in determining the control $\hat{q} = \{\hat{q}_1, \ldots, \hat{q}_N\} \in \widehat{Q} = \mathbb{R}^N$. Finally, we introduce the observation boundary $\widehat{\Gamma}_O$ that is used as evaluation boundary to measuring the wall stresses.

It is sufficient to use the harmonic mesh motion because we work in a stationary regime in which large structural deformations are not expected.
Then, the solution $\hat{U} = \{\hat{v}_f, \hat{v}_s, \hat{u}_f, \hat{u}_s, \hat{p}_f, \hat{p}_s\} \in \hat{X}_D^0$, where $\hat{X}_D^0 = \{\hat{v}_f^D + \hat{V}_{f,\hat{v}}^0\} \times \hat{L}_s \times \{\hat{u}_f^D + \hat{V}_{f,\hat{u}}^0\} \times \{\hat{u}_s^D + \hat{V}_s^0\} \times \hat{L}_f^0 \times \hat{L}_s^0$, is determined by the semi-linear form of the state equation:

$$\begin{aligned}
\hat{A}(\hat{q}, \hat{U})(\hat{\Psi}) = {} & (\hat{\rho}_f \hat{J}(\widehat{F}^{-1}\hat{v}_f \cdot \widehat{\nabla})\hat{v}_f), \hat{\psi}_f^v)_{\widehat{\Omega}_f} + (\hat{J}\hat{\sigma}_f\widehat{F}^{-T}, \widehat{\nabla}\hat{\psi}_f^v)_{\widehat{\Omega}_f} + (\widehat{F}\widehat{\Sigma}, \widehat{\nabla}\hat{\psi}_s^v)_{\widehat{\Omega}_s} \\
& - \langle \hat{g}_f, \hat{\psi}_f^v \rangle_{\widehat{\Gamma}_N} - (\hat{v}_s, \hat{\psi}_s^u)_{\widehat{\Omega}_s} + (\alpha_u \widehat{\nabla}\hat{u}_f, \widehat{\nabla}\hat{\psi}_f^u)_{\widehat{\Omega}_f} \\
& + (\widehat{\text{div}}(\hat{J}\hat{F}^{-1}\hat{v}_f), \hat{\psi}_f^p)_{\widehat{\Omega}_f} + (\hat{P}_s, \hat{\varphi}_s^p)_{\widehat{\Omega}_s} - \langle \hat{q}, \hat{n}_f \cdot \hat{\psi}_f^v \rangle_{\widehat{\Gamma}_Q} \\
= {} & 0 \quad \forall \hat{\Psi} \in \hat{X},
\end{aligned} \tag{4.1}$$

where $\hat{\Psi} = \{\hat{\psi}_f^v, \hat{\psi}_s^v, \hat{\psi}_f^u, \hat{\psi}_s^u, \hat{\psi}_f^p, \hat{\psi}_s^p\}$ and $\hat{X} = \hat{V}_{f,\hat{v}}^0 \times \hat{L}_s \times \hat{V}_{f,\hat{u},\widehat{\Gamma}_i}^0 \times \hat{V}_s^0 \times \hat{L}_f^0 \times \hat{L}_s^0$ and $\langle \cdot, \cdot \rangle_{\widehat{\Gamma}_Q}$ denotes the $L^2(\widehat{\Gamma}_Q)$ scalar product.

4.2 The optimal control problem

The goal of our optimal control problem is to determine the rate $\hat{q}_i$ (i.e., the mean value of the normal flux of the state) such that wall stresses measured on $\widehat{\Gamma}_O$ become as small as possible. The force coefficient c_{y} is evaluated with the help of

$$i(\hat{U}) = c_{\text{y}} = \int_{\widehat{\Gamma}_O} \hat{J}\hat{\sigma}_f\widehat{F}^{-T}\hat{n}_f\,\hat{d}\,\mathrm{d}\hat{s}, \tag{4.2}$$

where $\hat{d}$ is a unit vector in the mean flow direction. This quantity of interest is completed by a regularization term of Tikhonov type, which involves a corresponding regularization

parameter α_T. Then, the cost functional reads:

$$J(\hat{q}, \hat{U}) = i(\hat{U}) + \frac{\alpha_T}{2}||\hat{q}||_Q^2, \tag{4.3}$$

where $||\cdot||_Q$ denotes the standard L^2-norm used for the control $\hat{q}$. We consider the following optimization problem:

Problem 4.1 (Constrained optimization). *Minimize the cost functional $J(\hat{q}, \hat{U})$ subject to the state equation $\hat{A}(\hat{q}, \hat{U})(\hat{\Psi}) = 0$ (as defined in (4.1)) for $(\hat{q}, \hat{U}) \in \widehat{Q} \times \widehat{X}$.*

The constrained optimization problem on the space $\widehat{Q} \times \widehat{X}$ is reformulated into an unconstrained optimization problem on the space $\widehat{Q}$. Therefore, we assume the existence of the solution operator $\hat{S} : \widehat{Q} \to \widehat{X}$ with a unique solution $\hat{U} = \hat{S}(\hat{q})$. Herewith, we define the reduced cost functional $j : \widehat{Q} \to \mathbb{R}$ by

$$j(\hat{q}) := J(\hat{q}, \hat{S}(\hat{q})). \tag{4.4}$$

Thus, the constrained optimization problem can be formulated by means of

Problem 4.2 (Unconstrained optimization). *Minimize $j(\hat{q})$ for $\hat{q} \in \widehat{Q}$.*

Because of the nonlinear structure of the state equation (4.1), the reduced functional is in general not convex (even if the cost functional $J(\hat{q}, \hat{U})$ is convex).

The reduced formulation in Problem 4.2 is useful to apply the classical existence theorem from the calculus of variations to the abstract optimization problem at hand (see, e.g., [99]). However, the usage of the reduced formulation requires the differentiability of the solution operator S, which is taken as an assumption here.

For the statement of the solution process of Problem 4.2 and the corresponding optimality conditions, we briefly recall the definitions of differentiability in normed vector spaces.

Definition 4.1 (Directional derivative). *Let V and W be normed vector spaces and let $V_0 \subset V$ be non-empty. Let $f : V_0 \to W$ be a given mapping. If the limit*

$$f'(v)(\delta v) := \lim_{\epsilon \to 0} \frac{f(v + \delta v) - f(v)}{\epsilon}, \quad v \in V_0, \delta v \in V$$

exists, then $f'(v)(\delta v)$ is called the directional derivative of the mapping f at v in direction δv. If the directional derivative exists for all $\delta v \in V$, then f is called directionally differentiable at v.

Definition 4.2 (Gâteaux derivative). *Let the assumptions hold as in Definition 4.1. A directional-differentiable mapping as defined in Definition 4.1, is called Gâteaux differentiable at $v \in V_0$, if the directional derivative $f'(v)$ is a continuous linear mapping from V to W.*

Below, we derive the optimality system optimal control governed by fluid-structure interaction in which the derivatives are computed with help of the previous formulas.

The solution to the unconstrained Problem 4.2 is obtained with

$$j'(\hat{q})(\delta\hat{q}) = 0 \quad \forall \delta\hat{q} \in \widehat{Q}, \tag{4.5}$$

which is the first-order necessary-optimality condition; for a proof, we refer to [75, 132]. The second-order necessary-optimality condition reads [75, 132]:

$$j''(\hat{q})(\delta\hat{q}, \delta\hat{q}) \geq 0 \quad \forall \delta\hat{q} \in \widehat{Q}. \tag{4.6}$$

Before we continue with the formal derivation of the directional derivatives that are required to solve the unconstrained optimization problem, we recall a theoretical result how to characterize the (local) existence of optimal controls.

Lemma 4.1 (Existence of a local optimal control $\hat{q}$). *Let the reduced cost functional $j(\hat{q})$ be two times continuously Fréchet differentiable (e.g. [145]) on a neighborhood $\widehat{Q}_0 \subseteq \widehat{Q}$ of $\hat{q}$. Moreover, let the control $\hat{q}$ fulfill the first-order necessary-optimality condition*

$$j'(\hat{q})(\delta\hat{q}) = 0 \quad \forall \delta\hat{q} \in \widehat{Q}.$$

Further, we assume the existence of some constant $\gamma > 0$ such that the second-order sufficient-optimality condition

$$j''(\hat{q})(\delta\hat{q}, \delta\hat{q}) \geq \gamma ||\delta\hat{q}||_Q^2 \quad \forall \delta\hat{q} \in \widehat{Q}$$

is valid. Then, there exists a constant $\epsilon > 0$ such that the quadratic growth condition

$$j(\hat{q} + \delta\hat{q}) \geq j(\hat{q}) + \frac{\gamma}{4} ||\delta\hat{q}||_Q^2$$

holds for all $\delta\hat{q} \in \widehat{Q}$ with $||\delta\hat{q}||_Q^2 \leq \epsilon$. Then, the control $\hat{q}$ is a local solution of the reduced optimization problem.

The proof of this Lemma can be found in [132].

In many situations, the differentiability of $j(\cdot)$ in Lemma 4.1 is obtained in the space $\widehat{Q}_{\text{strong}} \subset \widehat{Q}$, whereas the coercivity of $j''(\cdot)$ can be shown in $\widehat{Q}$, a difficulty that is known as the *two-norm-discrepancy*. For a detailed discussion, we refer to Tröltzsch [132], p. 184ff.

In the following, we concentrate on the (formal) computation of the optimality conditions that are employed for the implementation. The most easily way to express them is done by means of the Lagrangian $\mathcal{L} : \widehat{Q} \times \widehat{X} \times \widehat{X} \to \mathbb{R}$:

$$\mathcal{L}(\hat{q}, \hat{U}, \hat{Z}) := J(\hat{q}, \hat{U}) - \hat{A}(\hat{q}, \hat{U})(\hat{Z}). \tag{4.7}$$

With the help of the Lagrangian, we derive the optimality system (Karush-Kuhn-Tucker - KKT system) for a triple $(\hat{q}, \hat{U}, \hat{Z}) \in \widehat{Q} \times \widehat{X} \times \widehat{X}$:

$$\begin{aligned}
&\mathcal{L}'_{\hat{Z}}(\hat{q}, \hat{U}, \hat{Z})(\hat{\Psi}) = 0 \quad \forall \hat{\Psi} \in \widehat{X} \quad \text{(State Equation)},\\
&\mathcal{L}'_{\hat{U}}(\hat{q}, \hat{U}, \hat{Z})(\hat{\Psi}) = 0 \quad \forall \hat{\Psi} \in \widehat{X} \quad \text{(Adjoint Equation)},\\
&\mathcal{L}'_{\hat{q}}(\hat{q}, \hat{U}, \hat{Z})(\delta\hat{q}) = 0 \quad \forall \delta\hat{q} \in \widehat{Q} \quad \text{(Gradient Equation)},
\end{aligned}$$

or equivalently

$$\begin{aligned}
\hat{A}(\hat{q}, \hat{U})(\hat{\Psi}) &= 0 && \forall \hat{\Psi} \in \widehat{X},\\
\hat{A}'_{\hat{U}}(\hat{q}, \hat{U})(\hat{\Psi}, \hat{Z}) &= J'_{\hat{U}}(\hat{q}, \hat{U})(\hat{\Psi}) && \forall \hat{\Psi} \in \widehat{X},\\
\hat{A}'_{\hat{q}}(\hat{q}, \hat{U})(\delta\hat{q}, \hat{Z}) &= J'_{\hat{q}}(\hat{q}, \hat{U})(\delta\hat{q}) && \forall \delta\hat{q} \in \widehat{Q}.
\end{aligned} \tag{4.8}$$

The KKT system is equivalent to the first-order necessary-optimality condition stated before if the linearization of the semi-linear form is regular enough. We note that this system can be directly discretized with a Galerkin finite element method. Another approach (see [14, 15, 102]) that uses of the reduced formulation is discussed below. To date, the optimality conditions are formally derived for the implementation; their rigorous analysis is under investigation [151].

The optimality system for Neumann boundary control

The KKT system is formally derived from (4.1) reads as follows: Find $(\hat{q}, \hat{U}, \hat{Z}) \in \widehat{Q} \times \widehat{X} \times \widehat{X}$ with the primal solution $\hat{U} = \{\hat{v}_f, \hat{v}_s, \hat{u}_f, \hat{u}_s, \hat{p}_f, \hat{p}_s\}$ and the adjoint solution $\hat{U} = \{\hat{z}^v_f, \hat{z}^v_s, \hat{z}^u_f, \hat{z}^u_s, \hat{z}^p_f, \hat{z}^p_s\}$, such that

State equation

$$\begin{aligned}
\hat{A}(\hat{q}, \hat{U})(\hat{\Psi}) = {} & (\hat{\rho}_f \hat{J}(\widehat{F}^{-1}\hat{v}_f \cdot \widehat{\nabla})\hat{v}_f), \hat{\psi}^v_f)_{\widehat{\Omega}_f} + (\hat{J}\widehat{\sigma}_f \widehat{F}^{-T}, \widehat{\nabla}\hat{\psi}^v_f)_{\widehat{\Omega}_f} + (\widehat{F}\widehat{\Sigma}, \widehat{\nabla}\hat{\psi}^v_s)_{\widehat{\Omega}_s}\\
& - \langle \hat{g}_f, \hat{\psi}^v_f \rangle_{\widehat{\Gamma}_N} - (\hat{v}_s, \hat{\psi}^u_s)_{\widehat{\Omega}_s} + (\alpha_u \widehat{\nabla}\hat{u}_f, \widehat{\nabla}\hat{\psi}^u_f)_{\widehat{\Omega}_f}\\
& + (\widehat{\mathrm{div}}(\hat{J}\hat{F}^{-1}\hat{v}_f), \hat{\psi}^p_f)_{\widehat{\Omega}_f} + (\hat{P}_s, \hat{\varphi}^p_s)_{\widehat{\Omega}_s} - \langle \hat{q}, \hat{n}_f \cdot \hat{\psi}^v_f \rangle_{\widehat{\Gamma}_Q}\\
= {} & 0 \quad \forall \hat{\Psi} \in \widehat{X},
\end{aligned}$$

with $\hat{\Psi} \in \widehat{X}$ as previously defined.

Adjoint equation

$$\begin{aligned}
\hat{A}'_{\hat{U}}(\hat{q},\hat{U})(\hat{\Psi},\hat{Z}) &= \hat{\rho}_f \left(\widehat{\nabla}\hat{\psi}^v \hat{J}\widehat{F}^{-1}\hat{v}_f + \widehat{\nabla}\hat{v}_f \hat{J}\widehat{F}^{-1}\hat{\psi}^v, \hat{z}_f^v\right)_{\widehat{\Omega}_f} \\
&\quad + \hat{\rho}_f \left(\widehat{\nabla}\hat{v}_f [\hat{J}\widehat{F}^{-1}]'(\hat{\psi}^u)\hat{v}_f, \hat{z}_f^v\right)_{\widehat{\Omega}_f} \\
&\quad + \left(\hat{\rho}_f \nu_f (\widehat{\nabla}\hat{\psi}^v \widehat{F}^{-1} + \widehat{F}^{-T}(\widehat{\nabla}\hat{\psi}^v)^T)\hat{J}\widehat{F}^{-T}, \widehat{\nabla}\hat{z}_f^v\right)_{\widehat{\Omega}_f} \\
&\quad + \left(\hat{\rho}_f \nu_f (\widehat{\nabla}\hat{v}_f [\widehat{F}^{-1}]'(\hat{\psi}^u) + [\widehat{F}^{-T}]'(\hat{\psi}^u)\widehat{\nabla}\hat{v}_f^T)\hat{J}\widehat{F}^{-T}, \widehat{\nabla}\hat{z}_f^v\right)_{\widehat{\Omega}_f} \\
&\quad + \left(\hat{\rho}_f \nu_f (\widehat{\nabla}\hat{v}_f \widehat{F}^{-1} + \widehat{F}^{-T}\widehat{\nabla}\hat{v}_f^T)[\hat{J}\widehat{F}^{-T}]'(\hat{\psi}^u), \widehat{\nabla}\hat{z}_f^v\right)_{\widehat{\Omega}_f} \\
&\quad - \left(\hat{p}_f [\hat{J}\widehat{F}^{-T}]'(\hat{\psi}^u), \widehat{\nabla}\hat{z}_f^v\right)_{\widehat{\Omega}_f} - \left(\hat{\psi}^p \hat{J}\widehat{F}^{-T}, \widehat{\nabla}\hat{z}_f^v\right)_{\widehat{\Omega}_f} \\
&\quad + \left(\lambda_s (\mathrm{tr}\widehat{E}'(\hat{\psi}^u)\widehat{F} + \mathrm{tr}\widehat{E}\widehat{F}'(\hat{\psi}^u)) + 2\mu_s (\widehat{F}'(\hat{\psi}^u)\widehat{E} + \widehat{F}\widehat{E}'(\hat{\psi}^u)), \widehat{\nabla}\hat{z}_s^v\right)_{\widehat{\Omega}_s} \\
&\quad - \left(\hat{\psi}^v, \hat{z}_s^u\right)_{\widehat{\Omega}_s} + (\alpha_u \widehat{\nabla}\hat{\psi}^u, \widehat{\nabla}\hat{z}_f^u)_{\widehat{\Omega}_f} \\
&\quad + \left(\hat{\partial}_1 \hat{\psi}^{v_1} + \hat{\partial}_2 \hat{\psi}^{v_2}, \hat{z}_f^p\right)_{\widehat{\Omega}_f} \\
&\quad + \left(\hat{\partial}_2 \hat{\psi}^{u_1} \hat{\partial}_1 \hat{v}_{f,1} - \hat{\partial}_2 \hat{\psi}^{u_2} \hat{\partial}_1 \hat{v}_{f,2} - \hat{\partial}_1 \hat{\psi}^{u_2} \hat{\partial}_2 \hat{v}_{f,1} + \hat{\partial}_1 \hat{\psi}^{u_1} \hat{\partial}_{f,2} \hat{v}_2, \hat{z}_f^p\right)_{\widehat{\Omega}_f} \\
&\quad + \left(\hat{\psi}^p, \hat{z}_s^p\right)_{\widehat{\Omega}_s} \\
&= J'_{\hat{U}}(\hat{q},\hat{U})(\hat{\Psi}) \quad \forall \hat{\Psi} \in \hat{X},
\end{aligned}$$

with $\hat{\Psi} \in \hat{X}$ as previously defined.

Gradient equation

$$\hat{A}'_{\hat{q}}(\hat{q},\hat{U})(\delta\hat{q},\hat{Z}) = \langle \delta\hat{q}, \hat{z}_f^v \cdot \hat{n}_f \rangle_{\widehat{\Gamma}_Q} = 0 \quad \forall \delta\hat{q} \in \widehat{Q}.$$

In this context, the KKT system is derived by using exact linearization to express the directional derivatives. The concrete evaluation of the inner derivatives, for instance $\partial_u \widehat{F}^{-T}(\delta\hat{u}) =: [\widehat{F}^{-T}]'(\delta\hat{u})$, are discussed in Section 5.6.1. The exact evaluation is important to identify optimal convergence of the Newton method for optimal control problems [15].

The Lamé coefficient μ_s as control

We also consider a second optimization problem, where the structural parameter μ_s is taken as control $\hat{q}$. This example is motivated by heart-valve settings with artificial valves in which it is possible to influence the valve model by adapting the structural parameter. In the corresponding KKT system, we have to replace μ_s with $\hat{q}$ and $\lambda_s := \lambda_s(\hat{q})$ in the state equation and the adjoint equation. Finally, the gradient equation reads:

$$\hat{A}'_{\hat{q}}(\hat{q},\hat{U})(\delta\hat{q},\hat{Z}) = (\widehat{F}(\lambda'_s(\delta\hat{q})(\mathrm{tr}\widehat{E})\hat{I} + 2\delta\hat{q}\widehat{E}), \widehat{\nabla}\hat{z}_s^v)_{\widehat{\Omega}_s} = 0 \quad \forall \delta\hat{q} \in \widehat{Q}.$$

4.3 Solution process of the reduced formulation

In the following, we discuss the solution process of the unconstrained optimal control problem. The philosophy of this section follows exactly [14, 15, 102]; but we also mention the earlier articles [74, 131]. The algorithms presented in this prior work are applied to fluid-structure interaction, which is consequently the novel aspect.

We are already prepared with the first and second-order necessary conditions for an optimal control, see (4.5) and (4.6). To express these derivatives in terms of the reduced functional $j(\hat{q})$ (that was defined in (4.4)), we use the Lagrangian (4.7). Following [15, 102], we briefly recall three auxiliary problems that are used to formulate the derivatives of $j(\hat{q})$.

Problem 4.3 (Dual Equation). *For a given control $\hat{q} \in \widehat{Q}$ and a solution $\hat{U} = \hat{S}(\hat{q}) \in \widehat{X}$, find the dual solution $\hat{Z} \in \widehat{X}$, such that*

$$\mathcal{L}'_{\hat{U}}(\hat{q}, \hat{U}, \hat{Z})(\hat{\Psi}) = 0 \quad \forall \hat{\Psi} \in \widehat{X},$$

or equivalently (see the second equation of the KKT system (4.8))

$$\hat{A}'_{\hat{U}}(\hat{q}, \hat{U})(\hat{\Psi}, \hat{Z}) = J'_{\hat{U}}(\hat{q}, \hat{U})(\hat{\Psi}) \quad \forall \hat{\Psi} \in \widehat{X}.$$

Problem 4.4 (Tangent Equation). *For given $\hat{q} \in \widehat{Q}$, $\hat{U} = \hat{S}(\hat{q}) \in \widehat{X}$, and a given direction $\delta\hat{q} \in \widehat{Q}$, find the tangent solution $\delta\hat{U} \in \widehat{X}$, such that*

$$\mathcal{L}''_{\hat{q}\hat{Z}}(\hat{q}, \hat{U}, \hat{Z})(\delta\hat{q}, \hat{\Psi}) + \mathcal{L}''_{\hat{U}\hat{Z}}(\hat{q}, \hat{U}, \hat{Z})(\delta\hat{U}, \hat{\Psi}) = 0 \quad \forall \hat{\Psi} \in \widehat{X},$$

or equivalently

$$\hat{A}'_{\hat{U}}(\hat{q}, \hat{U})(\delta\hat{U}, \hat{\Psi}) = -\hat{A}'_{\hat{q}}(\hat{q}, \hat{U})(\delta\hat{q}, \hat{\Psi}) \quad \forall \hat{\Psi} \in \widehat{X}.$$

Problem 4.5 (Dual for the Hessian Equation). *Let $\hat{q} \in \widehat{Q}$, $\hat{U} = \hat{S}(\hat{q}) \in \widehat{X}$, the dual solution $\hat{Z} \in \widehat{X}$ obtained in Problem 4.3, and the tangent solution $\delta\hat{U} \in \widehat{X}$ obtained in Problem 4.4 be given. Find the dual Hessian $\delta\hat{Z} \in \widehat{X}$, such that*

$$\mathcal{L}''_{\hat{q}\hat{U}}(\hat{q}, \hat{U}, \hat{Z})(\delta\hat{q}, \hat{\Psi}) + \mathcal{L}''_{\hat{U}\hat{U}}(\hat{q}, \hat{U}, \hat{Z})(\delta\hat{U}, \hat{\Psi}) + \mathcal{L}''_{\hat{Z}\hat{U}}(\hat{q}, \hat{U}, \hat{Z})(\delta\hat{Z}, \hat{\Psi}) = 0 \quad \forall \hat{\Psi} \in \widehat{X},$$

or equivalently

$$\hat{A}'_{\hat{U}}(\hat{q}, \hat{U})(\hat{\Psi}, \delta\hat{Z}) = J''_{\hat{U}\hat{U}}(\hat{q}, \hat{U})(\delta\hat{U}, \hat{\Psi}) - \hat{A}''_{\hat{U}\hat{U}}(\hat{q}, \hat{U})(\delta\hat{U}, \hat{\Psi}, \hat{Z}) - \hat{A}''_{\hat{q}\hat{U}}(\hat{q}, \hat{U})(\delta\hat{q}, \hat{\Psi}, \hat{Z}) \quad \forall \hat{\Psi} \in \widehat{X}.$$

Examining the previous declared expressions for the consideration of a Neumann boundary control problem using the semi-linear form (4.1), we explicitly obtain:

Example 4.1 (Dual Equation). *The term* $\hat{A}'_{\hat{U}}(\hat{q},\hat{U})(\hat{\Psi},\hat{Z})$ *corresponds to the second equation of the Lagrangian and it was already explicitly stated as* adjoint *equation in the previous section. The second term, the derivative of the cost functional reads:*

$$J'_{\hat{U}}(\hat{q},\hat{U})(\hat{\Psi}) = \int_{\widehat{\Gamma}_O} \Big(\partial_u \hat{J}(\delta\hat{u}_f)\widehat{\sigma}_f \widehat{F}^{-T} + \hat{J}\partial_U \widehat{\sigma}_f(\delta\hat{U}_f)\widehat{F}^{-T} + \hat{J}\widehat{\sigma}_f \partial_u \widehat{F}^{-T}(\delta\hat{u}_f)\Big)\hat{n}_f \, \hat{d}\,\mathrm{d}\hat{s}.$$

We refer to Section 5.6.1 for the explicit representation of the derivatives

$$\partial_u \hat{J}(\delta\hat{u}_f), \quad \partial_U \widehat{\sigma}_f(\delta\hat{U}_f), \quad \partial_u \widehat{F}^{-T}(\delta\hat{u}_f).$$

Example 4.2 (Tangent Equation). *The first term* $\hat{A}'_{\hat{U}}(\hat{q},\hat{U})(\delta\hat{U},\hat{\Psi})$ *can formally be obtained with the help of the dual equation term* $\hat{A}'_{\hat{U}}(\hat{q},\hat{U})(\hat{\Psi},\hat{Z})$*, by simply switching test function and direction, where the latter variable is replaced with* $\delta\hat{U}$*. The second term is given by*

$$\hat{A}'_{\hat{q}}(\hat{q},\hat{U})(\delta\hat{q},\hat{\Psi}) = -\langle \delta\hat{q}, \hat{\psi}^v_f \cdot \hat{n}_f \rangle_{\widehat{\Gamma}_Q}.$$

Example 4.3 (Dual for Hessian Equation). *The left-hand-side term* $\hat{A}'_{\hat{U}}(\hat{q},\hat{U})(\hat{\Psi},\delta\hat{Z})$ *can formally be obtained with the help of the dual equation term* $\hat{A}'_{\hat{U}}(\hat{q},\hat{U})(\hat{\Psi},\hat{Z})$*, where* $\hat{Z}$ *is replaced with* $\delta\hat{Z}$*. The first expression on the right hand side reads formally*

$$\begin{aligned} J''_{\hat{U}\hat{U}}(\hat{q},\hat{U})(\delta\hat{U},\hat{\Psi}) = \int_{\widehat{\Gamma}_O} \Big(&\partial_U(\partial_u \hat{J}(\delta\hat{u}_f)\widehat{\sigma}_f \widehat{F}^{-T})(\delta\hat{U}_f) \\ &+ \partial_U(\hat{J}\partial_U \widehat{\sigma}_f(\delta\hat{U}_f)\widehat{F}^{-T})(\delta\hat{U}_f) \\ &+ \partial_U(\hat{J}\widehat{\sigma}_f \partial_u \widehat{F}^{-T}(\delta\hat{u}_f))(\delta\hat{U}_f)\Big)\, \hat{n}_f \, \hat{d}\,\mathrm{d}\hat{s}. \end{aligned}$$

We omit the explicit representation of the second derivatives for the convenience of the reader. The next term $\hat{A}''_{\hat{U}\hat{U}}(\hat{q},\hat{U})(\delta\hat{U},\hat{\Psi},\hat{Z})$ *can be derived from the dual equation* $\hat{A}'_{\hat{U}}(\hat{q},\hat{U})(\hat{\Psi},\hat{Z})$ *and by computing its derivative in the direction* $\delta\hat{U}$*. As an example, we consider the term* $(\hat{\psi}^p_f \hat{J}\widehat{F}^{-T}, \widehat{\nabla}\hat{z}^v_f)_{\widehat{\Omega}_f}$*. The derivative in the direction* $\delta\hat{U}_f$ *of the first argument reads*

$$\partial_u \hat{\psi}^p_f \hat{J}\widehat{F}^{-T}(\delta\hat{u}_f) = \hat{\psi}^p_f \partial_u \hat{J}(\delta\hat{u}_f)\widehat{F}^{-T} + \hat{\psi}^p_f \hat{J}\partial_u \widehat{F}^{-T}(\delta\hat{u}_f).$$

We emphasize that several terms vanish because they are constant with respect to $\delta\hat{U}_f$*:*

$$-\left(\hat{\psi}^v_s, \hat{z}^u_s\right)_{\widehat{\Omega}_s} + \left(\alpha_u \widehat{\nabla}\hat{\psi}^u_f, \widehat{\nabla}\hat{z}^u_f\right)_{\widehat{\Omega}_f} + \left(\hat{\partial}_1 \hat{\psi}^{v_1}_f + \hat{\partial}_2 \hat{\psi}^{v_2}_f, \hat{z}^p_f\right)_{\widehat{\Omega}_f} + \left(\hat{\psi}^p_s, \hat{z}^p_s\right)_{\widehat{\Omega}_s}.$$

The last term $\hat{A}''_{\hat{q}\hat{U}}(\hat{q},\hat{U})(\delta\hat{q},\hat{\Psi},\hat{Z})$ *is equal to zero for Neumann boundary control because there appears no control* $\hat{q}$ *in the expression* $\hat{A}'_{\hat{U}}(\hat{q},\hat{U})(\hat{\Psi},\hat{Z})$*. However, for material stiffness control, the term* $\hat{A}'_{\hat{U}}(\hat{q},\hat{U})(\hat{\Psi},\hat{Z})$ *is nonvanishing.*

It holds (see [15]):

Proposition 4.2. *With the above computed expressions, we are able to state the derivatives of the reduced functional $j(\hat{q})$. Let $\hat{q} \in \widehat{Q}, \hat{U} = \hat{S}(\hat{q}) \in \widehat{X}$ and $\hat{Z} \in \widehat{X}$ obtained in Problem 4.3 be given. Then the residual of Newton's method is defined as*

$$j'(\hat{q})(\delta\hat{q}) = \mathcal{L}'_{\hat{q}}(\hat{q}, \hat{U}, \hat{Z})(\delta\hat{q}),$$

or in explicit representation

$$j'(\hat{q})(\delta\hat{q}) = \alpha_T(\hat{q}, \tau\hat{q})_Q - \hat{A}'_{\hat{q}}(\hat{q}, \hat{U})(\tau\hat{q}, \hat{Z}).$$

For the left-hand-side of Newton's method, the Hessian matrix, we also must express the second derivatives by means of the above introduced problems. Let $\hat{q} \in \widehat{Q}, \hat{U} = \hat{S}(\hat{q}) \in \widehat{X}$ and $\hat{Z} \in \widehat{X}$ be given. Additionally, let $\delta\hat{q} \in \widehat{Q}$ be given, and $\delta\hat{U} \in \widehat{X}$ fulfills the equation of the tangent problem 4.4, and $\delta\hat{Z} \in \widehat{X}$ fulfills the equation of the dual Hessian problem 4.5. Then

$$\begin{aligned} &j''(\hat{q})(\delta\hat{q}, \tau\hat{q}) \\ &= \mathcal{L}''_{\hat{q}\hat{q}}(\hat{q}, \hat{U}, \hat{Z})(\delta\hat{q}, \tau\hat{q}) + \mathcal{L}''_{\hat{U}\hat{q}}(\hat{q}, \hat{U}, \hat{Z})(\delta\hat{U}, \tau\hat{q}) + \mathcal{L}''_{\hat{Z}\hat{q}}(\hat{q}, \hat{U}, \hat{Z})(\delta\hat{Z}, \tau\hat{q}), \end{aligned}$$

for all $\tau\hat{q} \in \widehat{Q}$ and in explicit representation

$$\begin{aligned} &j''(\hat{q})(\delta\hat{q}, \tau\hat{q}) \\ &= \alpha_T(\delta\hat{q}, \tau\hat{q})_Q - \hat{A}''_{\hat{q}\hat{q}}(\hat{q}, \hat{U})(\delta\hat{q}, \tau\hat{q}, \hat{Z}) - \hat{A}''_{\hat{U}\hat{q}}(\hat{q}, \hat{U})(\delta\hat{U}, \tau\hat{q}, \hat{Z}) - \hat{A}'_{\hat{q}}(\hat{q}, \hat{U})(\tau\hat{q}, \delta\hat{Z}). \end{aligned}$$

Proof. For the proof of a time-dependent version of this statement, we refer to Becker et al. [15]. The stationary version of this proposition is easily derived by neglecting all time derivatives, which concludes the proof. □

Example 4.4 (Residual of Newton's method). *The first term, $\alpha_T(\hat{q}, \tau\hat{q})_Q$, denotes the first derivative of the regularization term. The second term $\hat{A}'_{\hat{q}}(\hat{q}, \hat{U})(\tau\hat{q}, \hat{Z})$ corresponds to the third equation of the Lagrangian and it was already explicitly stated as* Gradient *equation in the previous section.*

Example 4.5 (Hessian matrix of Newton's method). *The first term, $\alpha_T(\hat{q}, \tau\hat{q})_Q$, denotes the second derivative of the regularization term. The second term $\hat{A}'_{\hat{q}\hat{q}}(\hat{q}, \hat{U})(\delta\hat{q}, \tau\hat{q}, \hat{Z})$ is obtained by differentiating the Gradient term again. The third term vanishes for the Neumann boundary control setting and the last term is derived from the Gradient term $\hat{A}'_{\hat{q}}(\hat{q}, \hat{U})(\tau\hat{q}, \hat{Z})$ by simply replacing $\hat{Z}$ by $\delta\hat{Z}$.*

With these preliminary work, we use the standard Newton method to solve the optimal control problem. Therefore, we consider a finite-dimensional control space $\widehat{Q}_h$ (in fact it holds $\widehat{Q} = \widehat{Q}_h$) with the basis

$$\left\{ \tau\hat{q}_i \,|\, i = 1, 2, 3, \ldots, N_{\widehat{Q}} \right\}.$$

where $N_{\widehat{Q}} := \dim \widehat{Q}_h$. Specifically, the control space $\widehat{Q}_h$ of the prototypical bypass configuration is specified with

$$\text{span} < \hat{q}_1 >=: \widehat{Q}_h = \mathbb{R}^1,$$

with $N_{\widehat{Q}} = 1$. For instance, the modeling of $N_{\widehat{Q}}$ bypass inflow sections, would require

$$\text{span} < \hat{q}_1, \ldots, \hat{q}_{N_{\widehat{Q}}} >=: \widehat{Q}_h = \mathbb{R}^{N_{\widehat{Q}}}.$$

Then, Newton's method reads:

$$\begin{aligned} j''(\hat{q}^n)(\delta\hat{q}, \tau\hat{q}) &= -j'(\hat{q}^n)(\tau\hat{q}) \quad \tau\hat{q} \in \widehat{Q}, \\ \hat{q}^{n+1} &= \hat{q}^n + \omega\delta\hat{q}, \end{aligned}$$

with a line search parameter $\omega \in (0, 1]$. The solution of the linear equation system is derived using the conjugate gradients method. Specifically, we do not build up the entire Hessian, i.e., $j''(\hat{q}^n)(\delta\hat{q}, \tau\hat{q})$. For details on this algorithm, we refer to [15, 102]. Moreover, the authors also explain a second optimization algorithm, where the whole Hessian is assembled. In addition, they also compare the efficiency of the both strategies in several numerical tests. The convergence properties of the Newton method itself depends on a clever choice of line search and globalization techniques; we refer to [75, 102, 153]. Finally, we point out that the derivation of analytic expressions for the Hessian can be replaced with a *good* approximation of the analytically-computed derivatives or even using finite differences. In such a case, we still deal with a *Newton-like* method.

4.4 Discretization

We close this chapter with a brief account how discretize the continuous optimal control problem.

The fully discrete version of Problem 4.1 reads:

$$J(\hat{q}_h, \hat{U}_h) \rightarrow \min, \quad \hat{A}(\hat{q}_h, \hat{U}_h)(\hat{\Psi}_h) = 0 \quad \text{for } (\hat{q}_h, \hat{U}_h) \in \widehat{Q}_h \times \widehat{X}_h,$$

where $\widehat{X}_h \times \widehat{Q}_h \subset \widehat{X} \times \widehat{Q}$.

Discretization of the KKT system

Thus, we could solve the KKT system (4.8) directly using a standard finite element Galerkin method. The local solutions correspond to saddle points $(\hat{q}_h, \hat{U}_h, \hat{Z}_h) \in \widehat{Q}_h \times \widehat{X}_h \times \widehat{X}_h$ of the discrete problem

$$\begin{aligned} \hat{A}(\hat{q}_h, \hat{U}_h)(\hat{\Psi}_h) &= 0 && \forall \hat{\Psi}_h \in \widehat{X}_h, \\ \hat{A}'_{\hat{U}}(\hat{q}_h, \hat{U}_h)(\hat{\Psi}_h, \hat{Z}_h) &= J'_{\hat{U}}(\hat{q}_h, \hat{U}_h)(\hat{\Psi}_h) && \forall \hat{\Psi}_h \in \widehat{X}_h, \\ \hat{A}'_{\hat{q}}(\hat{q}_h, \hat{U}_h)(\delta\hat{q}_h, \hat{Z}_h) &= J'_{\hat{q}}(\hat{q}_h, \hat{U}_h)(\delta\hat{q}_h) && \forall \delta\hat{q}_h \in \widehat{Q}_h. \end{aligned}$$

Using the KKT system might be a good oportunity for solving nonstationary optimal control with fluid-structure interaction. In such cases, the analytical expressions for the second derivatives are circumvented.

Discretization of the reduced problem

Because we already worked with a discrete control space, we only must account for the discretization of the state variable. The Problems 4.3, 4.4, 4.5, that are derived with the help of the Lagrangian is discretized with a standard Galerkin finite element scheme. For their extension to space-time discretizations, we refer to [15, 102].

Outlook to subsequent chapters

In this chapter, we derived an optimal control setting subject to fluid-structure interaction. Specifically, we discussed a setting for Neumann boundary control. For this setting, we stated explicit expressions of the derivatives, which are required for the unconstrained solution process. The theoretical findings of this chapter are substantiated by two numerical examples in Section 7.3.

5 Discretization

This chapter is devoted to the discretization of the monolithically coupled fluid-structure interaction problem that was introduced in the previous chapters. The temporal discretization is performed using finite difference schemes (such that we can employ the Fractional-Step-θ scheme). Specifically, we analyze the stability of the time-discretized system. These findings are substantiated by a numerical comparison of all relevant second-order time-stepping schemes by means of a fully unsteady fluid-structure benchmark configuration. The spatial discretization is treated by a Galerkin finite element method. Moreover, we briefly describe a stabilization technique to treat convection-dominated flows. After that description, we present the linearization of the nonlinear problem. In this section, the Jacobian is derived by exact linearization, which is demonstrated for the complete problem. We close with a description of the inner form of the arising systems of linear equations at each Newton step and explain how to derive an efficient solution process.

The practicable variational formulation in an abstract setting

In the domain $\widehat{\Omega}$ and the time interval $I = [0, T]$, we consider the fluid-structure interaction Problem 3.6 with harmonic or linear-elastic mesh motion in an abstract setting (the biharmonic problem is straightforward): Find $\hat{U} = \{\hat{v}_f, \hat{v}_s, \hat{u}_f, \hat{u}_s, \hat{p}_f, \hat{p}_s\} \in \widehat{X}_D^0$, where $\widehat{X}_D^0 := \{\hat{v}_f^D + \hat{V}_{f,\hat{v}}^0\} \times \hat{L}_f \times \{\hat{u}_f^D + \hat{V}_{f,\hat{u}}^0\} \times \{\hat{u}_s^D + \hat{V}_s^0\} \times \hat{L}_f^0 \times \hat{L}_s^0$, such that

$$\int_0^T \hat{A}(\hat{U})(\hat{\Psi})\, dt = \int_0^T \widehat{F}(\hat{\Psi})\, dt \quad \forall \hat{\Psi} \in \widehat{X}, \tag{5.1}$$

where $\hat{\Psi} = \{\hat{\psi}_f^v, \hat{\psi}_s^v, \hat{\psi}_f^u, \hat{\psi}_s^u, \hat{\psi}_f^p, \hat{\psi}_s^p\}$ and $\widehat{X} = \hat{V}_{f,\hat{v}}^0 \times \hat{L}_f \times \hat{V}_{f,\hat{u},\widehat{\Gamma}_i}^0 \times \hat{V}_s^0 \times \hat{L}_f^0 \times \hat{L}_s^0$. The time integral is defined in an abstract sense such that the equation holds for *almost* all time steps.

Problem 5.1 (Semi-linear form of FSI using harmonic mesh motion). *Using the harmonic mesh motion model leads to the following expressions of* $\hat{A}(\hat{U})(\hat{\Psi})$ *and* $\widehat{F}(\hat{\Psi})$*:*

$$\widehat{F}(\hat{\Psi}) = (\hat{\rho}_s \hat{f}_s, \hat{\psi}_s^v)_{\widehat{\Omega}_s}, \tag{5.2}$$

and

$$\begin{aligned}\hat{A}(\hat{U})(\hat{\Psi}) = &(\hat{J}\hat{\rho}_f\partial_t\hat{v}_f, \hat{\psi}^v_f)_{\widehat{\Omega}_f} + (\hat{\rho}_f\hat{J}(\widehat{F}^{-1}\hat{v}_f \cdot \widehat{\nabla})\hat{v}_f), \hat{\psi}^v_f)_{\widehat{\Omega}_f} \\ &- (\hat{\rho}_f\hat{J}(\widehat{F}^{-1}\hat{w} \cdot \widehat{\nabla})\hat{v}_f), \hat{\psi}^v_f)_{\widehat{\Omega}_f} - \langle \hat{g}_f, \hat{\psi}^v_f\rangle_{\widehat{\Gamma}_N} - (\hat{\rho}_f\hat{J}\hat{f}_f, \hat{\psi}^v_f)_{\widehat{\Omega}_f} \\ &+ (\hat{J}\hat{\sigma}_f\widehat{F}^{-T}, \widehat{\nabla}\hat{\psi}^v_f)_{\widehat{\Omega}_f} + (\hat{\rho}_s\partial_t\hat{v}_s, \hat{\psi}^v_s)_{\widehat{\Omega}_s} + (\widehat{F}\widehat{\Sigma}, \widehat{\nabla}\hat{\psi}^v_s)_{\widehat{\Omega}_s} \\ &+ (\hat{\rho}_s\partial_t\hat{u}_s, \hat{\psi}^u_s)_{\widehat{\Omega}_s} - (\hat{\rho}_s\hat{v}_s, \hat{\psi}^u_s)_{\widehat{\Omega}_s} + (\alpha_u\widehat{\nabla}\hat{u}_f, \widehat{\nabla}\hat{\psi}^u_f)_{\widehat{\Omega}_f} \\ &+ \gamma_w(\hat{v}_s, \hat{\psi}^v_s)_{\widehat{\Omega}_s} + \gamma_s(\hat{\epsilon}(\hat{v}_s), \widehat{\nabla}\hat{\psi}^v_s)_{\widehat{\Omega}_s} \\ &+ (\widehat{div}(\hat{J}\widehat{F}^{-1}\hat{v}_f), \hat{\psi}^p_f)_{\widehat{\Omega}_f} + (\hat{P}_s, \hat{\psi}^p_s)_{\widehat{\Omega}_s}. \end{aligned} \tag{5.3}$$

The fluid convection term in (5.3) *is decomposed into two parts for later purposes.*

5.1 Temporal discretization

The abstract problem (5.1) can either be treated by a full time-space Galerkin formulation, which was investigated previously for fluid problems in Besier et al. [22, 23, 123]. Alternatively, the Rothe method can be used in cases where the time discretization is based on finite difference schemes. A classical scheme for problems with a stationary limit is the (implicit) backward Euler scheme (BE), which is strongly A-stable (but only from first order) and dissipative. It is later used in the numerical Examples, where a stationary limit must be achieved.

In contrast, the (implicit) Crank-Nicolson scheme is of second order, A-stable, and has very little dissipation but suffers from case-to-case instabilities caused by rough initial and/or boundary data. These properties are due to weak stability (it is not *strongly* A-stable). A variant of the Crank-Nicolson scheme is called *shifted* Crank-Nicolson scheme, is analyzed in Rannacher et al. [71, 113], which allows for global stability of the solution. These time-stepping schemes are addressed in more detail below. The third scheme summarizes the advantages of the other two and is known as the Fractional-Step-θ scheme for computing unsteady-state simulations [62]. This scheme has second-order accuracy and is strongly A-stable, and it is therefore well-suited for computing solutions with rough data and long-term computations for problems on fixed meshes. This property also holds for ALE-transformed fluid equations, which is demonstrated in a numerical test in Section 5.4.2. We also refer the reader to a modification of the Fractional-Step-θ scheme [136].

After semi-discretization in time, we obtain a sequence of generalized steady-state fluid-structure interaction problems that are completed by appropriate boundary values at every time step. These problems are formulated as *One-step-θ scheme* (see, e.g., [133, 136]). This design has the advantage that it can easily be extended to the Fractional-Step-θ scheme.

Practicable time-stepping schemes

Let

$$I = \{0\} \cup I_1 \cup \ldots \cup I_N$$

be a partition of the time interval $I = [0, T]$ into half open subintervals $I_n := (t_{n-1}, t_n]$ of (time step) size $k_n := t_n - t_{n-1}$ with

$$0 = t_0 < \cdots < t_N = T.$$

We (formally) define the following semi-linear forms and group them into four categories: time equation terms (including the time derivatives), implicit terms (e.g., the incompressibility of the fluid), pressure terms, and all remaining terms (stress terms, convection, damping, etc.):

$$\begin{aligned}
\hat{A}_T(\hat{U})(\hat{\Psi}) &= (\hat{J}\hat{\rho}_f \partial_t \hat{v}_f, \hat{\psi}_f^v)_{\widehat{\Omega}_f} - (\hat{\rho}_f \hat{J}(\widehat{F}^{-1}\hat{w} \cdot \widehat{\nabla})\hat{v}_f), \hat{\psi}_f^v)_{\widehat{\Omega}_f} \\
&\quad + (\hat{\rho}_s \partial_t \hat{v}_s, \hat{\psi}_s^v)_{\widehat{\Omega}_s} + (\hat{\rho}_s \partial_t \hat{u}_s, \hat{\psi}_s^u)_{\widehat{\Omega}_s}, \\
\hat{A}_I(\hat{U})(\hat{\Psi}) &= (\alpha_u \widehat{\nabla} \hat{u}_f, \widehat{\nabla} \hat{\psi}_f^u)_{\widehat{\Omega}_f} \\
&\quad + (\widehat{\operatorname{div}}\,(\hat{J}\widehat{F}^{-1}\hat{v}_f), \hat{\psi}_f^p)_{\widehat{\Omega}_f} + (\hat{P}_s, \hat{\psi}_s^p)_{\widehat{\Omega}_s}, \\
\hat{A}_E(\hat{U})(\hat{\Psi}) &= (\hat{\rho}_f \hat{J}(\widehat{F}^{-1}\hat{v}_f \cdot \widehat{\nabla})\hat{v}_f), \hat{\psi}_f^v)_{\widehat{\Omega}_f} + (\hat{J}\hat{\sigma}_{f,vu}\widehat{F}^{-T}, \widehat{\nabla}\hat{\psi}_f^v)_{\widehat{\Omega}_f} \\
&\quad + (\widehat{F}\widehat{\Sigma}, \widehat{\nabla}\hat{\psi}_s^v)_{\widehat{\Omega}_s} + \gamma_w(\hat{v}_s, \hat{\psi}_s^v)_{\widehat{\Omega}_s} + \gamma_s(\hat{\epsilon}(\hat{v}_s), \widehat{\nabla}\hat{\psi}_s^v)_{\widehat{\Omega}_s} - (\hat{\rho}_s \hat{v}_s, \hat{\psi}_s^u)_{\widehat{\Omega}_s}, \\
\hat{A}_P(\hat{U})(\hat{\Psi}) &= (\hat{J}\hat{\sigma}_{f,p}\widehat{F}^{-T}, \widehat{\nabla}\hat{\psi}_f^v)_{\widehat{\Omega}_f} + (\hat{J}\hat{\sigma}_{s,p}\widehat{F}^{-T}, \widehat{\nabla}\hat{\psi}_s^v)_{\widehat{\Omega}_s},
\end{aligned} \tag{5.4}$$

where the reduced stress tensors $\widehat{\sigma}_{f,vu}$, $\widehat{\sigma}_{f,p}$, and $\widehat{\sigma}_{s,p}$ are defined as:

$$\begin{aligned}
&\widehat{\sigma}_{f,p} = -\hat{p}_f \hat{I}, \quad \widehat{\sigma}_{f,vu} = \rho_f \nu_f (\widehat{\nabla}\hat{v}_f \widehat{F}^{-1} + \widehat{F}^{-T}\widehat{\nabla}\hat{v}_f^T), \\
&\widehat{\sigma}_{s,p} = -\hat{p}_s \hat{I}, \quad \text{(if we deal with the INH or IMR material)},
\end{aligned}$$

and $\widehat{\Sigma}$ denotes as usual the structure tensor of the INH, IMR, or STVK material. The time derivative in $\hat{A}_T(\hat{U})(\hat{\Psi})$ is approximated by a backward difference quotient. For the time step $t_n \in I$ for $n = 1, 2, \ldots, N$ ($N \in \mathbb{R}$), we compute $\hat{v}_i := \hat{v}_i^n, \hat{u}_i := \hat{u}_i^n$ $(i = f, s)$ via

$$\begin{aligned}
\hat{A}_T(\hat{U}^{n,k})(\hat{\Psi}) \approx{}& \frac{1}{k}\Big(\hat{\rho}_f \hat{J}^{n,\theta}(\hat{v}_f - \hat{v}_f^{n-1}), \hat{\psi}^v\Big)_{\widehat{\Omega}_f} - \frac{1}{k}\Big(\hat{\rho}_f(\hat{J}\widehat{F}^{-1}(\hat{u}_f - \hat{u}_f^{n-1}) \cdot \widehat{\nabla})\hat{v}_f, \hat{\psi}^v\Big)_{\widehat{\Omega}_f} \\
&+ \frac{1}{k}\Big(\hat{\rho}_s(\hat{v}_s - \hat{v}_s^{n-1}), \hat{\psi}^v\Big)_{\widehat{\Omega}_s} + \Big(\hat{u}_s - \hat{u}_s^{n-1}, \hat{\psi}^u\Big)_{\widehat{\Omega}_s},
\end{aligned} \tag{5.5}$$

where we introduce a parameter θ, which is clarified below. Furthermore, we use

$$\hat{J}^{n,\theta} = \theta \hat{J}^n + (1 - \theta)\hat{J}^{n-1},$$

and $\hat{u}_i^n := \hat{u}_i(t_n)$, $\hat{v}_i^n := \hat{v}_i(t_n)$, and $\hat{J} := \hat{J}^n := \hat{J}(t_n)$. The former time step is given by $\hat{v}_i^{n-1}$, etc. for $i = f, s$.

The One-Step-θ scheme

Let the previous time step solution $\hat{U}^{n-1} = \{\hat{v}_f^{n-1}, \hat{v}_s^{n-1}, \hat{u}_f^{n-1}, \hat{u}_s^{n-1}, \hat{p}_f^{n-1}, \hat{p}_s^{n-1}\}$ and the time step $k := k_n = t_n - t_{n-1}$ be given.

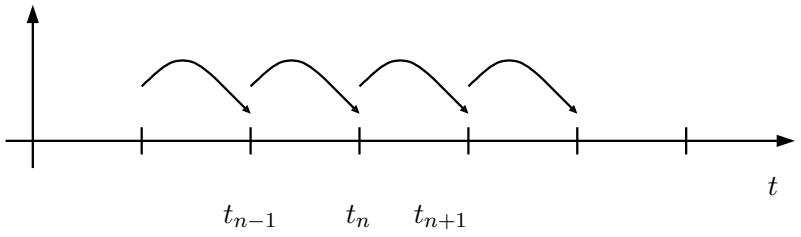

Figure 5.1. Time step computation using One-Step-θ schemes.

Find $\hat{U}^n = \{\hat{v}_f^n, \hat{v}_s^n, \hat{u}_f^n, \hat{u}_s^n, \hat{p}_f^n, \hat{p}_s^n\}$ such that

$$\begin{aligned} &\hat{A}_T(\hat{U}^{n,k})(\hat{\Psi}) + \theta\hat{A}_E(\hat{U}^n)(\hat{\Psi}) \\ +&\hat{A}_P(\hat{U}^n)(\hat{\Psi}) + \hat{A}_I(\hat{U}^n)(\hat{\Psi}) \;=\; -(1-\theta)\hat{A}_E(\hat{U}^{n-1})(\hat{\Psi}) \\ &\qquad\qquad + \theta\widehat{F}^n(\hat{\Psi}) + (1-\theta)\widehat{F}^{n-1}(\hat{\Psi}), \end{aligned} \tag{5.6}$$

where $\widehat{F}^n(\hat{\Psi}) = (\hat{\rho}_s\hat{f}_s^n, \hat{\psi}_s^v)_{\widehat{\Omega}_s}$ with $\hat{f}_s^n := \hat{f}_s(t_n)$. The concrete scheme depends on the choice of the parameter θ. Specifically, we get the backward Euler scheme for $\theta = 1$, the Crank-Nicolson scheme for $\theta = \frac{1}{2}$, and the shifted Crank-Nicolson for $\theta = \frac{1}{2} + k_n$ [71, 113].

The Fractional-Step-θ scheme

We choose $\theta = 1 - \frac{\sqrt{2}}{2}, \theta' = 1 - 2\theta$, and $\alpha = \frac{1-2\theta}{1-\theta}, \beta = 1 - \alpha$. The time step is split into three consecutive sub-time steps. Let $\hat{U}^{n-1} = \{\hat{v}_f^{n-1}, \hat{v}_s^{n-1}, \hat{u}_f^{n-1}, \hat{u}_s^{n-1}, \hat{p}_f^{n-1}, \hat{p}_s^{n-1}\}$ and the time step $k := k_n = t_n - t_{n-1}$ be given.

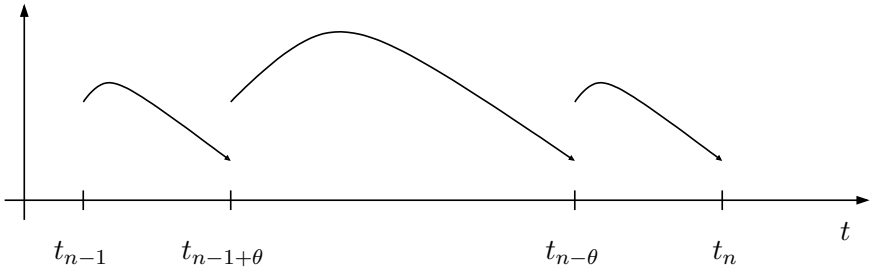

Figure 5.2. Time step computation using the Fractional-Step-θ scheme.

Find $\hat{U}^n = \{\hat{v}_f^n, \hat{v}_s^n, \hat{u}_f^n, \hat{u}_s^n, \hat{p}_f^n, \hat{p}_s^n\}$ such that

$$\begin{aligned}
&\hat{A}_T(\hat{U}^{n-1+\theta,k})(\hat{\Psi}) + \alpha\theta\hat{A}_E(\hat{U}^{n-1+\theta})(\hat{\Psi}) \\
&\quad +\theta\hat{A}_P(\hat{U}^{n-1+\theta})(\hat{\Psi}) + \hat{A}_I(\hat{U}^{n-1+\theta})(\hat{\Psi}) = -\beta\theta\hat{A}_E(\hat{U}^{n-1})(\hat{\Psi}) + \theta\hat{F}^{n-1}(\hat{\Psi}),
\end{aligned}$$

$$\begin{aligned}
&\hat{A}_T(\hat{U}^{n-\theta,k})(\hat{\Psi}) + \alpha\theta\hat{A}_E(\hat{U}^{n-\theta})(\hat{\Psi}) \\
&\quad +\theta'\hat{A}_P(\hat{U}^{n-\theta})(\hat{\Psi}) + \hat{A}_I(\hat{U}^{n-\theta})(\hat{\Psi}) = -\alpha\theta'\hat{A}_E(\hat{U}^{n-1+\theta})(\hat{\Psi}) + \theta'\hat{F}^{n-\theta}(\hat{\Psi}),
\end{aligned}$$

$$\begin{aligned}
&\hat{A}_T(\hat{U}^{n,k})(\hat{\Psi}) + \alpha\theta\hat{A}_E(\hat{U}^{n})(\hat{\Psi}) \\
&\quad +\theta\hat{A}_P(\hat{U}^{n})(\hat{\Psi}) + \hat{A}_I(\hat{U}^{n})(\hat{\Psi}) = -\beta\theta\hat{A}_E(\hat{U}^{n-1})(\hat{\Psi}) + \theta\hat{F}^{n-\theta}(\hat{\Psi}).
\end{aligned} \tag{5.7}$$

With the help of the previous considerations, we formulate a statement for the time-discretized equations:

Problem 5.2. *Let the semi-linear form $\hat{A}(\cdot)(\cdot)$ be formulated in terms of the previous arrangement, such that*

$$\hat{A}(\hat{U})(\hat{\Psi}) := \hat{A}_T(\hat{U})(\hat{\Psi}) + \hat{A}_I(\hat{U})(\hat{\Psi}) + \hat{A}_E(\hat{U})(\hat{\Psi}) + \hat{A}_P(\hat{U})(\hat{\Psi}).$$

After time discretization, let the time derivatives are approximated with

$$\hat{A}_T(\hat{U})(\hat{\Psi}) \approx \hat{A}_T(\hat{U}^{n,k})(\hat{\Psi}),$$

such that the time-discretized semi-linear form reads

$$\hat{A}(\hat{U}^n)(\hat{\Psi}) := \hat{A}_T(\hat{U}^{n,k})(\hat{\Psi}) + \hat{A}_I(\hat{U}^n)(\hat{\Psi}) + \hat{A}_E(\hat{U}^n)(\hat{\Psi}) + \hat{A}_P(\hat{U}^n)(\hat{\Psi}).$$

Then, we aim to find $\hat{U}^n = \{\hat{v}_f^n, \hat{v}_s^n, \hat{u}_f^n, \hat{u}_s^n, \hat{p}_f^n, \hat{p}_s^n\} \in \widehat{X}_D^0$, where $\widehat{X}_D^0 := \{\hat{v}_f^D + \hat{V}_{f,\hat{v}}^0\} \times \hat{L}_s \times \{\hat{u}_f^D + \hat{V}_{f,\hat{u}}^0\} \times \{\hat{u}_s^D + \hat{V}_s^0\} \times \hat{L}_f^0 \times \hat{L}_s^0$ and $\widehat{X} = \hat{V}_{f,\hat{v}}^0 \times \hat{L}_s \times \hat{V}_{f,\hat{u},\widehat{\Gamma_i}}^0 \times \hat{V}_s^0 \times \hat{L}_f^0 \times \hat{L}_s^0$, for all $n = 1, 2, \ldots, N$ such that

$$\hat{A}(\hat{U}^n)(\hat{\Psi}) = \widehat{F}(\hat{\Psi}) \quad \forall\hat{\Psi} \in \widehat{X},$$

where this equation is treated with one specific time-stepping scheme as introduced previously.

Time-stepping schemes in moving domains

The practicable time-stepping schemes in the reference domain are not convenient for a priori stability analysis after semi-discretization in time. Therefore, we use the same methodology applied in Section 3.4, and we keep the fluid equations in the moving domain. Specifically, we are interested in the analysis of the second-order Crank-Nicolson scheme. Consequently, we first introduce the time-discretized equations in moving domains in the following [52, 107].

Following Formaggia and Nobile [52], we consider the following modification of the classical Crank-Nicolson scheme (i.e., it is a Gauss-Legendre implicit second-order Runge-Kutta method)

$$v_f^{n+1} - v_f^n = kg\left(t_{n+\frac{1}{2}}, \frac{v_f^{n+1} + v_f^n}{2}\right), \tag{5.8}$$

where $g(t, v_f(t))$ denotes the right-hand-side of a differential equation. This modified scheme can be reduced to the classical scheme for a linear advection-diffusion problem on a fixed domain and time-independent coefficients. Moreover, the *geometric conservation law* is satisfied for this scheme in two-dimensional domains [52, 107] if the ALE transformation is reconstructed linearly in time (i.e., using a constant in time-mesh velocity w). We consider this aspect in more detail below.

To derive a stability result for the Crank-Nicolson scheme, we provide some further notation. In the rest of this section, we are going to work with an ALE mapping that is defined from the previous time step t_{n-1} to the the present time step t_n. This is an extension to our previous definitions, where the reference configuration coincided with the configuration at the initial time step, i.e., $\Omega^0 = \widehat{\Omega}$. In the following, we denote by Ω^n the reference configuration at time step t_n and we use $v^n \in \Omega^n$ as an approximation of $v(t_n)$. This value is transported from Ω^n to any other configuration Ω^l (for $l \neq n$) through the ALE mapping ([107]):

$$\hat{\mathcal{A}}_{n,l} = \hat{\mathcal{A}}_l \circ \hat{\mathcal{A}}_n^{-1}.$$

For the sake of notation, we omit the explicit representation of the ALE mapping when we work with the value v^n in a domain Ω_l with $n \neq l$, i.e.,

$$\int_{\Omega_l} v^n \,\mathrm{d}x := \int_{\Omega_l} v^n \circ \hat{\mathcal{A}}_{n,l} \,\mathrm{d}x, \quad \text{and} \quad ||v^n||_{\Omega^l} := ||v^n \circ \hat{\mathcal{A}}_{n,l}||_{\Omega^l},$$

which we use frequently in the following.

With these preparations, the application of the relation (5.8) to the Navier-Stokes equations (3.1) reads in the weak formulation:

Problem 5.3. *Find $\{v_f, p_f\} \in \{v_f^D + V_f^0\} \times L_f^0$, such that $v_f(0) = v_f^0$ is satisfied, and for $n = 0, 1, 2, \ldots, N$ holds:*

$$\begin{aligned}
&\rho_f\Big(v_f^{n+1} - v_f^n, \psi^v\Big)_{\Omega_f^{n+1}} + k\rho_f\left(\left[v_f^{n+\frac{1}{2}} - w^{n+1}\right] \cdot \nabla\Big(\frac{v_f^{n+1} + v_f^n}{2}\Big), \psi^v\right)_{\Omega_f^{n+1}} \\
&\quad + 2k\rho_f\nu_f\left(D\Big(\frac{v_f^{n+1} + v_f^n}{2}\Big), \nabla\psi^v\right)_{\Omega_f^{n+1}} - k\Big(\frac{p_f^{n+1} + p_f^n}{2}, \nabla\cdot\psi^v\Big)_{\Omega_f^{n+1}} = 0 \quad \forall \psi^v \in V_f^0, \\
&\qquad \left(\nabla\cdot\Big(\frac{v_f^{n+1} + v_f^n}{2}\Big), \psi^p\right)_{\Omega_f^{n+1}} = 0 \quad \forall \psi^p \in L_f^0,
\end{aligned} \tag{5.9}$$

where $v_f^{n+\frac{1}{2}}$ *can be chosen as* $v_f^{n+\frac{1}{2}} = 2^{-1}(v_f^{n+1} + v_f^n)$ *to obtain a fully implicit nonlinear convection term. Otherwise, one can approximate* $v_f^{n+\frac{1}{2}}$ *by extrapolating the former time steps* v_f^{n-1} *and* v_f^{n-2} *such that* $v_f^{n+\frac{1}{2}} = \frac{1}{2}\Big(3v_f^{n-1} - v_f^{n-2}\Big)$.

We supplement this scheme with homogeneous boundary conditions and admissible initial conditions:

$$\begin{aligned} v_f^n &= 0 \quad \text{on } \partial\Omega_f, \quad n = 1, 2, \ldots, N+1 \\ v_f^0 &= v_0 \quad \text{in } \Omega_f^0 = \widehat{\Omega}_f. \end{aligned}$$

In the case of Neumann conditions, we add in the first equation of (5.9) the term

$$2k\rho_f\nu_f \left\langle D\Big(\frac{v_f^{n+1} + v_f^n}{2}\Big) n_f, \psi^v \right\rangle_{\Gamma_{f,N}^{n+1}}. \tag{5.10}$$

As usual, this is the outcome of partial integration of the stress term. This term must be incorporated in the case of fluid-structure interaction problems because it contributes to the energy exchange on the interface.

For the structure subproblem, we also use the Crank-Nicolson scheme. First, we state the following weak form of the structure Equations (2.17):

Problem 5.4. *Find* $\{\hat{v}_s, \hat{u}_s\} \in \hat{L}_s \times \{\hat{u}_s^D + \hat{V}_s^0\}$*, such that* $\hat{v}_s(0) = \hat{v}_s^0$ *and* $\hat{u}_s(0) = \hat{u}_s^0$ *are satisfied, and for almost all time steps* $t \in I$ *holds:*

$$\begin{aligned} \hat{\rho}_s(\partial_t \hat{v}_s, \hat{\psi}^v)_{\widehat{\Omega}_s} + (\widehat{F}\widehat{\Sigma}, \widehat{\nabla}\hat{\psi}^v)_{\widehat{\Omega}_s} - \langle \widehat{F}\widehat{\Sigma}\hat{n}_s, \hat{\psi}^v\rangle_{\widehat{\Gamma}_{s,N}} \\ +\gamma_w(\hat{v}_s, \hat{\psi}^v)_{\widehat{\Omega}_s} + \gamma_s(\hat{\epsilon}(\hat{v}_s), \widehat{\nabla}\hat{\psi}^v)_{\widehat{\Omega}_s} - \gamma_s\langle\hat{\epsilon}(\hat{v}_s)\hat{n}_s, \hat{\psi}^v\rangle_{\widehat{\Gamma}_{s,N}} = 0 \quad \forall \hat{\psi}^v \in \hat{V}_s^0, \\ \hat{\rho}_s(\partial_t \hat{u}_s, \hat{\psi}^u)_{\widehat{\Omega}_s} - \hat{\rho}_s(\hat{v}_s, \hat{\psi}^u)_{\widehat{\Omega}_s} = 0 \quad \forall \hat{\psi}^u \in \hat{L}_s. \end{aligned}$$

Problem 5.4 is obtained from 3.4, neglecting volume forces.

Temporal discretization of the structure Problem 5.4 with the Crank-Nicolson scheme yields:

Problem 5.5. *Find* $\{\hat{v}_s^{n+1}, \hat{u}_s^{n+1}\} \in \hat{L}_s \times \{\hat{u}_s^D + \hat{V}_s^0\}$ *for* $n = 0, 1, 2, \ldots, N$*:*

$$\begin{aligned} \hat{\rho}_s \frac{1}{k}\Big(\hat{v}_s^{n+1} - \hat{v}_s^n, \hat{\psi}^v\Big)_{\widehat{\Omega}_s} + \theta\Big(\widehat{F}\widehat{\Sigma}(\hat{u}_s^{n+1} + \hat{u}_s^n), \widehat{\nabla}\hat{\psi}^v\Big)_{\widehat{\Omega}_s} \\ -\theta\Big\langle \widehat{F}\widehat{\Sigma}(\hat{u}_s^{n+1} + \hat{u}_s^n)\hat{n}_s, \hat{\psi}^v\Big\rangle_{\widehat{\Gamma}_{s,N}} + \gamma_w\theta\Big(\hat{v}_s^{n+1} + \hat{v}_s^n, \hat{\psi}^v\Big)_{\widehat{\Omega}_s} \\ +\gamma_s\theta\Big(\hat{\epsilon}(\hat{v}_s^{n+1} + \hat{v}_s^n), \widehat{\nabla}\hat{\psi}^v\Big)_{\widehat{\Omega}_s} - \gamma_s\theta\Big\langle\hat{\epsilon}(\hat{v}_s^{n+1} + \hat{v}_s^n)\hat{n}_s, \hat{\psi}^v\Big\rangle_{\widehat{\Gamma}_{s,N}} = 0 \quad \forall \hat{\psi}^v \in \hat{V}_s^0, \\ \hat{\rho}_s \frac{1}{k}\Big(\hat{u}_s^{n+1} + \hat{u}_s^n, \hat{\psi}^u\Big)_{\widehat{\Omega}_s} - \hat{\rho}_s\theta\Big(\hat{v}_s^{n+1} + \hat{v}_s^n, \hat{\psi}^u\Big)_{\widehat{\Omega}_s} = 0 \quad \forall \hat{\psi}^u \in \hat{L}_s, \end{aligned} \tag{5.11}$$

with $\theta = 0.5$.

5.2 Stability of the ALE fluid problem using the Crank-Nicolson scheme

It is already well-known from pure fluid problems on fixed meshes, that the second order ordinary Crank-Nicolson scheme suffers from instabilities, particularly for long-term computations [71]. The normally unconditionally stable Crank-Nicolson scheme is restricted by the condition

$$k \leq ch^{2/3}. \tag{5.12}$$

where k and h denote the time-step size and the mesh-size parameter, respectively, and c is some constant. However, the scheme can be stabilized by moving the θ-parameter slightly to the implicit side, leading to the shifted Crank-Nicolson scheme [101, 113]. On the other hand, several authors detected numerical instabilities on moving domains for higher order time-stepping schemes caused by the ALE convection term [45, 51, 52, 98].

Specifically, this term is a numerical artifact that only appears on moving domains [51, 52, 107]. However, the relevance in numerical computations is not yet completely understand. The stability is closely related to the verification of the *Geometric Conservation Law* (GCL) [45, 51, 52, 98]. Formaggia and Nobile [52], p. 4098, state that they found no example of blow-up caused by the ALE convection term for linear advection-diffusion equations. Moreover, they proved that the GCL condition does not degrade the accuracy of the numerical schemes.

To get an analogous stability result for the time-discretized Crank-Nicolson scheme on moving domains, we use the methodology used in [51, 52, 107]. It holds:

Lemma 5.1. *For the time-discretized solution of the Crank-Nicolson scheme* (5.9) *holds:*

$$\rho_f ||v_f^{n+1}||^2_{\Omega_f^{n+1}} + k\rho_f \nu_f ||D(v_f^{n+1} + v_f^n)||^2_{\Omega_f^{n+1}} + \frac{k\rho_f}{4} \int\limits_{\Omega_f^{n+1}} \nabla \cdot w^{n+\frac{1}{2}} \, |v_f^{n+1} + v_f^n|^2 \, \mathrm{d}x$$

$$= \rho_f ||v_f^n||^2_{\Omega_f^{n+1}},$$

For $\nabla \cdot w > 0$ for all $x \in \Omega_f$ and for all $t \in I$ (a uniform contraction of the mesh), the CN scheme is unconditionally stable. Otherwise, the ALE convection term causes instabilities that restricts the choice of the time step size. Specifically, it holds:

$$k \leq \frac{1}{\delta_w}.$$

Before we proof the Lemma, we consolidate:

Remark 5.1 (Mesh contraction). A uniform mesh contraction was observed in the numerical test 8.1. In the other numerical examples we monitored with changing mesh contractions.

Proof. To proof the assertion, we use the arguments presented in [52, 107]. In Problem 5.3, we take the test functions $\psi^v = v_f^{n+1} + v_f^n$ and $\psi^p = p_f^{n+1} + p_f^n$. We observe that with this choice, the pressure term in the first equation can be removed thanks to the incompressibility condition. The mass term can be written as

$$\rho_f(v_f^{n+1} - v_f^n, v_f^{n+1} + v_f^n)_{\Omega_f^{n+1}} = \rho_f ||v_f^{n+1}||^2_{\Omega_f^{n+1}} + \rho_f ||v_f^n||^2_{\Omega_f^{n+1}}. \tag{5.13}$$

Using the identity

$$\Big(D(v_f^{n+1}), \nabla v_f^{n+1}\Big)_{\Omega_f^{n+1}} = \Big(D(v_f^{n+1}), D(v_f^{n+1})\Big)_{\Omega_f^{n+1}} \quad \forall n = 0, 1, 2, \dots,$$

brings us to

$$2k\rho_f\nu_f \left(D\Big(\frac{v_f^{n+1} + v_f^n}{2}\Big), D(v_f^{n+1} + v_f^n)\right)_{\Omega_f^{n+1}} = k\rho_f\nu_f ||D(v_f^{n+1} + v_f^n)||^2_{\Omega_f^{n+1}}. \tag{5.14}$$

So far, we assume that homogenous Dirichlet conditions are prescribed on the outer boundaries. Otherwise, the following term would remain on Neumann parts:

$$-\frac{k}{2}\Big\langle \sigma(v_f^{n+1} + v_f^n)n_f, v_f^{n+1} + v_f^n \Big\rangle_{\Gamma_{f,N}^{n+1}}. \tag{5.15}$$

It remains to consider the convection term using the fully nonlinear discretization $v_f^{n+\frac{1}{2}} = 2^{-1}(v_f^{n+1} + v_f^n)$. We plug-in the test function $\psi^v = v_f^{n+1} + v_f^n$, which gives us:

$$\begin{aligned} &k\rho_f \left(\left[\Big(\frac{v_f^{n+1} + v_f^n}{2} \Big) - w^{n+1} \right] \cdot \nabla \Big(\frac{v_f^{n+1} + v_f^n}{2} \Big), v_f^{n+1} + v_f^n \right)_{\Omega_f^{n+1}} \\ &= \frac{k\rho_f}{4} \int\limits_{\Omega_f^{n+1}} \Big[(v_f^{n+1} + v_f^n) - w^{n+1} \Big] \cdot \nabla \left| v_f^{n+1} + v_f^n \right|^2 \mathrm{d}x. \end{aligned}$$

Using the explicit representation of the integral and using integration by parts, yields

$$\begin{aligned} &\frac{k\rho_f}{4} \int\limits_{\Omega_f^{n+1}} \Big[(v_f^{n+1} + v_f^n) - w^{n+1} \Big] \cdot \nabla \left| v_f^{n+1} + v_f^n \right|^2 \mathrm{d}x \\ &= \frac{k\rho_f}{4} \int\limits_{\Gamma_{f,N}^{n+1}} \Big[(v_f^{n+1} + v_f^n) - w^{n+1} \Big] \cdot n_f \left| v_f^{n+1} + v_f^n \right|^2 \mathrm{d}x \\ &- \frac{k\rho_f}{4} \int\limits_{\Omega_f^{n+1}} \nabla \cdot \Big[(v_f^{n+1} + v_f^n) - w^{n+1} \Big] \left| v_f^{n+1} + v_f^n \right|^2 \mathrm{d}x. \end{aligned} \tag{5.16}$$

The boundary term vanishes, thanks again to the homogeneous Dirichlet boundary conditions. Using the incompressibility of the fluid, brings us to

$$\frac{k\rho_f}{4} \int\limits_{\Omega_f^{n+1}} \nabla \cdot [w^{n+1}] \left| v_f^{n+1} + v_f^n \right|^2 \mathrm{d}x. \tag{5.17}$$

We note that the last step is admissible because we are still working in spatially infinite-dimensional spaces, where the incompressibility of the fluid is satisfied in each time step. This property gets lost after spatial discretization and the incompressibility term requires attention (see e.g., [107]). Adding the contributions (5.13), (5.14), and (5.17) finishes the proof. □

Remark 5.2. In the case of a fluid-structure interaction problem, the boundary term (the middle term of Equation (5.16)) that is achieved by partial integration of the convection term, also contains the interface term

$$\frac{k\rho_f}{4} \int\limits_{\Gamma_i^{n+1}} \left[(v_f^{n+1} + v_f^n) - w^{n+1} \right] \cdot n_f \, |v_f^{n+1} + v_f^n|^2 \, \mathrm{d}x.$$

From this expression, we extract the coupling condition on the interface that is needed for a monolithically coupled system:

$$\frac{1}{2}(v_f^{n+1} + v_f^n) - w^{n+1} = 0 \quad \text{on } \Gamma_i.$$

Remark 5.3. The extension of the Lemma to a nonvanishing right-hand-side force and Neumann boundary conditions is shown elsewhere [52].

To obtain a guess for the largest allowable time step, we estimate the convection term as follows:

$$\begin{aligned} &\frac{k\rho_f}{4} \int\limits_{\Omega_f^{n+1}} \nabla \cdot w^{n+1} \, |v_f^{n+1} + v_f^n|^2 \, \mathrm{d}x \\ &\leq \frac{k\rho_f}{4} ||\nabla \cdot w^{n+1}||_{L^\infty(\Omega_f^{n+1})} \, ||v_f^{n+1} + v_f^n||^2_{\Omega_f^{n+1}} \\ &\leq k\delta_w \left(||v_f^{n+1}||^2_{\Omega_f^{n+1}} + ||v_f^n||^2_{\Omega_f^{n+1}} \right), \end{aligned}$$

in which we use the Young inequality to estimate the last term. Finally, we set

$$\delta_w := \frac{\rho_f}{2} ||\nabla \cdot w^{n+1}||_{L^\infty(\Omega_f^{n+1})}.$$

From [52, 107], we obtain the largest allowable time step with help of the discrete Gronwall Lemma:

$$k \leq \frac{1}{\delta_w}.$$

Combining this result with the restriction (5.12), which was analyzed in [71, 113], provides us

Lemma 5.2. *Using the ordinary (i.e., unstabilized) Crank-Nicolson scheme leads to the following time step condition for pure fluid problems on moving domains:*

$$k \leq \min \left\{ ch^{2/3}, \frac{1}{\delta_w} \right\}. \tag{5.18}$$

Using the shifted Crank-Nicolson scheme [113], the first condition in (5.18) *can be removed, such that*

$$k \leq \min\left\{k^*, \frac{1}{\delta_w}\right\},$$

with some constant k^* that only depends on the problem.

We mention that the time step restriction induced by the mesh movement seems to be of lower order and it has less influence than the first condition $k \leq ch^{2/3}$. In fact, the authors of [52] state that they were not able to construct cases with blow-up of the solution. This might be due to the fact that the ALE convection term is only defined on a lower-dimensional manifold and not over the whole domain.

The global stability of solutions throughout the whole time interval can be granted with the help of the Lemma 5.2. It is summarized in the Hypothesis 5.5 below and it is substantiated with several numerical tests in Section 5.4.

5.3 Stability of the time-discretized coupled system

We utilize the results of the previous section to analyze the monolithically coupled fluid-structure interaction system. We still work with the time-discretized equations. First, let us recall the basics of stability and energy conservation of time-discretized (linear) structure equations.

Time stability of second-order hyperbolic equations

We recall results (neglecting the damping terms) from the theory [6, 21, 67]:

- *Stability in the L^2-norm:* the One-Step-θ scheme (5.6) is unconditionally stable, i.e., there is no time step restriction on k if and only if $\theta \in [\frac{1}{2}, 1]$.
- *Energy conservation:* the one-step-θ scheme (5.6) preserves energy only for the choice $\theta = \frac{1}{2}$. For $\theta > \frac{1}{2}$ (e.g., the implicit Euler scheme for the choice $\theta = 1$) the scheme dissipates energy.

Consequently, the Crank-Nicolson scheme is an optimal time-stepping scheme for hyperbolic equations. Possible restrictions with respect to the time-step size are weaker for hyperbolic problems than for parabolic differential equations [67]. This finding leads us to the assumption that the fluid problem has stronger influence on stability aspects than the structural problem.

In the following, we consider the stability of the monolithically coupled problem. First, we recall the coupling conditions that are required for an implicit solution algorithm:

$$\begin{aligned} \hat{u}_f^{n+1} = \hat{u}_s^{n+1} \quad \text{on } \widehat{\Gamma}_i, \qquad \hat{w}^{n+1} = \frac{1}{k}(\hat{u}_f^{n+1} - \hat{u}_f^n) \quad \text{in } \widehat{\Omega}_f, \\ 2^{-1}(v_f^{n+1} + v_f^n) = w_f^{n+1} \quad \text{on } \Gamma_i, \qquad \hat{u}_s^{n+1} = 0 \quad \text{on } \widehat{\Gamma}_{s,D}. \end{aligned} \tag{5.19}$$

Using the Crank-Nicolson scheme for temporal discretization, the second relation in (5.19), can be further developed into

$$\hat{w}^{n+1} = \frac{1}{k}(\hat{u}_f^{n+1} - \hat{u}_f^n) = \frac{1}{2}(\hat{v}_f^{n+1} + \hat{v}_f^n). \tag{5.20}$$

Using these coupling conditions with a slight modification of the second term,

$$v_f^{n+1} = w_f^{n+1} \quad \text{on } \Gamma_i,$$

an unconditioned stability (without restrictions on the time-step size) was obtained by Fernández and Gerbeau [48]. In their study, the authors use the backward Euler scheme to discretize the fluid. The structure is discretized using a second-order mid-point rule. In this thesis, we upgrade these findings to a stability result in which the Crank-Nicolson time discretization scheme is performed for the both subproblems. Moreover, we incorporate the damping of the structure equations.

We emphasize, that fluid flows on moving meshes with a Crank-Nicolson time discretization only serve for a conditioned stability (see Lemma 5.1). Consequently, we cannot expect a better result for the overall problem.

We use the Equations (5.9) with the stability result proven in Lemma 5.1. For fluid-structure interaction, we must consider the interface term (we refer to the term (5.15)):

$$-\frac{k}{2}\Big\langle \sigma_f(v_f^{n+1} + v_f^n)n_f, v_f^{n+1} + v_f^n \Big\rangle_{\Gamma_i^{n+1}}. \tag{5.21}$$

The coupling term on the interface that is needed for the next statement reads:

$$\sigma_f(v_f^{n+1} + v_f^n)n_f + \widehat{F}\widehat{\Sigma}(\hat{u}_s^{n+1} + \hat{u}_s^n)\hat{n}_s + \gamma_s\hat{\epsilon}(\hat{v}_s^{n+1} + \hat{v}_s^n)\hat{n}_s = 0. \tag{5.22}$$

Theorem 5.3. *Let the fluid-structure interaction problem be coupled via an implicit solution algorithm and let both subproblems be time-discretized with the second order Crank-Nicolson scheme. The coupled problem is assumed to be isolated, i.e., $v_f^{n+1} = 0$ on $\partial\Omega_f \setminus \Gamma_i$ and $\widehat{F}\widehat{\Sigma}(\hat{u}_s^{n+1})\hat{n}_s = 0$ on $\partial\widehat{\Omega}_s \setminus \widehat{\Gamma}_i$. Further, in the case of strong damping $\gamma_w > 0$, let $\hat{\epsilon}(\hat{v}_s^{n+1})\hat{n}_s = 0$ on $\partial\widehat{\Omega}_s \setminus \widehat{\Gamma}_i$. Then,*

$$\begin{aligned}
&\rho_f||v_f^{n+1}||^2_{\Omega_f^{n+1}} + \hat{\rho}_s||\hat{v}_s^{n+1}||^2_{\widehat{\Omega}_s} + \int_{\widehat{\Omega}_s} W\Big(\widehat{F}(\hat{u}_s^{n+1})\Big)\,\mathrm{d}x \\
&+ k\rho_f\nu_f||D(v_f^{n+1} + v_f^n)||^2_{\Omega_f^{n+1}} + \frac{k\rho_f}{4}\int_{\Omega_f^{n+1}} \nabla\cdot w^{n+1}|v_f^{n+1} + v_f^n|^2\,\mathrm{d}x \\
&+ \frac{k\gamma_w}{2}||\hat{v}_s^{n+1}||^2_{\widehat{\Omega}_s} + \frac{k\gamma_s}{2}||\hat{\epsilon}(\hat{v}_s^{n+1})||^2_E \\
\leq\ &\rho_f||v_f^n||^2_{\Omega_f^{n+1}} + \rho_s||\hat{v}_s^n||^2_{\widehat{\Omega}_s} + \int_{\widehat{\Omega}_s} W(\widehat{F}(\hat{u}_s^n))\,\mathrm{d}x \\
&+ \frac{k\gamma_w}{2}||\hat{v}_s^n||^2_{\widehat{\Omega}_s} + \frac{k\gamma_s}{2}||\hat{\epsilon}(\hat{v}_s^n)||^2_E.
\end{aligned}$$

Proof. The fluid subproblem is attacked with the help of Lemma 5.1 and by taking the test functions $\psi_f^v = \frac{1}{2}(v_f^{n+1} + v_f^n)$ and $\psi_f^p = \frac{1}{2}(p_f^{n+1} + p_f^n)$. With this choice, the following two terms remain on the interface Γ_i:

$$-\frac{k}{2}\Big\langle \sigma_f(v_f^{n+1} + v_f^n)n_f, v_f^{n+1} + v_f^n \Big\rangle_{\Gamma_i^{n+1}},$$
$$\frac{k\rho_f}{4} \int\limits_{\Gamma_i^{n+1}} \Big[(v_f^{n+1} + v_f^n) - w^{n+1}\Big] \cdot n_f |v_f^{n+1} + v_f^n|^2 \,\mathrm{d}x.$$

The first term appears due to integration by parts of the fluid stress term and it becomes part of the coupling condition on Γ_i. The second term is obtained in (5.16) by using partial integration in the convection term. This term vanishes on the interface because we require the coupling condition (see (5.19)):

$$\frac{1}{2}(v_f^{n+1} + v_f^n) - w^{n+1} = 0 \quad \text{on } \Gamma_i^{n+1}.$$

In the following, we consider the structure subproblem 5.5. We take as test functions $\hat{\psi}^v := \hat{\psi}_s^v = \frac{1}{k}(\hat{u}_s^{n+1} - \hat{u}_s^n)$ and $\hat{\psi}^u := \hat{\psi}_s^u = \frac{1}{k}(\hat{v}_s^{n+1} - \hat{v}_s^n)$ in the Equations (5.11). This choice of test functions is admissible, thanks to the coupling conditions (5.19). This choice implies $\hat{\psi}_f^v = \hat{\psi}_s^v$ on $\widehat{\Gamma}_i$, i.e.,

$$\hat{\psi}_s^v = \frac{1}{k}(\hat{u}_s^{n+1} - \hat{u}_s^n) = \frac{1}{2}(\hat{v}_f^{n+1} + \hat{v}_f^n) = \hat{\psi}_f^v.$$

Subtraction of the second equation from the first equation in Problem 5.5 and multiplication through by k leads to

$$\begin{aligned}
&\hat{\rho}_s(\hat{v}_s^{n+1} + \hat{v}_s^n, \hat{v}_s^{n+1} - \hat{v}_s^n)_{\widehat{\Omega}_s} \\
&+ \frac{1}{2}\Big(\widehat{F}\widehat{\Sigma}(\hat{u}_s^{n+1} + \hat{u}_s^n), \widehat{\nabla}(\hat{u}_s^{n+1} - \hat{u}_s^n)\Big)_{\widehat{\Omega}_s} \\
&- \frac{1}{2}\Big\langle \widehat{F}\widehat{\Sigma}(\hat{u}_s^{n+1} + \hat{u}_s^n)\hat{n}_s, \hat{u}_s^{n+1} - \hat{u}_s^n \Big\rangle_{\widehat{\Gamma}_{s,N}} \\
&= 0.
\end{aligned}$$

For the moment, we omit the damping terms. The mass term reads:

$$\hat{\rho}_s ||\hat{v}_s^{n+1}||_{\widehat{\Omega}_s}^2 - \hat{\rho}_s ||\hat{v}_s^n||_{\widehat{\Omega}_s}^2 = 0. \tag{5.23}$$

To treat the stress term, we use

$$\frac{1}{2}\Big(\widehat{F}\widehat{\Sigma}(\hat{u}_s^{n+1} + \hat{u}_s^n), \widehat{\nabla}(\hat{u}_s^{n+1} - \hat{u}_s^n)\Big)_{\widehat{\Omega}_s} = \frac{1}{2}\Big(\widehat{F}\widehat{\Sigma}(\hat{u}_s^{n+1} + \hat{u}_s^n), \widehat{F}(\hat{u}_s^{n+1} - \hat{u}_s^n)\Big)_{\widehat{\Omega}_s}.$$

With this, we proceed as in [48], to deduce:

$$\begin{aligned}
&\frac{1}{2}\Big(\widehat{F}\widehat{\Sigma}(\hat{u}_s^{n+1}+\hat{u}_s^n),\widehat{\nabla}(\hat{u}_s^{n+1}-\hat{u}_s^n)\Big)_{\widehat{\Omega}_s}\\
&=\frac{1}{2}\Big(\partial_F W(\widehat{F}(\hat{u}_s^{n+1}+\hat{u}_s^n)),\widehat{F}(\hat{u}_s^{n+1}-\hat{u}_s^n)\Big)_{\widehat{\Omega}_s}\\
&=\int_{\widehat{\Omega}_s} W\Big(\widehat{F}(\hat{u}_s^{n+1}-\hat{u}_s^n)\Big)\,\mathrm{d}x\\
&=\int_{\widehat{\Omega}_s} W\Big(\widehat{F}(\hat{u}_s^{n+1})\Big)-W\Big(\widehat{F}(\hat{u}_s^n)\Big)\,\mathrm{d}x. \qquad (5.24)
\end{aligned}$$

It remains to discuss the boundary terms. The data on outer boundaries vanish due to our assumption that we work in an isolated system. Thus, it remains to consider the interface term:

$$-\frac{1}{2}\Big\langle\widehat{F}\widehat{\Sigma}(\hat{u}_s^{n+1}+\hat{u}_s^n)\hat{n}_s,\hat{u}_s^{n+1}-\hat{u}_s^n\Big\rangle_{\widehat{\Gamma}_i}. \qquad (5.25)$$

We remind the reader to recall the interface condition that is seen from the fluid side. Now we employ (5.20), such that

$$-\frac{k}{2}\Big\langle\sigma_f(v_f^{n+1}+v_f^n)n_f,v_f^{n+1}+v_f^n\Big\rangle_{\Gamma_i^{n+1}}=-\frac{1}{2}\Big\langle\sigma_f(v_f^{n+1}+v_f^n)n_f,u_f^{n+1}-u_f^n\Big\rangle_{\Gamma_i^{n+1}}. \qquad (5.26)$$

Thus, by adding (5.25) and (5.26), we get

$$-\frac{1}{2}\Big\langle\sigma(v_f^{n+1}+v_f^n)n_f,u_f^{n+1}-u_f^n\Big\rangle_{\Gamma_i^{n+1}}-\frac{1}{2}\Big\langle\widehat{F}\widehat{\Sigma}(\hat{u}_s^{n+1}+\hat{u}_s^n)\hat{n}_s,\hat{u}_s^{n+1}-\hat{u}_s^n\Big\rangle_{\widehat{\Gamma}_i}=0, \qquad (5.27)$$

which corresponds to the already introduced strong form of the coupling conditions (except of the damping interface term). Finally, we consider the damping terms of the structure equations:

$$\frac{\gamma_w}{2}\Big(\hat{v}_s^{n+1}+\hat{v}_s^n,\hat{\psi}^v\Big)_{\widehat{\Omega}_s}+\frac{\gamma_s}{2}\Big(\hat{\epsilon}(\hat{v}_s^{n+1}+\hat{v}_s^n),\widehat{\nabla}\hat{\psi}^v\Big)_{\widehat{\Omega}_s}-\frac{\gamma_s}{2}\Big(\hat{\epsilon}(\hat{v}_s^{n+1}+\hat{v}_s^n)\hat{n}_s,\hat{\psi}^v\Big)_{\widehat{\Gamma}_{s,N}}=0.$$

Taking again $\hat{\psi}_s^v=\frac{1}{k}(\hat{u}_s^{n+1}-\hat{u}_s^n)$ yields:

$$\frac{\gamma_w}{2}\Big(\hat{v}_s^{n+1}+\hat{v}_s^n,\hat{u}_s^{n+1}-\hat{u}_s^n\Big)_{\widehat{\Omega}_s}+\frac{\gamma_s}{2}\Big(\hat{\epsilon}(\hat{v}_s^{n+1}+\hat{v}_s^n),\widehat{\nabla}(\hat{u}_s^{n+1}-\hat{u}_s^n)\Big)_{\widehat{\Omega}_s}=0.$$

Estimating the both terms by using the relation between the velocities and the displacements (i.e., (5.15)):

$$\frac{\hat{u}_s^{n+1}-\hat{u}_s^n}{k}=\frac{1}{2}(\hat{v}_s^{n+1}+\hat{v}_s^n),$$

yields for the first term (using the Young inequality):

$$\begin{aligned}
&\frac{\gamma_w}{2}(\hat{v}_s^{n+1}+\hat{v}_s^n, \hat{u}_s^{n+1}-\hat{u}_s^n)_{\widehat{\Omega}_s} \\
&= \frac{k\gamma_w}{4}(\hat{v}_s^{n+1}+\hat{v}_s^n, \hat{v}_s^{n+1}+\hat{v}_s^n)_{\widehat{\Omega}_s} \\
&= \frac{k\gamma_w}{4}||\hat{v}_s^{n+1}+\hat{v}_s^n||^2_{\widehat{\Omega}_s} \\
&\leq \frac{k\gamma_w}{2}(||\hat{v}_s^{n+1}||^2_{\widehat{\Omega}_s}+||\hat{v}_s^n||^2_{\widehat{\Omega}_s}).
\end{aligned} \tag{5.28}$$

The second term is treated in a similar fashion by using the definition of the energy norm (3.17):

$$\begin{aligned}
&\frac{\gamma_s}{2}\Big(\hat{\epsilon}(\hat{v}_s^{n+1}+\hat{v}_s^n), \widehat{\nabla}(\hat{u}_s^{n+1}-\hat{u}_s^n)\Big)_{\widehat{\Omega}_s} \\
&= \frac{k\gamma_s}{4}\Big(\hat{\epsilon}(\hat{v}_s^{n+1}+\hat{v}_s^n), \widehat{\nabla}(\hat{v}_s^{n+1}+\hat{v}_s^n)\Big)_{\widehat{\Omega}_s} \\
&= \frac{k\gamma_s}{4}||\hat{\epsilon}(\hat{v}_s^{n+1}+\hat{v}_s^n)||^2_E \\
&\leq \frac{k\gamma_s}{2}(||\hat{\epsilon}(\hat{v}_s^{n+1})||^2_E+||\hat{\epsilon}(\hat{v}_s^n)||^2_E).
\end{aligned} \tag{5.29}$$

It remains to discuss the interface term of strong damping on $\widehat{\Gamma}_i$:

$$-\gamma_s\frac{1}{2}\Big\langle\hat{\epsilon}(\hat{v}_s^{n+1}+\hat{v}_s^n)\hat{n}_s, \hat{u}_s^{n+1}-\hat{u}_s^n\Big\rangle_{\widehat{\Gamma}_i}.$$

Together with (5.27), this gives immediately the interface condition for the balance of the coupling (see Equation (5.22)). By adding (5.23), (5.24), (5.28), (5.29), with Lemma 5.1, we achieve the desired result. □

In a similar way as already illustrated for the continuous case (see Theorem 3.3 and Corollary 3.4), we derive from Theorem 5.3 an adequate result for damping in an artificial domain. Thus, we formulate the stress coupling conditions on $\widehat{\Gamma}_i^{\text{in}} = \widehat{\Omega}_s^{\text{phys}} \cap \widehat{\Omega}_s^{\text{ext}}$:

$$\widehat{F}\widehat{\Sigma}_s(\hat{u}_s^{n+1}+\hat{u}_s^n)\hat{n}_s = \widehat{F}\widehat{\Sigma}_s^{\text{ext}}(\hat{u}_s^{n+1}+\hat{u}_s^n)\hat{n}_s^{\text{ext}} + \gamma_s\hat{\epsilon}_s(\hat{v}_s^{n+1}+\hat{v}_s^n)\hat{n}_s^{\text{ext}} \quad \text{on } \widehat{\Gamma}_i^{\text{in}}. \tag{5.30}$$

Corollary 5.4. *Let the assumptions hold of Theorem 5.3. In addition, we divide the structural subdomain into a physical domain and an artificial domain:* $\widehat{\Omega}_s = \widehat{\Omega}_s^{phys} \cup \widehat{\Omega}_s^{ext}$. *The damping terms are only employed in* $\widehat{\Omega}_s^{ext}$, *i.e.,* $\gamma_w = \gamma_s = 0$ *in* $\widehat{\Omega}_s^{phys}$ *and* $\gamma_w > 0$, $\gamma_s > 0$ *in* $\widehat{\Omega}_s^{ext}$. *If* (5.30) *holds true, then*

$$
\begin{aligned}
&\rho_f ||v_f^{n+1}||^2_{\Omega_f^{n+1}} + \hat{\rho}_s ||\hat{v}_s^{n+1}||^2_{\widehat{\Omega}_s \cup \widehat{\Omega}_s^{ext}} + \int\limits_{\widehat{\Omega}_s \cup \widehat{\Omega}_s^{ext}} W\Big(\widehat{F}(\hat{u}_s^{n+1})\Big)\,\mathrm{d}x \\
&+ k\rho_f \nu_f ||D(v_f^{n+1} + v_f^n)||^2_{\Omega_f^{n+1}} + \frac{k\rho_f}{4} \int\limits_{\Omega_f^{n+1}} \nabla \cdot w^{n+1} |v_f^{n+1} + v_f^n|^2\,\mathrm{d}x \\
&+ \frac{k\gamma_w}{2} ||\hat{v}_s^{n+1}||^2_{\widehat{\Omega}_s^{ext}} + \frac{k\gamma_s}{2} ||\hat{\epsilon}(\hat{v}_s^{n+1})||^2_E \\
\leq\ & \rho_f ||v_f^n||^2_{\Omega_f^{n+1}} + \rho_s ||\hat{v}_s^n||^2_{\widehat{\Omega}_s \cup \widehat{\Omega}_s^{ext}} + \int\limits_{\widehat{\Omega}_s \cup \widehat{\Omega}_s^{ext}} W(\widehat{F}(\hat{u}_s^n))\,\mathrm{d}x \\
&+ \frac{k\gamma_w}{2} ||\hat{v}_s^n||^2_{\widehat{\Omega}_s^{ext}} + \frac{k\gamma_s}{2} ||\hat{\epsilon}(\hat{v}_s^n)||^2_E,
\end{aligned}
$$

Comparing Lemma 5.1 and Theorem 5.3, we notice that global stability of solutions depends only on the uncertainty of the ALE convection term. We draw the following conclusion from our previous findings:

Hypothesis 5.5 (Stable long-term computations of FSI problems). *Numerically stable long-term computations of fluid-structure interaction can be computed by (at least) strictly A-stable time-stepping schemes (such as the shifted Crank-Nicolson scheme and the Fractional-Step-θ scheme) provided that the time step* k *is restricted by*

$$k \leq \frac{1}{\delta_w}$$

as shown in Lemma 5.2.

It is obvious that we are interested in the simulation of fully nonstationary fluid-structure interactions. In fact, we could use the strongly A-stable implicit Euler scheme for numerical simulations, which yields a global stability result for the coupled problem [48]. However, this scheme is not appropriate for the simulation of dynamic processes because it introduces numerical diffusion for large time steps k.

Finally, we notice that the fluid domain velocity is bounded by the fluid velocity. In Ω_f, we estimate

$$||w_{\mathrm{dom}}||_{H^1(\Omega_f)} \leq c||w||_{H^1(\Omega_f)} \leq c||w||_{H^{1/2}(\Gamma_i)} = c||v_f||_{H^{1/2}(\Gamma_i)} \leq c||v_f||_{H^1(\Omega_f)},$$

where c is some constant. The variable w_{dom} explicitly denotes the fluid domain velocity, and w is its extension with the help of the structure velocity on Γ_i (solved by one of the mesh motion models). In the first estimate, we use the stability of w, and we employ the

inverse theorem (see, e.g., [152]) with sufficient conditions on the domain. The coupling condition is given by $v_f = w$ on Γ_i; and finally we employ the trace inequality. This observation is important to note because an unbounded (or infinitely high) velocity to move the fluid mesh would not make sense.

5.4 Numerical observations for long-term FSI computations

In this section, we first explain the different time discretization techniques for the ALE convection term. After these considerations, we substantiate the findings of the previous two sections with numerical tests. Specifically, we are interested in the following:

- The identification of the influence of the ALE convection term using different time discretizations. First, we consider a discretization that implicitly uses the fluid domain velocity of $\frac{1}{k}(\hat{u}_f^{n+1} - \hat{u}_f^n)$. Second, we use an explicit version (and discretization) of the fluid domain velocity, i.e., $\hat{w}^{n+1} = \frac{1}{k}(\hat{u}_f^{n+1} - \hat{u}_f^n)$.
- The detection of instabilities (or even the blow-up of solutions in finite time) for the ordinary (i.e., unstabilized) Crank-Nicolson scheme. If we observe any, we are able to resolve them using the aforementioned techniques, i.e., Hypothesis 5.5, or by the choice of a sufficiently small time step.
- Finally, we compare the standard second-order time-stepping schemes for the simulation of nonstationary fluid flows/fluid-structure interactions such as the Crank-Nicolson scheme, the shifted Crank-Nicolson scheme, and the Fractional-Step-θ scheme.

5.4.1 Discretization techniques for the ALE convection term

In this chapter, we discuss possible temporal discretizations of the ALE convection term. From Problem 3.1, we extract

$$(v_f - w) \cdot \nabla v_f = v_f \cdot \nabla v_f - w \cdot \nabla v_f \quad \text{in } \Omega_f.$$

We remind the reader that the GCL condition for two dimensional problems is fulfilled for the backward Euler scheme and the Crank-Nicolson scheme [51, 52], when the ALE mapping is a piecewise linear in time interpolation. This means, we consider linear interpolation of the domain movement in the time interval $I_n = [t_n, t_{n+1}]$:

$$u_f(t) = u_f^{n+1} \frac{(t - t_n)}{k} - u_f^n \frac{(t - t_{n+1})}{k},$$

with the mesh velocity that is constant in time:

$$w := w(t) = \frac{u_f^{n+1} - u_f^n}{k}.$$

Our goal is to monitor the numerical solution for long-term computations and different types of discretization of the ALE convection term. In detail, we consider the following different time discretizations of the ALE convection term. The first variant is simply the unstabilized Crank-Nicolson scheme, where the standard convection is discretized with the (secant) Crank-Nicolson scheme. In the second version, the secant Crank-Nicolson is used for the full ALE convection term. The third variant makes use of the tangent Crank-Nicolson scheme, which is often used for theoretical analysis [115]. Moreover, we run computations with the first variant and using the Fractional-Step-θ scheme. In detail, we present

Problem 5.6 (Secant $CN(v)$).

$$\theta v_f \cdot \nabla v_f + (1-\theta) v_f^{n-1} \cdot \nabla v_f^{n-1} - k^{-1}(u_f - u_f^{n-1}) \cdot \nabla v_f, \tag{5.31}$$

with $\theta = 0.5$ *or* $\theta = 0.5 + k_n$.

Problem 5.7 (Secant $CN(vw)$).

$$\theta v_f \cdot \nabla v_f + (1-\theta) v_f^{n-1} \cdot \nabla v_f^{n-1} - \theta w \cdot \nabla v_f - (1-\theta) w^{n-1} \cdot \nabla v_f^{n-1}, \tag{5.32}$$

with $\theta = 0.5$ *or* $\theta = 0.5 + k_n$.

Problem 5.8 (Tangent $CN(vw)$).

$$\theta(v_f + v_f^{n-1}) \cdot \nabla\theta(v_f + v_f^{n-1}) - \theta(w + w^{n-1}) \cdot \nabla\theta(v_f + v_f^{n-1})$$

with $\theta = 0.5$.

The tangential scheme is used for a stability and accuracy analysis for pure fluid problems [71]. This scheme is slightly more stable than the secant Crank-Nicolson scheme [115], which we also observed in our numerical tests (see the top of Figure 5.4).

However, we expect no significant differences between these three discretization techniques of the ALE convection term because all of them belong to the same class of time-stepping schemes.

5.4.2 Numerical tests and observations

The following conclusions were obtained by studying the fluid-structure interaction benchmark test FSI 2 [84]. The configuration is presented in Section 8.2. To detect numerical artefacts is a delicate task, therefore, we study (qualitative) convergence with respect to space and time on three different (globally-refined) mesh levels with 1914, 7176 and 27744 degrees of freedom using the Q_2^c/P_1^{dc} element (which is introduced in the next section). Moreover, we use three different time levels with the time steps $k = 0.01, 0.005$ and 0.001. It is sufficient to study the results for the drag evaluation because we observed the same qualitative behavior for all the four quantities of interest (the x- and the y-displacement, the drag, and the lift).

Observation 1

We detected differences in the transient oscillation of all the different time-stepping schemes, as illustrated in Figure 5.3. Specifically, the unstabilized CN scheme with vw ALE discretization has a smaller transient oscillation for the large time step $k = 0.01$ but approaches the other schemes when the time step is reduced. Indeed, we also observed that numerical artefacts appears earlier when working with the secant Crank-Nicolson scheme than working with the tangential method.

Observation 2

Second, we observed in our computations that there are only minor differences in the drag evaluation computed with the unstabilized Crank-Nicolson scheme using the different ALE convection term discretizations defined in the problems above. Specifically, we observed unstable behavior (blow-up) for computations over long-term intervals, as illustrated in Figure 5.4. Naturally, we expected this behavior from our previous numerical analysis.

Observation 3

As expected, the shifted Crank-Nicolson scheme and the Fractional-Step-θ scheme showed no stability problems in long-term computations, even for the large time step $k = 0.01$ (see the top of Figure 5.5). This result indicates that the instabilities induced by the ALE convection term have minor consequences, and our observation is in agreement with the statement in [52]. Furthermore, all time-stepping schemes are stable over the entire time interval for a sufficiently small time step $k = 0.001$; (see the bottom Figure 5.5). Consequently, we were able to find a suitable bound such that the requirements of Lemma 5.2 are satisfied.

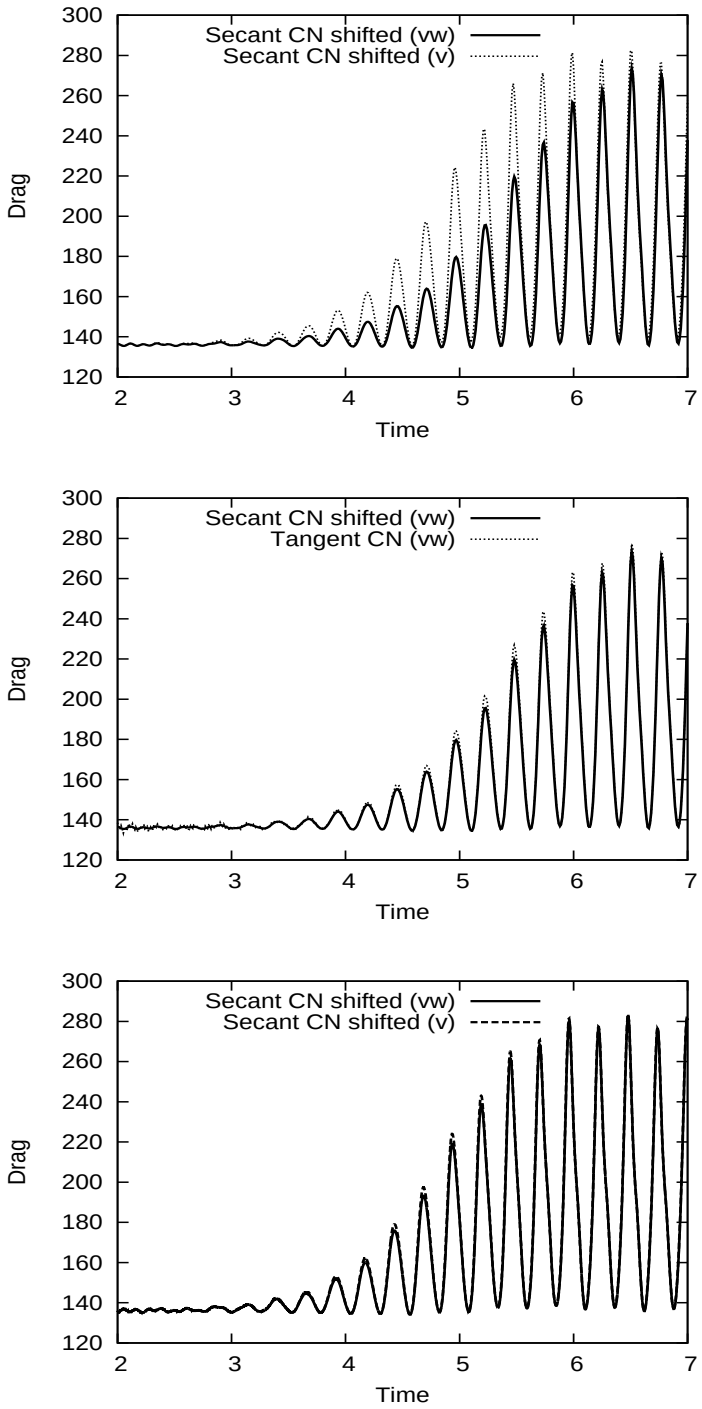

Figure 5.3. Top and middle: we observe for the time step $k = 0.01$ different transient oscillations of the three time-stepping schemes. Bottom: the transient oscillation almost coincides for the smaller time step $k = 0.001$. The unit of the time axis is s, whereas the drag unit is $kg/m\,s^2$.

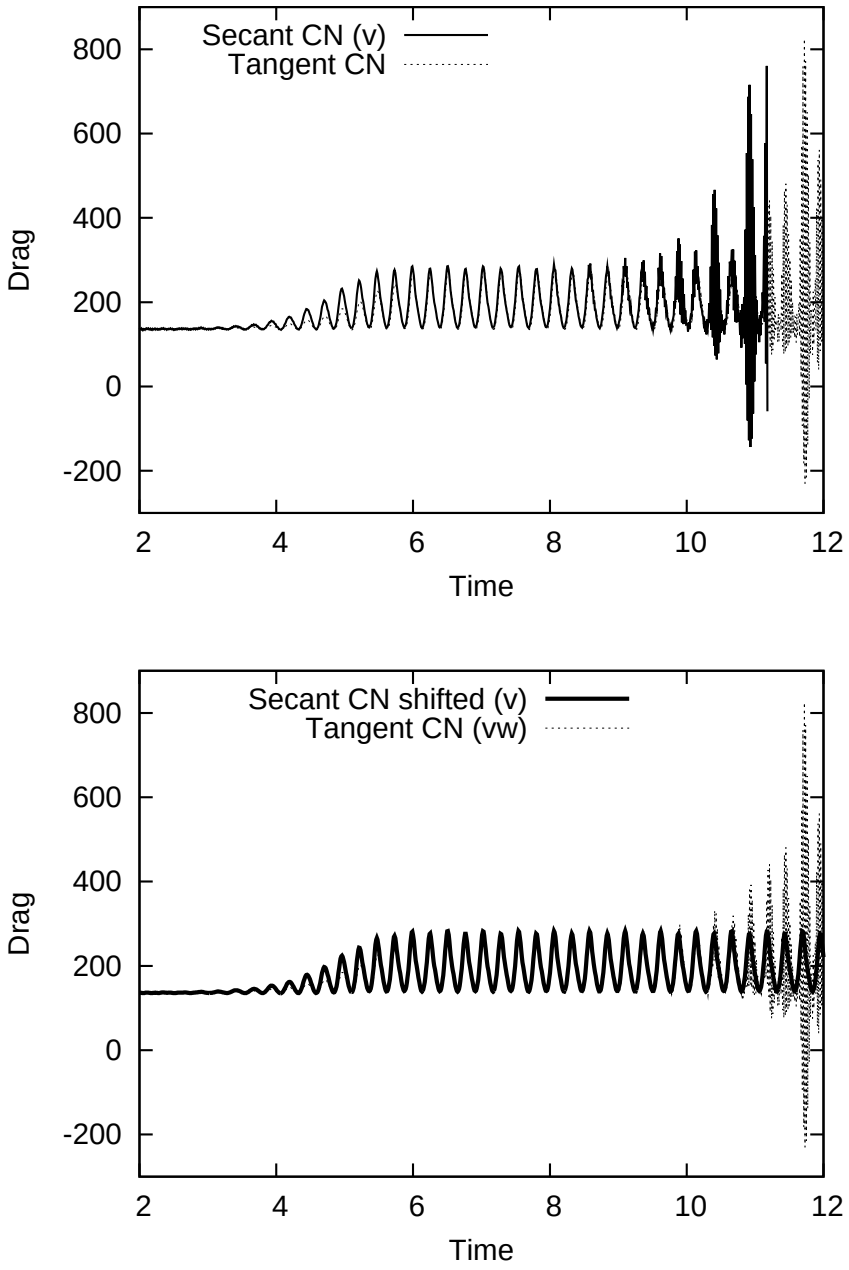

Figure 5.4. Blow-up (using the time step $k = 0.01$) of the unstabilized Crank-Nicolson schemes (secant and tangent) whereas the shifted Crank-Nicolson schemes is stable throughout the whole time interval. We notice that the secant Crank-Nicolson scheme exhibits the instabilities earlier than the tangent version. The unit of the time axis is s, whereas the drag unit is $kg/m\,s^2$.

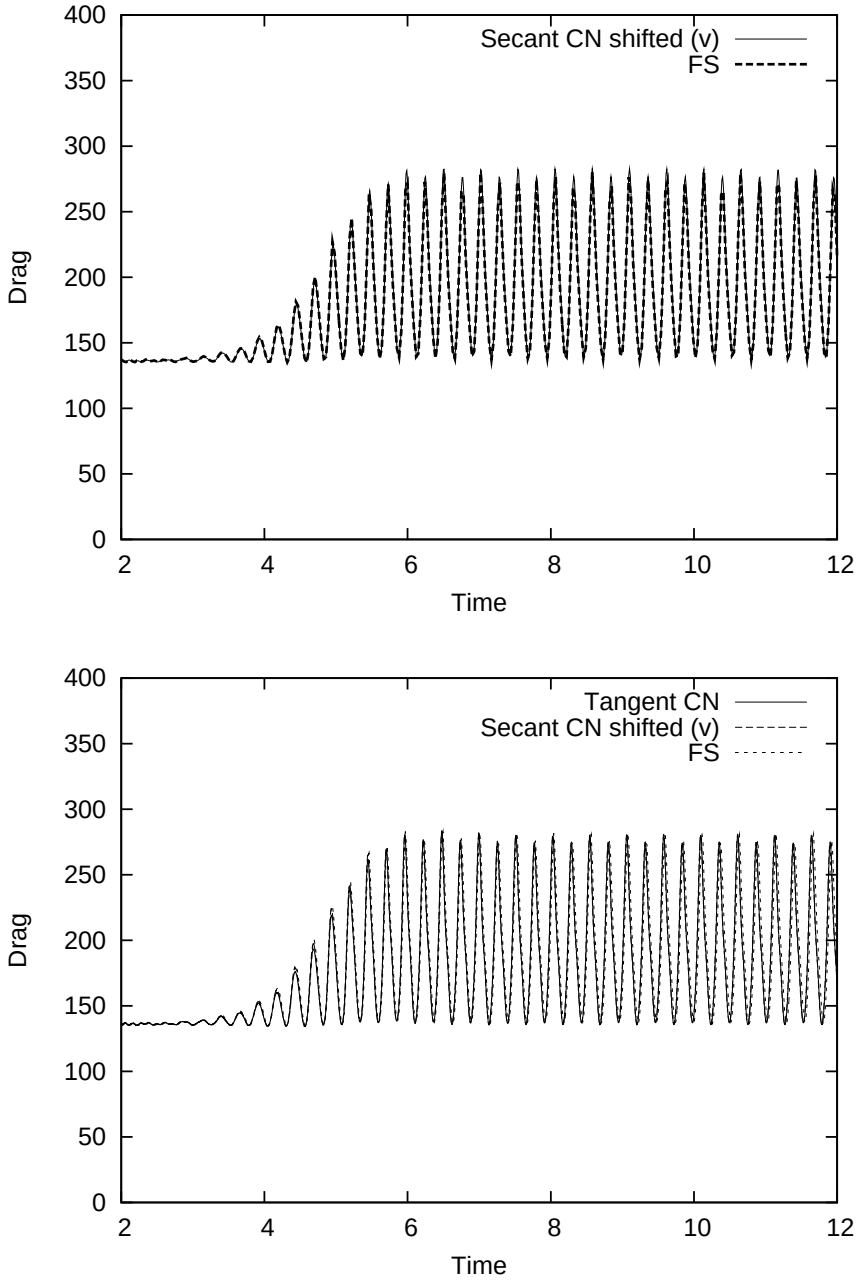

Figure 5.5. Top: stable solution (using the large time step $k = 0.01$) computed with the shifted Crank-Nicolson and the Fractional-Step-θ scheme. Recall the blow-up of the unstabilized Crank-Nicolson scheme in this case. Bottom: using the smaller time step $k = 0.001$ yields stable solutions for any time-stepping scheme. The unit of the time axis is s, whereas the drag unit is $kg/m\,s^2$.

5.5 Spatial discretization

The time-discretized equations are the starting point for a finite element Galerkin discretization method in space. So far, the equations still contain the continuous spatial spaces $\hat{V}, \hat{V}^0$ and $\hat{L}^0$, etc. In the following, we discuss the spatial discretization of the semi-discrete problems obtained in the previous section. To this end, we construct finite dimensional subspaces $\hat{V}_h \subset \hat{V}$, $\hat{V}_h^0 \subset \hat{V}^0$, $\hat{L}_h^0 \subset \hat{L}^0$, etc., of piecewise polynomial functions up to order l. The spatial terms are computed in a fixed reference configuration. This is the advantage of *practicable* fluid-structure interaction because it can be directly employed in a programming code.

5.5.1 Finite element spaces

The computational domain $\widehat{\Omega}$ is partitioned into open cells $\hat{K}$ that depend on the spatial dimension d. A mesh consists of quadrilateral or hexahedron cells $\hat{K}$. They perform a non-overlapping cover of the computation domain $\widehat{\Omega} \subset \mathbb{R}^d$, $d = 2, 3$. The mesh $\hat{\mathcal{T}}_h = \{\hat{K}\}$ of $\widehat{\Omega}$ is formed by taking all cells. The cell parameter $\hat{h}$ is given as a cell-wise constant function $\hat{h}_K := \operatorname{diam}(\hat{K})$ (where $\operatorname{diam}(\hat{K})$ denotes the diameter $\hat{h}_K$ of a cell $\hat{K}$). The maximum diameter is denoted by $\hat{h} := \max_{\hat{K} \in \hat{\mathcal{T}}_h} \hat{h}_k$.

We follow the standard literature ([26, 27, 34]) to formulate the following statements:

Definition 5.1 (Regularity). *A mesh $\hat{\mathcal{T}}_h = \{\hat{K}\}$ is called regular if the following conditions are fulfilled:*

1) $\overline{\widehat{\Omega}} = \bigcup_{\hat{K} \in \hat{\mathcal{T}}_h} \overline{\hat{K}}$.

2) $\hat{K}_1 \cap \hat{K}_2 = \emptyset$ *for all cells* $\hat{K}_1, \hat{K}_2 \in \hat{\mathcal{T}}_h$ *with* $\hat{K}_1 \neq \hat{K}_2$.

3) Any face of any cell $\hat{K}_1 \in \hat{\mathcal{T}}_h$ *is either a subset of the boundary* $\partial\widehat{\Omega}$ *or a face of another cell* $\hat{K}_2 \in \hat{\mathcal{T}}_h$.

The last condition is too restrictive for our purposes and is weakened for the following reason. To facilitate adaptive mesh refinement and to avoid connecting elements, we use the concept of *hanging nodes*. Cells are allowed to have nodes that lie on the midpoints of the faces or edges of neighboring cells. At most, one hanging node is allowed on each face or edge. In three dimensions, this concept is generalized to subplanes and faces because we must deal with two types of lower manifolds.

We define continuous H^1-conforming finite element spaces $\hat{V}_h^l$ by (see [27, 34, 91]):

$$\hat{V}_h^l := \left\{ \hat{v}_h \in C(\overline{\widehat{\Omega}}) | \quad \hat{v}_h|_{\hat{K}} \in \mathcal{Q}(\hat{K}) \quad \forall \hat{K} \in \hat{\mathcal{T}}_h \right\} \subseteq H^1(\widehat{\Omega}).$$

Here, $\mathcal{Q}(\hat{K})$ denotes the space of polynomial-like functions on $\hat{K} \in \hat{\mathcal{T}}_h$. In the following, we introduce the space $\mathcal{Q}_l(\hat{K})$ of tensor product polynomials up to degree l. On the reference cell $\hat{K}_{\text{unit}} = (0,1)^d$ they are defined as

$$\hat{\mathcal{Q}}_l(\hat{K}_{\text{unit}}) := \text{span}\left\{ \prod_{i=1}^{d} \hat{x}_i^{\alpha_i} |\, \alpha_i \in \{0,1,\ldots,l\} \right\}.$$

We consider for each $\hat{K} \in \hat{\mathcal{T}}_h$ the bilinear transformation $\hat{\sigma}_K : \hat{K}_{\text{unit}} \to \hat{K}$. Then, the Q_1^c element is defined as

$$\begin{aligned} Q_1^c(\hat{K}) &= \{\hat{q} \circ \hat{\sigma}_K^{-1} : \hat{q} \in \text{span} < 1, \hat{x}, \hat{y}, \hat{x}\hat{y} >\} && (d=2), \\ Q_1^c(\hat{K}) &= \{\hat{q} \circ \hat{\sigma}_K^{-1} : \hat{q} \in \text{span} < 1, \hat{x}, \hat{y}, \hat{z}, \hat{x}\hat{y}, \hat{x}\hat{z}, \hat{y}\hat{z}, \hat{x}\hat{y}\hat{z} >\} && (d=3), \end{aligned}$$

with dim $Q_1^c = 4$ (in 2D) and $Q_1^c = 8$ (in 3D) in which the dimension denotes the local degrees of freedom on a single cell. The Q_2^c element (in two dimensions) is defined as

$$Q_2^c(\hat{K}) = \{\hat{q} \circ \hat{\sigma}_K^{-1} : \hat{q} \in \text{span} < 1, \hat{x}, \hat{y}, \hat{x}\hat{y}, \hat{x}^2, \hat{y}^2, \hat{x}^2\hat{y}, \hat{y}^2\hat{x}, \hat{x}^2\hat{y}^2 >\},$$

with dim $Q_2^c = 9$. Finally, the P_1^{dc} element is defined with the help of linear functions and it reads

$$P_1^{dc}(\hat{K}) = \{\hat{q} \circ \hat{\sigma}_K^{-1} : \hat{q} \in \text{span}, < 1, \hat{x}, \hat{y} >\}$$

with dim $P_1^{dc}(\hat{K}) = 3$. If the transformation $\hat{\sigma}_K$ itself is an element of $\hat{\mathcal{Q}}_l(\hat{K})^d$, the corresponding finite element space is called *isoparametric*.

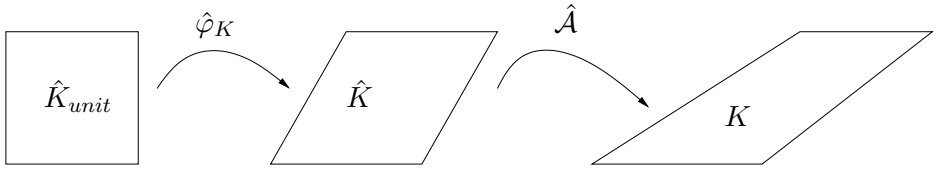

Figure 5.6. Transformation $\hat{\varphi}_K$ from the unit cell $\hat{K}_{unit}$ to the ALE cell $\hat{K}$ and from that cell via the ALE mapping $\hat{\mathcal{A}}$ to the physical cell K.

Extending these concepts to finite element spaces in the case of hanging nodes requires some remarks. To enforce global continuity (i.e., global conformity), the degrees of freedom located on the interface between different refinement levels have to satisfy additional constraints. They are determined by interpolation of neighboring degrees of freedom. Therefore, hanging nodes do not carry any degrees of freedom. For more details on this, we refer to [31].

To ensure the approximation properties of the finite element spaces, additional conditions on the geometry of the cells are required. The two classical assumptions from the literature ([26, 27]) are the so-called *uniformity* and the weaker *quasi-uniformity*:

Definition 5.2 (Quasi-Uniformity). *A family of meshes* $\{\hat{\mathcal{T}}_h | h \searrow 0\}$ *is called quasi-uniform if there is a constant* κ *such that the following two conditions are fulfilled:*

1) For each transformation $\widehat{\sigma}_K : \hat{K}_{unit} \to \hat{K}$ *it holds*

$$\frac{\sup\{||\nabla\widehat{\sigma}_K(\hat{x})\hat{x}||\ |\hat{x} \in \hat{K},\ ||\hat{x}|| = 1\}}{\inf\{||\nabla\widehat{\sigma}_K(\hat{x})\hat{x}||\ |\hat{x} \in \hat{K},\ ||\hat{x}|| = 1\}} \leq \kappa, \qquad \hat{K} \in \bigcup_h \hat{\mathcal{T}}_h. \tag{5.33}$$

2) It holds

$$\frac{\hat{h}_K}{\hat{\rho}_K} \leq \kappa \quad \forall \hat{K} \in \bigcup_h \hat{\mathcal{T}}_h.$$

5.5.2 Finite elements for fluid-structure interactions

To compute fluid-structure interactions problems, we prefer the biquadratic, discontinuous-linear Q_2^c/P_1^{dc} element. The continuity of the velocity values across different mesh cells is one property of the Q_2^c/P_1^{dc} element. In contrast, the pressure is allowed to be discontinuous across faces because it is defined utilizing discontinuous test functions. In addition, this element preserves local mass conservation, is of low order, gains the *inf-sup stability*, and it is therefore an optimal choice for both fluid problems and fluid-structure interaction problems. Because there is no relationship between fluid and structure pressure (beyond the fact that there is no physical meaning of pressure for compressible materials), the Q_2^c/P_1^{dc} is a good choice for fluid-structure interactions. In addition, using discontinuous pressure elements facilitates the extension to multiple structure systems because the different structure pressures can be computed independently.

Bearing the three mesh motion models in mind, the computation of fluid-structure interaction with biharmonic mesh motion incurs a greater computational cost at each time step than using only a harmonic model or the equations of linear elasticity because an additional equation is added to the problem (see Problem 3.7). In the context of a Galerkin finite element scheme, the spatial discretization of the mixed biharmonic equation is stable for equal-order discretization on polygonal domains, which is one of our assumptions. In this thesis, we work with Q_2^c elements for $\hat{u}_h$ and $\hat{\eta}_h$.

For the next statement, let $\hat{v}_{f,h}^D$, $\hat{u}_{f,h}^D$, and $\hat{v}_{s,h}^D$ be suitable extensions of Dirichlet inflow data. Having these preparations, the spatially (and temporal) discretized problem of (5.1) reads:

Problem 5.9. *Let the semi-linear form be composed as shown in Problem 5.2. Find* $\hat{U}_h^n = \{\hat{v}_{f,h}^n, \hat{v}_{s,h}^n, \hat{u}_{f,h}^n, \hat{u}_{s,h}^n, \hat{p}_{f,h}^n, \hat{p}_{s,h}^n\} \in \widehat{X}_{h,D}^0$*, where* $\widehat{X}_{h,D}^0 := \{\hat{v}_{f,h}^D + \hat{V}_{f,\hat{v},h}^0\} \times \hat{L}_{s,h} \times \{\hat{u}_{f,h}^D + \hat{V}_{f,\hat{u},h}^0\} \times \{\hat{u}_{s,h}^D + \hat{V}_{s,h}^0\} \times \hat{L}_{f,h}^0 \times \hat{L}_{s,h}^0$*, for all* $n = 1, 2, \ldots, N$ *such that*

$$\hat{A}(\hat{U}_h^n)(\hat{\Psi}_h) = \widehat{F}(\hat{\Psi}_h) \quad \forall \hat{\Psi}_h \in \widehat{X}_h,$$

with $\hat{\Psi}_h = \{\hat{\psi}_{f,h}^v, \hat{\psi}_{s,h}^v, \hat{\psi}_{f,h}^u, \hat{\psi}_{s,h}^u, \hat{\psi}_{f,h}^p, \hat{\psi}_{s,h}^p\}$ *and* $\widehat{X}_h = \hat{V}_{f,\hat{v},h}^0 \times \hat{L}_{s,h} \times \hat{V}_{f,\hat{u},\widehat{\Gamma}_i,h}^0 \times \hat{V}_{s,h}^0 \times \hat{L}_{f,h}^0 \times \hat{L}_{s,h}^0$.

5.5.3 Stabilization for convection-dominated flows

In the case of higher Reynolds numbers (such as blood flow at the exit of the aortic valve with Reynolds number of ~ 4500 [56]) the flow becomes convection dominated and needs to be stabilized. Residual based stabilization is first introduced in Brooks and Hughes [28] and is intensively analyzed in Wall [143]. Our method of choice is a rough simplification of the streamline upwind Petrov-Galerkin (SUPG) method.

We start with a consistent formulation for the fluid problem that is given on the continuous level in a time-dependent domain Ω_f (see Equation (3.1)). Then, the stabilization term reads (in which we omit for the moment the subscripts 'h' and 'n' in the equations):

$$S_{\text{stab}}(U_h^n)(\Psi) := \sum_{K\in\mathcal{T}_h} (\rho_f \hat{\partial}_t v_f + \rho_f (v_f - w)\cdot\nabla v_f - \text{div}\sigma_f, \delta_{K,n}(v_f\cdot\nabla)\psi_f^v)_K$$

with

$$\delta_{K,n} = \delta_0 \frac{h_K^2}{6\nu_f + h_K ||v_h^n||_K}, \quad \delta_0 = 0.1.$$

For more details on the choice of these parameters, we refer the reader to [25].

From the computational point of view, the major disadvantage comes from the necessity of computing second derivatives contained in the stress tensor σ_f, because we must consider the strong formulation. Specifically, in the case of fluid-structure interaction problems, this formulation is a serious drawback. To this end, we only use a nonconsistent simplified version (in Ω_f):

$$S_{\text{stab}}(U_h^n)(\Psi) := \sum_{K\in\mathcal{T}_h} (\rho_f v_f\cdot\nabla v_f, \delta_{K,n}(v_f\cdot\nabla)\psi_f^v)_K.$$

This term can be rewritten in the reference configuration $\widehat{\Omega}_f$ and reads:

$$\hat{S}_{\text{stab}}(\hat{U}_h^n)(\hat{\Psi}) := \sum_{\widehat{K}\in\mathcal{T}_h} (\hat{\rho}_f(\hat{J}\widehat{F}^{-1}\hat{v}_f\cdot\widehat{\nabla})\hat{v}_f, \delta_{K,n}(\widehat{F}^{-1}\hat{v}_f\cdot\widehat{\nabla})\hat{\psi}_f^v)_{\widehat{K}}. \tag{5.34}$$

Remark 5.4. The previous introduced stabilization term was used in this thesis for the numerical simulation of the nonstationary heart-valve dynamics (see Example 8.4). The fluid-structure benchmark test FSI 2 and FSI 3 (see Example 8.2) were computed without using stabilization techniques.

Problem 5.10. *Let the semi-linear form be composed as shown in Problem 5.2. Find* $\hat{U}_h^n = \{\hat{v}_{f,h}^n, \hat{v}_{s,h}^n, \hat{u}_{f,h}^n, \hat{u}_{s,h}^n, \hat{p}_{f,h}^n, \hat{p}_{s,h}^n\} \in \widehat{X}_{h,D}^0$, *where* $\widehat{X}_{h,D}^0 := \{\hat{v}_{f,h}^D + \hat{V}_{f,\hat{v},h}^0\} \times \hat{L}_{s,h} \times \{\hat{u}_{f,h}^D + \hat{V}_{f,\hat{u},h}^0\} \times \{\hat{u}_{s,h}^D + \hat{V}_{s,h}^0\} \times \hat{L}_{f,h}^0 \times \hat{L}_{s,h}^0$, *for all* $n = 1, 2, \ldots, N$ *such that*

$$\hat{A}(\hat{U}_h^n)(\hat{\Psi}_h) + \hat{S}_{stab}(\hat{U}_h^n)(\hat{\Psi}) = \widehat{F}(\hat{\Psi}_h) \quad \forall \hat{\Psi}_h \in \widehat{X}_h,$$

with $\hat{\Psi}_h = \{\hat{\psi}_{f,h}^v, \hat{\psi}_{s,h}^v, \hat{\psi}_{f,h}^u, \hat{\psi}_{s,h}^u, \hat{\psi}_{f,h}^p, \hat{\psi}_{s,h}^p\}$ *and* $\widehat{X}_h = \hat{V}_{f,\hat{v},h}^0 \times \hat{L}_{s,h} \times \hat{V}_{f,\hat{u},\widehat{\Gamma}_i,h}^0 \times \hat{V}_{s,h}^0 \times \hat{L}_{f,h}^0 \times \hat{L}_{s,h}^0$.

5.6 Linearization with Newton's method

Time and spatial discretization end at each single time step in a nonlinear quasi-stationary problem

$$\hat{A}(\hat{U}_h^n)(\hat{\Psi}) = \hat{F}(\hat{\Psi}) \quad \forall \hat{\Psi} \in \hat{X}_h,$$

which is solved with a Newton-like method. Given an initial Newton guess $\hat{U}_h^{n,0}$, find for $j = 0, 1, 2, \ldots$ the update $\delta\hat{U}_h^n$ of the linear defect-correction problem

$$\begin{aligned} \hat{A}'(\hat{U}_h^{n,j})(\delta\hat{U}_h^n, \hat{\Psi}) &= -\hat{A}(\hat{U}_h^{n,j})(\hat{\Psi}) + \widehat{F}(\hat{\Psi}), \\ \hat{U}_h^{n,j+1} &= \hat{U}_h^{n,j} + \lambda\delta\hat{U}_h^n. \end{aligned} \tag{5.35}$$

In this algorithm, $\lambda \in (0, 1]$ is used as damping parameter for line search iterations. A crucial role for (highly) nonlinear problems includes the appropriate determination of λ. A simple strategy is to modify the update step in (5.35) as follows: For given $\lambda \in (0, 1)$ determine the minimal $l^* \in \mathbb{N}$ via $l = 0, 1, \ldots, N_l$, such that

$$\begin{aligned} R(\hat{U}_{h,l}^{n,j+1}) &< R(\hat{U}_{h,l}^{n,j}), \\ \hat{U}_{h,l}^{n,j+1} &= \hat{U}_h^{n,j} + \lambda^l\delta\hat{U}_h^n. \end{aligned}$$

For the minimal l, we set

$$\hat{U}_h^{n,j+1} := \hat{U}_{h,l^*}^{n,j+1}.$$

In this context, the nonlinear residual $R(\cdot)$ is defined as

$$R(\hat{U}_h^n) := \max_i \left\{ \hat{A}(\hat{U}_h^n)(\hat{\Psi}_i) - \hat{F}(\hat{\Psi}_i) \right\} \quad \forall \hat{U}_h^n \in \widehat{X}_h,$$

where $\{\hat{\Psi}_i\}$ denotes the nodal basis of $\widehat{X}_h$.

The directional derivative $\hat{A}'(\hat{U})(\delta\hat{U}, \hat{\Psi})$ that is utilized previously, is defined in the same fashion (as Gâteaux derivative) as introduced in Definition 4.1. The application to a semi-linear form reads:

$$\hat{A}'(\hat{U})(\delta\hat{U}, \hat{\Psi}) := \lim_{\varepsilon \to 0} \frac{1}{\varepsilon} \left\{ \hat{A}(\hat{U} + \varepsilon\delta\hat{U})(\hat{\Psi}) - \hat{A}(\hat{U})(\hat{\Psi}) \right\} = \frac{d}{d\varepsilon} \left. \hat{A}_h(\hat{U} + \varepsilon\delta\hat{U})(\hat{\Psi}) \right|_{\varepsilon=0}.$$

5.6.1 Evaluation of the directional derivatives

Due to the large size of the Jacobian matrix and the strongly nonlinear behavior of fluid-structure interaction problems in the monolithic ALE framework, the calculation of the Jacobian matrix can be cumbersome. Nevertheless, in this context, we use the exact Jacobian matrix to identify the optimal convergence properties of the Newton method. The derivation of directional derivatives is also illustrated by means of several examples presented elsewhere [47, 117, 149]. For more details on the computation of the directional derivatives on the interface, we refer the reader to [42, 118]. Evaluation of the

directional derivatives for fluid-structure interaction with help of *automatic differentiation* is demonstrated by Dunne [42].

As before, let the solution $\hat{U}_h^n = \{\hat{v}_{f,h}^n, \hat{v}_{s,h}^n, \hat{u}_{f,h}^n, \hat{u}_{s,h}^n, \hat{p}_{f,h}^n, \hat{p}_{s,h}^n\} \in \widehat{X}_h$ be given. Further, let $\delta\hat{U}_h^n = \{\delta\hat{v}_{f,h}^n, \delta\hat{v}_{s,h}^n, \delta\hat{u}_{f,h}^n, \delta\hat{u}_{s,h}^n, \delta\hat{p}_{f,h}^n, \delta\hat{p}_{s,h}^n\} \in \widehat{X}_h$. In the following, we omit explicit notation of 'h' and 'n'.

The Jacobian $\hat{A}'(\hat{U})(\delta\hat{U}, \hat{\Psi})$ is split up into fluid contributions and structure terms:

$$\hat{A}'(\hat{U})(\delta\hat{U}, \hat{\Psi}) := \hat{A}'_f(\hat{U}_f)(\delta\hat{U}_f, \hat{\Psi}_f) + \hat{A}'_s(\hat{U})(\delta\hat{U}_s, \hat{\Psi}_s).$$

Using the previous arrangement (5.4), we deal with

$$\begin{aligned} &\hat{A}'_f(\hat{U}_f)(\delta\hat{U}_f, \hat{\Psi}_f) \\ &= \hat{A}'_{f,T}(\hat{U}_f)(\delta\hat{U}_f, \hat{\Psi}_f) + \hat{A}'_{f,I}(\hat{U}_f)(\delta\hat{U}_f, \hat{\Psi}_f) + \hat{A}'_{f,E}(\hat{U}_f)(\delta\hat{U}_f, \hat{\Psi}_f) + \hat{A}'_{f,P}(\hat{U}_f)(\delta\hat{U}_f, \hat{\Psi}_f), \end{aligned} \tag{5.36}$$

and

$$\begin{aligned} &\hat{A}'_s(\hat{U}_s)(\delta\hat{U}_s, \hat{\Psi}_s) \\ &= \hat{A}'_{s,T}(\hat{U}_s)(\delta\hat{U}_s, \hat{\Psi}_s) + \hat{A}'_{s,I}(\hat{U}_s)(\delta\hat{U}_s, \hat{\Psi}_s) + \hat{A}'_{s,E}(\hat{U}_s)(\delta\hat{U}_s, \hat{\Psi}_s) + \hat{A}'_{s,P}(\hat{U}_s)(\delta\hat{U}_s, \hat{\Psi}_s). \end{aligned} \tag{5.37}$$

The concrete evaluation of each term on the fully discrete level is derived in the following.

Basic relations

In the sequel, we often use the short-hand-notation

$$\partial_b A(\delta z) := \frac{\partial A}{\partial b}(\delta z),$$

for the derivative of a tensor A w.r.t. b in direction δz. We begin with the basic relations that are required for each of the subproblems. For the deformation gradient $\widehat{F}$, it holds in a direction $\delta\hat{z} \in H^1(\widehat{\Omega})$:

$$\partial_z \widehat{F}(\delta\hat{z}) = \widehat{\nabla}\delta\hat{z}, \quad \partial_z \widehat{F}^T(\delta\hat{z}) = \widehat{\nabla}\delta\hat{z}^T. \tag{5.38}$$

In the following, we recall the evaluation of the inverse relations (see, e.g., [78])

$$\partial_z \widehat{F}^{-1}(\delta\hat{z}) = -\widehat{F}^{-1}\widehat{\nabla}\delta\hat{z}\widehat{F}^{-1}, \quad \partial_z \widehat{F}^{-T}(\delta\hat{z}) = -\widehat{F}^{-T}\widehat{\nabla}\delta\hat{z}^T\widehat{F}^{-T}.$$

Finally, the derivative of the determinant $\hat{J}$ can be expressed as

$$\partial_z \hat{J}(\delta z) = \hat{J}\mathrm{tr}(\widehat{F}^{-1}\widehat{\nabla}\delta z).$$

Fluid's Cauchy stress tensor

In the fluid part, we are concerned with the evaluation of directional derivatives in the three directions $\delta\hat{v}_f, \delta\hat{p}_f$ and $\delta\hat{u}_f$. We start with the Cauchy stress tensor $\widehat{\sigma}_f = \widehat{\sigma}_{f,vu} + \widehat{\sigma}_{f,p}$:

$$\begin{aligned}
\partial_v\widehat{\sigma}_{f,vu}(\delta\hat{v}_f) &= 2\hat{\rho}_f\nu_f(\widehat{\nabla}\delta\hat{v}_f\widehat{F}^{-1} + \widehat{F}^{-T}\widehat{\nabla}\delta\hat{v}_f^T),\\
\partial_p\widehat{\sigma}_{f,p}(\delta\hat{p}_f) &= -\delta\hat{p}_f\hat{I},\\
\partial_u\widehat{\sigma}_{f,vu}(\delta\hat{u}_f) &= 2\hat{\rho}_f\nu_f(\widehat{\nabla}\hat{v}_f(-\widehat{F}^{-1}\widehat{\nabla}\delta\hat{u}\widehat{F}^{-1}) + (-\widehat{F}^{-T}\widehat{\nabla}\delta\hat{u}^T\widehat{F}^{-T})\widehat{\nabla}\hat{v}_f^T).
\end{aligned}$$

Summarizing these contributions yields

$$\partial_U\widehat{\sigma}_{f,vu}(\delta\hat{U}_f) = \partial_v\widehat{\sigma}_{f,vu}(\delta\hat{v}_f) + \partial_u\widehat{\sigma}_{f,vu}(\delta\hat{u}_f), \qquad \partial_U\widehat{\sigma}_{f,p}(\delta\hat{U}_f) = \partial_p\widehat{\sigma}_{f,p}(\delta\hat{v}_p).$$

Thus, the derivative of the transformed Cauchy stress tensor in the reference domain reads:

$$\partial_U(\hat{J}\widehat{\sigma}_f\widehat{F}^{-T})(\delta\hat{U}_f) = \hat{J}\mathrm{tr}(\widehat{F}^{-1}\widehat{\nabla}\delta\hat{u}_f)\widehat{\sigma}_f\widehat{F}^{-T} + \hat{J}\partial_U\widehat{\sigma}_f(\delta\hat{U}_f)\widehat{F}^{-T} + \hat{J}\widehat{\sigma}_f(-\widehat{F}^{-T}\widehat{\nabla}\delta\hat{u}_f^T\widehat{F}^{-T}).$$

The Cauchy stress tensor is decomposed by reason motivated in Problem 5.2. It is obvious that this decomposition must be considered in the linearization process, too.

Fluid's convection term

For the treatment of the convection term (also including the ALE convection term), we use the relation $\hat{u}_f \cdot \widehat{\nabla}\hat{v}_f = \widehat{\nabla}\hat{v}_f\,\hat{u}_f$ and decompose the convection term as

$$\hat{\rho}_f\hat{J}(\widehat{F}^{-1}(\hat{v}_f - \hat{w})\cdot\widehat{\nabla})\hat{v}_f = \hat{\rho}_f\hat{J}(\widehat{\nabla}\hat{v}_f\widehat{F}^{-1})\hat{v}_f - \hat{\rho}_f\hat{J}(\widehat{\nabla}\hat{w}\widehat{F}^{-1})\hat{v}_f.$$

With the help of the previously introduced basic relations, the derivative of the first part reads:

$$\begin{aligned}
\partial_U(\hat{\rho}_f\hat{J}(\widehat{\nabla}\hat{v}_f\widehat{F}^{-1})\hat{v}_f)(\delta\hat{U}_f) = {}& \hat{\rho}_f\hat{J}\mathrm{tr}(\widehat{F}^{-1}\widehat{\nabla}\delta\hat{u}_f)(\widehat{\nabla}\hat{v}_f\widehat{F}^{-1})\hat{v}_f\\
&+ \hat{\rho}_f\hat{J}(\widehat{\nabla}\delta\hat{v}_f\widehat{F}^{-1})\hat{v}_f\\
&+ \hat{\rho}_f\hat{J}(\widehat{\nabla}\hat{v}_f(-\widehat{F}^{-1}\widehat{\nabla}\delta\hat{u}_f\widehat{F}^{-1})\hat{v}_f\\
&+ \hat{\rho}_f\hat{J}(\widehat{\nabla}\hat{v}_f\widehat{F}^{-1})\delta\hat{v}_f. \qquad (5.39)
\end{aligned}$$

In the second part, we cannot directly differentiate the fluid domain velocity $\hat{w}$. As previously discussed in Section 5.4.1, this term is constructed (linear in time) with the help of the displacements $\hat{u}_f$. Thus, in Equation (5.39), we only must replace the second term. Using the construction of $\hat{w} = \frac{1}{k}(\hat{u}_f - \hat{u}_f^{n-1})$ in which $\hat{u}_f^{n-1}$ denotes the solution of the previous time step (as shown in Equation (5.31)), we readily get

$$\partial_u\hat{w}(\delta\hat{u}_f) := \partial_u\frac{1}{k}(\hat{u}_f - \hat{u}_f^{n-1})(\delta\hat{u}_f) = \frac{1}{k}\delta\hat{u}_f. \qquad (5.40)$$

With this, we obtain for the second equation on the right-hand-side in (5.39)

$$\frac{1}{k}\hat{\rho}_f\hat{J}(\widehat{\nabla}\delta\hat{u}_f\widehat{F}^{-1})\hat{v}_f.$$

In the remaining terms of (5.39), we replace $\widehat{\nabla}\hat{v}_f$ with $\widehat{\nabla}\hat{w}$.

Fluid's time derivative

We continue with the time derivative of the fluid term:

$$\hat{\rho}_f \hat{J} \partial_t \hat{v}_f \approx \hat{\rho}_f \hat{J}^{n,\theta} \frac{\hat{v}_f - \hat{v}_f^{n-1}}{k},$$

where we employ (5.5) for the temporal discretization. First, we obtain

$$\partial_u \hat{J}^{n,\theta}(\delta\hat{u}_f) = \partial_u(\theta\hat{J} + (1-\theta)\hat{J}^{n-1})(\delta\hat{u}_f) = \theta \hat{J} \mathrm{tr}(\widehat{F}^{-1}\widehat{\nabla}\delta\hat{u}_f). \tag{5.41}$$

Next, we get

$$\partial_v \frac{1}{k}(\hat{v}_f - \hat{v}_f^{n-1})(\delta\hat{v}_f) = \frac{1}{k}\delta\hat{v}_f.$$

With this equation, we compute for (5.41):

$$\partial_U \Big(\hat{\rho}_f \frac{1}{k}\hat{J}^{n,\theta}(\hat{v}_f - \hat{v}_f^{n-1})\Big)(\delta\hat{U}_f) = \hat{\rho}_f \frac{\theta}{k}\hat{J}\mathrm{tr}(\widehat{F}^{-1}\widehat{\nabla}\delta\hat{u}_f)(\hat{v}_f - \hat{v}_f^{n-1}) + \hat{\rho}_f \frac{1}{k}\hat{J}^{n,\theta}(\delta\hat{v}_f).$$

Fluid's incompressibility

We proceed with the incompressibility term of the fluid. To compute the derivative, we utilize a byproduct of the divergence relation of the Piola transformation:

$$\widehat{\mathrm{div}}(\hat{J}\widehat{F}^{-1}\hat{v}_f) = \hat{J}\mathrm{tr}(\widehat{\nabla}\hat{v}_f\widehat{F}^{-1}).$$

Then, we get

$$\begin{aligned}
\partial_v \hat{J}\mathrm{tr}(\widehat{\nabla}\hat{v}_f\widehat{F}^{-1})(\delta\hat{v}_f) &= \hat{J}\mathrm{tr}(\widehat{\nabla}\delta\hat{v}_f\widehat{F}^{-1}),\\
\partial_u \hat{J}\mathrm{tr}(\widehat{\nabla}\hat{v}_f\widehat{F}^{-1})(\delta\hat{u}_f) &= \hat{J}\mathrm{tr}(\widehat{F}^{-1}\widehat{\nabla}\delta\hat{u}_f)\mathrm{tr}(\widehat{\nabla}\hat{v}_f\widehat{F}^{-1}) - \hat{J}\mathrm{tr}(\widehat{\nabla}\hat{v}_f\widehat{F}^{-1}\widehat{\nabla}\delta\hat{u}_f\widehat{F}^{-1}).
\end{aligned}$$

Fluid's mesh motion

It remains to consider the derivative of the mesh motion equation. Using the harmonic mesh motion model (see definition of $\widehat{\sigma}_{\mathrm{mesh}}$ in (3.11)), we readily obtain

$$\partial_u(\alpha_u\widehat{\nabla}\hat{u}_f)(\delta\hat{u}_f) = \alpha_u\widehat{\nabla}\delta\hat{u}_f.$$

Using the linear-elastic mesh motion model (see definition of $\widehat{\sigma}_{\mathrm{mesh}}$ in (3.14)), we get

$$\partial_u(\alpha_\lambda(\mathrm{tr}\,\hat{\epsilon})\hat{I} + 2\alpha_\mu\hat{\epsilon})(\delta\hat{u}_f) = \alpha_\lambda\frac{1}{2}(\mathrm{tr}\,(\widehat{\nabla}\delta\hat{u}_f + \widehat{\nabla}\delta\hat{u}_f^T)\hat{I} + \alpha_\mu(\widehat{\nabla}\delta\hat{u}_f + \widehat{\nabla}\delta\hat{u}_f^T).$$

Fluid's do-nothing condition

Next, we consider the derivative of the boundary term $\hat{g}_f := -\hat{\rho}_f \nu_f \widehat{F}^{-T} \widehat{\nabla} \hat{v}_f^T$ on $\widehat{\Gamma}_{f,N}$ (see (3.4)):

$$\partial_U(-\hat{\rho}_f \nu_f \widehat{F}^{-T} \widehat{\nabla} \hat{v}_f^T)(\delta \hat{U}_f) = \hat{\rho}_f \nu_f (\widehat{F}^{-T} \widehat{\nabla} \delta \hat{u}_f^T \widehat{F}^{-T}) \widehat{\nabla} \hat{v}_f^T + \hat{\rho}_f \nu_f \widehat{F}^{-T} \widehat{\nabla} \delta \hat{v}_f^T.$$

Fluid's stabilization

Finally, we explain the differentiation of the stabilization term. In this expression, we only differentiate the first argument although the second argument also depends on the solution variable. Using the derivative of the convection term, we readily obtain

$$\hat{S}'_{\text{stab}}(\hat{U}_f)(\delta \hat{U}_f, \hat{\Psi}_f) = (\partial_U(\hat{\rho}_f \hat{J}(\widehat{\nabla} \hat{v}_f \widehat{F}^{-1}) \hat{v}_f)(\delta \hat{U}_f), \delta_{K,n}(\widehat{F}^{-1} \hat{v}_f \cdot \widehat{\nabla}) \hat{\psi}_f^v)_{\widehat{K}_f}, \tag{5.42}$$

on each cell $\widehat{K}_f \in \mathcal{T}_h$.

Structure's constitutive tensors

We continue with the description for the derivatives of the structure subproblem. Using standard elasticity (i.e., the damping terms are omitted) with the STVK model, we only must compute the derivatives with respect to $\hat{u}_s$. In the presence of incompressible materials, we also account for the pressure $\hat{p}_s$. Finally, the consideration of strong damping makes it necessary to compute derivatives with respect to $\hat{v}_s$.

Let us begin with the Green-Lagrange tensor (defined in (2.10)) that is employed to formulate the STVK material:

$$\partial_u \widehat{E}(\delta \hat{u}_s) = \frac{1}{2}(\widehat{\nabla} \delta \hat{u}_s^T \widehat{F} + \widehat{F}^T \widehat{\nabla} \delta \hat{u}_s).$$

Then, the constitutive tensor $\widehat{\Sigma} := \widehat{\Sigma}(\hat{u}_s)$ reads

$$\partial_u \widehat{\Sigma}(\delta \hat{u}_s) = \lambda_s \frac{1}{2} \text{tr}(\widehat{\nabla} \delta \hat{u}_s^T \widehat{F} + \widehat{F}^T \widehat{\nabla} \delta \hat{u}_s) \hat{I} + \mu_s (\widehat{\nabla} \delta \hat{u}_s^T \widehat{F} + \widehat{F}^T \widehat{\nabla} \delta \hat{u}_s).$$

For the incompressible IMR material (defined in (2.12)), we obtain

$$\begin{aligned}
&\partial_p \widehat{\sigma}_{\text{IMR}}(\delta \hat{p}_s) = -\delta \hat{p}_s \hat{I}, \\
&\partial_u \widehat{\sigma}_{\text{IMR}}(\delta \hat{u}_s) = \mu_1 (\delta \hat{u}_s \widehat{F}^T + \widehat{F} \delta \hat{u}_s^T) - \mu_2 (\widehat{F}^{-T} \widehat{\nabla} \delta \hat{u}_s^T \widehat{F}^{-T} \widehat{F}^{-1} + \widehat{F}^{-T} \widehat{F}^{-1} \widehat{\nabla} \delta \hat{u}_s \widehat{F}^{-1},
\end{aligned}$$

and from this, we readily deduce

$$\begin{aligned}
\partial_p \widehat{\sigma}_{\text{INH}}(\delta \hat{p}_s) &= -\delta \hat{p}_s \hat{I}, \\
\partial_u \widehat{\sigma}_{\text{INH}}(\delta \hat{u}_s) &= \mu_1 (\delta \hat{u}_s \widehat{F}^T + \widehat{F} \delta \hat{u}_s^T).
\end{aligned}$$

Structure's damping terms

Finally, using strong damping, we compute the derivatives in the direction $\delta \hat{v}_s$ of $\hat{\epsilon}(\hat{v}_s)$. Then,

$$\partial_v \hat{\epsilon}(\hat{v}_s)(\delta \hat{v}_s) = \frac{1}{2}(\widehat{\nabla} \delta \hat{v}_s + \widehat{\nabla} \delta \hat{v}_s^T).$$

Proposition 5.6. *At each Newton step* (5.35)*, we solve a linear system, where (an example of) its residual* $\hat{A}(\hat{U})(\hat{\Psi}) - \widehat{F}(\hat{\Psi})$ *on the continuous level is defined in Problem 5.1. The Jacobian of this problem is split into*

$$\hat{A}'(\hat{U})(\delta\hat{U}, \hat{\Psi}) := \hat{A}'_f(\hat{U}_f)(\delta\hat{U}_f, \hat{\Psi}_f) + \hat{A}'_s(\hat{U}_s)(\delta\hat{U}_s, \hat{\Psi}_s).$$

Using the arrangements (5.36) *and* (5.37)*, we deal with the following expressions:*

$$\begin{aligned}
\hat{A}'_{f,T}(\hat{U}_f)(\delta\hat{U}_f, \hat{\Psi}_f) &= \hat{\rho}_f \frac{\theta}{k}(\hat{J}tr(\widehat{F}^{-1}\widehat{\nabla}\delta\hat{u}_f)(\hat{v}_f - \hat{v}_f^{n-1}), \hat{\psi}_f^v)_{\widehat{\Omega}_f} + \hat{\rho}_f \frac{1}{k}(\hat{J}^{n,\theta}(\delta\hat{v}_f), \hat{\psi}_f^v)_{\widehat{\Omega}_f} \\
&\quad + \hat{\rho}_f(\hat{J}(\widehat{\nabla}\hat{v}_f\widehat{F}^{-1})(\delta\hat{v}_f - k^{-1}\delta\hat{u}_f), \hat{\psi}_f^v)_{\widehat{\Omega}_f}, \\
\hat{A}'_{f,E}(\hat{U}_f)(\delta\hat{U}_f, \hat{\Psi}_f) &= \hat{\rho}_f(\hat{J}tr(\widehat{F}^{-1}\widehat{\nabla}\delta\hat{u}_f)(\widehat{\nabla}\hat{v}_f\widehat{F}^{-1})(\hat{v}_f - \hat{w}), \hat{\psi}_f^v)_{\widehat{\Omega}_f} \\
&\quad + \hat{\rho}_f(\hat{J}(\widehat{\nabla}\delta\hat{v}_f\widehat{F}^{-1})(\hat{v}_f - \hat{w}), \hat{\psi}_f^v)_{\widehat{\Omega}_f} \\
&\quad + \hat{\rho}_f(\hat{J}(\widehat{\nabla}\hat{v}_f(-\widehat{F}^{-1}\widehat{\nabla}\delta\hat{u}_f\widehat{F}^{-1})(\hat{v}_f - \hat{w}), \hat{\psi}_f^v)_{\widehat{\Omega}_f} \\
&\quad + (\partial_U(\hat{J}\hat{\sigma}_{f,vu}\widehat{F}^{-T})(\delta\hat{U}_f), \hat{\psi}_f^v)_{\widehat{\Omega}_f} + \langle\partial_U g_f(\delta\hat{U}), \hat{\psi}_f^v\rangle_{\widehat{\Gamma}_N} \\
&\quad - (\rho_f\hat{J}tr(\widehat{F}^{-1}\widehat{\nabla}\delta\hat{u}_f)\hat{f}_f, \hat{\psi}_f^v)_{\widehat{\Omega}_f}, \\
\hat{A}'_{f,I}(\hat{U}_f)(\delta\hat{U}_f, \hat{\Psi}_f) &= (\alpha_u\widehat{\nabla}\delta\hat{u}_f, \widehat{\nabla}\hat{\psi}_f^u)_{\widehat{\Omega}_f} \\
&\quad + (\hat{J}tr(\widehat{\nabla}\delta\hat{v}_f\widehat{F}^{-1}), \hat{\psi}_f^p)_{\widehat{\Omega}_f} + (\hat{J}tr(\widehat{F}^{-1}\widehat{\nabla}\delta\hat{u}_f)tr(\widehat{\nabla}\hat{v}_f\widehat{F}^{-1}), \hat{\psi}_f^p)_{\widehat{\Omega}_f} \\
&\quad - (\hat{J}tr(\widehat{\nabla}\hat{v}_f\widehat{F}^{-1}\widehat{\nabla}\delta\hat{u}_f\widehat{F}^{-1}), \hat{\psi}_f^p)_{\widehat{\Omega}_f}, \\
\hat{A}'_{f,P}(\hat{U}_f)(\delta\hat{U}_f, \hat{\Psi}_f) &= (\partial_U(\hat{J}\hat{\sigma}_{f,p}\widehat{F}^{-T})(\delta\hat{U}_f), \widehat{\nabla}\hat{\psi}_f^v)_{\widehat{\Omega}_f}, \\
\hat{S}'_{stab}(\hat{U}_f)(\delta\hat{U}_f, \hat{\Psi}_f) &= (\partial_U(\hat{\rho}_f\hat{J}(\widehat{\nabla}\hat{v}_f\widehat{F}^{-1})\hat{v}_f)(\delta\hat{U}_f), \delta_{K,n}(\widehat{F}^{-1}\hat{v}_f \cdot \widehat{\nabla})\hat{\psi}_f^v)_{\widehat{K}_f},
\end{aligned}$$

and

$$\begin{aligned}
\hat{A}'_{s,T}(\hat{U}_s)(\delta\hat{U}_s, \hat{\Psi}_s) &= k^{-1}(\hat{\rho}_s\delta\hat{v}_s, \hat{\psi}_s^v)_{\widehat{\Omega}_s} + k^{-1}(\hat{\rho}_s\hat{u}_s, \hat{\psi}_s^u)_{\widehat{\Omega}_s} - (\hat{\rho}_s\delta\hat{v}_s, \hat{\psi}_s^u)_{\widehat{\Omega}_s} \\
&\quad + (\partial_U\hat{P}(\delta\hat{U}_s, \hat{\psi}_s^p)_{\widehat{\Omega}_s}, \\
\hat{A}'_{s,E}(\hat{U}_s)(\delta\hat{U}_s, \hat{\Psi}_s) &= (\partial_u(\widehat{F}\widehat{\Sigma})(\delta\hat{u}_s), \widehat{\nabla}\hat{\psi}_s^v)_{\widehat{\Omega}_s} \\
&\quad + \gamma_w(\delta\hat{v}_s, \hat{\psi}_s^v)_{\widehat{\Omega}_s} + \gamma_s(\partial_v\hat{\epsilon}(\hat{v}_s)(\delta\hat{v}_s), \hat{\psi}_s^v)_{\widehat{\Omega}_s}, \\
\hat{A}'_{s,I}(\hat{U}_s)(\delta\hat{U}_s, \hat{\Psi}_s) &= (\partial_U\hat{P}(\delta\hat{U}_s), \hat{\psi}_s^p)_{\widehat{\Omega}_s}, \\
\hat{A}'_{s,P}(\hat{U}_s)(\delta\hat{U}_s, \hat{\Psi}_s) &= (\partial_U(\hat{J}\hat{\sigma}_{s,p}\widehat{F}^{-T})(\delta\hat{U}_s), \widehat{\nabla}\hat{\psi}_s^v)_{\widehat{\Omega}_f}.
\end{aligned}$$

5.7 Solution of the linear equation systems

At each Newton step (5.35), we must solve a linear equation system. An explicit representation of the Jacobian is shown in Problem 5.6. Using a nodal basis representation $\{\hat{\Psi}_i\}$ of $\widehat{X}_h$, the Jacobian matrix of the system reads:

$$A = (A_{ij})_{i,j=1}^{N}, \quad \text{with } A_{ij} := \hat{A}'(\hat{U})(\hat{\Psi}_j, \hat{\Psi}_i).$$

Then, the corresponding linear system reads:

$$A\,\delta U = b, \tag{5.43}$$

in which the solution vector $\delta\hat{U}$ is represented by

$$\delta\hat{U} = \sum_{j=1}^{N} \delta\hat{U}_j \hat{\Psi}_j,$$

and the residual is denoted by $b = (b_i)_{i=1}^{N}$. The block-matrix A is ill-conditioned and unsymmetric. For this reason, standard linear solvers like the generalized minimal residual (GMRES) solver, only work with good preconditioners.

In this section, we investigate the inner form of the Jacobian matrix A and we give an idea how to solve the linear equation system efficiently. The latter part is exemplified for a harmonic mesh model used in a stationary setting. Specifically, we use the inner block form of the linear system, to discover its characteristics and to formulate the solution algorithm. For instance, this is the basis to develop a block Schur preconditioner that is used for solving the coupled problem with help of iterative methods. To ease the notation in this section, we omit the *hats*, and the indications of 'n' and 'h' because it is clear that we are still working in the discrete reference configuration $\widehat{\Omega}$.

5.7.1 Solution techniques using harmonic mesh motion

In this part, we discuss the development of a preconditioner for the nonlinear coupled problem after discretization and linearization at each Newton step (5.35). We examine the nonstationary fluid-structure interaction problem with the harmonic mesh motion model as derived in Problem 3.6.

The contribution of the fluid subdomain to the global problem (5.35) has the following form:

$$\begin{pmatrix} \frac{M_{vv}}{k} + K + L_{vv} & B & S_{vu} \\ B^T & 0 & S_{pu} \\ 0 & 0 & L_{uu} \end{pmatrix} \begin{pmatrix} \delta v_f \\ \delta p_f \\ \delta u_f \end{pmatrix} = \begin{pmatrix} b_{f,v} \\ b_{f,p} \\ b_{f,u} \end{pmatrix}, \tag{5.44}$$

whereas the contribution of compressible structure materials (i.e., the STVK model) reads

$$\begin{pmatrix} \frac{M_{vv}}{k} & 0 & L_{vu} \\ 0 & M_{pp} & 0 \\ M_{uv} & 0 & \frac{M_{uu}}{k} \end{pmatrix} \begin{pmatrix} \delta v_s \\ \delta p_s \\ \delta u_s \end{pmatrix} = \begin{pmatrix} b_{s,v} \\ b_{s,p} \\ b_{s,u} \end{pmatrix}, \tag{5.45}$$

and the contribution in the case of incompressible structure materials (i.e., the INH or the IMR model) reads

$$\begin{pmatrix} \frac{M_{vv}}{k} & B_{vp} & L_{vu} \\ 0 & 0 & M_{pu} \\ M_{uv} & 0 & \frac{M_{uu}}{k} \end{pmatrix} \begin{pmatrix} \delta v_s \\ \delta p_s \\ \delta u_s \end{pmatrix} = \begin{pmatrix} b_{s,v} \\ b_{s,p} \\ b_{s,u} \end{pmatrix}. \tag{5.46}$$

Using incompressible structure models, the pressure is incorporated as Lagrange multiplier, which corresponds to the block entries B_{vp} and M_{pu}. The corresponding pressure entry in the STVK matrix can be eliminated directly, such that the remaining system reads

$$\begin{pmatrix} \frac{M_{vv}}{k} & L_{vu} \\ M_{uv} & \frac{M_{uu}}{k} \end{pmatrix} \begin{pmatrix} \delta v_s \\ \delta u_s \end{pmatrix} = \begin{pmatrix} b_{s,v} \\ b_{s,u} \end{pmatrix}. \tag{5.47}$$

The introduced matrices are characterized as follows. In the fluid domain, we deal with a mass term M_{vv}, the convection term K, the Laplacian-like tensor L_{vv}, the gradient matrix B, and two coupling terms S_{vu} and S_{pu}. Moreover, the entry of the mesh motion is denoted by L_{uu}. In the structure domain, we deal with three mass terms M_{vv}, M_{uv} and M_{uu}, the constitutive structure tensor L_{vu}, and a pressure mass term M_{pp} (which corresponds to $\hat{p}_s = 0$ and can therefore be directly eliminated). Using incompressible materials, we define a structure pressure that leads to the additional terms B_{vp} and the (mass term) M_{pu}.

For stationary settings (see Problem 3.8), we derive from (5.44) for the fluid subproblem the following form

$$\begin{pmatrix} K + L_{vv} & B & S_{vu} \\ B^T & 0 & S_{pu} \\ 0 & 0 & L_{uu} \end{pmatrix} \begin{pmatrix} \delta v_f \\ \delta p_f \\ \delta u_f \end{pmatrix} = \begin{pmatrix} b_{f,v} \\ b_{f,p} \\ b_{f,u} \end{pmatrix}. \tag{5.48}$$

For the STVK problem, we obtain from (5.47):

$$\begin{pmatrix} 0 & L_{vu} \\ M_{uv} & 0 \end{pmatrix} \begin{pmatrix} \delta v_s \\ \delta u_s \end{pmatrix} = \begin{pmatrix} b_{s,v} \\ b_{s,u} \end{pmatrix}, \tag{5.49}$$

which can be further simplified to

$$L_{vu} \delta u_s = b_{s,v}, \tag{5.50}$$

because the velocity in the structure part is zero and therefore, $\delta \hat{v}_s = 0$. For the incompressible structure models, we obtain from (5.46) the following form in a stationary setting

$$\begin{pmatrix} 0 & B_{vp} & L_{vu} \\ 0 & 0 & M_{pu} \\ M_{uv} & 0 & 0 \end{pmatrix} \begin{pmatrix} \delta v_s \\ \delta p_s \\ \delta u_s \end{pmatrix} = \begin{pmatrix} b_{s,v} \\ b_{s,p} \\ b_{s,u} \end{pmatrix}. \tag{5.51}$$

Using again the previous argument ($\delta \hat{v}_s = 0$) yields

$$\begin{pmatrix} B_{vp} & L_{vu} \\ 0 & M_{pu} \end{pmatrix} \begin{pmatrix} \delta p_s \\ \delta u_s \end{pmatrix} = \begin{pmatrix} b_{s,p} \\ b_{s,u} \end{pmatrix}. \tag{5.52}$$

The last system already has a block-triangular form, such that the structure subsystem can be solved without further rearrangement of the system matrix.

To solve system (5.43), we precondition with a matrix P^{-1} and arrive at

$$P^{-1}A\,\delta U = P^{-1}b. \tag{5.53}$$

If we find appropriate entries for P^{-1} such that the condition number of $P^{-1}A$ is moderate, then the whole system converges in a few iterations. However, in the case of fluid-structure interaction the two subproblems are only defined in non-overlapping subdomains. For this reason, we write the system matrix as a composition of the two submatrices in which we use suitable rectangular matrices R_f and R_s (for their definition we refer to Bastian [10]), which allows us to resize the both matrices, such that they can be combined into one matrix (a similar approach is used for the non-overlapping Schwarz method (see [10, 124]):

$$A = R_f A_f R_f^T + R_s A_s R_s^T.$$

Ideally, we construct preconditioners for the two subproblems, such that

$$P_f^{-1} \approx R_f A_f^{-1} R_f^T \quad \text{and} \quad P_s^{-1} \approx R_s A_s^{-1} R_s^T.$$

Hence, we write

$$P^{-1} = P_f^{-1} + P_s^{-1}.$$

With these observations, we are able to formulate the linear system as displayed in (5.53). The solution of this system can be obtained by solving the two subproblems separately (which was discussed in Heil [68, 69]).

To solve the stationary reduced system (5.48) and (5.50), we follow [68]. Using this idea, we decouple the system, such that we solve the both problems independently. The structure problem is directly treated with

$$L_{vu}\delta u_s = b_{s,v}.$$

Next, we solve the mesh motion problem in the fluid problem

$$L_{uu}\delta u_f = b_{f,u},$$

followed by the right-hand-side update

$$\begin{pmatrix} \tilde{b}_{f,v} \\ \tilde{b}_{f,p} \end{pmatrix} = \begin{pmatrix} b_{f,v} \\ b_{f,p} \end{pmatrix} + \begin{pmatrix} S_{vu}\,\delta u_f \\ S_{pu}\,\delta u_f \end{pmatrix}. \tag{5.54}$$

In the last step, we solve the remaining Navier-Stokes problem

$$\begin{pmatrix} K + L_{vv} & B \\ B^T & 0 \end{pmatrix} \begin{pmatrix} \delta v_f \\ \delta p_f \end{pmatrix} = \begin{pmatrix} \tilde{b}_{f,v} \\ \tilde{b}_{f,p} \end{pmatrix}. \tag{5.55}$$

To solve the Navier-Stokes problem efficiently, it can be further preconditioned with help of a Schur complement iteration [133].

We finally mention the development of a monolithic solver for the monolithically coupled stationary system [89]. In this work, the authors develop a Schur complement preconditioner

P^{-1} for the whole system. However, this preconditioner suffered from the fact that the solution variables are only defined in subdomains and not in the whole domain. This deficiency reduces the performance of the GMRES method, which is used as linear solver.

5.7.2 Form of the system matrix using the biharmonic mesh model

Extending the ideas of the previous section, we identify the global linear equation system in each Newton step (5.35) for nonstationary fluid-structure interaction using biharmonic fluid mesh motion. We split again the system into fluid variables and structure variables. Then, we get for the fluid part

$$\begin{pmatrix} \frac{M_{vv}}{k} + N_{vv} + L_{vv} & B & S_{vu} & 0 \\ B^T & 0 & S_{pu} & 0 \\ 0 & 0 & 0 & \alpha_u L_{u\eta} \\ 0 & 0 & \alpha_u L_{\eta u} & \alpha_u M_{\eta\eta} \end{pmatrix} \begin{pmatrix} \delta v_f \\ \delta p_f \\ \delta u_f \\ \delta \eta_f \end{pmatrix} = \begin{pmatrix} b_{v,f} \\ b_{p,f} \\ b_{u,f} \\ b_{\eta,f} \end{pmatrix}. \tag{5.56}$$

In addition to the previous section, we deal with the Laplacians of the mesh motion $L_{u\eta}, L_{\eta u}$, and the mass matrix $M_{\eta\eta}$. We obtain for the structure subproblem (using the STVK material)

$$\begin{pmatrix} \frac{M_{vv}}{k} & 0 & L_{vu} & 0 \\ 0 & M_{pp} & 0 & 0 \\ M_{uv} & 0 & \frac{M_{uu}}{k} & 0 \\ 0 & 0 & \alpha_u L_{\eta u} & \alpha_u M_{\eta\eta} \end{pmatrix} \begin{pmatrix} \delta v_s \\ \delta p_s \\ \delta u_s \\ \delta \eta_s \end{pmatrix} = \begin{pmatrix} b_{v,s} \\ b_{p,s} \\ b_{u,s} \\ b_{\eta,s} \end{pmatrix}. \tag{5.57}$$

Using incompressible materials, we arrive at

$$\begin{pmatrix} \frac{M_{vv}}{k} & B_{vp} & L_{vu} & 0 \\ 0 & 0 & M_{pu} & 0 \\ M_{uv} & 0 & \frac{M_{uu}}{k} & 0 \\ 0 & 0 & \alpha_u L_{\eta u} & \alpha_u M_{\eta\eta} \end{pmatrix} \begin{pmatrix} \delta v_s \\ \delta p_s \\ \delta u_s \\ \delta \eta_s \end{pmatrix} = \begin{pmatrix} b_{v,s} \\ b_{p,s} \\ b_{u,s} \\ b_{\eta,s} \end{pmatrix}. \tag{5.58}$$

With this derivation, we can develop an iterative solution algorithm as explained in the previous section. Moreover, we emphasize that the derivation of a stationary version of the biharmonic mesh motion model is redundant because this mesh motion model is designed for large structural deflections, which cannot be expected in a fully stationary setting.

In this thesis, we use a direct solver (UMFPACK [37]) to compute the linear equations systems of forward problems. This is mostly because we are interested in long-term computations with a moderate number of spatial unknowns. Consequently, the aforementioned preparations become important for systems with many spatial unknowns in which we must use iterative solvers, eventually supported by a geometric multigrid method. This method was introduced in deal.II by Janssen and Kanschat [88]. Another challenge of iterative solvers must be overcome when we deal with anisotropic mesh cells, which degrades the performance of iterative solvers drastically.

5.7.3 Review of other results for solving monolithic FSI problems

As stated in the previous sections, for large, coupled problems with many unknowns (especially in three dimensions), the most challenging problem is the solution of systems of linear equations, which follow from the use of Newton's method. Therefore, we briefly explain what has been done previously by other authors.

Appropriate preconditioning strategies developed by others can be found in Heil et al. [68, 69] , Turek and Hron [83], Richter [116], and Badia et al. [5]. In the first two articles, the system is first solved by neglecting the coupling terms in the Jacobian, thereby leading to block-triangular approximations. The authors propose three ways to do this; however, they reported a failure of the Newton method for nonstationary computations. Second, the authors used the approximations as preconditioners in an iterative solution method, for example, with the generalized minimal residual (GMRES) method. In the third part, the authors develop appropriate Schur complements to control the computational cost, which becomes a significant deficiency when working with exact preconditioners.

Heil et al. [69] compared partitioned solution approaches with monolithic techniques. Specifically, the monolithic problem was solved with a direct solver but it was also treated with a Krylov subspace method (i.e., GMRES). In this study, the problem was partitioned on the discrete level using sophisticated preconditioning strategies. This allows the re-use of existing solvers for both subproblems.

Hron and Turek [83] used a geometric multigrid solver based on a hierarchy of grids. The iteration was performed in the standard fashion of a defect correction procedure with V or F-type cycles. On the finer grids, a Vanka-like smoother was used to compute the solution.

Badia et al. [5] investigated semi-implicit solution schemes for fluid-structure interactions. In this approach, the key idea was to decouple the computation of fluid velocity from the whole system, such that only structure and pressure variables remain. The advantages of this approach were a reduced computational cost and the ensured stability of the solution algorithm. The authors applied explicit-implicit splitting derived from algebraic factorization splitting methods, which are based on inexact factorization of the system matrix. This method was subsequently used as preconditioner which results in a predictor-corrector method.

One idea for solving stationary monolithic settings with a monolithic solver was the subject of the investigation from Richter [116]. In this method, the author used a monolithic geometric multigrid solver with a smoother in which the both subproblems were solved via a partitioned approach.

Outlook to the next chapter

In this section, we developed methods for the temporal and spatial discretization of monolithically coupled problems. In the following chapter, we account for the error of certain functionals of interest between the continuous solution and its approximation on the discrete level. An efficient discretization can be designed using an a posteriori error estimator and corresponding solution-adapted mesh refinement.

6 Adaptive Mesh Refinement

This chapter is devoted to efficient mesh refinement techniques for solving fluid-structure interaction problems. The main goal is to derive *a posteriori error estimates* that accounts for the error between the continuous solution and the discrete solution with respect to a given quantity of interest (such as point deflections or the measurement of wall stresses). This a posteriori error estimator is used for the mesh adaptation of (stationary) fluid-structure interaction problems. The adaptive solution is derived by employing the *dual weighted residual* (DWR) method. This method was systematically developed in Becker and Rannacher [18] and requires a common, i.e., monolithic, variational formulation of the coupled problem as introduced above. In recent years, the DWR method of spatial refinement has been successfully utilized in various kinds of applications. The extension to a fully space-time DWR approach is derived in Besier et al. [22–24, 123]. Specifically, the DWR method (for spatial refinement) for fluid-structure interaction problems was investigated in various articles [41, 42, 65, 117, 137]. In contrast to most of the other works, e.g., Richter [117], we herein use the strong residual for the error estimator, as originally suggested by Becker and Rannacher [17].

The main motivation for such developments is that error measurements in global norms not provide useful error bounds for the error of the quantity of interest. Thus, a new aspect in this work (compared with the previously cited work) is the application of a simplified version of the DWR method for stationary valve simulations [146, 147]. Indeed, the validation of the DWR method for valve settings and the choice of wall stress measurement as the target functional has important consequences for the numerical solution of such problems. First, the measurement of wall stress is important for clinical applications and (possible) comparisons with clinical data. Second, realistic valve simulations must be performed in three dimensions, for which global mesh refinement becomes prohibitive. Thus, the prototypical investigations of this chapter form a basis for future development.

We examine and compare the following mesh refinement techniques:

- Global mesh refinement.
- Geometry-based refinement.
- Smoothness-based mesh refinement.
- Goal-oriented mesh refinement with the DWR method.

The first procedure is self-explanatory. The second technique is based on the assumption that we know a priori in which region we need local mesh adaption. For the third technique, we measure the jumps of the first derivatives over all edges that correspond to measures

of the smoothness in the discrete solution. The fourth technique is addressed in more detail in the following discussion. For coupled problems the DWR method is still under investigation and becomes costly for space-time-dependent problems. For this reason, we test our developments for a stationary setting.

6.1 Heuristic mesh refinement techniques

In this section, we discuss two refinement techniques that are used for several numerical tests presented in the upcoming chapters.

Geometry-based mesh adaptivity

The mesh is refined during the computation in such regions (namely, along the interface of the fluid and the structure) such that it takes the main characteristics into account. This procedure is easy to use because the position of the interface is a priori known. For instance, it is used for the fluid-structure interaction benchmark tests and the CSM tests in which the measurement of forces along the interface is required. Moreover, the initial mesh for the heart-valve configurations was adapted manually. Specifically, the extended domain (which is not intended to reflect any physical counterpart), was not prerefined. However, this method is a purely heuristic adaptation process because we do not account for the remaining parts of the configuration and their (possible) influence on the solution.

Smoothness-based mesh refinement

One possibility to obtain refinement indicators that drive a mesh adaption procedure is based on the measurement of the jumps over the cell edges in the computed discrete solution $\hat{U}_h$. The local error indicators that are used to adapt the mesh read

$$\eta_{\hat{K}}^2 = \hat{h} \int_{\hat{K}} [\partial_n \hat{U}_h]^2 \, \mathrm{d}\hat{s}, \tag{6.1}$$

where $[\cdot]$ denotes the jump across inter-cell boundaries. The mesh is adapted in those regions in which the largest jumps are evaluated. This heuristic procedure is often used for mesh adaption in the literature [154, 155]. However, all local error indicators have the same influence on the total error and therefore on the mesh refinement. For instance, the discrete solution $\hat{U}_h$ consists of the contributions

$$\hat{v}_{f,h}, \hat{v}_{s,h}, \hat{u}_{f,h}, \hat{u}_{s,h}, \hat{p}_{f,h}, \hat{p}_{s,h}.$$

By appropriate weighting of the single solutions, one can influence the behavior of this estimator dramatically. How to weight the local error contributions appropriately by solving an adjoint problem is subject of the discussion in the following.

6.2 Goal oriented mesh adaption with the DWR method

The Galerkin approximation to Problem 5.1 (neglecting the time derivatives and stabilization terms), reads: Find $\hat{U}_h = \{\hat{v}_{f,h}, \hat{v}_{s,h}, \hat{u}_{f,h}, \hat{u}_{s,h}, \hat{p}_{f,h}, \hat{p}_{s,h}\} \in \widehat{X}^0_{h,D}$, where $\widehat{X}^0_{h,D} := \{\hat{v}^D_{f,h} + \hat{V}^0_{f,\hat{v},h}\} \times \hat{L}_{s,h} \times \{\hat{u}^D_{f,h} + \hat{V}^0_{f,\hat{u},h}\} \times \{\hat{u}^D_{s,h} + \hat{V}^0_{s,h}\} \times \hat{L}^0_{f,h} \times \hat{L}^0_{s,h}$, such that

$$\hat{A}(\hat{U}_h)(\hat{\Psi}_h) = \hat{F}(\hat{\Psi}_h) \quad \forall \hat{\Psi}_h \in \widehat{X}_h. \tag{6.2}$$

The solution $\hat{U}_h$ is used to calculate an approximation $J(\hat{U}_h)$ of the goal-functional $J(\hat{U}) : \widehat{X} \to \mathbb{R}$. This functional is assumed to be sufficiently differentiable. Concretely, it is used for the evaluation of point values (the deflection of the valve), line integrals (the computation of the stresses), or domain integrals (L^2-norm of the velocity).

Example 6.1. *The error of a deflection $\hat{u}_s$ in the y-direction at some point $\hat{p} \in \widehat{\Omega}$ can be estimated by using the following (regularized) functional:*

$$J(\hat{u}_{s,y}) := |B_\varepsilon|^{-1} \int_\varepsilon \hat{u}_{y,s} \, \mathrm{d}\hat{x} = \hat{u}_{y,s}(\hat{p}) + O(\varepsilon^2),$$

where B_ε is the ε-ball around the point $\hat{p}$.

Example 6.2. *The error of mean normal fluxes over lower-dimensional manifolds. For example, we compute the error of wall stresses in the y-direction along the interface between the fluid and the structure, which can be computed with*

$$J(\hat{U}) := \int_{\hat{S}} \hat{J}\hat{\sigma}_f \widehat{F}^{-T} \hat{n}_f \, \hat{d} \, \mathrm{d}\hat{s},$$

where $\hat{d}$ is a unit vector perpendicular to the mean flow direction. Later, we compute the wall stresses along the interface of the aorta $\hat{S} := \widehat{\Gamma}_{aorta}$.

To derive a computable representation of the approximation error $J(\hat{U}) - J(\hat{U}_h)$, we use the (formal) Euler-Lagrange method, and formulate the error estimation problem as an optimization problem:

$$\min\{J(\hat{U}) - J(\hat{U}_h)\} \quad \text{s.t. } \hat{A}(\hat{U})(\hat{\Psi}) = \hat{F}(\hat{\Psi}) \quad \forall \hat{\Psi} \in \widehat{X}.$$

As already examined in Section 4.2 for optimal control problems, we introduce a dual variable $\hat{Z}$ (usually referred to as *sensitivity*) to formulate the Lagrangian functional

$$\mathcal{L}(\hat{U}, \hat{Z}) := J(\hat{U}) + \hat{F}(\hat{Z}) - \hat{A}(\hat{U})(\hat{Z}), \tag{6.3}$$

from which we obtain the optimality system (compare to (4.8))

$$\begin{aligned}
&\mathcal{L}'_{\hat{Z}}(\hat{U}, \hat{Z})(\hat{\Psi}) = \widehat{F}(\hat{\Psi}) - \hat{A}(\hat{U})(\hat{\Psi}) = 0 \quad \forall \hat{\Psi} \in \widehat{X}, \\
&\mathcal{L}'_{\hat{U}}(\hat{U}, \hat{Z})(\hat{\Phi}) = J'_{\hat{U}}(\hat{U})(\hat{\Phi}) - \hat{A}'_{\hat{U}}(\hat{U})(\hat{\Phi}, \hat{Z}) = 0 \quad \forall \hat{\Phi} \in \widehat{X}.
\end{aligned}$$

The first equation is referred to as the *primal* problem, whereas the second is called the *dual* problem. Using an appropriate discrete space $\widehat{X}_h \subset \widehat{X}$, the discrete problem reads:

$$\mathcal{L}'_{\hat{Z}}(\hat{U}_h, \hat{Z}_h)(\hat{\Psi}_h) = \widehat{F}(\hat{\Psi}_h) - \hat{A}(\hat{U}_h)(\hat{\Psi}_h) = 0 \quad \forall \hat{\Psi}_h \in \widehat{X}_h, \tag{6.4}$$

$$\mathcal{L}'_{\hat{U}}(\hat{U}_h, \hat{Z}_h)(\hat{\Phi}_h) = J'_{\hat{U}}(\hat{U}_h)(\hat{\Phi}_h) - \hat{A}'_{\hat{U}}(\hat{U}_h)(\hat{\Phi}_h, \hat{Z}_h) = 0 \quad \forall \hat{\Phi}_h \in \widehat{X}_h. \tag{6.5}$$

For given solutions $\{\hat{U}, \hat{Z}\}$ and $\{\hat{U}_h, \hat{Z}_h\}$ we obtain the following identity for the approximation error:

$$J(\hat{U}) - J(\hat{U}_h) = \mathcal{L}(\hat{U}, \hat{Z}) - \mathcal{L}(\hat{U}_h, \hat{Z}_h).$$

This relation is the basis for a posteriori error estimation. To obtain a computable version in terms of the residuals, we state first the general result ([18]):

Proposition 6.1. *Let the functional $L(\cdot)$ on the function space $\widehat{X}$ be three times Gâteaux differentiable. Then, a stationary point $\hat{x} \in \widehat{X}$ is determined by*

$$L'(\hat{x})(\delta\hat{x}) = 0 \quad \forall \delta\hat{x} \in \widehat{X}.$$

We assume that the corresponding discrete problem

$$L'(\hat{x}_h)(\delta\hat{x}_h) = 0 \quad \forall \delta\hat{x}_h \in \widehat{X}_h.$$

has the respective discrete solution $\hat{x}_h \in \widehat{X}_h$. Then, we obtain the following error representation

$$L(\hat{x}) - L(\hat{x}_h) = \frac{1}{2} L'(\hat{x}_h)(x - \delta\hat{x}_h) + \mathcal{R}_h^{(3)} \quad \forall \delta\hat{x}_h \in \widehat{X}_h.$$

The reminder $\mathcal{R}_h^{(3)}$ is cubic in the error $\hat{e} := \hat{x} - \hat{x}_h$:

$$\mathcal{R}_h^{(3)} := \frac{1}{2} \int_0^1 L'''(\hat{x}_h + s\hat{e})(\hat{e}, \hat{e}, \hat{e}) s(s-1) \, \mathrm{d}\hat{s}.$$

Proof. We refer to [18] for a proof of this theorem. □

As a consequence, we apply Proposition 6.1 to the Lagrangian (6.3). Then, we obtain

Theorem 6.2. *For any solution of the Problem 6.2, we obtain the error representation*

$$J(\hat{U}) - J(\hat{U}_h) = \frac{1}{2}\rho(\hat{U}_h)(\hat{Z} - \hat{\Psi}_h) + \frac{1}{2}\rho^*(\hat{U}_h, \hat{Z}_h)(\hat{U} - \hat{\Phi}_h) + \mathcal{R}_h^{(3)}, \tag{6.6}$$

for all $\{\hat{\Phi}_h, \hat{\Psi}_h\} \in \widehat{X}_h \times \widehat{X}_h$ and with the primal and dual residuals:

$$\rho(\hat{U}_h)(\hat{Z} - \hat{\Psi}_h) := -\hat{A}(\hat{U}_h)(\cdot),$$
$$\rho^*(\hat{U}_h, \hat{Z}_h)(\hat{U} - \hat{\Phi}_h) := J'(\hat{U}_h)(\cdot) - \hat{A}'(\hat{U}_h)(\cdot, \hat{Z}_h)$$

The remainder term $\mathcal{R}_h^{(3)}$ is cubic in the primal and the dual errors. This error identity can be used to drive an automatic mesh refinement process and/or it can be adopted to estimate the error.

Proof. We refer to [18] for a proof of this theorem. □

The dual variable $\hat{Z} = \{\hat{z}_f^v, \hat{z}_s^v, \hat{z}_f^u, \hat{z}_s^u, \hat{z}_f^p, \hat{z}_s^p\}$ is computed by the corresponding (linearized) dual problem (which is extracted as dual equation from the discrete optimality system (6.4))

$$\hat{A}'_{\hat{U}}(\hat{U}_h)(\hat{\Psi}_h, \hat{Z}_h) = J'_{\hat{U}}(\hat{\Psi}_h) \quad \forall \hat{\Psi}_h \in \tilde{X}_h, \tag{6.7}$$

where not necessarily $\tilde{X}_h = \hat{X}_h$. The matrix $\hat{A}'(\hat{U}_h)(\cdot, \hat{Z}_h)$ denotes the transposed matrix of the primal problem (see (5.43)) and it is assembled as one further Newton Jacobian in the nonlinear solution process (5.35); we refer the reader to [9]. The dual Problem 6.7 can be solved using a global higher approximation or local higher interpolation. With these solutions, we obtain approximations of the differences $\hat{Z} - \hat{\Psi}_h$ in the error representation (6.6). The solvability of the primal problem and the dual problem is not for granted, we refer for a deeper discussion to [43].

To obtain a *computable* version of the error identity, we set up some assumptions. First, we neglect the remainder term $\mathcal{R}_h^{(3)}$. Second, we only use the primal residual $\rho(\hat{U}_h)(\hat{Z} - \hat{\Psi}_h)$ to estimate the error (a discussion on this topic can be found in [9]). Third, we transform (as originally suggested in [17]) the error identity by cell-wise partial integration into the strong form, leading to a challenging form of the Laplacian term of the transformed fluid equations. Because we are only dealing with moderate deformations, we assume (while computing the error) that $\widehat{F} = \hat{I}$ and $\hat{J} = 1$. Then, we readily obtain

$$(\hat{J}\widehat{\sigma}_{f,vu}\widehat{F}^{-T}, \widehat{\nabla}\hat{\psi}^v)_{\widehat{\Omega}_f}, \quad \widehat{\sigma}_{f,vu} := \hat{\rho}_f \nu_f (\widehat{\nabla}\hat{v}_f \widehat{F}^{-1} + \widehat{F}^{-T}\widehat{\nabla}\hat{v}_f^T),$$

leading to

$$(\widehat{\sigma}_{appr}, \widehat{\nabla}\hat{\psi}^v)_{\widehat{\Omega}_f}, \quad \widehat{\sigma}_{appr} := \hat{\rho}_f \nu_f (\widehat{\nabla}\hat{v}_f + \widehat{\nabla}\hat{v}_f^T).$$

This term is easily transformed to a strong representation. Basically the same idea is used for the constitutive tensor of the structure (here the STVK material):

$$(\widehat{F}\widehat{\Sigma}, \widehat{\nabla}\hat{\psi}^v)_{\widehat{\Omega}_s}, \quad \widehat{\Sigma} := (\lambda_s(\mathrm{tr}\widehat{E})\hat{I} + 2\mu_s\widehat{E}).$$

Consequently, the structure tensor is approximated with

$$\begin{aligned}
\widehat{\Sigma}_{\text{appr}} &:= (\lambda_s(\mathrm{tr}\widehat{E})\hat{I} + 2\mu_s\widehat{E}) \\
&\approx \lambda_s \mathrm{div}(\hat{u}_s)\hat{I} + 2\mu_s \frac{1}{2}(\widehat{\nabla}\hat{u}_s + \widehat{\nabla}\hat{u}_s^T) \\
&= \lambda_s \mathrm{div}(\hat{u}_s)\hat{I} + \mu_s(\widehat{\nabla}\hat{u}_s + \widehat{\nabla}\hat{u}_s^T).
\end{aligned}$$

Finally, we notice that the structure damping terms vanish in a fully stationary setting. This is due to the fact that the structure velocity equals zero, which is used for structural damping. Consequently, the damping terms are equal to zero, too.

Hence, we obtain the following error representation:

Proposition 6.3. *With the previous assumptions, we obtain for stationary fluid-structure interaction the error representation*

$$J(\hat{U}) - J(\hat{U}_h) \approx \eta_h^f + \eta_h^s + \eta_h^i,$$

in which we split the local error indicators into fluid η_h^f, structure η_h^s, and interface contributions η_h^i. In detail, we have

$$\begin{aligned}\eta_h^f := \sum_{\hat{K}_f \in \hat{\mathcal{T}}_h} \Big\{ & (-\hat{\rho}_f \hat{J}(\widehat{F}^{-1}\hat{v}_f \cdot \widehat{\nabla})\hat{v}_f + \widehat{\nabla} \cdot \widehat{\sigma}_{appr} - \widehat{\nabla}\hat{p}_f, \hat{z}_f^v - \hat{\psi}_h^v)_{\hat{K}_f} \\ & + \frac{1}{2}([\hat{J}\widehat{\sigma}_f \widehat{F}^{-T}\hat{n}_f], \hat{z}_f^v - \hat{\psi}_h^v)_{\partial\hat{K}_f \setminus \partial\widehat{\Omega} \cup \widehat{\Gamma}_i} + (\widehat{div}(\hat{J}\widehat{F}^{-1}\hat{v}_f), \hat{z}_f^p - \hat{\psi}_h^p)_{\hat{K}_f} \\ & + (\widehat{\nabla} \cdot \widehat{\sigma}_{mesh}, \hat{z}_f^u - \hat{\psi}_h^u)_{\hat{K}_f} + \frac{1}{2}([\widehat{\sigma}_{mesh}\hat{n}_f], \hat{z}_f^u - \hat{\psi}_h^u)_{\partial\hat{K}_f \setminus \partial\widehat{\Omega} \cup \widehat{\Gamma}_i} \Big\},\end{aligned}$$

and

$$\begin{aligned}\eta_h^s := \sum_{\hat{K}_s \in \hat{\mathcal{T}}_h} \Big\{ & (\widehat{\nabla} \cdot \widehat{\Sigma}_{appr}, \hat{z}_s^v - \hat{\psi}_h^v)_{\hat{K}_s} + \frac{1}{2}([\widehat{F}\widehat{\Sigma}_{appr}\hat{n}_s], \hat{z}_s^v - \hat{\psi}_h^v)_{\partial\hat{K}_s \setminus \partial\widehat{\Omega} \cup \widehat{\Gamma}_i} \\ & - (\hat{P}_s, \hat{z}_s^p - \hat{\psi}_h^p)_{\hat{K}_s} \Big\},\end{aligned}$$

and

$$\begin{aligned}\eta_h^i := \sum_{\hat{K} \in \hat{\mathcal{T}}_h} \Big\{ & \frac{1}{2}([\hat{J}\widehat{\sigma}_f \widehat{F}^{-T}\hat{n}_f], \hat{z}_f^v - \hat{\psi}_h^v)_{\widehat{\Gamma}_i} + \frac{1}{2}([\widehat{\sigma}_{mesh}\hat{n}_f], \hat{z}_f^u - \hat{\psi}_h^u)_{\widehat{\Gamma}_i} \\ & + \frac{1}{2}([\widehat{F}\widehat{\Sigma}_{appr}\hat{n}_s], \hat{z}_s^v - \hat{\psi}_h^v)_{\widehat{\Gamma}_i} \Big\},\end{aligned}$$

where $\widehat{\sigma}_{mesh}$ was defined in Section 3.3.2 and where $[\cdot]$ denotes the jump across inter-cell boundaries.

The previous declared error representation consists of the *cell residuals* (measuring the consistency of the discrete solution $\hat{U}_h$) and the edge terms $[\cdot]$ (measuring the discrete smoothness). The latter one has similar properties to the smoothness-based refinement indicators as introduced before. The residuals terms are weighted with the so-called *sensitivity factors*

$$\hat{z}_{f,s}^v - \hat{\psi}_h^v, \quad \hat{z}_{f,s}^u - \hat{\psi}_h^u, \quad \hat{z}_{f,s}^p - \hat{\psi}_h^p,$$

which are obtained by solving the dual Problem (6.7).

Proposition 6.4. *From the previous error representation, we derive the following approximate error estimate*

$$|J(\hat{U}) - J(\hat{U}_h)| \approx \sum_{\hat{K}\in\hat{\mathcal{T}}_h} \eta_{\hat{K}}, \quad \eta_{\hat{K}} := \sum_{i=1}^{8} \rho_K^{(i)}\omega_K^{(i)},$$

with the residual terms and the weights

$$\begin{aligned}
\rho_K^{(1)} &:= || - \hat{\rho}_f \hat{J}(\widehat{F}^{-1}\hat{v}_f \cdot \widehat{\nabla})\hat{v}_f + \widehat{\nabla}\cdot\widehat{\sigma}_{appr} - \widehat{\nabla}\hat{p}_f||_{\hat{K}}, & \omega_K^{(1)} &:= ||\hat{z}_f^v - \hat{\psi}_h^v||_{\hat{K}},\\
\rho_K^{(2)} &:= ||\widehat{\nabla}\cdot\widehat{\Sigma}_{appr}||_{\hat{K}}, & \omega_K^{(2)} &:= ||\hat{z}_s^v - \hat{\psi}_h^v||_{\hat{K}},\\
\rho_K^{(3)} &:= ||\widehat{\nabla}\cdot\widehat{\sigma}_{mesh}||_{\hat{K}}, & \omega_K^{(3)} &:= ||\hat{z}_f^u - \hat{\psi}_h^u||_{\hat{K}},\\
\rho_K^{(4)} &:= ||\widehat{div}(\hat{J}\widehat{F}^{-1}\hat{v}_f)||_{\hat{K}}, & \omega_K^{(4)} &:= ||\hat{z}_f^p - \hat{\psi}_h^p||_{\hat{K}},\\
\rho_K^{(5)} &:= ||\hat{P}_s||_{\hat{K}}, & \omega_K^{(5)} &:= ||\hat{z}_s^p - \hat{\psi}_h^p||_{\hat{K}},\\
\rho_K^{(6)} &:= \frac{1}{2}\hat{h}_K^{-1/2}|||[\hat{J}\widehat{\sigma}_f\widehat{F}^{-T}\hat{n}_f]|||_{\partial\hat{K}\cup\widehat{\Gamma}_i}, & \omega_K^{(6)} &:= \frac{1}{2}\hat{h}_K^{1/2}||\hat{z}_f^v - \hat{\psi}_h^v||_{\partial\hat{K}\cup\widehat{\Gamma}_i},\\
\rho_K^{(7)} &:= \frac{1}{2}\hat{h}_K^{-1/2}|||[\widehat{F}\widehat{\Sigma}_{appr}\hat{n}_s]|||_{\partial\hat{K}\cup\widehat{\Gamma}_i}, & \omega_K^{(7)} &:= \frac{1}{2}\hat{h}_K^{1/2}||\hat{z}_s^v - \hat{\psi}_h^v||_{\partial\hat{K}\cup\widehat{\Gamma}_i},\\
\rho_K^{(8)} &:= \frac{1}{2}\hat{h}_K^{-1/2}|||[\widehat{\sigma}_{mesh}\hat{n}_f]|||_{\partial\hat{K}\cup\widehat{\Gamma}_i}, & \omega_K^{(8)} &:= \frac{1}{2}\hat{h}_K^{1/2}||\hat{z}_f^u - \hat{\psi}_h^u||_{\partial\hat{K}\cup\widehat{\Gamma}_i}.
\end{aligned}$$

The weights $\omega^{(i)}$ are approximated by post-processing of the discrete dual solution.

A mesh adaptation algorithm

Let an error tolerance TOL be given. The mesh adaption is realized using extracted local error indicators from an a posteriori error estimate on the mesh $\hat{\mathcal{T}}_h$.

$$|J(\hat{U}) - J(\hat{U}_h)| \le \eta := \sum_{\hat{K}\in\mathbb{T}_h} \eta_{\hat{K}} \quad \text{for all cells } \hat{K} \in \hat{\mathcal{T}}_h.$$

This information is used to adapt the mesh using the following strategy:

1. Compute the primal solution $\hat{U}_h$ and the dual solution $\hat{Z}_h$ on the present mesh $\hat{\mathcal{T}}_h$.
2. Determine the cell indicator $\eta_{\hat{K}}$ at each cell $\hat{K}$.
3. Compute the sum of all indicators $\eta := \sum_{\hat{K}\in\hat{\mathcal{T}}_h} \eta_{\hat{K}}$.
4. Check, if the stopping criterion is satisfied: $|J(\hat{U}) - J(\hat{U}_h)| \le \eta \le TOL$, then accept $\hat{U}_h$ within the tolerance TOL. Otherwise, proceed to the following step.
5. Mark all cells $\hat{K}_i$ that have values $\eta_{\hat{K}_i}$ above the average $\frac{\alpha\eta}{N}$ (where N denotes the total number of cells of the mesh $\mathbb{T}_h$ and $\alpha \approx 1$).

Other mesh adaption strategies are discussed in the literature [9, 18].

Outlook to the next chapter

In this chapter, we introduced techniques for local mesh refinement. These methods are used to avoid (expensive) global mesh refinement. In Section 7.2, we compare different refinement techniques for two distinct goal functionals. In a first setting, the goal functional accounts for a point value evaluation. In a second test, we define the goal functional in terms of wall stress measurement evaluated on a part of the interface.

7 Numerical Results for Stationary Problems

In the following two chapters, we discuss several numerical tests for stationary and nonstationary settings. The tests are designed to reach our final goal of a prototypical heart-valve simulation; consequently, they serve as a validation of our proposed concepts.

In this chapter, we present the first three examples, which are two-dimensional test cases with different goals in mind. In the fourth example, we upgrade our previous considerations to a computation of a three-dimensional test case. We start by analyzing different fluid mesh moving techniques, and we also validate our programming code with the first example. These results were previously published elsewhere [149]. In the second numerical test, we conduct a comparison of different mesh refinement techniques using the DWR method (summarized in [146, 147]). In the third example, we consider an optimal control problem with wall stress minimization, where the state is given by means of a fluid-structure interaction system. In the last example, we compute a prototypical three-dimensional fluid-structure interaction problem that was published previously [149]. This programming code is designed for the computation of fully nonstationary three-dimensional fluid-structure interaction problems. We validate this code by computing a stationary problem within a pseudo-time-stepping procedure with the help of the backward Euler time-stepping scheme.

7.1 CSM tests

In this section, we compare the different mesh motion models introduced in Section 3.3.2. The tests are two dimensional, based on the Computational Structure Mechanics (CSM) test [84]. We compare our results to the results given in this reference and upgrade the CSM test to a new configuration to show the improved performance of the biharmonic model with regard to the mesh motion.

In these test cases, the fluid is set to be initially at rest in $\widehat{\Omega}_f$. An external gravitational force $\hat{f}_s$ is applied only to the elastic beam, producing a visible deformation. The tests are performed as time-dependent problems (backward Euler), leading to a steady state solution. For the harmonic and linear-elastic model, we use the time step size $k = 0.02s$; for the biharmonic model we use $k = 0.1s$.

In the first test case CSM 1, for the validation of the programming code, the parameters proposed by Hron and Turek [84] are used. The primary goal is a comparison of different

mesh motion approaches. Specifically, we run one computation based on the harmonic mesh motion model without a mesh-position dependent material parameter. It turns out that the harmonic model does not hold any more. The reference values are taken from [84]. In the second example, CSM 4, only the gravitational force is increased causing the elastic beam to become much more deformed.

Configuration

The computational domain has length $L = 2.5m$ and height $H = 0.41m$. The circle center is positioned at $C = (0.2m, 0.2m)$ with radius $r = 0.05m$. The elastic beam has length $l = 0.35m$ and height $h = 0.02m$. The right lower end is positioned at $(0.6m, 0.19m)$, and the left end is attached to the circle.

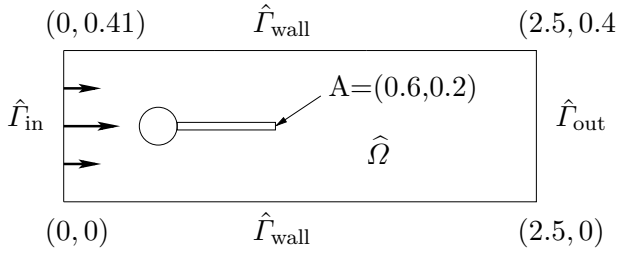

Figure 7.1. Elastic beam attached at a cylinder with circle-center $C = (0.2, 0.2)$ and radius $r = 0.05$.

The control point $A(t)$ (with $A(0) = (0.6, 0.2)$) is fixed at the trailing edge of the structure, measuring x- and y-deflections of the beam.

Boundary conditions

For the upper, lower, and left boundaries, the *no-slip* conditions for velocity and no zero displacement for structure are given. When using the second type of boundary conditions with the biharmonic mesh motion model, the displacement should be zero in the normal direction and free in the tangential direction. This allows the fluid mesh to *move* along the boundary and it ends in a better partition of the fluid mesh.

At the outlet $\widehat{\Gamma}_{\text{out}}$, the *do-nothing* outflow condition is imposed, leading to a zero mean value of the pressure at this part of the boundary.

Parameters

We choose for our computation the following parameters. For the (resting) fluid we use $\varrho_f = 10^3 kgm^{-3}$, $\nu_f = 10^{-3} m^2 s^{-1}$. The elastic structure is characterized by $\varrho_s = 10^3 kgm^{-3}$, $\nu_s = 0.4$, $\mu_s = 5 * 10^5 kgm^{-1}s^{-2}$. The vertical force is chosen as $\hat{f}_s = 2ms^{-2}$.

Discussion of the CSM 1 test

We observe that the harmonic mesh motion without the mesh-position dependent parameter leads to mesh degeneration and therefore, it preforms worse in this example. A quantitative study is displayed in Figure 7.2 in which the minimal values, $\min(\hat{J})$, of the ALE-transformation determinant $\hat{J}$ are sketched as function plots. Our results indicate that using the harmonic approach (which is the simplest one) is sufficient for this numerical test.

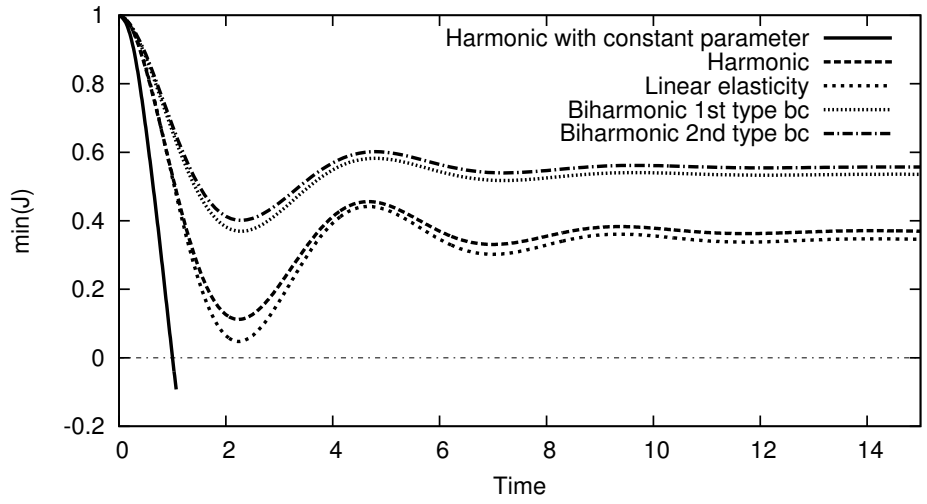

Figure 7.2. Comparison of the $\min(\hat{J})$ for the harmonic, linear-elastic, and biharmonic mesh motion models for the CSM 1 test. Degeneration of the mesh cells corresponds to negative values of $\hat{J}$, which is the case using the harmonic mesh motion model with a constant parameter.

Discussion of the CSM 4 test

Due to the higher gravitational force $\hat{f}_s = 4ms^{-2}$ applied to the structure, the beam is deformed to a greater extent than in the previously described test.

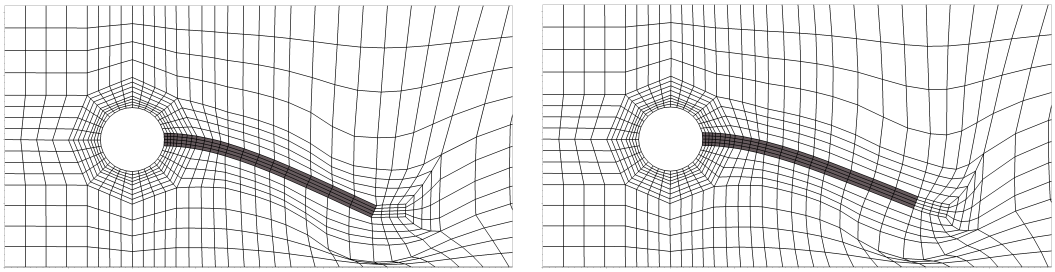

Figure 7.3. CSM 4 test with the harmonic and linear-elastic mesh motion models and gravitational force $\hat{f}_s = 4ms^{-2}$. Both models lead to mesh distortion close to the lower boundary.

For this test case, only the biharmonic mesh motion model equipped with the second type of boundary conditions leads to results. This effect occurs because the outermost mesh layer is not deformed when using the first type of boundary conditions. However, the second type can deal with this factor because the mesh is allowed to move in a tangential direction along the outer boundary and prevent mesh degeneration. The measurements can be observed in Table 7.1. Screenshots of the meshes are given in Figure 7.4. A quantitative study of the $\min(\hat{J})$ is provided in Figure 7.5.

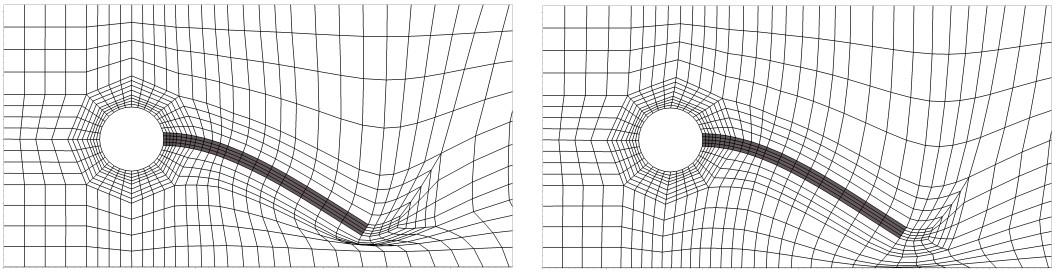

Figure 7.4. CSM 4 test with biharmonic mesh motion model and gravitational force $\hat{f}_s = 4ms^{-2}$. In the left picture the mesh cells distort using the first set of boundary conditions. In the right figure the second kind of boundary conditions are used.

Table 7.1. Results for the CSM 4 test with biharmonic mesh motion and second type of boundary conditions.

DoF	$u_x(A)[\times 10^{-3}m]$	$u_y(A)[\times 10^{-3}m]$
27744	-25.2199	-121.971
42024	-25.2805	-122.132
72696	-25.3101	-122.214
133992	-25.3268	-122.259

We observe that the biharmonic mesh motion model leads to a smoother fluid mesh compared to the other two mesh motion models, seen in the Figures 7.3 and 7.4. The function plots of the $\min(\hat{J})$ in the Figures 7.2 and 7.5 indicate that the global minimum of the biharmonic models is further away from zero compared to the global minimums of the harmonic and linear-elasticity approaches. In other words, the mesh distortion is smaller when using the biharmonic mesh motion model.

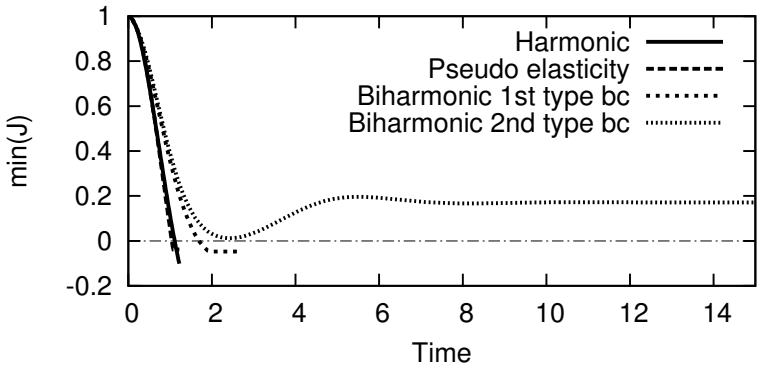

Figure 7.5. Function plots of $\min(\hat{J})$ for the mesh motion models of the CSM 4 test. Degeneration of mesh cells corresponds to negative values of $\hat{J}$, arising in the first three models.

7.2 Adaptive mesh refinement for steady-state heart-valve settings

In this section, we discuss the first part of a prototypical setting for a heart-valve simulation. This numerical example is designed to verify the theoretical considerations of Chapter 6. Consequently, this part is motivated to quantify different mesh refinement techniques for valve simulations, considering that the major disadvantage of our approach is a higher computational cost because we solve both the complete fluid equations and also the complete structure equations also in the artificial domain (see Figure 7.6). To overcome this deficiency, we could either solve reduced equations in the artificial layer L^{ext}, use a coarser initial mesh in the artificial part, or refine the mesh automatically during the solution process. We present a combination of the last two latter techniques. First, we coarsen the initial mesh manually in the artificial domain. Furthermore, we use refinement indicators that are obtained by measuring the smoothness of the discrete solutions. These indicators are achieved in a heuristic manner. To determine whether or not this refinement technique also holds for rigorous a posteriori error estimation, we discuss the DWR method for stationary valve settings. The results are summarized in [146, 147].

Configuration

The (reference) configuration $\widehat{\Omega}$ of the test case is illustrated in Figure 7.6. The principal dimensions are $L^{\text{heart}} + L^{\text{aorta}} = 6.0cm, L^{\text{ext}} = 3cm, H = 2.9cm, D = 2.5cm, d = 0.1cm$.

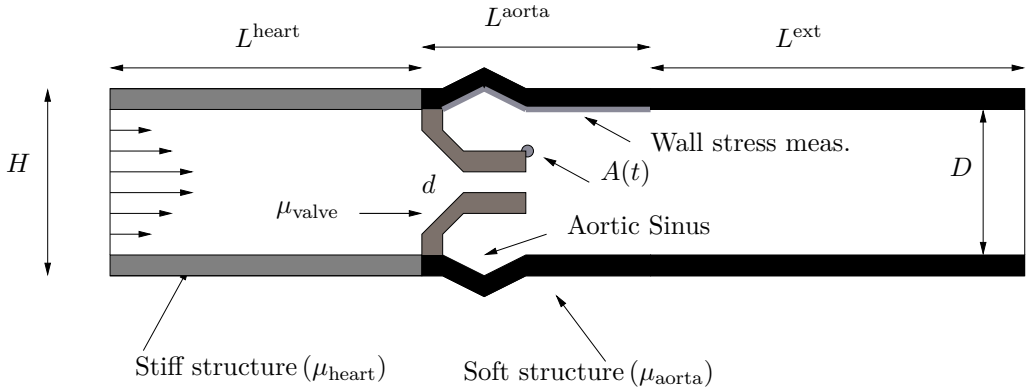

Figure 7.6. Configuration of the heart-valve setting for adaptive mesh refinement.

Inflow and boundary conditions

A parabolic constant inflow-velocity profile is prescribed on $\widehat{\Gamma}_{\text{in}}$ by

$$v_f(0,y) = \hat{v}^D \frac{(y - D/2)(y + D/2)}{0.25D^2}, \quad \hat{v}^D = 10^{-2} cm/s,$$

leading to a steady-state solution. The do-nothing condition is used on $\widehat{\Gamma}_{\text{out}}$ (right boundary D in Figure 7.6).

The structure is fixed on $\hat{\Gamma}_{\text{in}}$ and $\hat{\Gamma}_{\text{out}}$ and it is left free at the outer elastic walls, to allow them to move (however, in this test case, we do not expect large deformations of the outer structure).

Quantities of comparison and their evaluation

We evaluate the deflections in both the x- and the y-directions at the tail of the upper valve at the point $A(0) = (3.64, 0.35)$. In the first test case, the y-deflection of that point is taken as goal functional for mesh refinement with the DWR method (see Example (6.1) for its evaluation). In the second example, we take the line integral for the measurement of wall stress as goal functional, which is computed along the interface of the aorta and the blood (see Example (6.2) for its evaluation).

Parameters

For the fluid, we use the density $\rho_f = 1gcm^{-3}$, and the viscosity $\nu_f = 0.03cm^2s^{-1}$. The elastic structure is characterized by the density $\rho_s = 1gcm^{-3}$, the Poisson ratio $\nu_s = 0.3$, and the Lamé coefficients $\mu_{\text{heart}} = 10^8 gcm^{-1}s^{-2}$, $\mu_{\text{valve}} = 5.0 * 10^5 gcm^{-1}s^{-2}$, $\mu_{\text{aorta}} = 10^6 gcm^{-1}s^{-2}$, and $\mu_{\text{ext}} = 10^6 gcm^{-1}s^{-2}$. We remind the reader that the adjustment of the both damping parameters is redundant because $\hat{v}_s = 0$.

Discussion of the results for the point value evaluation

The deflections in the both principal directions are displayed for a sequence of locally refined meshes with the DWR method in Table 7.2. A comparison between the three proposed refinement types can be observed in Figure 7.7. The reference value for the error determination is computed on a very fine mesh obtained by global refinement and extrapolation of the solution. We monitor the same convergence rate for both global refinement and local mesh adaption with the DWR method. However, as expected, we detect a better constant when using the DWR method. The heuristic indicator performs worse than the other two procedures and should not be used for rigorous a posteriori mesh adaption in this numerical example. The corresponding meshes are displayed in Figure 7.8 for solutions on three different mesh levels.

Discussion of the results for the wall stress evaluation

In addition to the previous statements, we observe that both the DWR method and the heuristic mesh refiner beat global mesh refinement in the second test case. The corresponding meshes of the DWR method are displayed in Figure 7.9 for solutions on three different mesh levels. The good performance of the smoothness-based refinement for the computation of the wall stresses is exploited for the nonstationary examples in Section 8.4.

Table 7.2. The displacements of the control point A for a sequence of mesh levels of locally refined meshes with the DWR method. The goal functional is given by the y-component of the point A. The reference value is computed on a globally refined mesh (last row).

Cells	DoF	$A(x)[10^{-4}cm]$	$A(y)[10^{-4}cm]$
188	3996	2.6153	8.7667
233	5136	2.6921	9.1156
479	10556	2.7576	9.1793
926	20232	2.7674	9.1706
1721	37484	2.7700	9.1636
2882	62912	2.7742	9.1629
4685	101804	2.7763	9.1621
12032	242500	2.7651	9.1538

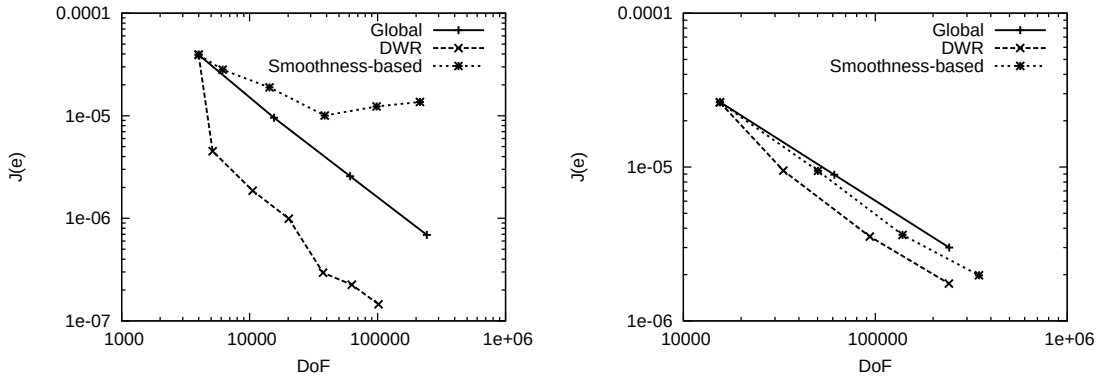

Figure 7.7. Error of the point y-evaluation at the tail A of the upper valve (left) and the wall stress evaluation (right) versus the number of degrees of freedom, for uniform refinement, the weighted indicator obtained with the DWR method, and smoothness-based indicators.

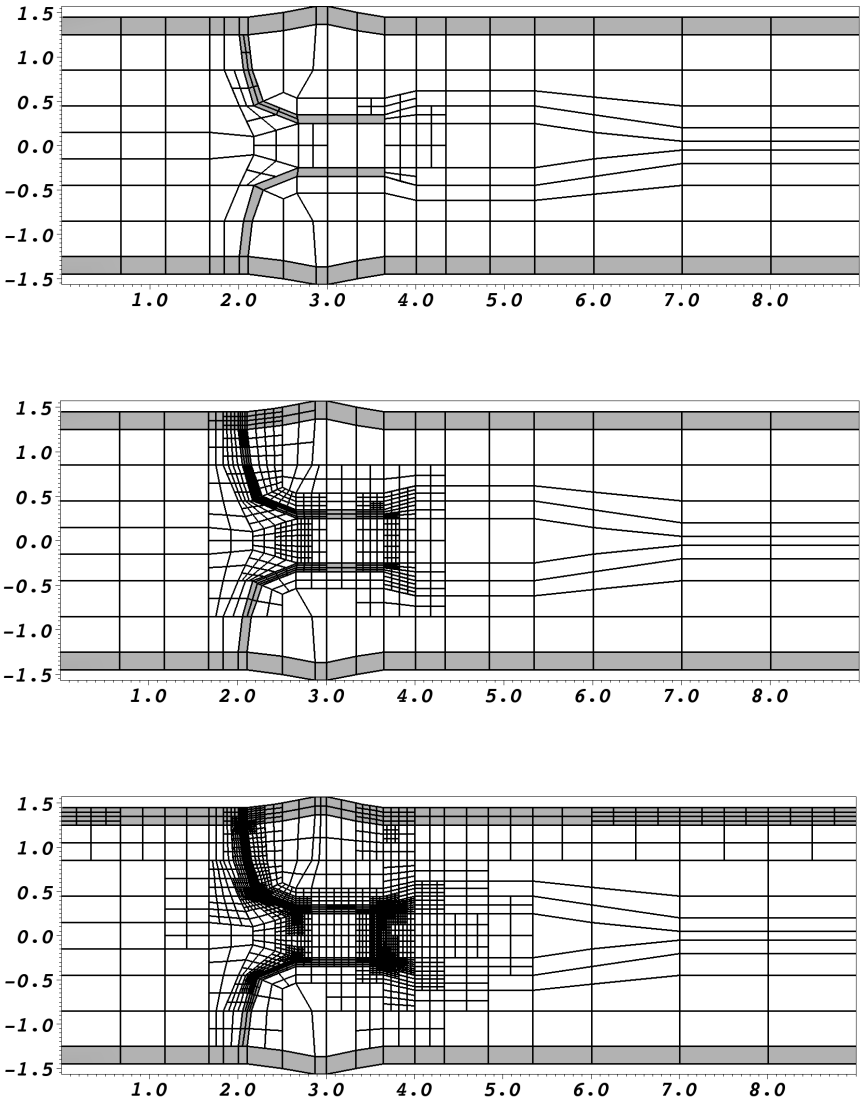

Figure 7.8. Meshes with 233, 926, and 4685 cells obtained with the DWR estimator for the point y-evaluation at A as target functional. The unit of the both axes is cm.

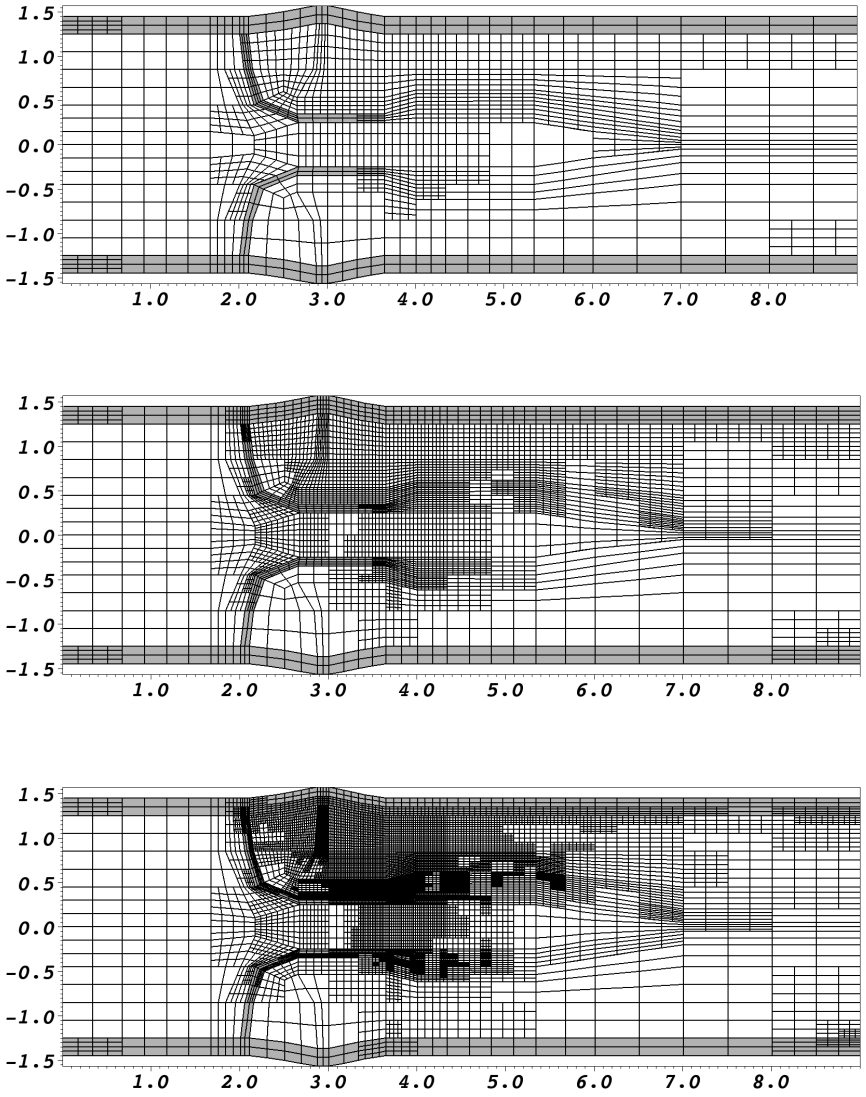

Figure 7.9. Meshes with 1580, 4496, and 11636 cells obtained by the DWR estimator for the wall stress evaluation along the interface of L^{aorta} as target functional. The unit of the both axes is *cm*.

7.3 Optimal control for heart-valve settings

In this example, we present the results of wall stress minimization where the state is given by a fluid-structure interaction system. The theoretical framework is explained in Chapter 4. We choose different mean inflow velocities on globally refined meshes. By increasing the inflow velocity, the state is slightly shifted to nonstationary behavior. Consequently, the optimization process is used to compensate the nonstationary character of the flow field. Other ideas of optimal control for fluid-structure interactions are presented in the literature [77, 121, 134], where the first article is based on [13].

Configuration and Parameters

The configuration is again inspired by a heart-valve setting. In the first example, we consider a bypass that is discharged into the channel. This hole is closed in the second example such that we deal with the configuration that is sketched in Figure 7.6. The principal dimensions are $L^{\text{heart}} + L^{\text{aorta}} = 6.0cm, L^{\text{ext}} = 6cm, H = 2.9cm, D = 2.5cm, d = 0.1cm$. The bypass diameter is given by $1cm$.

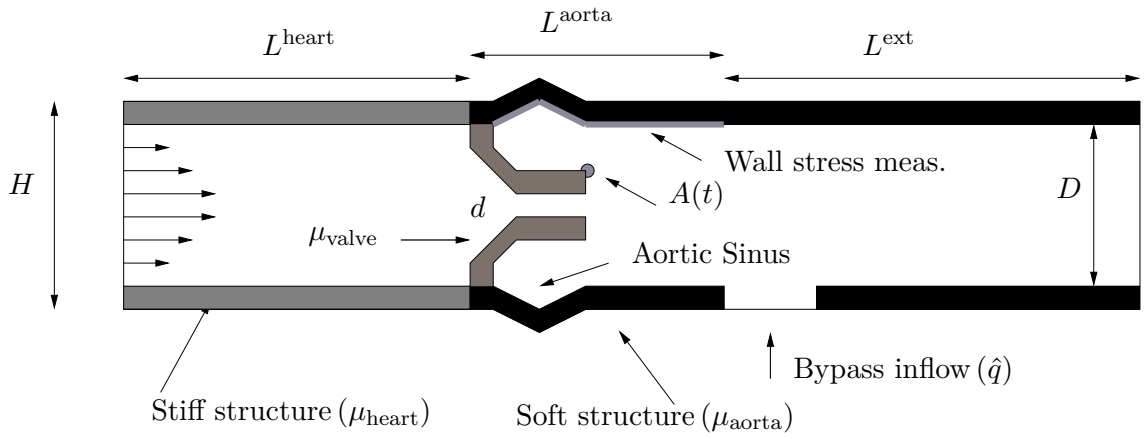

Figure 7.10. Configuration of the heart-valve setting with bypass inflow.

Boundary and initial conditions

A parabolic constant inflow velocity profile is prescribed on $\widehat{\Gamma}_{\text{in}}$ by

$$v_f(0, y) = \hat{v}^D \frac{(y - D/2)(y + D/2)}{0.25D^2},$$

where $\hat{v}^D$ is chosen as $0.005, 0.01, 0.02, 0.05$. As before, the do-nothing condition is used on $\widehat{\Gamma}_{\text{out}}$ (right boundary D in Figure 7.10). The structure is fixed on $\widehat{\Gamma}_{\text{in}}$ and $\widehat{\Gamma}_{\text{out}}$ and it is left free at the outer elastic walls as in Example 7.2.

A nonhomogeneous Neumann condition is prescribed on $\widehat{\Gamma}_Q$ (bypass inflow in Figure 7.10) in the case for the first optimal control problem. The initial control on $\widehat{\Gamma}_Q$ is prescribed

as

$$\hat{q}_0 = -0.1,$$

i.e., additional flow enters into the channel through the hole. We emphasize that some flow is sucked out (or pumped in) even for $\hat{q}_0 = 0$, because the pressure is implicitly normalized due to the do-nothing condition on $\widehat{\Gamma}_{\text{out}}$.

In the second example, we use $\mu_{\text{valve}} = \hat{q}$ as control, such that the material stiffness is optimized with respect to the cost functional.

Quantities of comparison and their evaluation

We compute and compare the wall stresses $WS(x)$ and $WS(y)$ with the help of the formula (4.2). The cost functional $J(\cdot,\cdot)$ is determined by (4.3). Further, we evaluate the deflections in both the x- and the y-directions at the tail of the upper valve at the point $A(0) = (3.64, 0.35)$.

Parameters

For the fluid, we use the density $\rho_f = 1gcm^{-3}$, and the viscosity $\nu_f = 0.03cm^2s^{-1}$. The elastic structure is characterized by the density $\rho_s = 1gcm^{-3}$, the Poisson ratio $\nu_s = 0.3$, and the Lamé coefficients $\mu_{\text{heart}} = 10^8 gcm^{-1}s^{-2}$, $\mu_{\text{valve}} = 5.0 * 10^5 gcm^{-1}s^{-2}$, $\mu_{\text{aorta}} = 10^6 gcm^{-1}s^{-2}$, and $\mu_{\text{ext}} = 10^6 gcm^{-1}s^{-2}$. As in the example before, the choice of damping parameters is redundant because $\hat{v}_s = 0$.

7.3.1 Wall stress minimization with Neumann fluid control

To analyze the convergence of the cost functional $J(\cdot,\cdot)$, the problem is computed on a sequence of globally-refined meshes. Moreover, the values for the drag and the lift are displayed in the Figures 7.3 and 7.4, together with their corresponding controls $\hat{q}$, for the four different fluid inflow data.

Table 7.3. Bypass optimal control: the uncontrolled quantities of interest are displayed in the last row. The unit of the wall stress WS is $g/cm\,s^2$.

DoF	$\hat{v}^D[10^{-3}]$	$J[10^{-3}]$	$WS(x)[10^{-3}]$	$WS(y)[10^{-3}]$	$\hat{q}[10^{-1}]$
14756	5	−0.641	+0.254	−1.332	+0.0379
58084	5	−0.641	+0.254	−1.332	+0.0383
230468	5	−0.756	+0.252	−1.477	+0.0386
230468	5	+770.271	−6.816	+270.271	−1.0000
14756	10	+0.910	+0.491	+0.189	+0.0387
58084	10	+0.820	+0.489	+0.077	+0.0391
230468	10	+0.764	+0.488	+0.011	+0.0394
230468	10	+770.912	−5.987	+270.912	−1.0000

Table 7.4. Bypass optimal control: the uncontrolled quantities of interest are displayed in the last row. The unit of the wall stress WS is $g/cm\,s^2$.

DoF	$\hat{v}^D[10^{-3}]$	$J[10^{-3}]$	$WS(x)[10^{-3}]$	$WS(y)[10^{-3}]$	$\hat{q}[10^{-1}]$
14756	20	3.680	+0.917	2.896	+0.0403
58084	20	3.543	+0.911	2.737	+0.0407
230468	20	3.467	+0.909	2.651	+0.0410
230468	20	771.907	−4.468	271.907	−1.0000
14756	50	8.796	+1.728	7.822	+0.0447
58084	50	8.517	+1.713	7.522	+0.0451
230468	50	8.384	+1.708	7.376	+0.0454
230468	50	772.002	−0.993	272.002	−1.0000

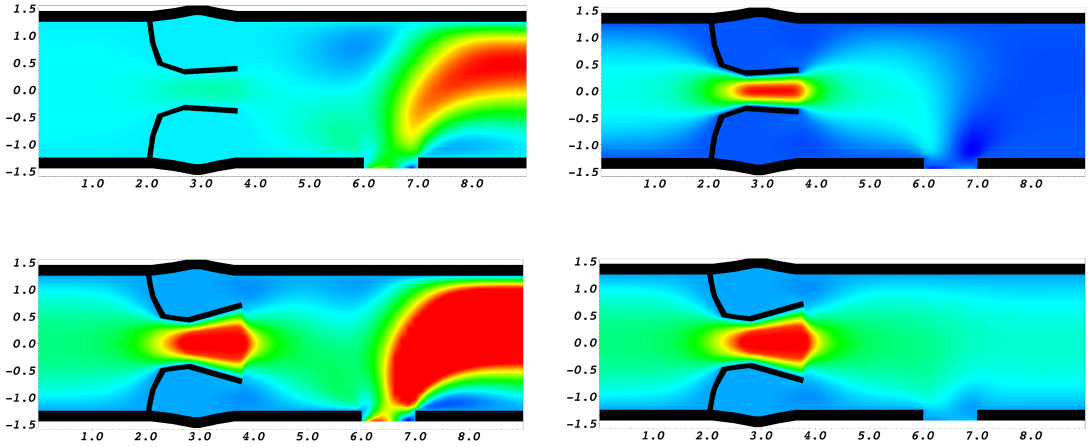

Figure 7.11. Bypass setting: wall stress optimization with Neumann control: x-velocity profile for inflow $\hat{v}^D = 0.01$ (top) and $\hat{v}^D = 0.05$ (bottom). The start solution of the state equation is displayed at the left side. The optimal state is sketched at the right side. The mesh motion displacement is scaled with a factor by 100 to obtain a visible deformation of the heart valves. The highest velocity is indicated in red (dark). The unit of the both axes is cm.

We emphasize that the optimal solution is not admissible in the physical sense because flow is sucked out through the bypass hole. However, it is admissible in the mathematical sense, which is the primary goal of this exercise. To illustrate the behavior of the flow field, two exemplary solutions of the state at the beginning of the optimization process and of the optimal state, are sketched in the Figure 7.11.

7.3.2 Wall stress minimization with structure stiffness control

In this example, we try to minimize again the wall stresses in the aorta, but using the Lamé coefficient $\mu_{\text{valve}} = \hat{q}$ as control. Such a setting might be of interest for artificial heart-valve modeling. In these cases, the surgeon has explicit influence on the stiffness of the valve material.

To analyze the convergence of the cost functional $J(\cdot,\cdot)$, the problem is computed on a sequence of globally-refined meshes. Moreover, the values for the drag and the lift are displayed in the Figures 7.5 and 7.6, together with their corresponding control $\hat{q}$, for the four different fluid inflow conditions. In this example, we also measure the deflections of the valves.

Table 7.5. Optimal control of the structure stiffness with $\hat{v}^D = 0.005$ and $\hat{v}^D = 0.01$. The uncontrolled quantities of interest are displayed in the last row. The wall stresses WS are measured in $g/cm\,s^2$, and the deflections at the point A are measured in cm.

DoF	$J[10^{-3}]$	$WS(x)[10^{-3}]$	$WS(y)[10^{-3}]$	$A(x)[10^{-4}]$	$A(y)[10^{-4}]$	$\hat{q}[10^5]$
14756	2.2346	0.2618	2.2304	0.0144	0.0469	704
58084	2.2244	0.2616	2.2244	0.0031	0.0098	3601
230468	2.2225	0.2617	2.2225	0.0044	0.0148	2229
230468	2.2235	0.2621	2.2235	1.3410	4.5064	5
14756	3.9143	0.5093	4.3803	0.0230	0.0746	883
58084	3.5124	0.5092	4.3690	0.0448	0.1467	445
230468	3.6521	0.5093	4.3652	0.0088	0.0235	3808
230468	3.6869	0.5105	4.3687	2.6545	8.9071	5

To illustrate the behavior of the flow field, two exemplary solutions of the state at the beginning of the optimization process and of the optimal state, are sketched in the Figure 7.12. The essence of the results of this exercise is that a minimal wall stress is obtained by making the valves stiffer, as illustrated in Figure 7.12.

Table 7.6. Optimal control of the structure stiffness with $\hat{v}^D = 0.02$ and $\hat{v}^D = 0.05$. The uncontrolled quantities of interest are displayed in the last row. The wall stresses WS are measured in $g/cm\,s^2$, and the deflections at the point A are measured in cm.

DoF	$J[10^{-3}]$	$WS(x)[10^{-3}]$	$WS(y)[10^{-3}]$	$A(x)[10^{-4}]$	$A(y)[10^{-4}]$	$\hat{q}[10^5]$
14756	8.4440	0.9577	8.4100	0.0438	0.1413	918
58084	8.3886	0.9577	8.3886	0.1037	0.3412	383
230468	8.3973	0.9582	8.3827	0.0023	0.0064	23481
230468	8.3973	0.9621	8.3973	5.2033	17.4053	5
14756	17.948	1.8472	17.728	0.1259	0.4036	764
58084	17.857	1.8518	17.700	0.0213	0.0640	5206
230468	17.834	1.8553	17.699	0.0215	0.0648	5148
230468	17.834	1.8828	17.834	12.2939	40.7247	5

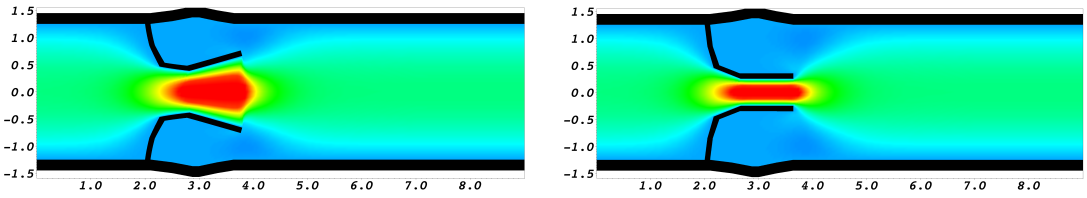

Figure 7.12. Optimal control of the structure stiffness: x-velocity profile for inflow $\hat{v}^D = 0.05$. The start solution of the state equation is displayed at the left side. The optimal state is sketched at the right side. The mesh motion displacement is scaled with a factor by 100 to obtain a visible deformation of the heart valves. The highest velocity is indicated in red (dark). A minimal wall stress is obtained by making the valves stiffer. The unit of the both axes is cm.

7.4 FSI in 3D: an elastic bar behind a square cross section

This section is devoted to a three-dimensional fluid-structure interaction problem. In these cases, it is challenging to deal with computational time (namely to solve the linear equation systems) and convection-dominated behavior. We developed a 3D-FSI code for nonstationary numerical tests that is validated for a quasi-stationary problem. Consequently, the solution is computed with help of a pseudo-time-stepping procedure using the backward Euler scheme. We compare the harmonic mesh motion model with the biharmonic model for moderate deformations. The results of this example are already published in [149].

Configuration and Parameters

The configuration is based on the fluid benchmark example proposed in [122].

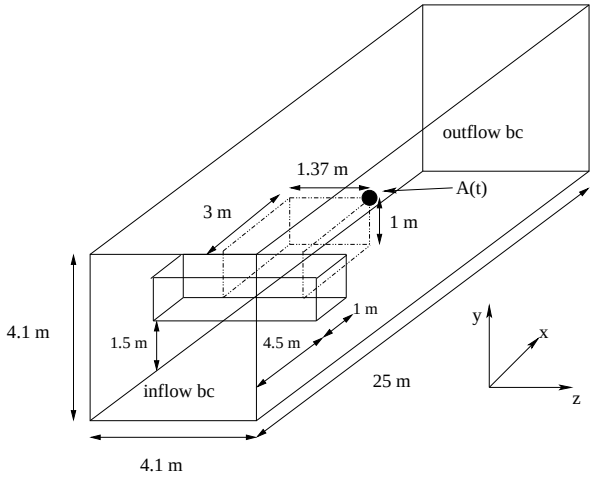

Figure 7.13. Configuration: flow around square cross section with elastic beam.

We use the following parameters to drive the simulation: $\varrho_f = 1.0\,kgm^{-3}$, and $\nu_f = 0.01\,m^2s^{-1}$ for the fluid. For the structure, we use $\varrho_s = 1.0\,kgm^{-3}$, $\nu_s = 0.4$, and $\mu_s = 500.0\,kgm^{-1}s^{-2}$.

Initial conditions and boundary conditions

A constant parabolic inflow velocity profile is given on $\hat{\Gamma}_{\text{in}}$ by

$$v_f(t,0,y) = 16.0\,\bar{v}\,yz\frac{(H-y)(H-z)}{H^4}, \quad \bar{v} = 0.45ms^{-1}.$$

At the outlet $\hat{\Gamma}_{\text{out}}$ the do-nothing outflow condition is used.

Quantities of comparison

1) x-, y-, and z-deflection of the beam at $A(t)$ with $A(0) = (8.5, 2.5, 2.73)[m]$.

2) Drag and lift around square cross section and elastic beam, with help of Equation (8.1).

Results

The results for the different quantities of interest are in agreement between both of the mesh motion models, as illustrated in Table 7.7.

Table 7.7. Results for the steady-state 3D FSI test case with harmonic (four upper rows) and biharmonic (four lower rows) mesh motion. Evaluation of x-,y-,and z-deflections (in $[m]$); each scaled by 10^{-6}. In the last two columns drag and lift forces are displayed (in $[N]$).

Cells	DoF	$u_x(A)$	$u_y(A)$	$u_z(A)$	F_D	F_L
78	5856	9.5106	32.7193	-4.0278	0.6633	0.0502
281	19694	23.8909	-17.7207	-2.9588	0.7647	-0.1996
624	39312	17.1212	-0.4168	-2.7161	0.7753	0.0103
4992	286368	18.6647	0.1522	-3.0243	0.7556	0.0113
78	8628	9.5115	32.7149	-4.0277	0.6632	0.0502
281	28979	23.794	-17.2999	-2.9692	0.7671	-0.1964
624	57720	17.123	-0.41921	-2.7155	0.7753	0.0103
4992	-	-	-	-	-	-

Computational cost for the numerical Tests 7.1 and 7.4 (from [149])

Finally, we summarize our observations with regard to the computational cost per Newton step. In each nonlinear step (see Equation (5.35)), the Jacobian matrix and the residual are evaluated and then solved by a direct solver (UMFPACK). Our results indicate that using the biharmonic equation is much more expensive in each Newton step. Concretely, the cost in two dimensions is five times higher for the biharmonic mesh motion model compared to the other two models. In three dimensions the factor for low amount of degrees of freedom (DoF) is again five. Whereas for 624 cells in three dimensions the factor becomes 70. It seems to be the linear solver, but it is still an open question. A detailed study is given in [149]. This result indicate, using the biharmonic model with UMFPACK in three dimensions becomes prohibitive in a sequential solution process. Consequently, one should use iterative solvers as discussed in Section 5.7 and/or a parallel programming code.

Outlook to the next chapter

In this chapter, we validated our theoretical findings of the previous chapters for stationary problems. In the following chapter, we upgrade our configurations to show the performance of our algorithms for computing nonstationary fluid-structure interactions.

8 Numerical Results for Nonstationary Problems

The last chapter of this work is devoted to the discussion of nonstationary fluid-structure interaction problems. In the first numerical example, we compare different fluid mesh motion models for large deflections of a continuously moving structure (we refer the reader also to Chapter 7, Example 7.1). The configuration is driven by prescribing pressure differences at the inflow and outflow boundaries. Parts of the results of this example have been published [149], but here we add a comparison study of the different structure models, which is the novel aspect of this work. In Section 8.2, we study the FSI 2 benchmark that was proposed by Turek and Hron [84] and which has been intensively analyzed in recent years [30]. This example is used to validate our programming code for fully nonstationary, long-term FSI computations. The next Section 8.3, provides numerical results of our discussion in Section 3.5 that may be important for future investigations and coupling techniques for fluids and pressures with structural conditions on artificial boundaries. Moreover, a numerical comparison of weak and strong structure damping is studied there. In the final Section 8.4, we approach the *heart* of this thesis, we apply the theoretical investigations of the damped structure equations and substantiate most of our theoretical findings.

8.1 Membrane on fluid test - large structural deformations

The purpose of this example is to test our framework for large structural deformations [11]. We modify the given configuration by enlarging the height of the membrane. We use the INH, the IMR, and the STVK models to characterize the structure. The IMR model was originally suggested for this test case [11]. Parts of the results of this section can be found in [149].

In addition to our previous findings, we add in this thesis a comparison study of the three different models for structures, namely the INH, the IMR, and the STVK model. The test is driven by a pressure difference between $\hat{\Gamma}_{\text{in}}$ and $\hat{\Gamma}_{\text{out}}$. We choose the time step size $k = 0.01$ and the implicit Euler time stepping scheme.

Configuration and Parameters

We use the following parameters to run the simulation: $\varrho_f = 1000.0\, kgm^{-3}$, and $\nu_f = 0.004\, m^2 s^{-1}$ for the fluid. For the structure, we use $\varrho_s = 800.0\, kgm^{-3}$, $\mu_s = 2.0 * 10^7\, Pa$, $\mu_2 = 1.0 * 10^5\, Pa$.

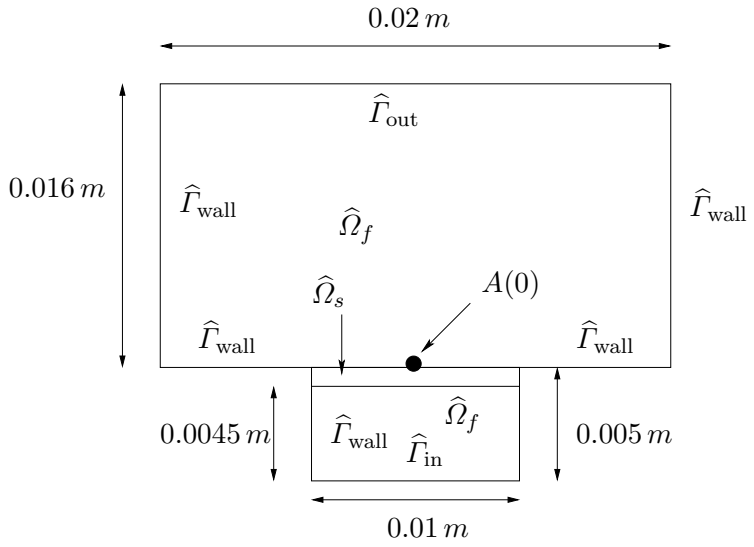

Figure 8.1. Configuration of the large deformation membrane on fluid test.

Initial conditions and boundary conditions

On the lower boundary $\hat{\Gamma}_{\text{in}}$ and upper boundary $\hat{\Gamma}_{\text{out}}$ boundary we prescribe a Robin-type boundary condition for the velocity and pressure and homogeneous Dirichlet conditions for the displacement. On all remaining parts we prescribe homogeneous Dirichlet conditions for the velocity and the displacement:

$$\begin{aligned}
\hat{u} &= 0 && \text{on } \hat{\Gamma}_{\text{in}} \cup \hat{\Gamma}_{\text{out}} \cup \hat{\Gamma}_{\text{wall}} \\
\hat{v} &= 0 && \text{on } \hat{\Gamma}_{\text{wall}} \\
\nu_f \partial_n \hat{u} - \hat{p}\hat{I} \cdot \hat{n}_f &= \hat{p}_{\text{in}} \cdot \hat{n}_f && \text{on } \hat{\Gamma}_{\text{in}}, \\
\nu_f \partial_n \hat{u} - \hat{p}\hat{I} \cdot \hat{n}_f &= 0 && \text{on } \hat{\Gamma}_{\text{out}}.
\end{aligned}$$

The pressure $\hat{p}_{\text{in}}$ is increased during the computation, i.e., $\hat{p}_{\text{in}} = t * \hat{p}_{\text{initial}}$ with $\hat{p}_{\text{initial}} = 5.0 * 10^6 Pa$.

Quantities of comparison

1) The y-deflection of the structure at the point $A(t)$ with $A(0) = (0.0, 0.005)[m]$.
2) The principal stretch of the fluid cells under the membrane, i.e., the stretch between the points $(0.0, 0.005)[m]$ and $(0.0, 0.0025)[m]$.
3) The measurement of $\min(\hat{J})$.

Discussion of the results

The qualitative behavior of the numerical results does agree with the findings in [11]. However, we use quadrilaterals for the discretization, whereas the other authors use triangles. This is one reason why we get a smaller maximal deformation of the membrane.

Moreover, we use the same overall mesh for the fluid and the structure domains, which leads to high anisotropies in the structure when working with a very thin membrane (see Figure 8.4). For this reason, we enlarged the membrane to prevent difficulties due to the anisotropies.

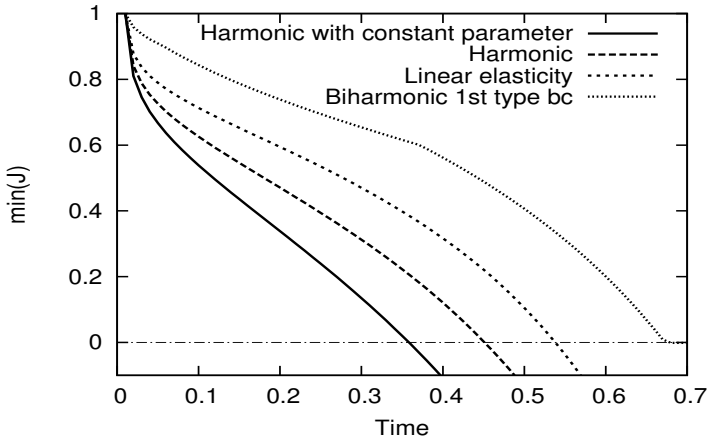

Figure 8.2. Function plots of $\min(\hat{J})$ for the mesh motion models of the membrane on fluid test. Degeneration of mesh cells corresponds to negative values of $\hat{J}$, arising in the first three models.

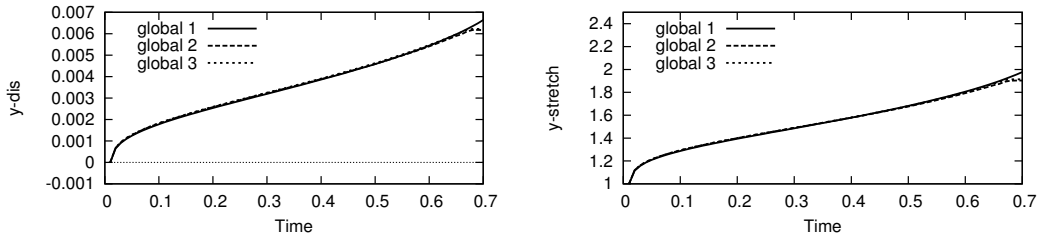

Figure 8.3. Large deformation membrane fluid test with the biharmonic mesh model for three different mesh levels. Left: vertical displacement of the point $(0.0, 0.005)$. Right: stretch of the cell under the membrane.

In the following, we compare the different structure models and in which we employ the STVK material with $\nu_s = 0.3$ and $\nu_s = 0.4$, respectively. We observe that the STVK model is not suitable to deal with large structural deformations as sketched in Figure 8.6.

The failure of the STVK material is due to the model properties because the mesh still behaves fine. This observation becomes clear when the minimal determinant $\hat{J}$ is monitored (see Figure 8.5), which does not degenerate using the STVK material. In contrast, the other two materials (INH and IMR) enables large deflections until the mesh degenerates. Moreover, we do not observe any significant difference between these two models (see Figure 8.6), from which we suggest, to work with the INH model in this test case because it is the simplest material model.

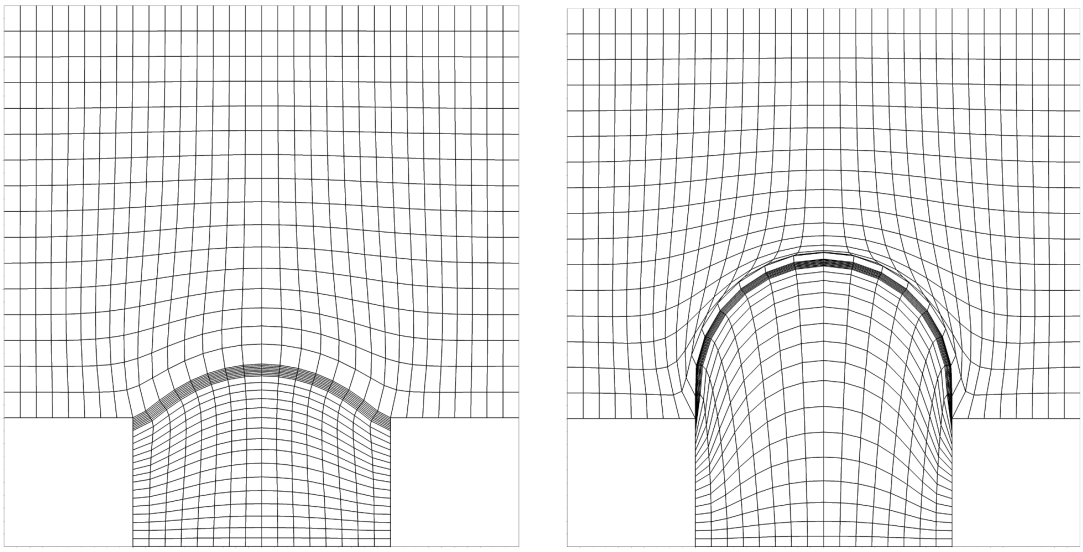

Figure 8.4. Large deformation membrane on fluid test. The mesh deformation using the biharmonic model at the times $t = 0.12$ (left) and $t = 0.7$ (right) are displayed.

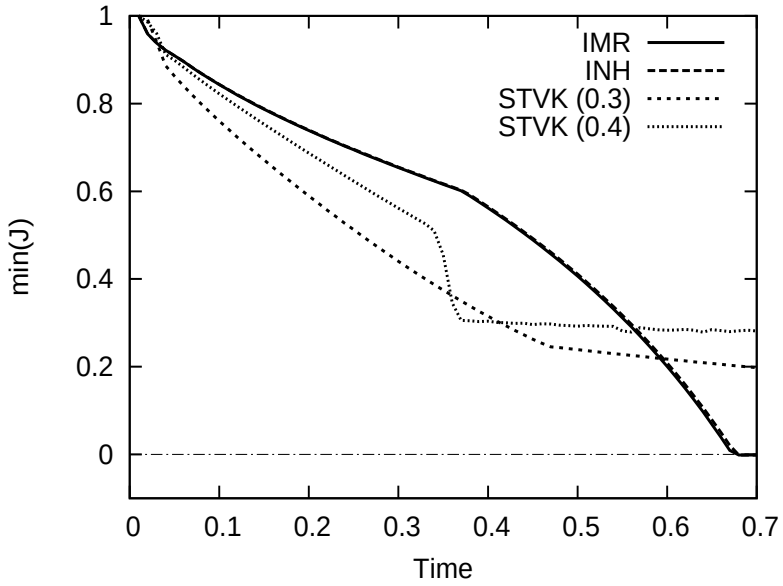

Figure 8.5. Function plots of $\min(\hat{J})$ for the comparison of structure models of the membrane on fluid test. Degeneration of mesh cells corresponds to negative values of $\hat{J}$, which can be monitored for the INH model and the IMR material.

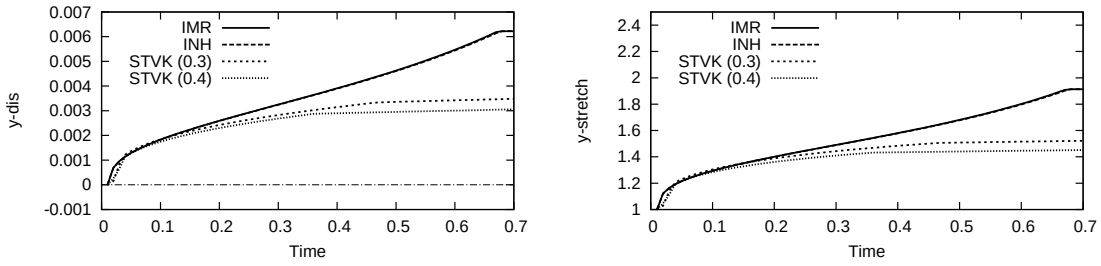

Figure 8.6. Large deformation membrane fluid test for the comparison of structure models. At left: the vertical displacement of the point $(0.0, 0.005)$. At right: the stretch of the cell under the membrane. For both quantities of interest the INH and the IMR models exhibits similar behavior.

8.2 FSI 2 benchmark

In this example, we have two different goals in mind. The first goal is the validation of our programming code for solving fully nonstationary fluid-structure interactions. We consider the numerical benchmark tests FSI 1, FSI 2 & 3 [84]. New results by other authors can be found in the literature [29, 30, 39, 134]. The second intention of this example is a comparison of the three proposed mesh motion models introduced in Section 3.3.2. The backward Euler scheme is utilized as pseudo-time-stepping scheme for the FSI 1 test. The Fractional-Step-θ scheme, as presented in Equation (5.7), is used for time discretization for the FSI 2 test. In the last test, FSI 3, the shifted Crank-Nicolson scheme is employed. The FSI 2 & 3 test cases are computed with different time steps in order to monitor the convergence with respect to time. Finally, we mention the comparison of different time-stepping schemes in Section 5.4, for which the present example serves as configuration.

Due to large deformations of the elastic beam, using the proper mesh motion model becomes crucial. The mesh-dependent parameters used for the harmonic and linear-elastic approaches are the same as were used for the CSM tests discussed previously. We also refer to Section 5.4, where we compare the different time-stepping schemes using the present configuration.

Configuration

The configuration is the same as for the CSM tests, which is sketched in Figure 7.1.

Boundary conditions (for FSI 2)

A parabolic inflow velocity profile is given on $\hat{\Gamma}_{\text{in}}$ by

$$v_f(0, y) = 1.5\bar{v}\frac{4y(H-y)}{H^2}, \quad \bar{v} = 1.0ms^{-1}.$$

At the outlet $\hat{\Gamma}_{\text{out}}$ the do-nothing outflow condition is imposed. The remaining boundary conditions are chosen as in Section 7.1.

Initial conditions

For the unsteady tests, a smooth increase of the velocity-profile in time is chosen:

$$v_f(t;0,y) = \begin{cases} v_f(0,y)\frac{1-\cos(\frac{\pi}{2}t)}{2} & \text{if } t < 2.0s \\ v_f(0,y) & \text{otherwise.} \end{cases}$$

Quantities of comparison and their evaluation

1) The x- and y-deflection of the beam at $A(t)$.

2) The forces exerted by the fluid on the whole body, i.e., the drag force F_D and lift force F_L on the rigid cylinder and the elastic beam. They form a closed path in which the forces are computed with the help of line integration. The formula is evaluated on the fixed reference domain $\hat{\Omega}$ and reads:

$$(F_D, F_L) = \int_{\widehat{\Gamma}_O} \hat{J}\hat{\sigma}_{all}\hat{F}^{-T} \cdot \hat{n}\, d\hat{s} = \int_{\widehat{\Gamma}_{\text{cylinder}}} \hat{J}\hat{\sigma}_f\hat{F}^{-T} \cdot \hat{n}_f\, d\hat{s} + \int_{\widehat{\Gamma}_i} \hat{J}\hat{\sigma}_f\hat{F}^{-T} \cdot \hat{n}_f\, d\hat{s}. \quad (8.1)$$

The quantities of interest for this time-dependent test case are represented by the mean value, amplitudes, and frequency of x- and y-deflections of the beam in one time period T of oscillations.

Parameters (for FSI 2)

We choose for our computation the following parameters. For the fluid, we use $\varrho_f = 10^3 kgm^{-3}$, $\nu_f = 10^{-3}m^2s^{-1}$. The elastic structure is characterized by $\varrho_s = 10^4 kgm^{-3}$, $\nu_s = 0.4$, $\mu_s = 5 * 10^5 kgm^{-1}s^{-2}$.

Discussion of the results

We observe the same qualitative behavior in each of our approaches for the quantities of interest ($u_x(A)$, $u_y(A)$, drag, and lift); these results are in agreement with [134].

The computed values are summarized in [149] in which the reference values are taken from [134]. In general, to verify convergence with respect to space and time, at least three different mesh levels and time step sizes should be presented. Three different mesh levels are not possible when working with the simplest approach: harmonic mesh motion. For the third mesh level, the $\min(\hat{J})$ becomes negative, and the ALE-mapping bursts off.

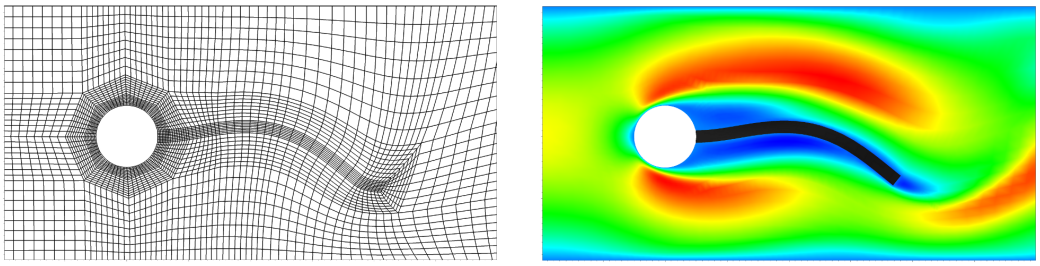

Figure 8.7. FSI 2 test case: mesh (left) and velocity profile in vertical direction (right) at time $t = 16.14s$. Specifically, we observe a smooth fluid mesh near the tip of the elastic beam. In this test, the fluid mesh motion was realized with help of the biharmonic model.

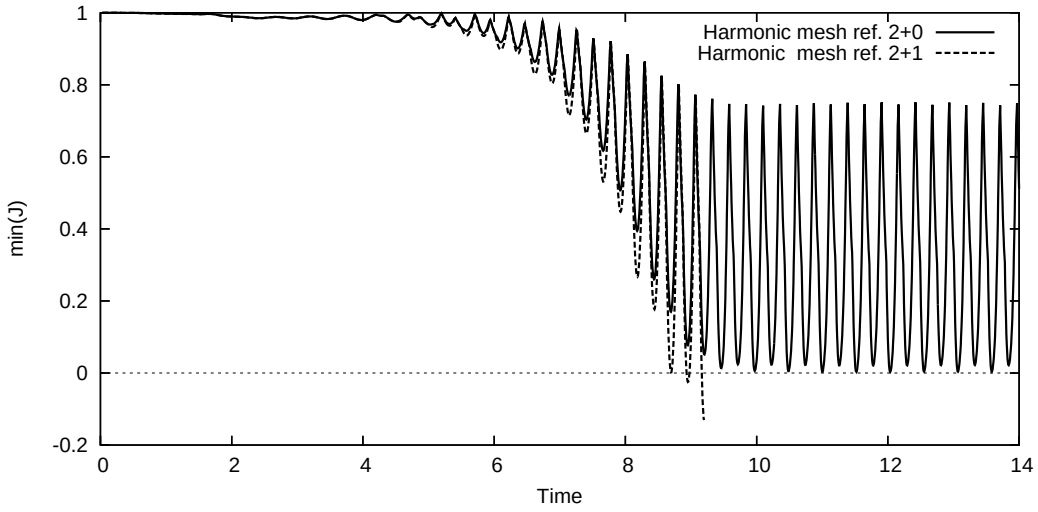

Figure 8.8. Comparison of the minimal values of $\hat{J}$ for the FSI 2 test case computed with harmonic mesh motion. The refinement cycle $2+0$ corresponds to 19488 unknowns, the other refinement cycle $2+1$ (two times globally refined and one times locally refined) represents 29512 unknowns. We observe mesh cell distortion for the $2+1$ refinement level.

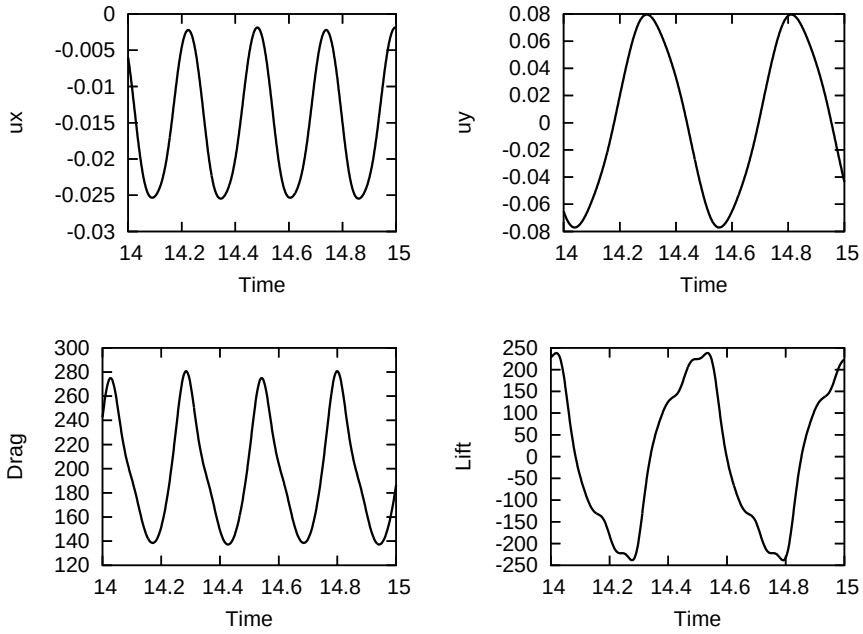

Figure 8.9. FSI 2: the deflections of the beam, $u_x(A)$ and $u_y(A)$ (in cm), and the drag and the lift evaluation (in $kg/m\,s^2$) are displayed versus time (in s).

Recapitulation of our findings for the FSI 2 test (taken from [149])

The x-displacements show the same behavior for all configurations. For the y-displacements, we observe the same behavior on the coarse mesh as we do for the harmonic and biharmonic approaches. However, the elastic approach yields nearly the same results on the different mesh levels. The drag values are similar for the first two mesh levels for each mesh motion model. The results on the finest mesh for the biharmonic approach match the reference values. The most difficult task is to compute the lift values. These difficulties are a well-known phenomenon from fluid mechanics and the related benchmark computations. These values also varies in the literature [39, 84, 134].

Recapitulation of our findings for the FSI 1 and FSI 3 tests (taken from [135])

The programming code for solving fluid-structure interaction was first validated by computing the FSI 1 and FSI 3 benchmark tests [30]. In the framework of the *Research Unit 493 (FOR 493) - Fluid-Structure Interaction: Modeling, Simulation, Optimization*, we computed (and compared) the previous mentioned benchmark settings. Our method is described in the book [29] in the last article [135] on page 419, Method 2b (Rannacher) and the results are displayed on the pages 422 and 423 (Method 2b). Our results are in comparison with the results obtained by the other groups. With this observation, we trust our numerical algorithms to work correctly.

8.3 Coupling of fluid and structure boundary conditions

This numerical example has two goals. First, we are interested in the numerical difference between weak and strong damping of the hyperbolic structure equations. Second, we conduct a preliminary step to account for pressure wave propagation in compliant vessels, such as arteries (or for heart-valve dynamics in the compliant aorta). Therefore, the aim is to investigate the interchange of the absorbing fluid conditions and the damped structure equations and their influence on blood vessel movement due to structure wave backflow. The theoretical background is described in Section 3.5.

We compute a prototypical numerical example (with the backward Euler scheme) to test our configuration. We use the time-step size $k = 0.001$ and the final time is chosen as $T = 1.0$. The geometry and the parameters are related to a carotid artery in the human body. They were taken from the literature [56] and are further discussed [105, 106].

Configuration

The (reference) configuration $\widehat{\Omega}$ of the numerical test case is illustrated in the Figure 1. In particular, we set $\hat{L} = 4.0cm$, $\hat{L}^{\text{ext}} = 0.75cm$, $\hat{H} = 0.6cm$, and $\hat{D} = 0.4cm/s$.

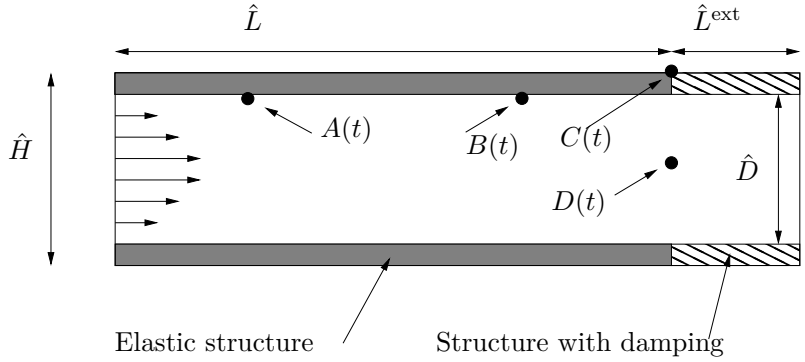

Figure 8.10. Configuration of the numerical tests for the coupling of absorbing fluid conditions with the damped wave equation.

Inflow and boundary conditions

A parabolic velocity impulse

$$v_f(0, y) = \bar{v} * \sin(t * \pi * 200) * (y - 0.2)(y + 0.2), \quad \bar{v} = 45.0\, cm/s,$$

is prescribed on $\widehat{\Gamma}_{\text{in}}$ (left boundary $\hat{H}$) during $0.005s$, i.e.,

$$v_f(t; 0, y) = \begin{cases} v_f(0, y) & \text{if } t < 0.005s \\ 0 & \text{otherwise.} \end{cases}$$

This configuration leads to the Reynolds number

$$Re = \frac{\bar{v}D}{\nu_f} = \frac{45 * 0.4}{0.035} = 514.$$

For the first set of tests, the do-nothing condition is used on $\widehat{\Gamma}_{\text{out}}$ (right boundary D). Second, the absorbing boundary conditions (described in Section 3.5) are prescribed on $\widehat{\Gamma}_{\text{out}}$, such that an proper mean pressure value is computed at each time step.

Quantities of comparison and their evaluation

We evaluate the structural deflections in both the x- and the y-direction at the points $A(t) = (1.0, 0.2)$, $B(t) = (3.0, 0.2)$, and $C(t) = (4.0, 0.2)$. At $D(t) = (4.0, 0.0)$, we evaluate the pressure. Furthermore, we measure the flux of the velocity on $\widehat{\Gamma}_{\text{out}}$ and the mean pressure on $\widehat{\Gamma}_{\text{out}}$.

Parameters

For the fluid, we use density $\rho_f = 1gcm^{-3}$, and the viscosity $\nu_f = 0.035cm^2s^{-1}$. The elastic structure is characterized by the density $\rho_s = 1.2gcm^{-3}$, the Poisson ratio $\nu_s = 0.3$, and the Lamé coefficient $\mu_{\text{wall}} = 1.15 \times 10^6 gcm^{-1}s^{-2}$, and $\mu_{\text{ext}} = 1.15 \times 10^6 gcm^{-1}s^{-2}$.

In the first example, we test weak, strong, and both damping terms together. To this end, we set $\gamma_w = 10^4$ and $\gamma_s = 10^3$. Thus, the strong damping parameter should be chosen one magnitude lower than the corresponding weak damping parameter. In the second example, we change the structural damping conditions by setting $\gamma_w = 0$ (nondamping) or $\gamma_w = 10^4$ (damping). Furthermore, we set $\gamma_s = 0$.

As in the final numerical tests for the heart-valve settings, the weak damping parameter should be chosen two orders of magnitude lower than the corresponding material parameter μ_{ext}.

8.3.1 Comparison of weak and strong damping

We monitor similar behavior for both damping strategies in Figure 8.11. We emphasize that the strong damping parameter γ_s is one order of magnitude smaller than γ_w. This is reasonable, because for the same choice of parameters, the strong damping is *stronger* than the weak damping. We this choice of parameters, we also encounter the influence of the both strategies using them at the same time in which we monitor further reduction of structure wave backflow.

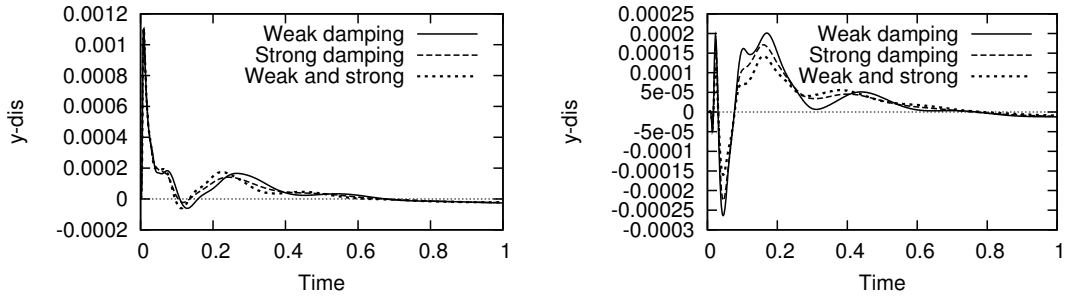

Figure 8.11. Comparison of weak ($\gamma_w = 10^4$) and strong ($\gamma_s = 10^3$) structure damping in the artificial layer at the point $C(t)$. The y-displacement is given in cm, whereas the time unit is s.

8.3.2 Coupling in a straight channel

Our results indicate that the combination of both techniques leads to the *best damping* of structure waves, i.e., the highest energy absorption. This observation is illustrated in Figure 8.12. Moreover, we also monitor that the pressure waves are *best absorbed* using structural wave damping, which is illustrated in Figure 8.13. As before, the combination of both techniques leads to greatest wave reductions.

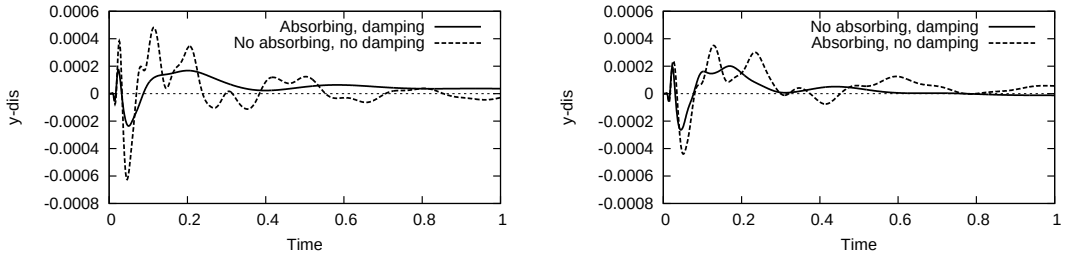

Figure 8.12. Coupling of absorbing fluid conditions with the damped structure equations: evaluation of y-displacement (in cm) at the point $C(t)$. The time unit is s.

We draw the following conclusions from the observations made in this section. A drastic reduction of backflow of structure and pressure waves, we suggest to use an artificial layer with a damped wave equation. However, this might be not the best condition when back-traveling waves caused by bifurcations or other disturbances propagate through the channel.

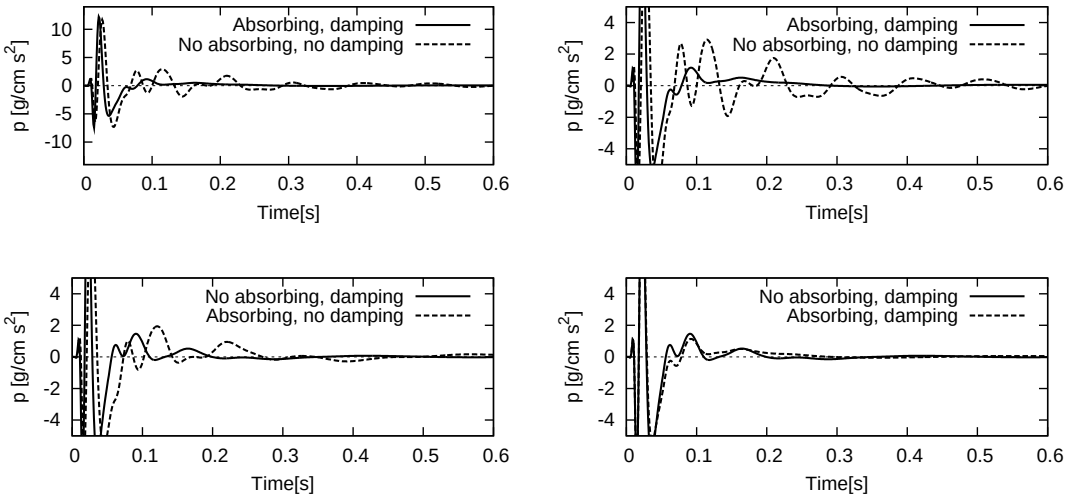

Figure 8.13. Coupling of absorbing fluid conditions with the damped structure equations: evaluation of the pressure at the point $D(t)$. At the upper left, the whole ordinate is shown such that the initial pressure waves can be seen. In the three remaining figures, we cut off the ordinate to be able to study the wave reflections after the first reflected wave at the outflow boundary. In the last figure (lower right), we compare the performance of pure structural damping combined with the absorbing conditions. It can be inferred from this figure that structural damping without absorbing fluid conditions already suffices to prevent back-traveling pressure waves.

8.4 Prototypical heart-valve simulations

In this *core* example, we apply the theoretical aspects of the Sections 2.5, 3.3, 3.4, 5.3. Specifically, we focus our attention on the performance of the damped structure equations for prototypical settings. The data for the material parameters and the geometry are taken from the literature [56, 110] and Figure 8.14, and have been discussed with the cardiologist Mizerski [103].

In this study, we consider a coupling of multiple structures with Newtonian fluid flows in a laminar (but convection-dominated) regime. By changing the material parameters, we are able to divide the structure into several different substructures. Specifically, the first part L^{heart}, is characterized by high stiffness. The material in the middle part, L^{aorta}, is much smoother, whereas the last part, L^{ext}, is used to absorb energy by employing structural damping. The aims of this test case are to study the behavior of the proposed structural outflow conditions with help of global mesh refinement and smoothness-based mesh refinement. To this end, the valves are at sufficient distance to avoid touching and any other associated difficulties.

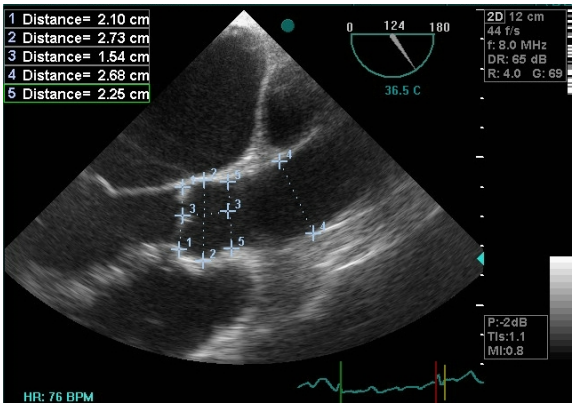

Figure 8.14. Long axis heart valve. Provided by Jeremi Mizerski [103].

One cardiac cycle has a time length of $T = [0s, 0.9s]$. Four time cycles are used to run the computation. The time step size k is chosen in the range of $0.02 - 0.001s$ to identify convergence with respect to time. The results are split into several sections. In the first set of computations, we compare different lengths of the artificial layer. Next, we validate the model in a straight channel. Afterwards, we present the results for a curved tube, which has a closer geometric relationship with the *real* aorta. Finally, we finish with a fluid-multi-structure problem, and a setting with two layers of arterial tissue.

Configuration

The (reference) configuration $\widehat{\Omega}$ of the numerical test case is illustrated in Figure 8.15. Specifically, we set $L^{\text{heart}} + L^{\text{aorta}} = 6.0cm$, $L^{\text{ext}} = 12cm$, $H = 2.9cm$, $D = 2.5cm$, and $d = 0.5cm$. The distance between the two valves is assumed to be sufficiently large to avoid topological difficulties.

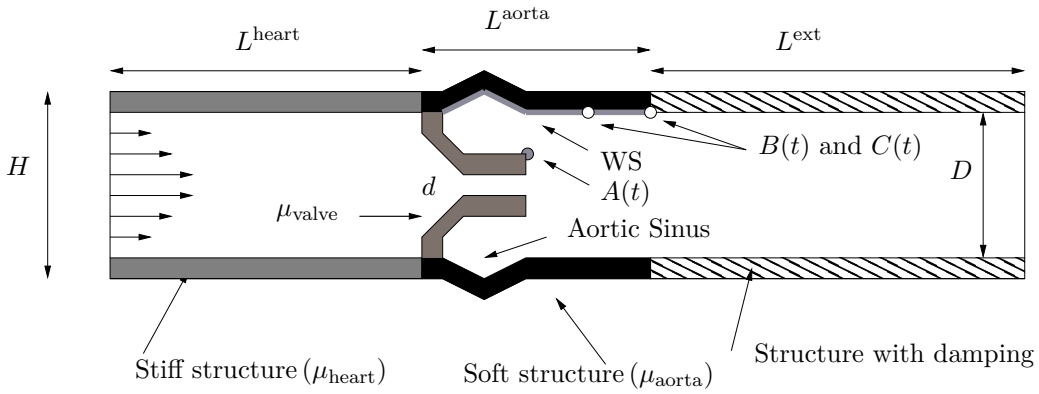

Figure 8.15. Configuration for the simulation of heart valve dynamics. The quantities of interest are the structural deflections of the points $A(t)$, $B(t)$, and $C(t)$, and the wall stress measurement WS along the interface of the aorta (indicated in grey).

Inflow and boundary conditions

A time-dependent parabolic velocity inflow profile leading to pulsatile flow in a laminar regime, is prescribed on $\widehat{\Gamma}_{\text{in}}$ (left boundary H), and is sketched in Figure 8.16. Specifically, we use

$$v_f(0,y) = \bar{v}(t)\frac{(y-D/2)(y+D/2)}{22.5\,D^2}.$$

This yields the maximum Reynolds number:

$$Re = \frac{v_{\max}D}{\nu_f} = \frac{13.2 * 2.5}{0.03} = 1100.$$

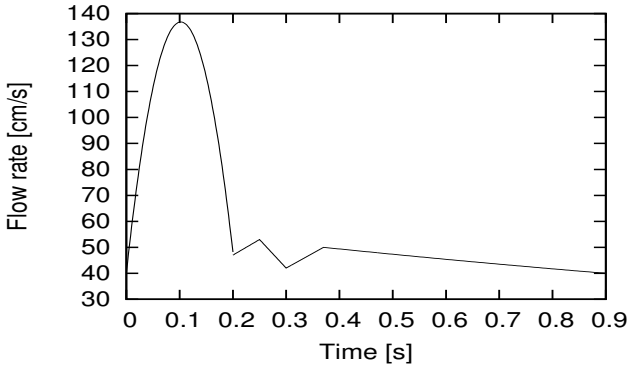

Figure 8.16. Interpolated flow rate profile $\bar{v}(t)$ in one cardiac cycle that is used to scale the inflow profile.

The do-nothing condition is used on $\widehat{\Gamma}_{\text{out}}$ (right boundary D).

The structure is clamped on $\widehat{\Gamma}_{\text{in}}$ and $\widehat{\Gamma}_{\text{out}}$. On the other parts, the structure is left free to allow the outer walls to move. Specifically, the structure on the outflow boundary of the extended domain L^{ext} is fixed by homogenous Dirichlet conditions. On this section, we assume that all reflections have already been absorbed by the damped structure equations.

As learned in Section 8.3, the best damping is achieved using a combination of absorbing conditions for the fluid and (weak) structural damping. Moreover, we identified similar behavior for weak and strong damping by a proper choice of the damping parameters. Because the different coupling strategies lead to similar results, we use in the present section (only) weak structural damping for solving heart-valve dynamics.

Quantities of comparison and their evaluation

We evaluate the deflections in both the x- and y-directions at the tails of one valve, at the point $A(0) = (3.64, 0.35)$. Furthermore, we evaluate in the first test the deflection of the arterial wall at $B(t) = (4.3, 1.25)$ and $C(t) = (6.0, 1.25)$. Moreover, we measure the wall stresses between the fluid and the structure in the upper part of the wall (over the length L^{aorta} at the interface between the fluid and the structure). The upper wall measurement is important in medical engineering applications in which high stresses behind the aortic heart valve can lead to an aortic dissection. We measured the minimal (min), maximal (max), and amplitude (ampl) values.

Parameters

For the fluid, we use the density $\rho_f = 1 g c m^{-3}$, and the viscosity $\nu_f = 0.03 c m^2 s^{-1}$. The elastic structure is characterized by the density $\rho_s = 1 g c m^{-3}$, the Poisson ratio $\nu_s = 0.3$, and the Lamé coefficients $\mu_{\text{heart}} = 10^8 g c m^{-1} s^{-2}$, $\mu_{\text{valve}} = 5.0 * 10^5 g c m^{-1} s^{-2}$, $\mu_{\text{aorta}} = 10^6 g c m^{-1} s^{-2}$, and $\mu_{\text{ext}} = 10^6 g c m^{-1} s^{-2}$. The (weak) damping parameter is given by $\gamma_w = 10^4$, the other one is set to $\gamma_s = 0$. Numerical experiences showed that the (weak) damping parameter should be chosen two orders of magnitude lower than the structure material parameter μ_{ext}. Using this value leads to *optimal* damping for the heart valve setting.

The challenge at the structure outflow boundary

As already mentioned, the blood vessel walls moves significantly in this example. In Figure 8.17, we illustrate a situation, where a incoming structure wave is reflected on the artificial outflow boundary using homogeneous Dirichlet conditions. This example is computed without the artificial layer L^{ext}, causing difficulties, because the reflected wave interacts later with other incoming waves leading to unexpected behavior.

Another difficulty comes through the carefree employment of the do-nothing condition in the situation sketched in Figure 8.17. This condition only holds for a fixed outflow boundary, which is, however, not the best idea for a moving structure. Because of this monitoring, our proposition, to extend the computational domain and to clamp the structure on the new outflow, overcomes also the challenge of appropriate outflow fluid conditions.

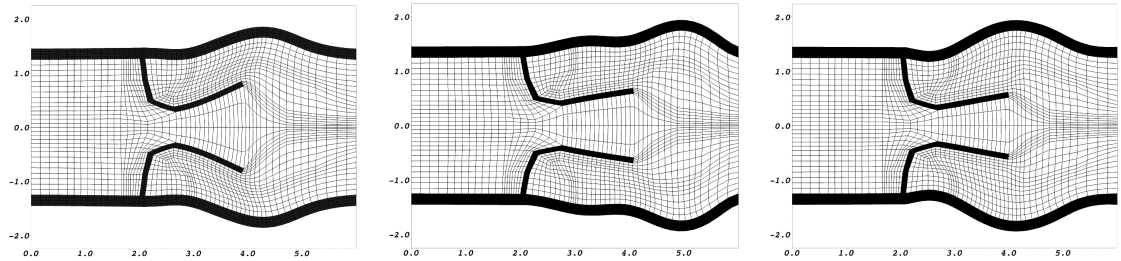

Figure 8.17. Time sequence of states of a structure wave that is reflected at the structure outflow boundary. The incoming wave is displayed in the left and middle figure. The reflected wave is shown in the right figure. The structure is fixed by homogeneous Dirichlet conditions on the outflow boundary, which is best seen in the middle figure. The unit of the both axes is cm.

8.4.1 Comparison of different lengths of the artificial layer

In the first part, we study different lengths of the artificial layer. We use $L^{\text{ext}} = 3, 6, 9cm$, and we choose the weak damping parameter $\gamma_w = 10^4$. In the results, we monitor qualitative similar behavior of the y-deflections of the valve-tip at $A(t)$; see Figure 8.18. Thus, the length of L^{ext} has no significant influence on this evaluation. However, we observe back-traveling structure waves at the point $C(t)$ the shorter L^{ext}, which can be monitored in Figure 8.19. There, we detect (in addition to the global maximum) a local maximum in each cardiac cycle. This local maximum vanishes the longer the artificial layer L^{ext}. This observation can also be monitored for the wall stresses in the y-direction. We infer from these results that $L^{\text{ext}} = 9cm$ is the most reasonable length for the artificial layer and therefore, it is used in the upcoming tests.

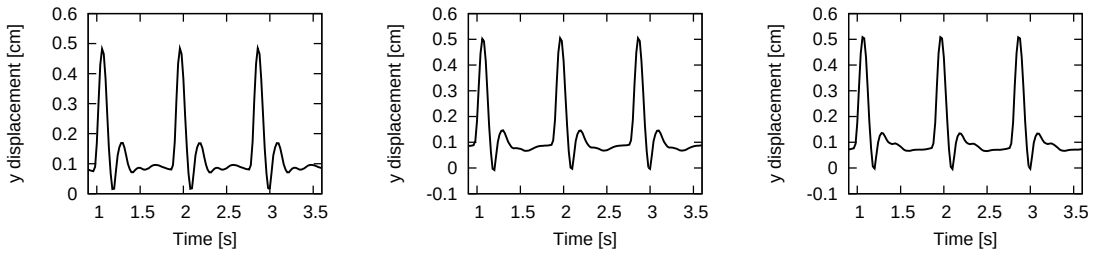

Figure 8.18. Comparison of the y-deflection of the point $A(t)$ during three cardiac cycles for $L^{\text{ext}} = 3, 6, 9cm$ (from left to right).

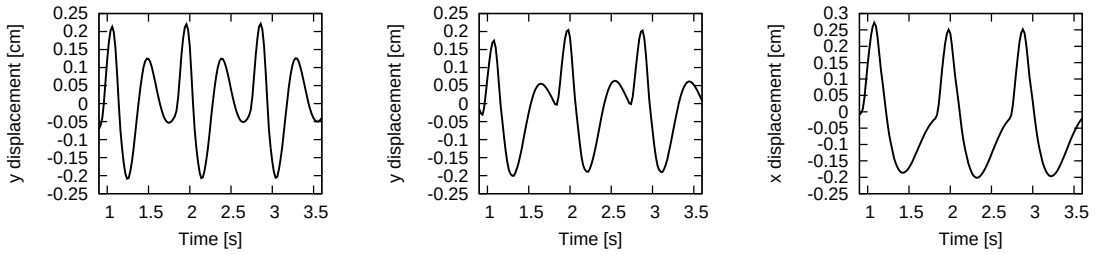

Figure 8.19. Comparison of the y-deflection of the point $C(t)$ during three cardiac cycles for $L^{\text{ext}} = 3, 6, 9cm$ (from left to right).

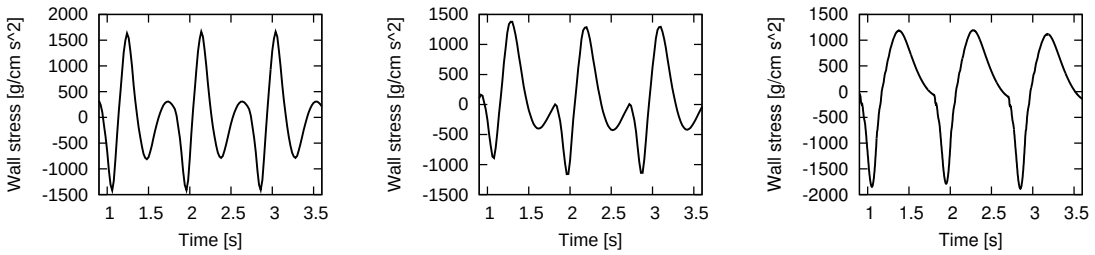

Figure 8.20. Comparison of the wall stresses in the y-direction along the interface of the aorta during three cardiac cycles for $L^{\text{ext}} = 3, 6, 9cm$ (from left to right).

8.4.2 Valve dynamics in a straight channel

The results of this numerical test and the three following tests are obtained for three different refinement levels, i.e., 5553, 21522, and 84726 degrees of freedom. Moreover, we use the time step sizes $k = 0.02, 0.01, 0.002$ and $k = 0.001$. The results indicate that our proposed model is suitable for solving valve dynamics for a prototypical configuration. The detailed measurements of the physical quantities and a comparison of these observations are summarized in another work [148].

The qualitative behavior of the quantities of interest for the last three cycles can be observed in Figure 8.21.

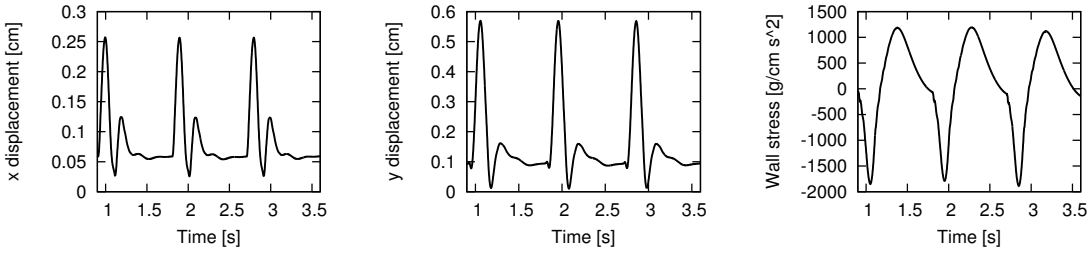

Figure 8.21. Evaluation of the x- and the y-displacements and wall stress in the y-directions (from left to right) for valve dynamics in a straight channel.

A time sequence of solutions indicating the x-velocity is illustrated in Figure 8.22 for one cardiac cycle.

We show the qualitative behavior of the results in the Figure 8.23. If the damping parameter γ_w is too low, structure waves propagate through the whole structure domain. On the other hand, if the damping parameter chosen is too high, the structure becomes too stiff and outgoing waves are reflected instead of being absorbed.

We emphasize that here we are mainly interested in a full absorption of the outgoing structure waves. This is a rather nonphysical choice because back-traveling waves can be induced by bifurcations for instance. By a careful choice of the damping parameters, we should be able to account for such a situation. We refer the reader to the outlook for a deeper discussion.

A time sequence of solutions on a locally refined mesh within one cardiac cycle can be studied in Figure 8.24. In this test, we used local mesh adaption with refinement indicators that are obtained by measuring the smoothness of the discrete solutions (see Equation (6.1)). As shown in Section 7.2, the heuristic mesh refinement procedure is an adequate tool (at least) to computing the wall stresses. This are good news, because the computation of wall stresses is quite important for clinical applications. Whereas the point value evaluation, where smoothness-based refinement failed, serves only for numerical studies.

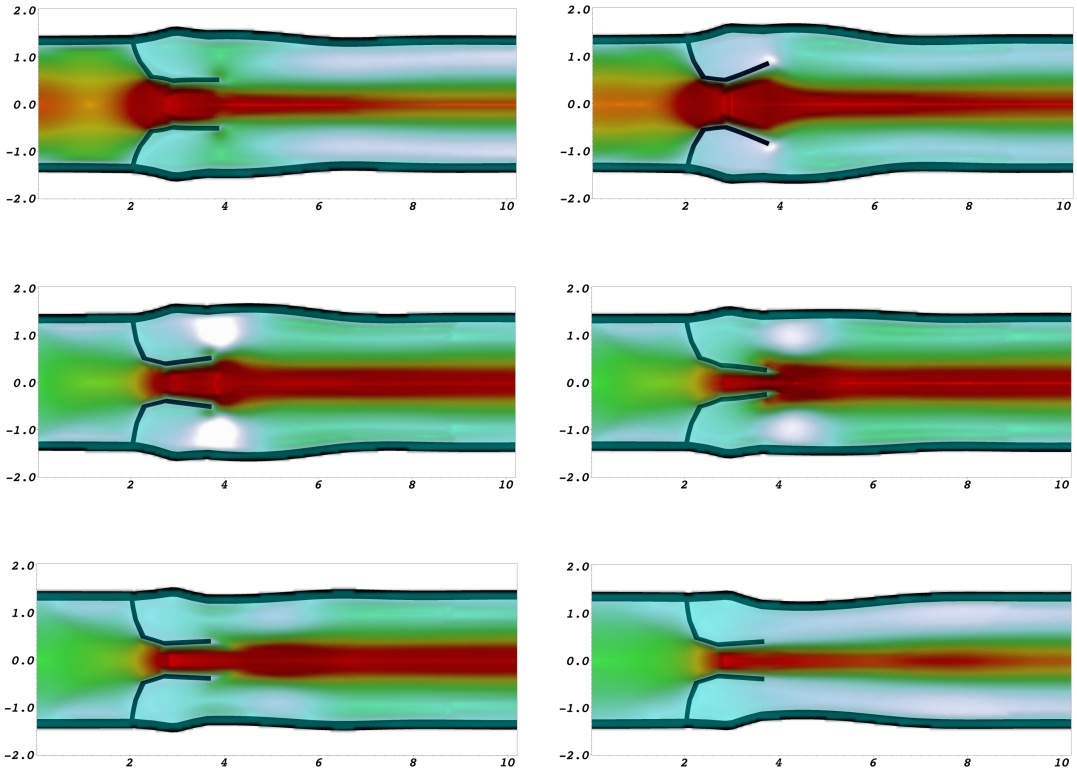

Figure 8.22. From left to right and from top to bottom: time sequence of solutions at the time steps $t = 0.994, 0.997, 1.0, 1.003, 1.007, 1.020$ (in s) of the x-velocity to the nonstationary valve simulations within one cardiac cycle. The highest velocity is indicated in red (dark) and it is up to $31 cm/s$. The back-flow of the velocity is indicated in white and in light blue, and it is caused by the compliance of the vessel walls and the incompressibility of the fluid. The lowest velocity is down to $-4 cm/s$ (i.e., fluid backflow). Specifically, we observed that the flow is also directed into the Sinus of Valsalva, where it forms a vortical flow (see also [56], p. 45). The unit of the both axes is cm.

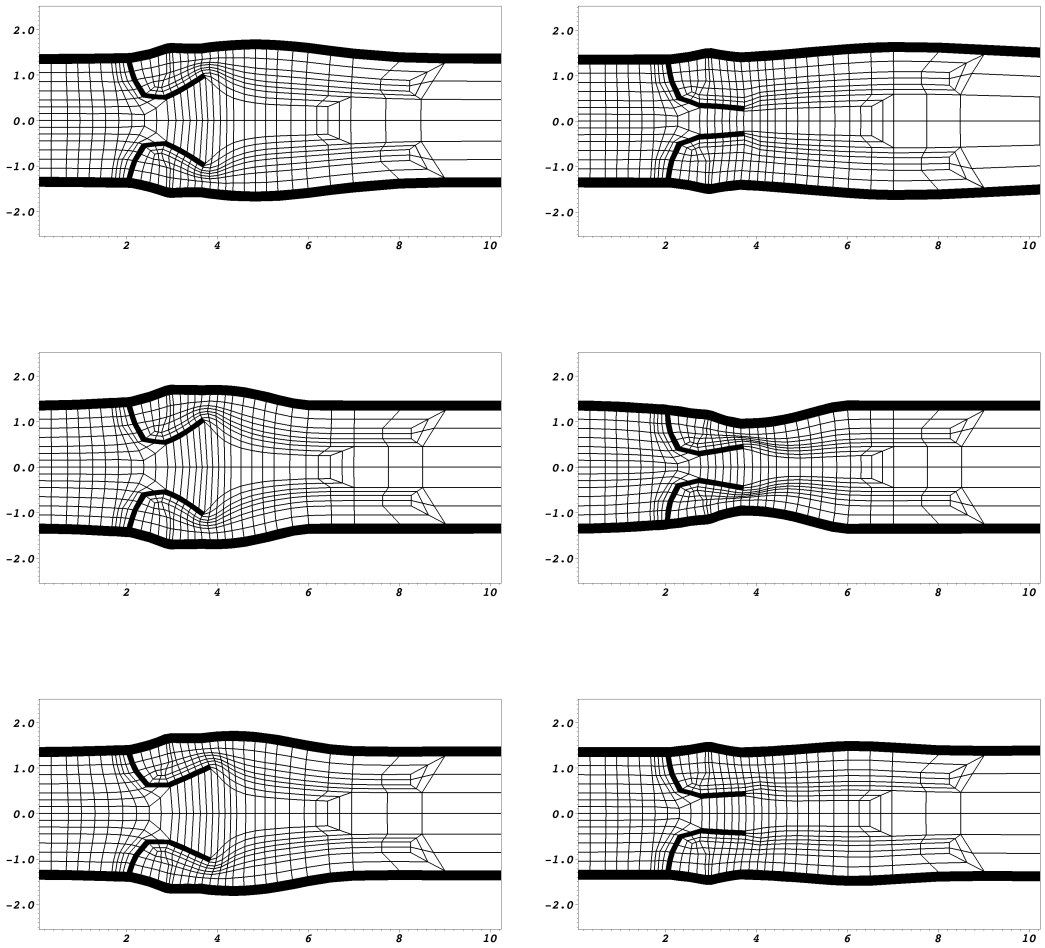

Figure 8.23. Valve simulations in a straight channel with too low damping $\gamma_w = 10^3$ (top), with too strong damping $\gamma_w = 10^6$ (middle), and with proper damping $\gamma_w = 10^4$ (bottom). The unit of the both coordinates is *cm*.

As we monitor in Figure 8.24, the mesh is refined along the interfaces of interest (namely along L^{aorta}) using smoothness-based mesh adaption. In addition, the mesh is only refined in the physical region of interest but not in the artificial layer.

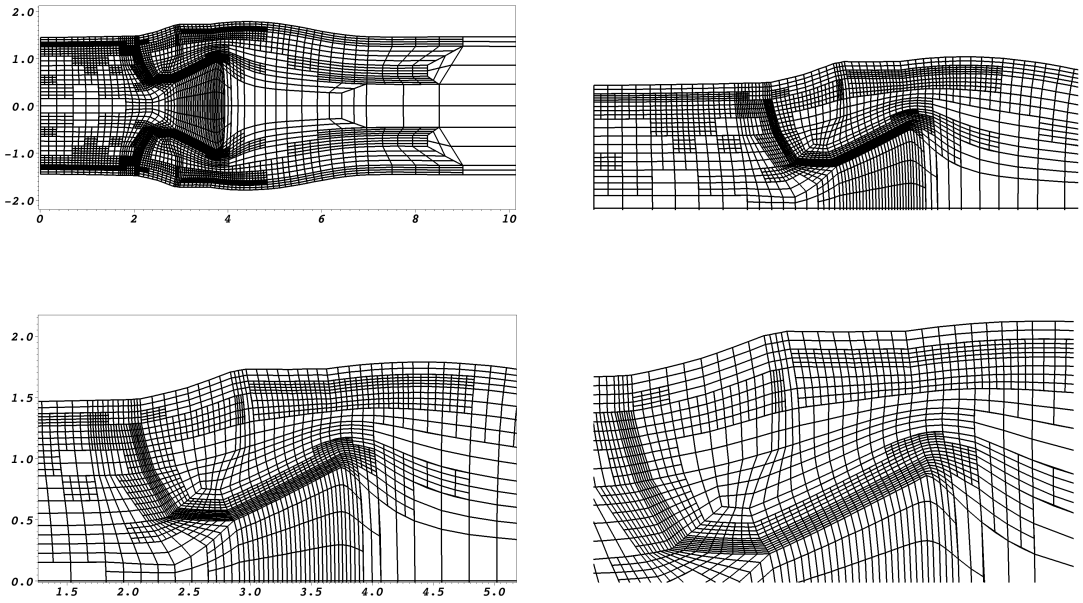

Figure 8.24. Nonstationary valve simulation on a three-times locally refined mesh with $145,206$ degrees of freedom. The indicators for the mesh refinement were obtained by smoothness measurement of the discrete solution. Specifically, the mesh is mainly refined in the region of interest and not in the artificial layer, which can be seen in the upper left figure. Zooming in the mesh (lower right), we observe good mesh quality mainly due to the biharmonic mesh motion model. The unit of the both axes is *cm*.

8.4.3 Valve dynamics in a curved channel

This example is a slight modification of the previous test. It is designed to illustrate that our proposed method works for curved channels, too. In fact, this geometry has a closer relation to a *real* blood vessel (see Figure 8.25). The qualitative behavior of the quantities of interest is comparable to the results of the straight channel, which is illustrated in Figure 8.26.

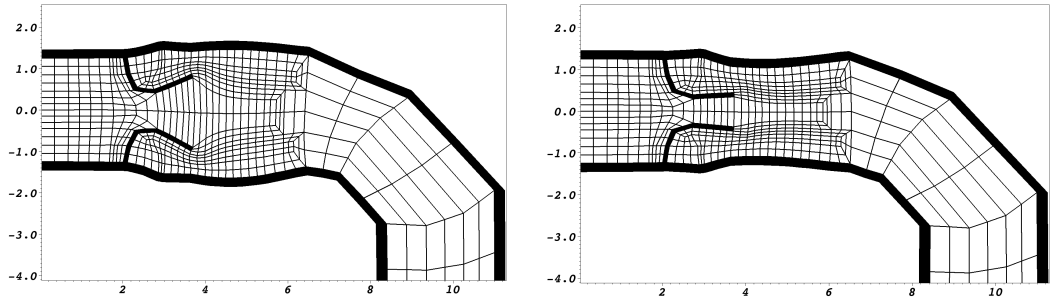

Figure 8.25. Valve simulations in a curved domain with proper damping $\gamma_w = 10^4$.

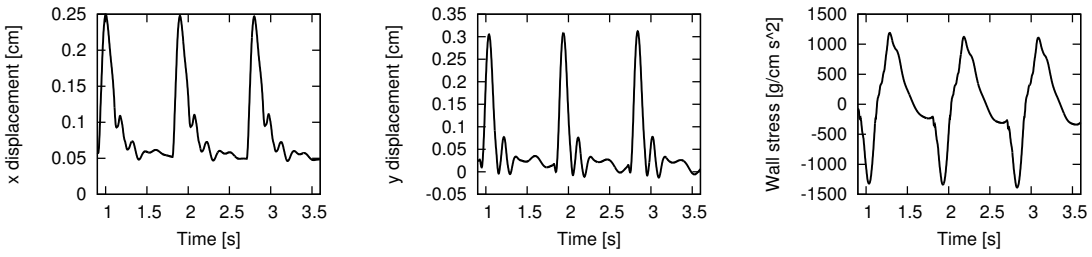

Figure 8.26. Evaluation of the x- and the y-displacements and the wall stress in the y-direction (from left to right) for the curved configuration.

8.4.4 Valve dynamics with different constitutive structure tensors

Until now, the structure has been described using the same structure model, namely the STVK material, but with varying coefficients. In this numerical example, we test our solution algorithm with different structure models in which the stress tensor changes entirely. In this section, the heart section, L^{heart}, and the leaflets are modeled with the INH material. The aorta, L^{aorta}, and the artificial structure, L^{ext}, are still described by the STVK material.

There are two purposes for this example. First, we are interested to detect any difficulties with our monolithic solution algorithm for computations with multiple structures. This observation is important for the simulation of multiple layers of arterial tissue, which is examined in the next numerical test case 8.4.5. Second, we compare the behavior of the quantities of interest to determine if they differ from the previous findings in Example 8.4.2.

To respond to the first issue, we monitor that the convergence of Newton's method at each time step is slightly better when incorporating the multi-structure model. This result indicates that the solution algorithm performs better when modeling the valves and the heart section with the INH material. This finding is in agreement with our observations of the comparison of the different structure models in Example 8.1. Therein, we observe a failure (and bad convergence of the Newton method) using the STVK material for large structural deformations. In the present test case, we again monitor bad convergence of the STVK material for large deflections. Second, we notice the same qualitative (nearly the identical) behavior for all quantities of interest (see Figure 8.28). This finding was expected for the wall stresses because we still used the STVK material in L^{aorta}.

8.4.5 Valve dynamics with two layers tissue

In this final section, we account for the different layers tissue in the arterial wall. Only the media (the middle layer) and the adventitia (the outermost layer) are taken into account, because the innermost layer (the intima) has an insignificant influence to the mechanical properties of the (healthy) arterial wall (see [79], p. 3). We assume that the media occupies two third of the arterial wall thickness (see [79], p. 18). Furthermore, it is suggested by Holzapfel [79], p. 19, to set the material coefficient μ_s^a of the adventitia one magnitude lower than the corresponding coefficient of the media, i.e., $\mu_s^a = 0.1 * \mu_s^m$. The configuration is sketched in Figure 8.27.

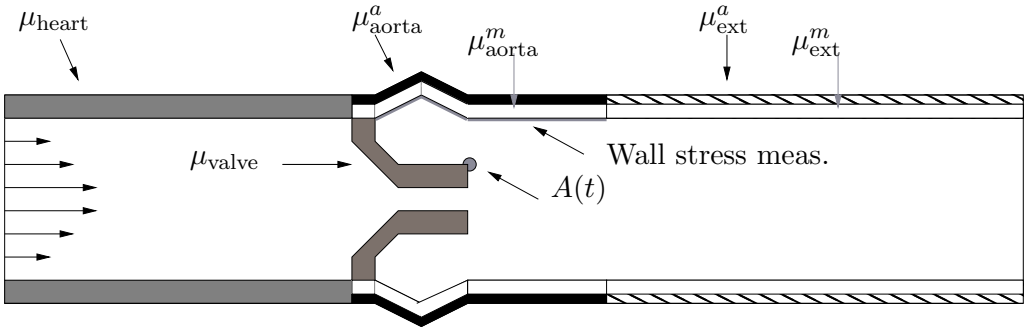

Figure 8.27. Configuration for the simulation of heart valve dynamics with two layers of arterial tissue and different constitutive structure tensors.

Parameters

The substructure parts are characterized by $\mu_{\text{heart}}^{\text{INH}} = 10^8 gcm^{-1}s^{-2}$, $\mu_{\text{valve}}^{\text{INH}} = 5.0{*}10^5 gcm^{-1}s^{-2}$, $\mu_{\text{aorta}}^{a,\text{INH}} = 10^5 gcm^{-1}s^{-2}$, $\mu_{\text{aorta}}^{m,\text{STVK}} = 10^6 gcm^{-1}s^{-2}$, $\mu_{\text{ext}}^{a,\text{STVK}} = 10^5 gcm^{-1}s^{-2}$, and $\mu_{\text{ext}}^{m,\text{STVK}} = 10^6 gcm^{-1}s^{-2}$.

Discussion of the results

We monitor a different behavior of the quantities of interest than in the examples before. The differences in the y-deflections are moderate, as illustrated in Figure 8.28. These differences are expected because we kept the constitutive material of the heart valve. However, we observe significant differences of wall stress measurement. This discrepancy was again expected because we changed the composition (division into two layers) of the material of the arterial wall.

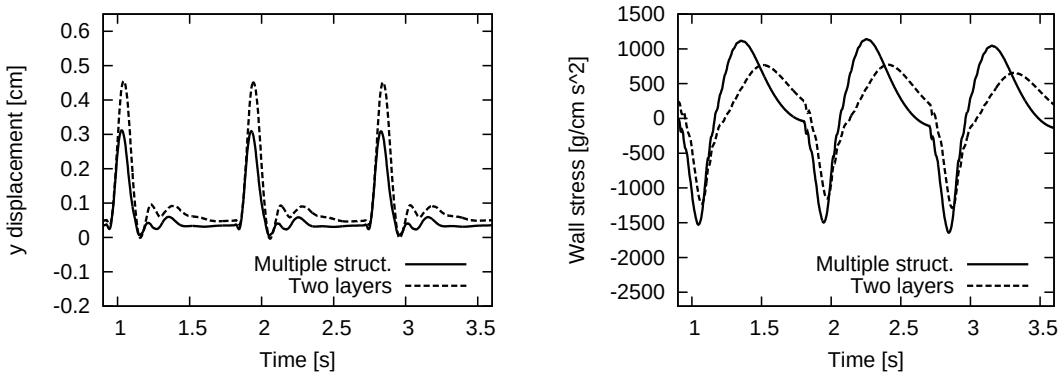

Figure 8.28. Evaluation of the y-displacement (left) and the wall stress in the y-direction (right) for the valve dynamics with multiple structures (Example 8.4.4) and two layers tissue (Example 8.4.5) in a straight channel.

Outlook to the last chapter

In this chapter, we validated our findings for computing nonstationary fluid-structure interaction problems. All examples (for fully nonstationary settings) were computed on (at least three) different mesh refinement levels and for (at least three) different time steps, such that we observed convergence of the quantities of interest. With these observations, we trust our numerical algorithms to work correctly. In the last chapter of this thesis, we summarize our results and we give perspectives and open questions for future work.

9 Conclusions and Outlook

In this thesis, we presented a further investigation of monolithically coupled fluid-structure interaction problems. Most of the development was motivated by a collaboration with a cardiologist from the University of Warsaw. In fact, there is an increasing interest in modeling hemodynamic applications with solution approaches that are based on fluid-structure interaction. Indeed, a great variety of research already exist about this topic. In particular, there are many three-dimensional studies (partially compared with experimental data) with realistic parameters computed for realistic geometries.

In contrast the prior work, we restricted ourselves to prototypical examples and the development of algorithms for still unresolved open questions in the community. For instance, it remains unclear what structural boundary conditions should be used on artificial boundaries. In this thesis, we tried a new approach to this topic. The idea was to apply the well-tested PML approach to fluid-structure interaction. Using this method, we extended the existing stability analysis for monolithically coupled fluid-structure interaction. Accordingly, we tested and compared different second-order time-stepping schemes for long-term computations.

Moreover, we further developed algorithms for gradient-based optimization and goal-oriented mesh refinement relevant to hemodynamic applications. Although their extension to nonstationary configurations requires deeper investigations of their applicability with respect to their efficiency, in particular, these two topics can be regarded as pioneering work. Our achievements to date have been substantiated by several numerical tests.

Finally, we believe that the large variety of numerical tests undertaken in this thesis, contributes significantly to demonstrating the performance of monolithic solution approaches. In fact, a substantial extension of our solver involved the consideration of several different structural equations with different material properties, which is not standard in the literature.

Outlook

Based on the achievement of the stated goals, we present several ideas for possible future developments:

Software development and implementation-related aspects

The development of a block Schur preconditioner for solving monolithic fluid-structure interaction with iterative solvers in the deal.II software library. Moreover, there is a need to parallelize the programming code for the efficient computation of three-dimensional problems.

Modeling and simulation of hemodynamic applications

Modeling and simulation of three-dimensional heart valve dynamics with the goal of comparison with experiments and clinical data. This task comprises efficient implementation and mesh adaption techniques to accurately measure certain quantities of interest. Further investigation of prestressed configurations with fiber-reinforced materials and finally, the use of realistic (three-dimensional) geometrical mesh data.

Further investigation of artificial boundary conditions

Coupling of conditions on the outflow boundary and further investigation of proper structure outflow conditions. This subject seems to be a particularly promising topic for future work because the interchange of different boundary conditions has consequences on theoretical aspects and physical quantification, and it remains an open problem. Specifically, the weak and the strong damping of the structure equations employed in this thesis, require further investigation. For example, *optimal* damping parameters should be determined to reflect accurately the underlying physics (e.g., in the presence of bifurcations). For this purpose, we believe that our proposed approach was a good choice because we were able to easily adapt both damping parameters. Additionally, determining an *optimal* length of the artificial layer would provide the best damping and the lowest computational cost.

Optimal control for fluid-structure interaction

The most promising aspect is the further development of optimal control problems governed by fluid-structure interaction equations. There is an ever-increasing need to develop theory and an efficient implementation (of nonstationary problems) for many applications. Concerning the theory, one could start by proving existence of an optimal control for such a coupled problem. In addition, the analytical framework of the optimality system requires a rigorous investigation. Regarding implementation, the solution of nonstationary forward problems of fluid-structure interaction remains a tough task. At the present stage, the simulation of such problems remains challenging. From the application point of view, the next step would be stress minimization in the arterial wall for nonstationary heart-valve dynamics and finally, a comparison with experimental data.

Fixed mesh methods for fluid-structure interaction and model adaptivity

Further development of fixed mesh approaches such as the fully Eulerian method, to simulate fluid-structure interaction processes would be useful. This step would overcome the major disadvantage of the ALE approach: the degeneration of mesh cells. In a fully Eulerian framework, it is possible to model large structural deformations and topology changes (when two valves meet). Because we are at the beginning of this research, a novel research field with existence results, regularity aspects, convergence analysis, and further comparison with existing methods can be established. Moreover, the disadvantage of this method, namely, that the interface intersects cells, requires a further development of spatial discretization techniques and offers promising new questions for the future. Finally, the combination of ALE-based techniques and fixed mesh approaches is promising; such methods could eventually be governed by an adaptive-choice algorithm determining where to use which method during a solution process.

Acknowledgments

I owe my deepest gratitude to my supervisor Prof. Rolf Rannacher and to Dr. med. Jeremi Mizerski (who was my co-supervisor in the heart-valve project) for suggesting this fascinating project. Both were always being open for discussing new questions, continuously support, and pointing at the key questions of my work. I would like to acknowledge Prof. Rolf Rannacher for the possibility to present my research at uncountable conferences (and for writing several letters of recommendation to apply for research grants of the Graduate Academy and the DAAD) and to gain fruitful experiences in supervising students and teaching. I thank Dr. med. Jeremi Mizerski for his invitation to Zamość and for fruitful discussions on heart-valve surgery.

Because I was a member of the *International Graduiertenkolleg IGK 710* of the University of Heidelberg and the University of Warsaw, I would like to express my gratitude to Prof. Marek Niedzkda and Dr. Ania Trykozko from the ICM (University of Warsaw) for organizing my research stays and for always pointing out the key questions after presenting my novel results at ICM seminar talks.

Next, I acknowledge Prof. Adelia Sequeira from the University in Lisbon for inviting me to her research group and for fruitful discussions on blood flow modeling.

Furthermore, I would like to acknowledge Prof. Franz-Theo Suttmeier who let me go from the University of Siegen for having the chance to find my fortune in Heidelberg. I thank the whole WiR-AG for having still contact and the possibility to meet.

Additionally, I acknowledge the funding towards my PhD from the German Research Foundation (DFG), first, through the International Research Training group (IGK) 710 'Complex Processes: Modeling, Simulation, and Optimization' at the Interdisciplinary Center of Scientific Computing (IWR). In the second part of PhD, I was supported through the HGS MathComp (HGS) that has been founded in the frame of the German Excellence Initiative. I am grateful for the possibilities the membership of these groups offered to me.

Moreover, I would like to thank my collaborators in preparing and doing joint work: Thomas R, Bärbel, Adelia and Alexandra, and Winni. Furthermore, I thank Timo, Bärbel, Martin, Adrian, Maria, and Herta Fitzer for organizing two workshops, namely the *deal.II Workshop* in August 2010, and the workshop on *analysis and numerics of non-Newtonian fluids* in January 2011. Last, I would like to thank Boris and Dominik, and Adelia and Alexandra for inviting me to research stays.

My special thanks are addressed to Bärbel Janssen with whom I shared an office for 1,064 days and neverending fruitful discussions on never countable topics. The second portion of special thanks are addressed to Thomas Richter who introduced me into many technical details of daily university life such as computer administration, paper writing, and giving talks at conferences. Specifically, he always had an attentive view on my research, which I appreciate really much. Furthermore, I would like to thank Michael Besier/Schmich for carefully proof-reading of my first research paper that was written by myself.

I would like to thank the DOpE developer team, Michael Geiger, Christian Goll, and Winnifried Wollner. Furthermore, I would like to thank the developers of RoDoBo for algorithmic aspects for the implementation of optimization problems and the developers of deal.II that provides the basic features of the DOpE software package.

I wish to thank the whole Numerical Analysis Group at the University of Heidelberg for an inspirational atmosphere, for an incredible flavor that was in the air, and always open doors to exchange ideas. Specifically, I thank my friends and colleagues Stefan K., Winni, Michael B., Matthias K., Jevgeni, Thomas R., Thomas C., Matthias M., Stefan F., Sara, Bärbel, Elfi, Michael G., Adrian, Daniel, Christian, and the Tuesday-evening-soccer-team.

Darüberhinaus danke ich meiner Familie für die unendliche Unterstützung in allen erdenklichen Formen. Insbesondere Marianne und Bodo, Dominik und Katrin. Außerdem danke ich Sven und Mine für erfrischende neue Gedanken.

Finalement, je remercie beaucoup ma famille française pour m'avoir permis mes séjours à Versailles (et à la Grande Motte) pour trouver de nouvelles idées.

Il y a une personne qui reste : c'est Marie-Cécile : merci pour tout. Je suis désolé de ne pas pouvoir commencer avec quelque chose de spécial parce qu'il y aurait trop de choses à dire et pour cette raison je dis seulement

danke, merci, thanks, dziękuję, obrigado !

Bibliography

[1] R. A. Adams, *Sobolev Spaces*, Academic Press, 1975.

[2] M. Asterino, F. Chouly, and F. Fernández, *An added-mass free semi-implicit coupling scheme for fluid-structure interaction*, C. R. Acad. Sci. Paris, Sér. I., 347 (2009), pp. 99–104.

[3] M. Asterino and C. Grandmont, *Convergence analysis of a projection semi-implicit coupling scheme for fluid-structure interaction problems*, Numer. Math., 116 (2008), pp. 721–767.

[4] F. Baaijens, *A fictitious domain/mortar element method for fluid-structure interaction*, Int. J. Num. Methods Fluids, 35 (2001), pp. 743–761.

[5] S. Badia, Q. Quaini, and A. Quarteroni, *Splitting methods based on algebraic factorization for fluid-structure interaction*, SIAM J. Sci. Comput., 30 (2008), pp. 1778–1805.

[6] W. Bangerth, M. Geiger, and R. Rannacher, *Adaptive Galerkin finite element methods for the wave equation*, Comput. Methods Appl. Math., 10 (2010), pp. 3–48.

[7] W. Bangerth, M. Grothe, and C. Hohenegger, *Finite element method for time dependent scattering: nonreflecting boundary conditions, adaptivity, and energy decay*, Comput. Methods Appl. Mech. Engrg., 193 (2004), pp. 2453–2482.

[8] W. Bangerth, R. Hartmann, and G. Kanschat, *Differential Equations Analysis Library*, 2010.

[9] W. Bangerth and R. Rannacher, *Adaptive Finite Element Methods for Differential Equations*, Birkhäuser, Lectures in Mathematics, ETH Zürich, 2003.

[10] P. Bastian, *Parallele Lösung großer Gleichungssysteme.* Vorlesungsskriptum, 2009.

[11] K.-J. Bathe and G. Ledezma, *Benchmark problems for incompressible fluid flows with structural interactions*, Comput. Struct., 85 (2007), pp. 628–644.

[12] Y. Bazilevs, V. M. Calo, T. Hughes, and Y. Zhang, *Isogeometric fluid-structure interaction: theory, algorithms, and computations*, Comput. Mech., 43 (2008), pp. 3–37.

[13] R. Becker, *Mesh adaptation for stationary flow control*, J. Math. Fluid Mech., 3 (2001), pp. 317–341.

[14] ——, *Adaptive finite elements for optimal control problems.* University of Heidelberg, 2004. Habilitationsschrift.

[15] R. Becker, D. Meidner, and B. Vexler, *Efficient numerical solution of parabolic optimization problems by finite element methods*, Optim. Methods Softw., 22 (2007), pp. 813–833.

[16] ——, *Optimization with Gascoigne*, 2010.

[17] R. Becker and R. Rannacher, *A feed-back approach to error control in finite element methods: basic analysis and examples*, East-West J. Numer. Math., 4 (1996), pp. 237–264.

[18] ——, *An optimal control approach to error control and mesh adaptation in finite element methods*, Acta Numerica 2001, Cambridge University Press, a. iserles ed., 2001, pp. 1–102.

[19] J. Berenger, *A perfectly matched layer for the absorption of electromagnetic waves*, J. Comput. Phys., 114 (1994).

[20] A. Bermudez, L. Hervella-Nieto, A. Prieto, and R. Rodriguez, *Perfectly matched layers for time-harmonic second order elliptic problems*, Arch. Comput. Methods Engrg., 17 (2010), pp. 77–107.

[21] C. Bernardi and E. Süli, *Time and space adaptivity for the second-order wave equation*, Math. Models Methods Appl. Sci., 15 (2005), pp. 199–225.

[22] M. Besier, *Adaptive Finite Element methods for computing nonstationary incompressible Flows*, PhD thesis, University of Heidelberg, 2009.

[23] M. Besier and R. Rannacher, *Goal-oriented space-time adaptivity in the finite element galerkin method for the computation of nonstationary incompressible flow*, Int. J. Num. Meth. Fluids, (accepted 2011).

[24] M. Besier and W. Wollner, *On the dependence of the pressure on the time step in incompressible flow simulations on varying spatial meshes*, Int. J. Num. Meth. Fluids, (2011).

[25] M. Braack, E. Burman, V. John, and G. Lube, *Stabilized finite element methods for the generalized Oseen equations*, Comput. Methods Appl. Mech. Engrg., 196 (2007), pp. 853–866.

[26] D. Braess, *Finite Elemente*, Springer-Verlag Berlin Heidelberg, Berlin, Heidelberg, vierte, überarbeitete und erweiterte ed., 2007.

[27] S. C. Brenner and L. R. Scott, *The mathematical theory of finite element methods*, no. 15 in Texts in applied mathematics ; 15 ; Texts in applied mathematics, Springer, New York, NY, 3. ed. ed., 2008.

[28] A. Brooks and T. Hughes, *Streamline upwind/Petrov-Galerkin formulations for convection dominated flows with particular emphasis on the incompressible Navier-Stokes equations*, Comput. Methods Appl. Mech. Engrg., 32 (1982), pp. 199–259.

[29] H.-J. Bungartz, M. Mehl, and M. Schäfer, *Fluid-Structure Interaction II: Modelling, Simulation, Optimization*, Lecture Notes in Computational Science and Engineering, Springer, 2010.

[30] H.-J. Bungartz and M. Schäfer, *Fluid-Structure Interaction: Modelling, Simulation, Optimization*, vol. 53 of Lecture Notes in Computational Science and Engineering, Springer, 2006.

[31] G. F. Carey and J. T. Oden, *Finite Elements. Volume III. Compuational Aspects*, The Texas Finite Element Series, Prentice-Hall, Inc., Englewood Cliffs, 1984.

[32] P. Causin, J.-F. Gerbeau, and F. Nobile, *Added-mass effect in the design of partitioned algorithms for fluid-structure problems*, Comput. Methods Appl. Mech. Engrg., 194 (2005), pp. 4506–4527.

[33] P. G. Ciarlet, *Mathematical Elasticity. Volume 1: Three Dimensional Elasticity*, North-Holland, 1984.

[34] P. G. Ciarlet, *The finite element method for elliptic problems*, North-Holland, Amsterdam [u.a.], 2. pr. ed., 1987.

[35] D. Coutand and S. Shkoller, *Motion of an elastic solid inside an incompressible viscous fluid*, Arch. Rational Mech. Anal., (2005), pp. 25–102.

[36] ——, *The interaction between quasilinear elastodynamics and the Navier-Stokes equations*, Arch. Rational Mech. Anal., 179 (2006), pp. 303–352.

[37] T. A. Davis and I. S. Duff, *An unsymmetric-pattern multifrontal method for sparse lu factorization*, SIAM J. Matrix Anal. Appl., 18 (1997), pp. 140–158.

[38] J. Degroote, P. Bruggeman, R. Haelterman, and J. Vierendeels, *Stability of a coupling technique for partitioned solvers in FSI applications*, Comput. Struct., (2008), pp. 2224–2234.

[39] J. Degroote, R. Haelterman, S. Annerel, P. Bruggeman, and J. Vierendeels, *Performance of partitioned procedures in fluid-structure interaction*, Comput. Struct., (2010), pp. 446–457.

[40] J. Donéa, P. Fasoli-Stella, and S. Giuliani, *Lagrangian and Eulerian finite element techniques for transient fluid-structure interaction problems*, in Trans. 4th Int. Conf. on Structural Mechanics in Reactor Technology, 1977.

[41] T. Dunne, *An Eulerian approach to fluid-structure interaction and goal-oriented mesh adaption*, Int. J. Numer. Methods in Fluids, 51 (2006), pp. 1017–1039.

[42] ——, *Adaptive Finite Element Approximation of Fluid-Structure Interaction Based on Eulerian and Arbitrary Lagrangian-Eulerian Variational Formulations*, PhD thesis, University of Heidelberg, 2007.

[43] T. Dunne, T. Richter, and R. Rannacher, *Numerical simulation of fluid-structure interaction based on monolithic variational formulations*, Comtemporary Challenges in Mathematical Fluid Mechanics, Springer, World Scientific, Singapore, 2010, pp. 1–75.

[44] B. Engquist and A. Majda, *Absorbing boundary conditions for the numerical simulation of waves*, Math. Comp., 31 (1977), pp. 629–651.

[45] C. Farhat, P. Geuzaine, and C. Grandmont, *The discrete geometrical conservation law and the nonlinear stability of the ALE schemes for the solution of flow problems on moving grids*, J. Comp. Phys., 174 (2001), pp. 669–694.

[46] Z. Feng and E. Michaelides, *The immersed boundary-lattice Boltzmann method for solving fluid-particles interaction problems*, J. Comp. Phys., 195 (2004), pp. 602–628.

[47] F. Fernández and M. Moubachir, *A newton method using exact jacobians for solving fluid-structure coupling*, Comput. Struct., 83 (2005), pp. 127–142.

[48] M. Fernández and J.-F. Gerbeau, *Algorithms for fluid-structure interaction problems*, vol. 1 of Formaggia et al. [53], 2009, pp. 307–346.

[49] L. Formaggia, J.-F. Gerbeau, F. Nobile, and A. Quarteroni, *On the coupling of 3d and 1d Navier-Stokes equations for flow problems in compliant vessels*, Comp. Methods Appl. Mech. Engig, 191 (2001), pp. 561–582.

[50] L. Formaggia, A. Moura, and F. Nobile, *On the stability of the coupling of 3d and 1d fluid-structure interaction models for blood flow simulations*, Tech. Rep. 94, MOX Institute, Milano, 2006.

[51] L. Formaggia and F. Nobile, *A stability analysis for the arbitrary Lagrangian Eulerian formulation with finite elements*, East-West Journal of Numerical Mathematics, 7 (1999), pp. 105 – 132.

[52] ——, *Stability analysis of second-order time accurate schemes for ALE-FEM*, Comp. Methods Appl. Mech. Engrg., 193 (2004), pp. 4097 – 4116.

[53] L. Formaggia, A. Quarteroni, and A. Veneziani, *Cardiovascular Mathematics: Modeling and simulation of the circulatory system*, Springer-Verlag, Italia, Milano, 2009.

[54] L. Formaggia and A. Veneziani, *Reduced and multiscale models for the human cardiovascular system*, Tech. Rep. 21, MOX Institute, Milano, 2003.

[55] L. Formaggia, A. Veneziani, and C. Vergara, *Flow rate boundary problems for an incompressible fluid in deformable domains: formulations and solution methods*, Comp. Methods Appl. Mech. Engrg., 199 (2010), pp. 677–688.

[56] Y. Fung, *Biodynamics: Circulation*, Springer-Verlag, first ed. ed., 1984.

[57] F. Gazzola and M. Squassina, *Global solutions and finite time blow up for damped semilinear wave equations*, Ann. I. H. Poincaré, 23 (2006), pp. 185–207.

[58] M. Geiger, C. Goll, T. Wick, and W. Wollner, *DOpE: Deal Optimization Environment*, 2010.

[59] J.-F. Gerbeau, *Direct and inverse modeling in hemodynamics*. Talk at the ENUMATH Conference in Leicester, 2011.

[60] O. Ghattas and X. Li, *A variational finite element method for stationary nonlinear fluid-solid interaction*, J. Comput. Phys., 121 (1995), pp. 347–356.

[61] V. Giraut and P.-A. Raviart, *Finite Element method for the Navier-Stokes equations*, Number 5 in Computer Series in Computational Mathematics, Springer-Verlag, 1986.

[62] R. Glowinski and J. Periaux, *Numerical methods for nonlinear problems in fluid dynamics*, in Proc. Intern. Seminar on Scientific Supercomputers, North Holland, Feb. 2-6 1987.

[63] C. Grandmont, *Existence for a three-dimensional steady state fluid-structure interaction problem*, Journal of Mathematical Fluid Mechanics, 4 (2002), pp. 76–94.

[64] C. Grandmont, *Existence of weak solutions for the unsteady interaction of a viscous*, SIAM J. Math. Anal., 40 (2008), pp. 716–737.

[65] T. Grätsch and K.-J. Bathe, *Goal-oriented error estimation in the analysis of fluid flows with structural interactions*, Comp. Methods Appl. Mech. Engrg., 195 (2006), pp. 5673–5684.

[66] P. Grisvard, *Elliptic Problems in Nonsmooth Domains*, vol. 24, Pitman Advanced Publishing Program, Boston, 1985.

[67] C. Grossmann and H.-G. Roos, *Numerische Behandlung partieller Differentialgleichungen*, Teubner-Studienbücher Mathematik ; Lehrbuch Mathematik, Teubner, Wiesbaden, 3., völlig überarb. und erw. aufl. ed., 2005.

[68] M. Heil, *An efficient solver for the fully coupled solution of large-displacement fluid-structure interaction problems*, Comput. Methods Appl. Mech. Engrg., 193 (2004), pp. 1–23.

[69] M. Heil, A. L. Hazel, and J. Boyle, *Solvers for large-displacement fluid-structure interaction problems: segregated versus monolithic approaches*, Comput. Mech., 43 (2008), pp. 91–101.

[70] B. Helenbrook, *Mesh deformation using the biharmonic operator*, Int. J. Numer. Methods Engrg., (2001), pp. 1–30.

[71] J. G. Heywood and R. Rannacher, *Finite-element approximation of the nonstationary Navier-Stokes problem part iv: Error analysis for second-order time discretization*, SIAM Journal on Numerical Analysis, 27 (1990), pp. 353–384.

[72] J. G. Heywood, R. Rannacher, and S. Turek, *Artificial boundaries and flux and pressure conditions for the incompressible Navier-Stokes equations*, International Journal of Numerical Methods in Fluids, 22 (1996), pp. 325–352.

[73] M. Hinze, *A variational discretization concept in control constrained optimization: The linear-quadratic case*, Comput. Optim. Appl., 30 (2005), pp. 45–61.

[74] M. Hinze and K. Kunisch, *Second order methods for optimal control of time-dependent fluid flows*, SIAM J. Control Optim., 40 (2001), pp. 925–946.

[75] M. Hinze, R. Pinnau, M. Ulbrich, and S. Ulbrich, eds., *Optimization with PDE constraints*, no. 23 in Mathematical modelling: theory and applications ; 23 ; Mathematical modelling: theory and applications, Springer, [Dordrecht u.a.], 2009.

[76] C. Hirth, A. Amsden, and J. Cook, *An arbitrary Lagrangian-Eulerian computing method for all flow speeds*, J. Comput. Phys., 14 (1974), pp. 227–253.

[77] M. Hojjat, E. Stavropoulou, T. Gallinger, U. Israel, R. Wüchner, and K.-U. Bletzinger, *Fluid-Structure Interaction in the Context of Shape Optimization and Computational Wind Engineering*, vol. 53, Springer-Verlag, 2010, pp. 355–386.

[78] G. Holzapfel, *Nonlinear Solid Mechanics: A continuum approach for engineering*, John Wiley and Sons, LTD, 2000.

[79] ——, *Structural and Numerical Models for the (Visco)elastic Response of Arterial Walls with Residual Stresses*, vol. 441, Springer-Verlag, Wien, New York, 2003, pp. 109–184.

[80] ——, *Material models for artery walls.* Talk at the university of Heidelberg, 2011.

[81] G. A. Holzapfel and R. W. Ogden, *Mechanics of Biological Tissue*, Springer, Heidelberg, 2006.

[82] J. Hron, *Fluid structure interaction with applications in biomechanics*, PhD thesis, Charles University Prague, 2001.

[83] J. Hron and S. Turek, *A monolithic FEM/Multigrid solver for ALE formulation of fluid structure with application in biomechanics*, vol. 53, Springer-Verlag, 2006.

[84] ——, *Proposal for numerical benchmarking of fluid-structure interaction between an elastic object and laminar incompressible flow*, vol. 53, Springer-Verlag, 2006, pp. 146 – 170.

[85] T. Hughes, W. Liu, and T. Zimmermann, *Lagrangian-Eulerian finite element formulation for incompressible viscous flows*, Comput. Methods Appl. Mech. Engrg., 29 (1981), pp. 329–349.

[86] J. Humphrey, *Cardiovascular Solid Mechanics: Cells, Tissues, and Organs*, Springer-Verlag New York, 2002.

[87] J. Janela, A. Moura, and A. Sequeira, *Absorbing boundary conditions for a 3d non-Newtonian fluid-structure interaction model for blood flow in arteries*, Int. J. Engrg. Sci., (2010).

[88] B. Janssen and G. Kanschat, *Adaptive multilevel methods with local smoothing for H^1- and H^{curl}-conforming high order finite element methods*, SIAM J. Sci. Comput, (2011). to be published.

[89] B. Janssen and T. Wick, *Block preconditioning with Schur complements for monolithic fluid-structure interactions*, in ECCOMAS CFD 2010, J. Pereira and A. Sequeira, eds., Lisbon, June 2010.

[90] Z. Jianhai, C. Dapeng, and Z. Shengquan, *ALE finite element analysis of the opening and closing process of the artificial mechanical valve*, Appl. Math. Mech., (2006), pp. 403–412.

[91] C. Johnson, *Numerical solution of partial differential equations by the finite element method*, Cambridge University Press, Campridge, 1987.

[92] D. Joseph and Y. Renardy, *Fundamentals of two-fluid dynamics. Part I*, Math. Theory and Applications, Springer, New York, 1993.

[93] ——, *Fundamentals of two-fluid dynamics. Part II*, Springer, New York, 1993.

[94] P. Kalita and R. Schaefer, *Mechanical models of artery walls*, Arch. Comput. Methods Eng., 15 (2008), pp. 1–36.

[95] K. Königsberger, *Analysis 2*, Springer Lehrbuch, Springer, Berlin – Heidelberg – New York, 2., korrigierte und erw. auflage ed., 1997.

[96] A. Ladd, *Numerical simulations of particulate suspensions via a discretized Boltzmann equation. part i: theoretical foundations*, Journal of Fluid Mechanics, 271 (1994).

[97] ——, *Numerical simulations of particulate suspensions via a discretized Boltzmann equation. part ii: numerical results*, Journal of Fluid Mechanics, 271 (1994).

[98] M. Lesoinne and C. Farhat, *Geometric conservation laws for flow problems with moving boundaries and deformable meshes and their impact on aeroelastic computations*, Comp. Methods Appl. Mech. Engrg., 34 (1996).

[99] J.-L. Lions, *Optimal Control of Systems Governed by Partial Differential Equations*, vol. 170 of Grundlehren Math. Wiss., Springer, Berlin, 1971.

[100] C. Liu and N. Walkington, *An Eulerian description of fluids containing visco-elastic particles*, Arch. Rat. Mech. Anal., 159 (2001), pp. 229–252.

[101] M. Luskin and R. Rannacher, *On the soothing property of the Crank-Nicolson scheme*, Applicable Analysis, 14 (1980), pp. 117 – 135.

[102] D. Meidner, *Adaptive Space-Time Finite Element Methods for Optimization Problems Governed by Nonlinear Parabolic Systems*, PhD thesis, University of Heidelberg, 2008.

[103] J. Mizerski, *Modeling heart valve dynamics.* Personal Correspondance, 2010.

[104] A. Moura, *The Geometrical Multiscale Modelling of the Cardiovascular System: Coupling 3D FSI and 1D Models*, PhD thesis, Instituto Superior Técnico, Technical University of Lisbon, 2007.

[105] A. Moura and A. Sequeira, *Coupling conditions for compliant channels.* Personal Correspondance, 2011.

[106] A. Moura, A. Sequeira, and T. Wick, *Coupling of structure outflow and absorbing fluid conditions for monolithically-coupled fluid-structure interactions applied to hemodynamical problems.* in preparation, 2011.

[107] F. Nobile, *Numerical Approximation of Fluid-Structure Interaction Problems with Applications to Haemodynamics*, PhD thesis, École Polytechnique Fédérale de Lausanne, 2001.

[108] W. Noh, *A time-dependent two-space-dimensional coupled Eulerian-Lagrangian code*, vol. 3 of Methods Comput. Phys., Academic Press, New York, 1964, pp. 117–179.

[109] C. Peskin, *The immersed boundary method*, Acta Numerica 2002, Cambridge University Press, 2002, pp. 1–39.

[110] A. Quarteroni, *What mathematics can do for the simulation of blood circulation*, tech. rep., MOX Institute, Milano, 2006.

[111] D. Rabinovich, D. Givoli, and E. Bécache, *Comparison of high-order absorbing boundary conditions and perfectly matched layers in the frequency domain*, International Journal for Numerical Methods in Biomedical Engineering, 26 (2010), pp. 1351–1369.

[112] D. Rabinovich, D. Givoli, J. Bielak, and T. Hagstrom, *A finite element scheme with a high order absorbing boundary condition*, Comput. Methods Appl. Mech. Engrg., 200 (2011), pp. 2048–2066.

[113] R. Rannacher, *On the stabilization of the Crank-Nicolson scheme for long time calculations.* Preprint, August 1986.

[114] R. Rannacher, *Numerische methoden der Kontinuumsmechanik (Numerische Mathematik 3).* Vorlesungsskriptum, 2001.

[115] R. Rannacher, *Differences between the secant and the tangent Crank-Nicolson scheme.* Personal Correspondance, 2011.

[116] T. Richter, *A monolithic multigrid solver for 3d fluid-structure interaction problems*, SIAM J. Sci. Comput., (2010). submitted.

[117] ——, *Goal-oriented error estimation for fluid-structure interaction problems*, Comp. Methods Appl. Mech. Engrg., (2011). submitted.

[118] T. Richter and T. Wick, *Finite elements for fluid-structure interaction in ALE and fully Eulerian coordinates*, Comp. Methods Appl. Mech. Engrg., 199 (2010), pp. 2633–2642.

[119] P. A. Sackinger, P. R. Schunk, and R. R. Rao, *A newton-raphson pseudo-solid domain mapping technique for free and moving boundary problems: a finite element implementation*, J. Comput. Phys., 125 (2005).

[120] N. D. D. Santos, J.-F. Gerbeau, and J. Bourgat, *A partitioned fluid-structure algorithm for elastic thin valves with contact*, Comp. Methods Appl. Mech. Engrg., 197 (2008), pp. 1750–1761.

[121] M. Schäfer, D. Sternel, G. Becker, and P. Pironkov, *Efficient Numerical Simulation and Optimization of Fluid-Structure Interaction*, vol. 53, Springer-Verlag, 2010, pp. 133–160.

[122] M. Schäfer and S. Turek, *Flow Simulation with High-Performance Computer II*, vol. 52 of Notes on Numerical Fluid Mechanics, Vieweg, Braunschweig Wiesbaden, 1996, ch. Benchmark Computations of laminar flow around a cylinder.

[123] M. Schmich and B. Vexler, *Adaptivity with dynamic meshes for space-time finite element discretizations of parabolic equations*, SIAM J. Sci. Comput., 30 (2008), pp. 369 – 393.

[124] H. Schwarz, *über einige Abbildungsaufgaben*, J. Reine Angew. Math., 70 (1869), pp. 105–120.

[125] X. Shi and N. Phan-Thien, *Distributed Lagrange multiplier/fictitious domain method in the framework of Lattice Boltzmann method for fluid-structure interaction*, J. Comput. Phys., 206 (2005), pp. 81–94.

[126] K. Stein, T. Tezduyar, and R. Benney, *Mesh moving techniques for fluid-structure interactions with large displacements*, J. Appl. Math., 70 (2003), pp. 58–63.

[127] P. L. Tallec and S. Mani, *Numerical analysis of a linearised fluid-structure interaction problem*, Numer. Math., 87 (2000), pp. 317–354.

[128] P. L. Tallec and J. Mouro, *Fluid structure interaction with large structural displacements*, Comput. Methods Appl. Mech. Engrg., 190 (2001), pp. 3039–3067.

[129] R. Temam, *Navier-Stokes Equations: Theory and Numerical Analysis*, AMS Chelsea Publishing, Providence, Rhode Island, 2001.

[130] T. E. Tezduyar, M. Behr, S. Mittal, and A. A. Johnson, *Computation of Unsteady Incompressible Flows With the Finite Element Methods—Space- Time Formulations, Iterative Strategies and Massively Parallel Implementations*, vol. 143 of New Methods in Transient Analysis, ASME, New York, 1992, pp. 7–24.

[131] F. Tröltzsch, *On the Lagrange-Newton-SQP method for the optimal control of semilinear parabolic equations*, SIAM J. Control Optim., 38 (1999), pp. 294–312.

[132] ——, *Optimale Steuerung partieller Differentialgleichungen - Theorie, Verfahren und Anwendungen*, Vieweg und Teubner, Wiesbaden, 2nd ed., 2009.

[133] S. Turek, *Efficient solvers for incompressible flow problems*, Springer-Verlag, 1999.

[134] S. Turek, J. Hron, M. Madlik, M. Razzaq, H. Wobker, and J. Acker, *Numerical simulation and benchmarking of a monolithic multigrid solver for fluid–structure interaction problems with application to hemodynamics*, tech. rep., Fakultät für Mathematik, TU Dortmund, Feb. 2010. Ergebnisberichte des Instituts für Angewandte Mathematik, Nummer 403.

[135] S. Turek, J. Hron, M. Razzaq, H. Wobker, and M. Schäfer, *Numerical benchmarking of fluid-structure interaction: a comparison of different discretization and solution approaches*, Fluid Structure Interaction II: modelling, simulation, optimization, Springer, Heidelberg, 2010, pp. 413–424.

[136] S. Turek, L. Rivkind, J. Hron, and R. Glowinski, *Numerical analysis of a new time-stepping θ-scheme for incompressible flow simulations*, tech. rep., TU Dortmund and University of Houston, 2005. Dedicated to David Gottlieb on the occasion of his 60th anniversary.

[137] K. van der Zee, E. van Brummelen, and R. de Borst, *Goal-oriented error estimation for Stokes flow interacting with a flexible channel*, International Journal of Numerical Methods in Fluids, 56 (2008), pp. 1551–1557.

[138] C. Vergara and T. Wick, *On boundary conditions for the structure outflow boundary.* Personal Correspondance at the SIMBIO conference, Bruxelles, Sep, 2011.

[139] B. Vexler, *Adaptive Finite Element Methods for Parameter Identification Problems*, PhD thesis, University of Heidelberg, 2004.

[140] J. Vierendeels, K. Dumont, and P. Verdonck, *A partitioned strongly coupled fluid-structure interaction method to model heart valve dynamics*, J. Comp. Appl. Math., (2008).

[141] I. Vignon-Clementel, C. Figueroa, K. Jansen, and C. Taylor, *Outflow boundary conditions for three-dimensional finite element modeling of blood flow and pressure in arteries*, Comp. Methods Appl. Mech. Engrg., 195 (2006), pp. 3776–3796.

[142] Visit, *Visit: an interactive parallel visualization and graphical analysis tool*, 2000.

[143] W. A. Wall, *Fluid-Struktur-Interaktion mit stabilisierten Finiten Elementen*, PhD thesis, University of Stuttgart, 1999.

[144] W. A. Wall, A. Gerstenberger, U. Küttler, and U. Mayer, *An XFEM based fixed-grid approach for 3D fluid-structure interaction*, Fluid Structure Interaction II: modelling, simulation, optimization, Springer, Heidelberg, 2010, pp. 327–349.

[145] D. Werner, *Funktionalanalysis*, Springer, 2004.

[146] T. Wick, *Adaptive finite elements for fluid-structure interactions on a prolongated domain: Applied to valve simulations*, in Comput. Methods Mech., Warsaw in Poland, May 9-12 2011.

[147] ——, *Adaptive finite elements for fluid-structure interactions on a prolongated domain: applied to valve simulations.* submitted to Arch. Mech. Engrg., 2011.

[148] ——, *An energy absorbing layer for the structure outflow boundary in fluid-structure interaction for heart valve dynamics.* submitted, 2011.

[149] ——, *Fluid-structure interactions using different mesh motion techniques*, Comput. Struct., 89 (2011), pp. 1456–1467.

[150] ——, *Solving monolithic fluid-structure interaction problems in arbitrary Lagrangian Eulerian coordinates with the deal.ii library*, tech. rep., IWR Heidelberg, 2011.

[151] T. Wick and W. Wollner, *A prototypical setting for optimal control problems governed by non-linear fluid-structure interaction.* Personal Correspondance, March 2011.

[152] J. Wloka, *Partielle Differentialgleichungen*, B. G. Teubner Verlag, Stuttgart, 1982.

[153] W. Wollner, *Adaptive Methods for PDE-based Optimal Conrol with Pointwise Inequality Constraints*, PhD thesis, University of Heidelberg, 2010.

[154] O. Zienkiewicz and J. Zhu, *The superconvergent patch recovery and a posteriori error estimates. part 1: The recovery technique*, Int. J. of Numer. Methods Engrg., 33 (1992), pp. 1331–1364.

[155] ——, *The superconvergent patch recovery and a posteriori error estimates. part 2: Error estimates and adaptivity*, Int. J. of Numer. Methods Engrg., 33 (1992), pp. 1365–1382.